Anderson localization in interacting quantum systems

Filippo Stellin

Filippo Stellin. Anderson localization in interacting quantum systems. Physics [physics]. Université Paris Cité, 2020. English. NNT : 2020UNIP7004 . tel-03141059v2

HAL Id: tel-03141059
https://hal.science/tel-03141059v2

THÈSE DE DOCTORAT DE L'UNIVERSITÉ DE PARIS

Spécialité : Physique

École doctorale n°564: Physique en Île-de-France

réalisée

au Laboratoire Matériaux et Phénomènes Quantiques

sous la direction de Giuliano ORSO

présentée par

Filippo STELLIN

Sujet de la thèse :

Anderson localization in interacting quantum systems

soutenue le 15 juin 2020

devant un jury composé de :

M.	Klaus M. FRAHM	PR	Université Toulouse III	Rapporteur
M.	Sergey E. SKIPETROV	DR	Université Grenoble Alpes	Rapporteur
M^{me}	Cécile MONTHUS	DR	CEA Saclay	Examinatrice
M.	Tommaso ROSCILDE	MCF, HDR	ENS Lyon	Examinateur
M.	Giuliano ORSO	MCF, HDR	Université de Paris	Directeur de thèse

CONTENTS

METADATA

Title: Anderson localization in interacting quantum systems

Abstract: In this thesis we theoretically investigate the behaviour of quantum particles (electrons, atoms, photons, etc.) moving in a random medium and undergoing Anderson localization. For non-interacting particles, the energy spectrum can possess one or more critical points, where the nature of the single-particle wavefunctions changes from extended to localized leading to a undergoes a metal-insulator phase transition, also known as Anderson transition.

A fundamental question is whether and how Anderson transitions survive in interacting quantum systems. Here we study a minimal model of two particles moving in a disordered lattice and subject to short-range mutual interactions. By combining large-scale numerics with Green's functions techniques, we show that two-particle Anderson transitions do occur in three dimensions and explore the phase diagram in the space of energy, disorder and interaction strength. The latter presents a rich structure, characterized by a doubly reentrant behavior, caused by the competion between scattering and bound states of the pair. We also show that previous claims of 2D Anderson transitions of the pair are essentially due to finite-size effects.

A second problem that we address in this thesis is the occurrence of 2D metal-insulator transitions for a single particle in the presence of a spatially correlated potential and subject to spin-orbit interactions, described by Rashba-Dresselhauss couplings. We illustrate that, irrespective of the properties of the disorder, there is a regime where the critical energy E_c depends linearly on the disorder strength. The slope and the intercept are studied in the vicinity of the spin-helix point, where the SU(2) symmetry is restored and the 2D metal-insulator transition disappears.

Keywords: Transport phenomena, Anderson localization, Anderson transitions, Few-body systems, Disordered lattices, Hubbard model, Green's function methods, Transfer-matrix calculations, Spin-orbit coupling, Cold atoms and matter waves.

Titre : Localisation d'Anderson dans des systèmes quantiques interagissants

Resumé : Dans cette thèse nous étudions au niveau théorique le comportement des particules quantiques (électrons, atomes, photons, etc.) se mouvant dans un milieu désordonné et sujets à la localisation d'Anderson. Pour des particules non interagissantes, le spectre de l'énergie peut posséder un ou plus points critiques, où les fonctions d'onde étendues deviennent localisées, en donnant lieu à une transition de phase métal-isolant connue comme Transition d'Anderson.

Une question fondamentale est si et comment les transitions d'Anderson survivent dans des systèmes quantiques interagissants. Dans cet ouvrage, nous étudions un modèle simple décrivant le cas de deux particules dans un réseau désordonné et sujettes à des interactions mutuelles à courte portée. En combinant des simulations numériques sur une grande échelle avec des techniques à la fonction de Green, nous montrons que les transitions d'Anderson à deux particules se produisent en trois dimensions et explorons le diagramme de phase dans l'espace de l'énergie, du désordre et de l'interaction. Cette dernière présente une structure riche, caractérisée par un double renfoncement de la limite de phase, engendrée par la compétition entre les états de diffusion et les états liés de la paire. Nous prouvons aussi que les annonces précédentes concernant l'apparition de transitions d'Anderson en deux dimensions étaient essentielment dues à des effets de taille finie.

Un deuxième problème que nous abordons dans cette thèse est celui de l'occurrence de transitions métal-isolant en deux dimensions pour une particule en la présence d'un potentiel spatialement corrélé et sujette à des interactions spin-orbite, modélisées par les couplages Rashba-Dresselhaus. On éclaire que, indépendamment des propriétés du désordre, il y a un régime où l'énergie critique E_c dépend linéairement du paramètre de désordre. La pente et l'intercepte sont étudiées en voisinage du point de symétrie spin-hélice persistant, dans lequel la symétrie SU(2) est restaurée et la transition métal-isolant disparaît.

Mots clés : Phénomènes de transport, Localisation d'Anderson, Transitions d'Anderson, Systèmes à plusieurs corps, Réseaux désordonnés, Modèle d'Hubbard, Méthodes de la fonction de Green, Méthodes de la matrice de transfert, Couplage spin-orbite, Atomes froids et ondes de matière.

REMERCIEMENTS

Les résultats présentés dans cette thèse son essentiellement fruit de mon travail, déroulé sous la supervision de Giuliano Orso, que je remercie d'abord pour la constance (et la patience) avec lesquelles il a suivi l'avancement dans le projets. Beaucoup plus orienté vers la résolution des problèmes que aux aspects formels, il a été en mèsure de me transmettre aussi des connaissances numériques, avec champ d'application allant bien au dela de mon domaine de recherche.

J'aimerais aussi remercier les rapporteurs Klaus Frahm et Sergey Skipetrov, qui m'ont permis d'améliorer sensiblement le manuscrit grâce à leurs commentaires, et les examinateurs Cécile Monthus et Tommaso Roscilde pour avoir pris le temps de lire le manuscrit et formuler des questions pertinentes et capable de mettre en évidence d'autres facettes des problèmes abordés. Le travail n'aurait été le même si je n'avais connu Nicolas Cherroret, qui m'a invité à participer à une École thèmatique et un workshop focalisés sur mon domaine et a fait partie du comité de suivi de ma thèse, ensemble avec Florent Baboux.

Même si je n'ai pas bénéficié de collaborateurs pour la réalisations de mes projets, la présence d'une brillante équipe théorique n'a pas été insignifiante, malgré mon attitude à resoudre les problèmes en solitaire. Parmi les postdoctorants, je tiens à remercier Alberto Biella, Ariane Soret, Nicola Bartolo et Riccardo Rota, avec lesquels j'ai partagé le bureau davantage, qui ont été, prodigues de conseils et disponibles. Je rappelle affecteusement aussi Manpreet Singh, très poli et perspicace, que j'ai aidé en particulier dans la phase de familiarisation avec l'ambiance du laboratoire. Parmi les doctorants qui ont soutenu leur thèse avant moi, je mentionne Jared Lolli, physicien interessé aussi aux aspects philosophiques des théories, Florent Storme, très adroit dans la réalisation des algorithmes, Fabrizio Minganti, théoricien enterprenant et intellecteuellement vitale, Filippo Vicentini, doué d'une grande intuition pour les aspects numériques. Je saisis aussi l'occasion pour remercier les doctorants qui ont accompagné les premiers jours auprès de MPQ, Aurianne de la Bretéche Minneci, attentive à la didactique, Sergueï Fedortchenko et Ibrahim Saideh, que j'ai côtoyé dans le premier bureau. Concernant les doctorants actuels que j'ai pu connaître, je souhaite une bonne rédaction de thèse et soutenance à Cassia Naudet-Baulieu, une fructueuse continuation à Zakari Denis, et des satisfaisantes recherches aux prometteurs Zejian Li et Kaelan Donatella. Je retourne par la pensée aussi à l'ancien stagiaire Zhu Zhaoxian pour les longues méditations devant l'ordinateur et ses discussions animées avec les chercheurs postdoctoraux.

Parmi les autres membres du laboratoire, je suis reconnaissant à Alexandre Le Boité de l'organisation des séminaires internes du *Theory Journal Club*, chercheur de vaste culture et rare sensibilité. Je remercie aussi les équipes organisatrices des séminaires thèsards qui se sont succédées au cours des années, Zahra Asghari, Louis Garbe, Gaël Massé, Nicolas Auvray et Félicien Appas, qui m'ont donné la possibilité de me tenir au courant des autres sujets d'investigation abordés au sein du Laboratoire ainsi que de présenter les résultats de mes recherches. Souvent en occasion des *Journées du Laboratoire*, j'ai eu l'opportunité d'entrer en contact avec d'autres membres, comme les doctorants Valerio Flavio Gili, Jacko Rastikian et Samantha Sbarra et les postdoctorants Giuseppe Marino et Simone Felicetti, et les permanents Cristiano Ciuti, Giuseppe Leo et Indranil Paul. Pour la gestion administrative et financière, je suis gré à Anne Servouze, Nathalie Merlet, Sandrine Di Concetto et Jocelyne Moreau, pour l'efficacité et la gentillesse dont elles ont fait preuve.

Je souhaite remercier aussi le personnes recontrès aux seminaires et aux conferences qui ont montré de l'interêt vers mes recherches, comme les doctorants Tamara Bardon-Brun, Sirio Belga Fedeli, Nicola Carlon Zambon, Thibault Scoquart, Jakub Janarek, Sergej Vilov, Baptiste Lecoutre, Ragheed Al-Hyder, Maxime Bertrand, les postdocs Stefano Cecchi et Gian Lorenzo Paravicini Bagliani et les permanents Grégoire Misguich, Dominique Delande, Leonardo Mazza, Nicolas Pavloff et Nicolas Roch.

Le financement à la thèse m'a été affecté dans le cadre du projet INSPIRE su programme europeen Marie Curie, qui a impliqué 60 doctorants internationaux dans des disciplines différentes. Je tiens donc à remercier le coordinateur du projet, Thomas Coudreau, les gestionnaires Lavanya Premvardhan et Sylvie Lefebvre, qui se sont relayées, et les assistants Delphine Meyer et Clément Bardoux, qui m'ont permis d'habiter à Paris auprès une résidence du Crous et m'ont orienté dans les relations avec la administration publique française. Parmi les doctorants avec lesquels j'ai plus interagi, je tourne mes pensées vers Pamela Aoun, Lakshmi Balasubramaniam, Pietro Salvatore Carollo, Saverio Francesconi, Antonino Madonia, Umberto Martino, Daniel Lopez Neumann, Mario Spagnuolo, Ana Marija Vargović, Minh Vo Hong Panh et Mathurin Wamba.

Cette thèse n'aurait vu la lumière sans le soutien moral et matériel de mes parents, Paolo et Flavia, ni sans les contributions de ma soeur Tatiana et de son fiancé Emanuele, qui m'ont aidé aussi lors de mes démenagements, et notamment lors du celui entre Paris et Orsay.

Une mention à part la mérite mon frère jumeau Gianluca, qui a suivi un parcours academique presque pareil à l'Université de Padoue, mais en choisissant de se spécialiser en physique nucléaire theorique. Après son diplôme de *Laurea magistrale*, titre italien équivalent au *Master 2* en France, il a obtenu une bourse de doctorat auprès de l'Université de Bonn, où il est maintenant en train de conclure la rédaction de sa thèse. Ce fait m'a permis encore une fois de me servir d'un conseil adapté, capable de donner contributions d'idées presque à tout moment, malgré l'éloignement. Il m'a également permis d'entrer en contact avec d'autres doctorants, même dans d'autres disciplines, comme Andria et Dimitri Agadžanov, Muhammad Naeem Anwar, Sahar Brahim, Cátia Domingos, Chaitra Kalmahalli Guruswamy, Francesca et Vittoria Lopez, Mikhail Mikhašenko, Stefan Ropertz, Nikolas Schlage, Martin Ueding, Falk Zimmermann, que je remercie vivement, en particulier pour les journées de fête passées ensemble.

Filippo Stellen

INTRODUCTION

Ordered systems, thanks to their symmetry and regularity, lend themselves to being described by mathematical models. On the other hand, impurities, defects and dislocations are abundant in nature and a quantitative description of their effect on the physical properties of materials represents a challenging task. In an infinite crystal, characterized by translational symmetry, the wavefunctions of valence electrons are described by Bloch functions, which are extended all over the medium. Then, the finiteness of conductivity in real samples is due to deviations of the ion positions from perfect periodicity, owing to thermal vibrations.

The addition of impurities results in perturbative (negative) corrections to the conductivity of the material, as long the De Broglie wavelength of electrons is smaller than their mean free path. At strong enough disorder the latter condition is no longer satisfied and a novel phenomenon takes place: the electron propagation is completely suppressed and its wavefunction becomes exponentially localized in space, with a characteristic length named localization length. Importantly, Anderson localization is not due to the complete filling of an energy band but rather to the scattering against randomly distributed impurities.

The occurrence of a transition from extended to localized states was first predicted in 1958 by P. W. Anderson, who was able to explain the origin of localization of spin excitations in doped semiconductors [1], experimentally observed in 1956 by Feher's group [2]. In particular the electronic excitations (resulting from the hyperfine coupling with nuclear spins) were localized at low electron concentrations, contrarily to theoretical expectations at that time, and localization was circumvented by thermally activated hopping between discrete localized states. By means of a pertubative expansion in terms of the tunnelling elements, Anderson proved that electronic eigenfunctions decay exponentially at strong disorder or close to the band edges (in the so-called Lifshitz tails [3,4]).

A decade later, Mott introduced the concept of mobility edge [5] as the energy value separating the metallic from the insulating regime while Thouless pointed out the sensitivity of conductance under changes of boundary conditions [6]. A great progress in the comprehension of the nature of Anderson localization was achieved in 1979, when the scaling theory was proposed by Abrahams et al. [7], who proved that in disordered systems localization persists also in two dimensions and explained the scaling behaviour of conductance, based on the ideas of Landauer and Thouless. It was demonstrated indeed that the latter quantity vanishes at zero temperature with a universal critical exponent.

Besides, the renormalization group theory, put forward by Wegner [8], was able to establish a connection with second-order phase transitions, using an approach analogous to the one used in spin systems. The nonlinear σ-model introduced in 1979 [9] and further developed by Efetov et al. [10], corroborated the scaling predictions in $d \leq 2$ and shed light upon the conductance fluctuations. Quantitative estimations of the relevant quantities involved in localization were obtained within the framework of the self-consistent theory elaborated by Wölfle and Vollhardt [11] [12] on the basis of the ideas of Abou-Chacra [13]. Although this theory is mean-field like and therefore cannot predict the correct values of the critical exponents, it nevertheless provides reasonably good estimates of the phase boundary between metallic and insulating states. Taking place in the strong scattering regime, the Anderson transition defies analytical treatments. Hence, the role of numerical simulations is crucial for a quantitative study of the phase transition, from the identification of the critical point to the computation of the universal critical exponents [14] [15]. Several techniques have been developed for this purpose going from transfer-matrix [16] [17] and Green's function [18] techniques, to approaches based on energy-level statistics [19–21] or multifractality [22, 23]. By studying the behaviour of the localization length, which diverges at the critical point in the thermodynamic limit, it is also possible to evaluate critical exponents and the parameters by means of the finite-size scaling procedure [17].

On the experimental front, the first setups have involved doped semiconductors, where the degree of disorder has been varied by tuning the concentration of dopant atoms, which have been prominently phosporous or boron atoms in silicon crystals [24]. These experiments provided large differences in the estimations of the relevant critical exponent, due probably to interaction between electrons as well as to the finiteness of the temperature of the sample, which introduces nonuniversal properties to the conductance and forces one to extrapolate the scaling behaviour at zero temperature.

Owing to the wavelike nature of localization, the phenomenon has been inquired in other platforms, involving also classical waves, which, differently from the quantum ones, neither interact nor localize at low frequencies, when the wavelength exceeds the typical size of the scatterer. Amidst the realizations concerning waves belonging to the former kind, we can mention those with electromagnetic [25], elastic [26], acoustic [27] and seismic waves [28]. The development in laser-cooling techniques has also opened the possibility to study Anderson localization in cold atoms. Compared to condensed-matter systems, in atomic gases the disorderd potential, generated by optical waves, can be more easily controlled and tuned, as well as the effective dimensionality, by varying the geometry of the confining potential. Furthermore, the particle statistics can be selected and even the strength of interactions can be adjusted, exploiting Feshbach resonances. However, a drawback of these lattices is the smallness of the samples analyzed, that are tipically tenths of millimeter [29]. The role of interactions on Anderson transitions has recently received considerable attention, evolving into the flourishing research field of many-body localization [30].

In this thesis we investigate interaction-induced Anderson transitions in two- and three-dimensional systems from the viewpoint of two-body physics, which is a largely unsolved problem due to the large computational complexity. In particular, by making use of large-scale calculations with state-

of-the-art supercomputers, we succeed to study the three-dimensional geometry, which has never been examined before. We unveil the complete phase diagram of the pair in the energy-disorder-interaction space.
Beyond mutual interactions, in this thesis we also inspect the role of spin-orbit coupling in disordered potentials endowed with spatial correlations, like the laser speckle pattern. More in detail, we consider a spin-orbit interaction, which breaks spin-rotation invariance, thus paving the way to the appearance of a metallic behaviour in two dimensions.

The dissertation is structured as follows. In Chapter 1 we first give a primer on Anderson localization as a wave-like phenomenon, that can take place in a plethora of different platforms. Afterwards we will introduce Anderson's model and review its localization properties, focusing on the three-dimensional case. In Chapter 2 we discuss how to extract the position of the critical point from transmission amplitude calculations performed on an elongated bar. We outline a new procedure which holds also for relatively short bars, which will be systematically exploited in the subsequent chapter. In Chapter 3 , after presenting the formalism and its numerical implementation, we show that the interaction-induced Anderson transition belongs to the orthogonal universality class. We build the complete phase diagram of the pair. In Chapter 4 we take up the one-particle problem, where an atom is subject to a spatially correlated random potential and to an artificial spin-orbit coupling. We investigate the behaviour of the mobility edge along the crossover from the symplectic to the orthogonal class. Overall conclusions and hints for further investigations are traced in the final chapter.

CHAPTER 1

LOCALIZATION IN DISORDERED SYSTEMS

In this chapter we will first present Anderson localization as a wavelike phenomenon, induced by disorder, with a particular attention on quantum particles. We will then provide an overview on experimental observations of this phenomenon in different platforms, both in the classical and in the quantum domain. Next, we present the mathematical model for disordered systems focusing on the Anderson's model, whose known results are reviewed, in particular, the mobility edge appearing in three-dimensional systems and the related phase diagram in the energy-disorder plane. Various theoretical frameworks have been proposed in order to describe the Anderson transition, and we will dwell upon the one-parameter scaling theory of localization, showing the crucial role played by the global symmetries of the Hamiltonian and the spatial dimension of the system. Another approach, able to explain transitions on the basis of changes in energy-level spacing statistics, known as random matrix theory, is briefly explained in Appendix A.1.

The last section of the chapter is devoted to the introduction of the two-particle problem in the presence of short-range interactions, a system which will be investigated in-depth in Chapter 3. In particular, we review some of the most significant results of previous theoretical works, summarizing the main findings on pair localization in low-dimensional geometries ($d \leq 2$).

1.1 General definition

As discussed in the interoduction, Anderson localization refers to a wavelike phenomenon in which propagation in a medium is halted by the presence of randomly placed impurities. Considering a travelling plane wave as shown in Fig. 1.1, the interference phenomena between the waves generated by its scattering off the sites can give rise to the suppression of diffusion if the lattice is disordered enough. As a result, a standing wave is produced within a certain region, where the wave amplitude decreases exponentially. The origin of this fact can be illustrated by expressing the transmission probability of a wave between the positions $\boldsymbol{r}, \boldsymbol{r}'$ in the space as the square modulus of the contributions from all

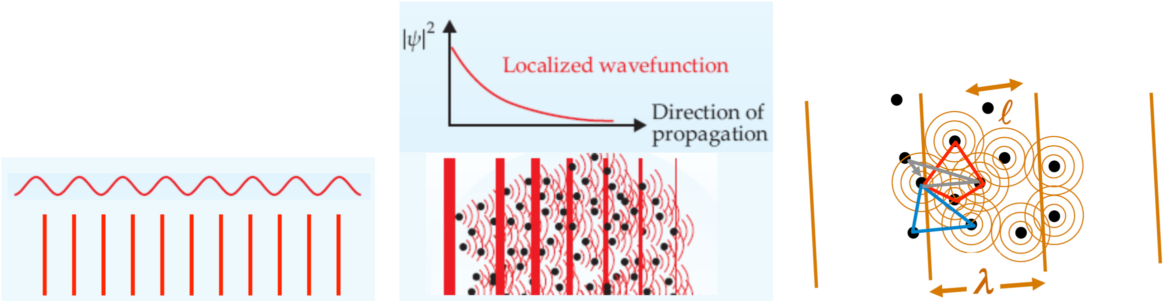

(a) Extended wave (b) Localized wave (c) Mean free path and wavelength

Figure 1.1 – An extended wave in the free espace (a) and a localized wave (b) in a disordered medium, where it acquires a characteristic exponential decay, as shown in the small panel on the top. In the one on the bottom the straight lines denote the wave front again, with a width proportional to the amplitude, as well as the wavelets rescattered by the randomly distributed obstacles. On the right panel (c), the definitions of wavelength and mean free path are shown qualitatively. From Ref. [31].

different paths between the two points,

$$P(\boldsymbol{r},\boldsymbol{r}') = \left| \sum_j A_j(\boldsymbol{r},\boldsymbol{r}') \mathrm{e}^{i\varphi(\boldsymbol{r},\boldsymbol{r}')} \right|^2 .$$

The latter relation can be rewritten isolating the summations on the incoherent contributions from the ones on the interference terms:

$$P = \left| \sum_j A_j \right|^2 + \sum_{j,k} A_j^* A_k \mathrm{e}^{\mathrm{i}(\varphi_k - \varphi_j)} . \tag{1.1}$$

Supposing that the dephasing between the individual scattering paths is random and that no absorption process occurs, the second term in Eq. (1.1) cancels out in infinitely large systems. Nevertheless, if time-reversal symmetry is present, the dephasing between paths with different propagation direction inside identical loops vanishes, so the summation on the right in Eq. (1.1) remains finite. The probability to come back to the origin is thus enhanced, an effect which depends of the dimensionality d of the lattice: in particular in $d = 1, 2$, $P(\boldsymbol{r},\boldsymbol{r}) = 1$, since the random walk is recurrent, whereas in $d = 3$, P varies according to the density of scatterers. More quantitatively, the occurrence of localization in the latter situation is related to the length of the mean free path ℓ, compared to the wavelength λ, as stated by the Ioffe-Regel criterion, introduced independently by A. Ioffe and A. Regel in 1960 [32], which reads

$$\ell \lesssim \frac{\lambda}{2\pi} ,$$

where ℓ decreases as the degree of disorder increases. When the latter quantity is weak, scattering events are very spaced and multiply scattered waves do not interfere, leading to incoherent transport, which is described by random walk of step ℓ. On the other hand, in $d = 1, 2$, a wave gets localized at any value of the mean free path ℓ, and thus at any degree of randomness of the medium.

In the case of a quantum particle, like an electron in a crystal, Bloch theorem affirms that all eigen-

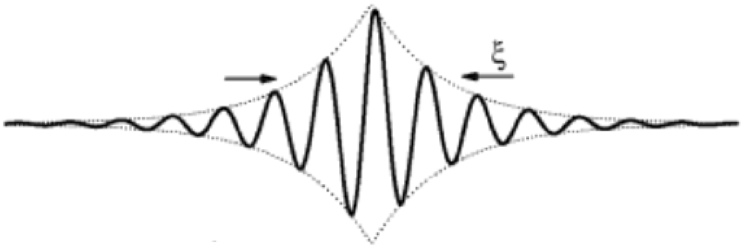

FIGURE 1.2 – The localization length ξ of a wavefunction in an one-dimensional random lattice. From Ref. [29].

states of valence are extended and thus their energy levels are separated by energy gaps where no states do exist, thanks to completely destructive wave interference. In the presence of defects, deviations from the translational-invariant case emerge, until localized states between the gaps appear. Neglecting interactions between electrons, the states obey the time-independent Schrödinger equation,

$$\left(-\frac{\hbar^2\nabla^2}{2m_e}+V(\boldsymbol{r})\right)\psi_E(\boldsymbol{r})=E\psi_E(\boldsymbol{r})\ , \tag{1.2}$$

where $V(\boldsymbol{r})$ represents the lattice potential. If the typical amplitude of the latter is high enough, then the eigenfunction at energy E has a maximum in the point $\boldsymbol{r}_n$ and satisfies the relation

$$|\psi_E(\boldsymbol{r})|\leq C_n\mathrm{e}^{-\frac{|\boldsymbol{r}-\boldsymbol{r}_n|}{2\xi}}\ , \tag{1.3}$$

in which C_n, $\boldsymbol{r}_n$ and ξ depend on energy, and the latter quantity is defined as the localization length, shown in Fig. 1.2. The eigenstates above an energy threshold E_c called mobility edge are extended in the whole lattice, whereas the ones lying below are localized as shown in Eq. (1.3). This implies that, if the Fermi energy is located below the mobility edge, the diffusion coefficient D vanishes at long times:

$$D=\frac{1}{2d}\lim_{t\to+\infty}\frac{\overline{\langle\boldsymbol{r}^2\rangle}}{t}=0\ ,$$

where the brackets $\langle\cdot\rangle$ denote the expectation value, while the bar $\bar{\cdot}$ indicates the average over the realizations of the disordered potential. Under this condition, the conductance at zero temperature decreases with the length of the sample L as

$$\sigma\propto\mathrm{e}^{-L/\xi}\ ,$$

where the localization length is evaluated at the Fermi energy. When $E_F>E_c$, the average square position $\overline{\langle\boldsymbol{r}^2\rangle}$ depends linearly on time, and the diffusion coefficient is constant.

1.2 Experimental evidence

Since it is a general wavelike phenomenon, Anderson localization has been investigated in several platforms, involving quantum as well as classical waves. The first experimental verification has been executed in charge-uncompensated semiconductors (in Si:P samples in particular) in 1983 by Paalanen and Thomas [24], who looked at the behaviour of conductivity and dielectric susceptibility on both sides of the transition, finding a critical exponents of 0.5, somewhat far from the prediction of the self-consistent theory ($\nu = 1$), available at the time. Another group [33], working on charge-compensated semiconductors extracted an exponent of 1, and the discrepancy was ascribed to the presence of local magnetic moments induced by Coulomb interactions [14] and to the finiteness of temperature [34]. In those systems, the typical disorder amplitude was controlled by varying the concentration of doping atoms [35] or the concentration of charge carriers by means of optical excitation in photoconductors. Due to the presence of interactions and to the difficulty in reducing the coupling with a thermal reservoir, observations in solids are hardly noiseless, and, thanks to the development in cooling techniques, cold atom gases established themselves as a more suitable setup for studying the phenomenon with quantum waves. Aside from matter waves, much interest has also been drawn by classical waves, since they do not interact and the fact that some additional properties (besides conductance), like the statistical distribution of intensity as well as the complex amplitude [36], can be measured. In particular, when the wavelength is much smaller than the other length scales (like mean free path ℓ or lattice spacing a), polarization can be neglected and elecromagnetic waves can be seen as classical waves satisfying Helmholtz equation.

Localization of electromagnetic waves has been demonstrated in different frequency domains, including the ones of microwaves and infrared, but not at lower frequencies, when Rayleigh scattering enhances the mean free path, due to the fact that the wavelength becomes much larger than the average spacing between the impurities. In low dimensions, light localization has been realized [37] and confirmed, and a particular setup is the one shown in Fig. 1.3, where a photonic crystal is portrayed. The dimensionality reduction is performed by considering a photorefractive crystal in which a 2D speckle pattern (for a quantitative description, see Sec. 4.1), generated by shining a laser into a diffusor, is added to the interference pattern of plane waves. The disorder lying in two dimensions gives rise to small fluctuations of $\frac{|\Delta n|}{n_0} \sim 2 \cdot 10^{-4}$ in the refractive index n_0, which plays the role of the random potential in the Schrodinger-like Helmholtz equation in paraxial approximation, satisfied by the amplitude of the probe beam in the medium, according to the approach developed in [38].

Photonic crystals represent also a suitable platform [39] for the realization of another disorder model bearing similarities with Anderson's one, the Aubry-André-Harper model [40], in which the lattice potential is pseudo-random, like the one reproduced by the superposition of two lattices with incommensurate spacings. The phase transition in that case shows up even in one-dimension [40].

On the other hand, for Anderson's model in three dimensions, the experimental results obtained by the groups of Lagendijk [41] and Maret [42] in fine GaAs and TiO_2 powders respectively have been recently questioned by Sperling et Al. [43], who attributed the exponential decay of the transmission

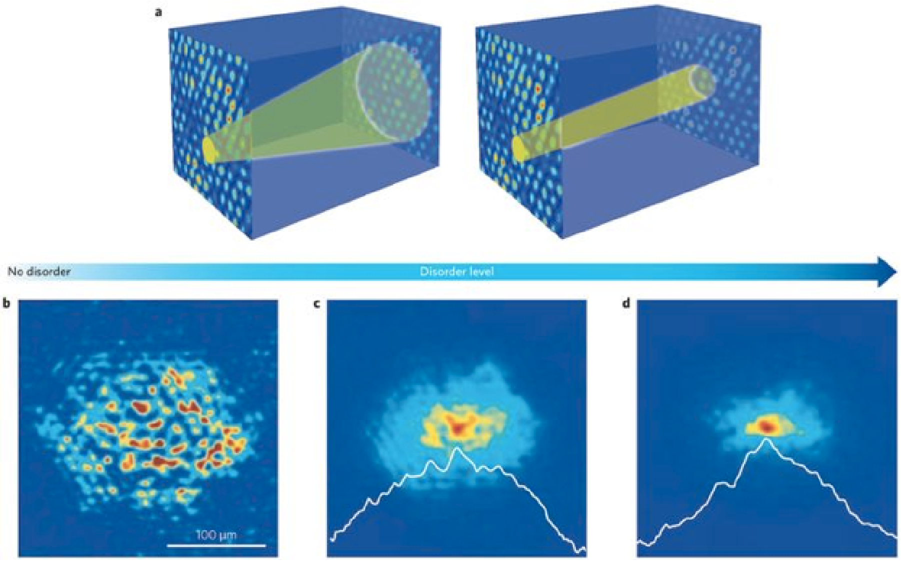

FIGURE 1.3 – Transverse localization and experimental results for light propagation in disordered lattices. In the upper panel (**a**) a probe beam entering a photorefractive crystal is shown at low (left image) and higher disorder (right one). In the lower panel, the pattern of the random potential on the transverse plane is displayed, at zero disorder (**b**), intermadiate (**c**) and higher enough to localize the beam intensity (**b**). The latter quantity, averaged over 100 disorder realizations, is portrayed as the white solid curve, setting logscale in abscissa. From Ref. [25].

coefficient to fluorescence. In the microwave range, experiments have been carried out in waveguides with randomly placed metallic spheres [44] as well as in dielectric samples [45] endowed with a quasi-1D geometry. In those systems, the achievement of localization was detected from scale-dependent diffusion and large fluctuations on the transmission. Therefore localization of electromagnetic waves in three dimensions is still an open problem, due to the fact that the phenomenon is hindered by absorption which also affects transmission coefficient as an exponential extinction, and recent works propose cold atoms subject to an external constant magnetic field [46] as a medium in which propagation of light can be halted.

Another kind of classical waves in which localization has been tested is given by elastic wave produced by vibrations in solids [26]. The first experimental observation was conducted on an network of aluminium beads brazed together [47], inspecting the angular dependence of the reflection coefficient, which possesses a peak around the backscattering direction. When the direct and the time-reversed paths start adding up coherently, the peak is enhanced and its width acquires a time-dependence dictated by the inverse of the diffusion coefficient: that manifestation is regarded as a precursor of strong localization. In a similar setup the propagation of ultrasound waves has been probed [48], obtaining the first demostration of Anderson transition in three dimensions with acoustic waves. In two-dimensions, the first realization was achieved by Weaver [27], who noticed around a point source a concentration of energy whose intensity slowly decayed owing to absorption, using inhomogeneous plates. Interestingly, coherent backscattering has also been detected in seismic waves, analysing the

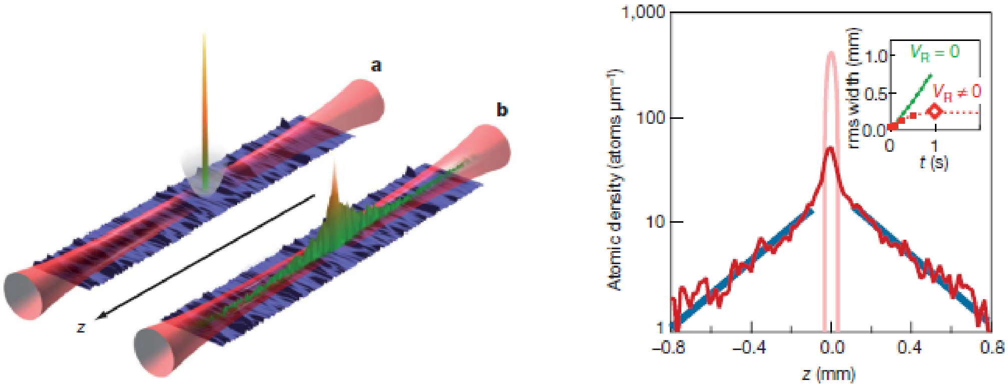

(A) Atomic gas expansion (B) Behaviour of the numerical density

FIGURE 1.4 – Observation of exponential localization in a one-dimensional lattice. On the left panel the experimental setup of [54] is portrayed, showing the expansion of the atomic cloud after the switching off of the longitudinal trap: on the bottom-right image (**b**) the exponential profile of atomic density, obtained by direct imaging, is displayed. The latter quantity is shown in detail in the right panel, where the scale in ordinate is logarithmic and also the fitting curve on the tails is present (blue solid curve). The clearer curve in the center represents the density before the release of the condensate. In the inset the behaviour of $\langle z^2 \rangle(t)$ is plotted at different values of the typical amplitude of the random potential V_R: when the latter quantity is finite, a stationary regime is reached after 0.5 s, in accordance with Eq. (1.2), thus signalling the onset of localization. From Ref. [54].

interference effects between waves artificially produced on Earth surface [28].

Unlike electronic systems, in atomic gases cooled at low temperature (of the order of the μK), disorder is not fixed by the specific realization of the sample and interactions can be tuned, by means of Feshbach resonances. The fact that the external potential commonly generated by optical means (exploiting the dipole-field interaction) can be adjusted makes also the dimensionality more controllable. Even the statistics of particles can be chosen, realizing atomic clouds with bosons, fermions or mixtures, but the size of the atomic systems are typically small, reaching the order of 10^6 atoms [29].

The first experiments with cold atoms exploited the (approximate) map between Anderson's model (in Eq. (1.9)) and the kicked-rotor one, which was proved by Prange et Al. in 1982 [49]. The latter paradigm, featuring localization in momentum space, describes a particle constrained on a ring and periodically kicked by a field. In the first realization with laser-cooled atoms, achieved in 1994 [50], the kicks were reproduced by a pulsed standing wave. In order to obtain the analogous of the three-dimensional Anderson model, modulations of the kick strength, with incommensurate frequencies, have to be introduced [51], as it was performed by Szriftgiser et al. [52]. The critical exponent found by the latter group proved to be compatible with the one of Anderson's model, in accordance with the numerical demonstration in [53].

Concerning the spatial domain, localization in $d = 1$ has been tested with Bose-Einstein condensates in [54] and [55], but in the previous one the disorder is given by the speckle potential (described in Sec. 4.1), whereas in the second one the random potential is built by superimposing two periodic lattices with incommensurate periods. This kind of potential, that guarantees a constant tunneling between nearest-neighbour sites, presents the peculiar feature of exhibiting a crossover between localized and extended states already in $d = 1$, as predicted by the Aubry-André model [40]. In the first demonstration, whose setup is displayed on the left panel of Fig. 1.4, the quantities of interest were the density of atoms as a function of the position, $n(z,t)$, plotted on the right panel of the aforementioned figure, and the average square position, $\langle z^2\rangle(t) := \int \mathrm{d}z\, z^2 n(z,t)$, which possesses a different time-evolution according to the disorder strength, as seen in Eq. (1.2). In three dimensions, Anderson transition has been recently detected in speckle potentials by De Marco's [56], Aspect's [57] and Inguscio's [58] groups, but on the position of the mobility edge the experimental results do not agree very well with the ones of numerical simulations [59].

1.3 Models of disordered systems

The Hamiltonian of a single particle moving in a background of randomly-distributed fixed impurities (quenched disorder) is given by:

$$H = -\frac{\hbar^2\boldsymbol{\nabla}^2}{2m} + V(\boldsymbol{r}) \,,$$

where m is the effective mass of the particle, and $V(\boldsymbol{r}) = \sum_{j=1}^{N} U_j(\boldsymbol{r} - \boldsymbol{R}_j)$, $\boldsymbol{R}_j$ is the random potential, generated by the impurities distributed at positions $\boldsymbol{R}_j$, with $j = 1, 2, \ldots, N$ denoting the positions of the impurities. If the scatterers are identical, $U_j \equiv U$ for any j, the Hamiltonian concides with the one introduced by Edwards [60].

A disordered potential is characterized by the on-site distribution function $P(V)$ and by a correlation function $C(\boldsymbol{r},\boldsymbol{r}') = \overline{V(\boldsymbol{r})V(\boldsymbol{r}')}$ where $\bar{\cdot} = \int \mathrm{d}V\, P(V)$ denotes the average over different disorder realizations. In cold-atom realizations a common lattice potential is given by the speckle pattern, which can be obtained by shining a laser on a diffusive plate, that lends a random phase to the electric field. The resulting dipole-field interaction possesses a random behaviour in coordinate space and its values are distributed according to Rayleigh law, as shown in Sec. 4.1. Uncorrelated potentials have $C(\boldsymbol{r},\boldsymbol{r}') = \delta^{(3)}(\boldsymbol{r} - \boldsymbol{r}')$, and their long-time and long-distance behaviour is equivalent to the one of models with finite-range correlations [61], with renormalized parameters. On the other hand, correlations with infinite range, beside shifting the mobility edge in $d = 3$, can even lead to the occurrence of transitions in $d = 1$ [62,63], in the absence of other interactions.

Because of the practical difficulty of finding solutions of Schrödinger equation when there is no long-range order in the potential, a possibility is to make use of the tight-binding model, in which the single-particle wave-function is expressed in terms of the orthogonalized orbitals around each scatterer of the medium. The stationary Schrödinger equation of the particle near the j-th scatterer reads:

$$H_j\psi(\boldsymbol{r}) = \left(-\frac{\hbar^2\boldsymbol{\nabla}^2}{2m} + U(\boldsymbol{r} - \boldsymbol{R}_j) + \Delta U(\boldsymbol{r})\right)\psi(\boldsymbol{r}) = E_j\psi(\boldsymbol{r}) \,, \tag{1.4}$$

where $\Delta U(\boldsymbol{r})$ denotes the correction to the single-scatterer potential $U(\boldsymbol{r}-\boldsymbol{R}_j)$ due to the presence of the other sites [64]. The wave-function can be expanded as:

$$\psi(\boldsymbol{r}) = \sum_{k=1}^{N}\sum_{\alpha} a_{k,\alpha}\langle \boldsymbol{r}|k,\alpha\rangle := \sum_{k=1}^{N}\sum_{\alpha} a_{k,\alpha}\phi_\alpha(\boldsymbol{r}-\boldsymbol{R}_k)\ . \tag{1.5}$$

By substituting the right-hand side of Eq. (1.5) into Eq. (1.4) and labeling the eigenvalues of the single-scatterer Hamiltonian as,

$$\left(-\frac{\hbar^2\boldsymbol{\nabla}^2}{2m}+U(\boldsymbol{r}-\boldsymbol{R}_k)\right)\phi_\alpha(\boldsymbol{r}-\boldsymbol{R}_k) = v_{\alpha,k}\phi_\alpha(\boldsymbol{r}-\boldsymbol{R}_k)\ ,$$

Eq. (1.4) becomes:

$$\sum_{k=1}^{N}\sum_{\alpha} v_{k,\alpha}a_{k,\alpha}\phi_\alpha(\boldsymbol{r}-\boldsymbol{R}_k)+\sum_{k=1}^{N}\sum_{\alpha}\Delta U(\boldsymbol{r})a_{k,\alpha}\phi_\alpha(\boldsymbol{r}-\boldsymbol{R}_k) = E_j\sum_{k=1}^{N}\sum_{\alpha} a_{k,\alpha}\phi_\alpha(\boldsymbol{r}-\boldsymbol{R}_k)\ . \tag{1.6}$$

By multiplying on the right both sides of Eq. (1.6) by $\phi^*_\beta(\boldsymbol{r}-\boldsymbol{R}_j)$ and integrating in the space coordinate, one finds:

$$v_{\beta,j}a_{\beta,j}+\sum_{k=1}^{N}\sum_{\alpha}\int \mathrm{d}\boldsymbol{r}\,\phi^*_\beta(\boldsymbol{r}-\boldsymbol{R}_j)\Delta U(\boldsymbol{r})\phi_\alpha(\boldsymbol{r}-\boldsymbol{R}_k)a_{k,\alpha} = E_j a_{j,\beta}$$

where the following orthonormality relation has been exploited,

$$\int \mathrm{d}\boldsymbol{r}\,\phi^*_\beta(\boldsymbol{r})\phi_\alpha(\boldsymbol{r}) = \delta_{\alpha,\beta}\ , \tag{1.7}$$

and the integrals involving only pairs of orbitals centered at different sites, like $\int \mathrm{d}\boldsymbol{r}\,\phi^*_\beta(\boldsymbol{r}-\boldsymbol{R}_j)\phi_\alpha(\boldsymbol{r}-\boldsymbol{R}_k)$ with $j\neq k$, have been neglected. Denoting the overlap integral in Eq. (1.7) as $J_{jk,\alpha\beta} := \int \mathrm{d}\boldsymbol{r}\,\phi^*_\beta(\boldsymbol{r}-\boldsymbol{R}_j)\Delta U(\boldsymbol{r})\phi_\alpha(\boldsymbol{r}-\boldsymbol{R}_k)$, the latter equation can be seen as an eigenvalue equation for the Hamiltonian $\hat{H}$ expressed in the 'Wannier' basis $\{|j,\alpha\rangle\}$:

$$\hat{H} = \sum_{j=1}^{N}\sum_{\alpha} v_{j,\alpha}|j,\alpha\rangle\langle j,\alpha| + \sum_{j,k=1}^{N}\sum_{\alpha,\beta} J_{jk,\alpha\beta}|k,\beta\rangle\langle j,\alpha|\ , \tag{1.8}$$

where the $J_{jk,\alpha\beta}$ represents the tunneling amplitude between the orbitals α and β, located in the sites j and k respectively. The model described by the tight-binding Hamiltonian (in Eq. (1.8)) is also the discrete analogue of the case of randomly-distributed identical scatterers, in the limit of a large number of orbitals per site. The framework is also suitable for the treatment of alloys whose components are randomly positioned in the lattice. In principle, both the on-site energies $v_{i,\alpha}$ and the tunneling amplitudes $J_{ij,\alpha\beta}$ are random variables and numerical simulations on that general case have reported an enhancement of localization [65] with respect to the original Anderson's model, where the

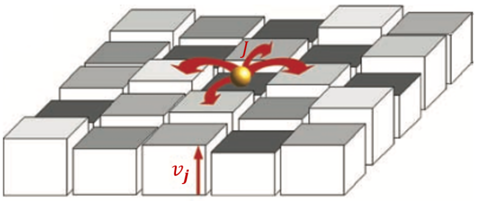

FIGURE 1.5 – A quantum particle in a two-dimensional disordered lattice in $d = 2$, where the physical meaning of the parameters of Anderson's model is also outlined. From Ref. [72].

tunneling terms are taken to be constant and the disorder is thus purely site-diagonal. The former case has been analysed in particular in low dimensions [66] [67], and even the case of complex hopping, reproducing the situation in which a charged particle is subject to an external randomly-oriented magnetic field [14], has been theoretically investigated [68]. On the contrary, when only off-diagonal randomness is present, the Hamiltonian can admit extended eigenstates even in $d = 1$ [69,70] and $d = 2$ [71].

1.3.1 The Anderson model

The simplest case of a disordered lattice described by a tight-binding Hamiltonian of the form given by Eq. (1.8), is the one in which only one orbital per site is accessible while the tunneling terms follow a so narrowly-peaked distribution that they can be regarded as constant. The resulting Hamiltonian is then the Anderson's one:

$$\hat{H} = \sum_{\boldsymbol{i}} v_{\boldsymbol{i}} |\boldsymbol{i}\rangle\langle\boldsymbol{i}| - J \sum_{\{\boldsymbol{i},\boldsymbol{j}\}} |\boldsymbol{i}\rangle\langle\boldsymbol{j}| \,, \tag{1.9}$$

where $|\boldsymbol{i}\rangle$ denotes the orbital of a single particle located in the site $\boldsymbol{i} \in \mathbb{Z}^d$ of a lattice with volume L^d and $v_{\boldsymbol{i}}$ labels the energy associated to that state. The on-site energies are statistically independent and follow the uniform distribution in the interval $[-W/2, W/2]$ [14],

$$p(v_{\boldsymbol{i}}) = \frac{1}{W} \Theta\left(\frac{W}{2} - |v_{\boldsymbol{i}}|\right) \,, \tag{1.10}$$

whereas the hopping amplitude J between nearest-neighbour sites is constant. The meaning of the parameters of Anderson's Hamiltonian is further clarified in Fig. 1.5, representing a quantum particle in a two-dimensional disordered lattice.

In order to find a finite-dimensional Hilbert space of dimension N^d, a convenient choice is to impose periodic boundary conditions on the eigenfunctions, thus obtaining a complete set of the latter. In the absence of disorder ($W = 0$), the one-particle Hamiltonian is translationally invariant and its eigenstates, defined by $\hat{H}|\psi\rangle = E|\psi\rangle$, are Bloch waves $\psi_{\boldsymbol{k}}(\boldsymbol{i}) = \mathrm{e}^{\mathrm{i}\boldsymbol{k}\cdot\boldsymbol{i}a} u_{\boldsymbol{k}}(\boldsymbol{j})$ with trivial periodic

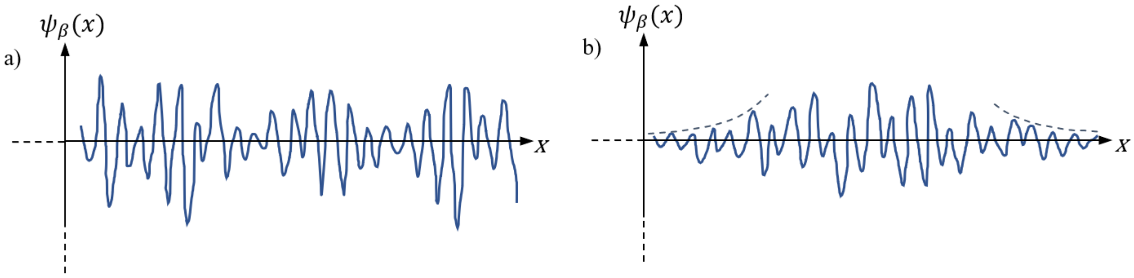

Figure 1.6 – Examples of eigenfunctions of Anderson's Hamiltonian plotted plotted as functions of one spatial coordinate. In a) an extended eigenstate, taking the appearance of a deformed Bloch state, is represented, while in b) a localized eigenstate, having asymptotically exponential tails (dashed curves) is portrayed.

function $u_{\boldsymbol{k}}(\boldsymbol{j}) = N^{-d/2}$:

$$\psi_{\boldsymbol{k}}(\boldsymbol{j}) := \langle \boldsymbol{j} | \psi_{\boldsymbol{k}} \rangle = \frac{\mathrm{e}^{i\boldsymbol{k}\cdot\boldsymbol{j}a}}{\sqrt{N^d}} \; , \tag{1.11}$$

where $a := \frac{L}{N}$ denotes the lattice constant and $\boldsymbol{k} = \frac{2\pi}{L}\boldsymbol{n}$, in which $\boldsymbol{n} \in \{0, ..., N-1\}^d$. The eigenenergies are given by:

$$E_{\boldsymbol{k}} = -2J \sum_{s=1}^{d} \cos\left(k_s a\right) \; . \tag{1.12}$$

In the presence of disorder ($W \neq 0$), the features of eigenstates change according to energy and dimensionality. The localized wave-functions, which represent the whole of the eigenfunctions in $d \leq 2$, possess asymptotic behaviour described by:

$$|\psi_\beta(\boldsymbol{j})| \sim \mathrm{e}^{-|\boldsymbol{j}-\boldsymbol{j}_{0,\beta}|a/\xi_\beta} \; ,$$

where ξ_β indicates the localization length of the eigenstate $\psi_\beta(\boldsymbol{j})$ (see Fig. 3.1). In $d = 1$, the former quantity depends on disorder typical amplitude as [73]

$$\xi = 2\ell \propto W^{-2} \; , \tag{1.13}$$

according to both numerical simulations [74] and a perturbative approach in the weak-disorder ($W \ll J$) limit [75].

In the limit of infinite disorder, eigenfunctions become localized in single sites of the lattice, $\Psi_{\boldsymbol{i}}(\boldsymbol{j}) = \delta_{\boldsymbol{i},\boldsymbol{j}}$ with eigenenergies corresponding to the on-site energies $E_{\boldsymbol{i}} = v_{\boldsymbol{i}}$.

In $d = 3$, however, all eigenstates of Anderson's Hamiltonian are localized when $W > W_c^{\max} \approx 16.536J$ [76]. For lower values of disorder strength, there exists an energy interval $E_{c,1} < E < E_{c,2}$, within which the states are delocalized. In infinite-sized lattices, $E_{c,1} = -E_{c,2}$, since an exact particle-

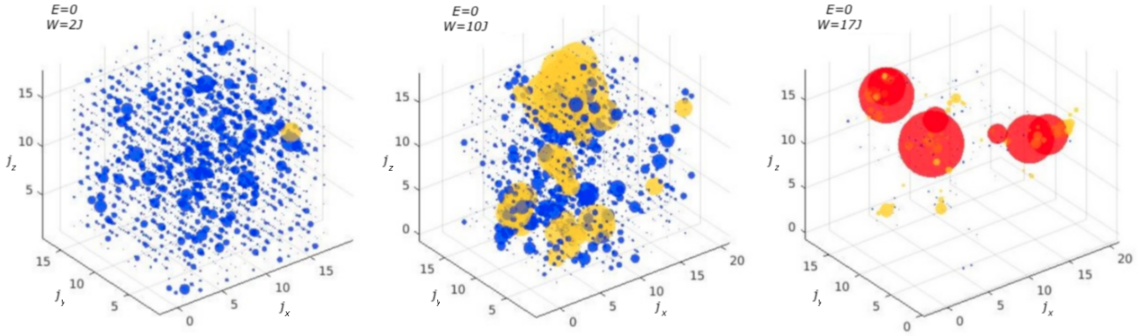

FIGURE 1.7 – Eigenfunction in cubic lattices with side $17a$ at $E = 0$ and variable disorder $W = \{2, 10, 17\}J$. The radii of the coloured spheres indicate the magnitude of probability density $|\psi(\boldsymbol{j})|^2$ at each grid point. Blue spheres display points where $|\psi(\boldsymbol{j})|^2 \leq 0.003a^{-3}$, yellow spheres show $0.003a^{-3} < |\psi(\boldsymbol{j})|^2 \leq 0.02a^{-3}$, and red spheres correspond to $|\psi(\boldsymbol{j})|^2 > 0.02a^{-3}$. Radii in the localized regime $W = 17J$ are plotted six times smaller than in the extended regime $W = \{2, 10\}J$. From Ref. [73].

hole symmetry is achieved, where for each eigenstate of energy E_j, there exists another eigenstate of energy $E_{j'}$ such that $E_{j'} = -E_j$ [67], and also the density of states satifies $\rho(E_j) = \rho(-E_j)$ [77]. Examples of the two distinct typologies of wavefunctions are plotted in Fig. 1.6, as functions of one coordinate, in the continuous space, whereas in Fig. 1.7 they are portrayed in the three-dimensional space within a discrete lattice. At the critical values of the energy, the eigenstates are neither extended nor localized but they exhibit strong fluctuations at all length scales and they are defined multifractal. The concept of mobility edge was pointed out by Mott, who stated that, at a given energy, localized and extended states cannot coexist [78]. While in periodic lattices the insulating property emerges from the position of the Fermi energy outside energy bands, in disordered systems this is due to the finite spatial extent of the eigenstate at the highest occupied level.

When the Anderson transition occurs, at $d = 3$, a curve in the (E, W) plane separating the region in which states are localized from the one in which they are extended, can be determined. The shape of the boundary is related to the critical behaviour and depends on the interplay between the effects of coherent interference and potential localization.

For instance, as shown in Fig. 1.8, the boundary separating the metallic region (shaded in dark orange) from the insulating one (in light blue) calculated by numerical means (dashed curve) and analytical approximations (solid line) is represented in an interval of positive energies. Due to the symmetry in the spectrum above highlighted, the critical disorder strength has to be symmetric under sign inversions of the energy.

At a given energy value E within the interval $6J \lesssim |E| \lesssim 8J$, two critical values of disorder are found. The upper one, signalling a transition from a metallic to an insulating behaviour of the system, as pointed out by Bulka-et-Al. [79] is predominantly due to the coherent superposition of scattered waves in the random lattice. On the contrary, the origin of the lower one has to be traced back to the

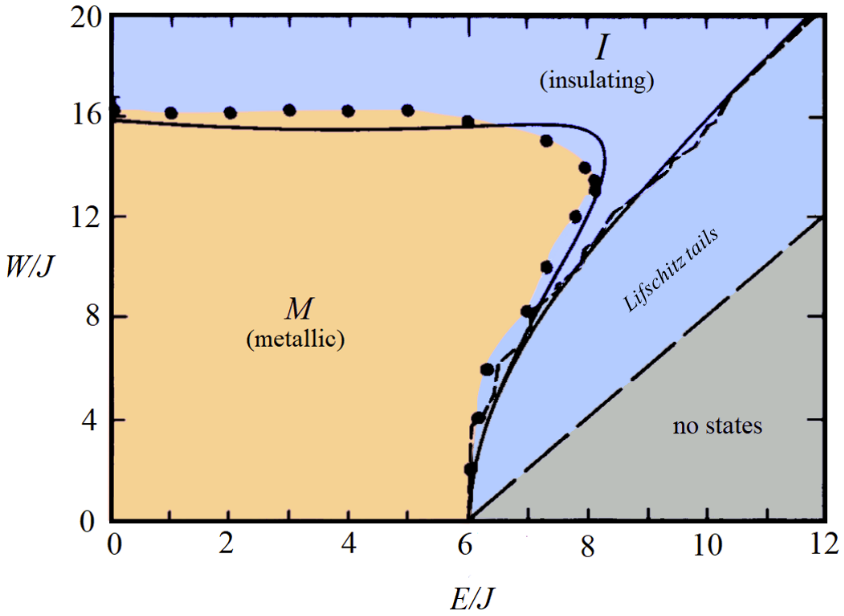

FIGURE 1.8 – Phase diagram of Anderson localization in $d = 3$ in the disorder-energy plane in units of the tunnelling amplitude J. The on-site energies follow the uniform distribution with width W, while z denotes the coordination number of the lattice, which is equal to 6 for $d = 3$. The solid line on the left separates the metallic (M) from the insulating (I) region, while the one on the right marks the band edge in CPA approximation, described in Sec. 2.2.1, both of them obtained within the framework of the Self-Consistent Theory [80]. The short-dashed line on the left represents the band edge found numerically by Bulka et Al. [79] using recursive Green's function approach, illustrated in Sec. 2.1.2, while, on the right, the exact upper bound $W_{\mathrm{BE}} = E - 6J$ is shown by means of the long-dashed line. The dots represent in turn the phase boundary determined numerically in [79] and mark the border of the region of localized wave-functions where the integrated density of states $n(E)$ exhibits Lifshitz tails (cf. Eq. (1.14)). Edited, from [81].

decrease of the density of states and to the onset of potential localization. In Fig. 1.8, the portion of space where no eigenstates do exist is also highlighted and its boundary is close to the phase separator at low disorder $W \lesssim 4J$ owing to the fact that at those points the states are Lifshitz's delocalized states.

A useful quantity for characterizing the localized behaviour of an eigenfunction is the inverse participation ratio (IPR), introduced by Bell and Dean [82], which measures the portion of the space where the amplitude of the wave-function differs markedly from zero and is defined as [83]:

$$I_{q,\beta} := \sum_{\boldsymbol{j}} |\psi_\beta(\boldsymbol{j})|^{2q} \ ,$$

where q is an integer.

For large but finite L, the scaling behaviour of this quantity is $I_q \sim 1$ for localized eigenfunctions, whereas it corresponds to $I_q \sim L^{d(1-q)}$ for delocalized ones. When $q = 2$, the IPR $I_{2,\beta}$ is always smaller or equal to 1, thanks to Cauchy-Schwartz inequality. The quantity has been extensively used for distinguishing the behaviour of the eigenstates of Anderson-Hubbard Hamiltonian [84, 85]. At the

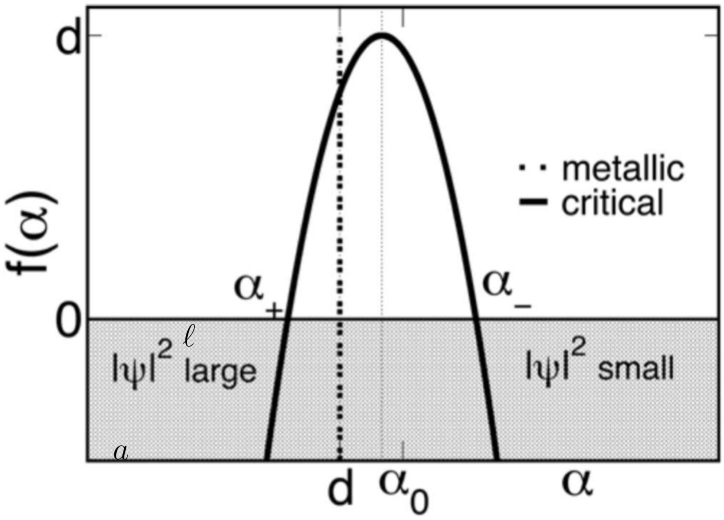

FIGURE 1.9 – The singularity spectrum $f(\alpha)$ at the criticality (convex curve), and in the metallic regime (needle-like plot). The shaded area corresponds to rare events, that typically can not be found in a single sample. From Ref. [86].

transition between the two opposite trends, the wave functions exhibit self-similarity and they are neither extended nor localized. This results in the appearance of a non-trivial fractal dimension D_q, where $0 < D_q < d$, characterizing the scaling of IPR as $I_q \sim L^{D_q(1-q)}$. The inverse participation ratio averaged over disorder configurations, can be expressed in terms of the probability density associated to the square modulus of the wave-function $|\psi|^2$ close to the mobility edge, as:

$$\overline{I_q} \sim \int \mathrm{d}|\psi|^2\, P\big(|\psi|^2\big)|\psi|^{2q} \sim \int \mathrm{d}|\psi|^2\, \frac{|\psi|^{2q}}{|\psi|^2} L^{-d+f\left(-\frac{\ln|\psi|^2}{\ln L}\right)} \,,$$

where f is a function known as the *singularity spectrum*. Within this framework, $\overline{I_q}$ can thus be seen as the q-th moment, $\overline{|\psi|^{2q}}$, of the distribution $P\big(|\psi|^2\big)$. Defining $\alpha = -\ln|\psi|^2/\ln L$, the previous relation an be recast in the form:

$$\overline{I_{q,\beta}} \sim \int_0^{+\infty} \mathrm{d}\alpha\, L^{-q\alpha+f(\alpha)} \,.$$

where the $f(\alpha)$ can be interpreted as the fractal dimension of the points $\boldsymbol{j}$ where the eigenfunction scales as $|\psi(\boldsymbol{j})|^2 \sim L^{-\alpha}$. The number of the points exhibiting this scaling behaviour thus amounts to $L^{f(\alpha)}$. The singularity spectrum of a multifractal $f(\alpha)$ is a convex function of α, $f''(\alpha) \le 0$, that possesses a maximum satisfying $\max f(\alpha) \le d$, as shown in Fig. 1.9. In the metallic regime, it would be formally defined as a function diverging at $-\infty$ for $\alpha \neq d$, and equal to d at $\alpha = d$ (see Fig. 3.2).

In the absbence of disorder ($W = 0$), the spectrum of the Hamiltonian in Eq. (1.9) in a finite lattice is discrete and takes values in the region $-zJ \le E \le zJ$, where z is the coordination number of

the lattice [6], that, for an hypercubic d-dimensional lattice, is equal to $z = 2d$.
In infinite lattices it becomes (absolutely) continuous, the eigenvectors converge (uniformly) to zero, $||\psi_k|| \sim L^{-d/2} \to_{L\to+\infty} 0$, and are not square-summable (in $\ell^2(\mathbb{Z}^d, \mathbb{C})$. In that limit, the local density of states becomes a continuous distribution, independent of the position in the lattice $\boldsymbol{j}$ [87]:

$$\rho(\boldsymbol{j}, E) = \sum_{\boldsymbol{k}} \delta(E - E_{\boldsymbol{k}}) |\langle \boldsymbol{k}|\boldsymbol{j}\rangle|^2 \sim_{L\to\infty} \int_{\boldsymbol{k}\in[0,2\pi]^d} \frac{\mathrm{d}^d\boldsymbol{k}}{(2\pi)^d}\, \delta\left(E + 2J \sum_{i=1}^{d} \cos(k_i)\right) .$$

The latter expression for $d = 1$, for instance, reduces to:

$$\rho(\boldsymbol{j}, E) = \frac{\theta(2J - |E|)}{\sqrt{4J^2 - E^2}} .$$

The integrated density of states, $n(E) := \sum_{\boldsymbol{j}} \int_{-\infty}^{E} \mathrm{d}E'\, \rho(\boldsymbol{j}, E')$, near the bottom of the spectrum $E_0 = -2dJ$, can be approximated as

$$n(E) \sim C(E - E_0)^{d/2} , \tag{1.14}$$

where C is a constant [88]. In the presence of disorder ($W \neq 0$), the spectrum is also discrete in finite lattices, in both the extended and the localized phase, and bounded in the interval $-W/2 - zJ \leq E \leq W/2 + zJ$, since the probability distribution of the on-site energies has compact support. However, for $L \to +\infty$, the eigenvalues corresponding to localized states form a discrete set (spectrum) $\sigma_p(H)$, since these states are actually bound states, while the eigenvalues related to extended states lead to a continuous set $\sigma_c(H)$ [87]. This fact allows one to decompose Hilbert space into the two respective orthogonal subspaces $\mathcal{H} = \mathcal{H}_p \bigoplus \mathcal{H}_c$. The local density of states $\rho(\boldsymbol{j}, E)$ reflects this feature and can be cast as $\rho(\boldsymbol{j}, E) = \rho_p(\boldsymbol{j}, E) + \rho_c(\boldsymbol{j}, E)$, where $\rho_p(\boldsymbol{j}, E) := \sum_\beta \delta(E - E_\beta)|\langle\beta|\boldsymbol{j}\rangle|^2$. In $d = 1$, the density of states and the localization length are connected by a relation determined by Thouless [89]:

$$\xi(E)^{-1} = \int \frac{\mathrm{d}E'}{L^d} \sum_{\boldsymbol{j}} \rho(\boldsymbol{j}, E') \ln|E' - E| .$$

In the limit of infinite disorder, the latter becomes simply $\rho_p(\boldsymbol{j}, E) = \delta(E - v_{\boldsymbol{j}})$. In particular, at the bottom of the band, where $E_0^{\pm} = \pm(zJ + \frac{W}{2})$, the integrated density of states is characterized by exponentially decaying edges, known as Lifshitz tails [3] [4]:

$$n(E) = C_1 \exp\left[-C_2(E - E_0)^{-d/2}\right]$$

where C_1 and C_2 are constants. Due to the lack of translational invariance, there are no divergencies (like the van Hove ones) in the integrated density of states, and its behaviour is smooth [9] in the region $-E_0 \leq E \leq E_0$.

1.4 Theoretical approaches

After the introduction of the concept of mobility edge by Mott in 1967 and the formulation of Landauer's theory of conductivity, the problem of localization induced by disorder has drawn an increasing attention in condensed matter physics. The analogy with a second-order phase transition has been outlined by Wegner [9], who mapped the original problem to the one of a ferromagnet with broken continuous symmetry. In particular, he traced a comparison between the diffusion constant, that vanishes in the localized regime, and the stiffness of a ferromagnet [90, 91]. Based on a field-theoretical approach to study the behaviour of conductiviy correlation length near the critical point, Wegner also pointed out the absence of a minimum metallic conductivity in a disordered medium [92], thus confuting one of Mott's predictions.

Another particular feature of Anderson localization is the lack of an upper critical dimension, above which a mean-field theory describes exactly the critical behaviour. The latter assertion was proved by the nonlinear σ-models, introduced by Wegner, using the replica trick in order to calculate disorder-averaged quantities. The theory was later enriched by supersymmetric versions by Efetov [93], using both commuting and anticommuting variables for the mapping of the original problem, and it was able to reproduce the results of the diagrammatic theory but using a non-perturbative treatment and demostrated the renormalizability of the theory.

In addition, the correlation function between the energy levels found within that framework coincided with the one predicted by random matrix theory, introduced by Wigner in 1951 [94] for explaining some features of nuclear spectra and then first extended by Gorkov in 1965 [95] to disordered metals. This theory, that is presented in App. A.1, has been able to assert that the distribution of the level spacings depends only on global symmetries of the Hamiltonian, and not on the particular form of the disorder potential. Besides it was argued that Anderson transition is not characterized by any symmetry breaking and does not possess a conventional order parameter, since the one resulting from nonlinear σ-models, i.e. the local density of states [96] does not vanish in any phase. Later, in the context of the Typical Medium theory, the geometrically averaged (called 'typical') density of states was proposed by Nikolić [97] as a good order parameter.

Almost at the same time of the σ-models, a macroscopical theory was formulated by Abrahams et Al. [7], to the end of characterizing the critical behaviour of localization length, by introducing a one-parameter scaling hypothesis, that has been later supported by numerical results. A microscopical approach was proposed by the diagrammatic Self-Consistent theory [11, 12, 98], who used a renomalized perturbative approach to describe the occurrence of the transition in terms of the quantum interference processes between the paths of a particle in a random lattice.

In the following we will review some of the results of the scaling theory, who have been relevant for the subsequent investigation of the interplay between localization and interactions.

1.4.1 Scaling theory of Anderson Localization

The scaling theory, proposed by Abrahams et al. [7], on the basis of the results of the renormalization group approach developed by Wegner [8] and on the contributions of Landauer [99] and Thouless [6], aims at pointing out the transport properties of a disordered medium, by starting from the behaviour of the systems under changes of scales $L \mapsto bL$. This involves taking into account scale-dependent interference effects, that are primarily important at low dimensions, even at small disorder. The singular backscattering process deeply affects localization, since the terms containg interferences between time-reversed paths survive from averaging over disorder realizations [100] [14] [91].

The formalism is able to capture the universal behaviour of macroscopic quantities, like conductivity and diffusion coefficient, in the vicinity of the critical point, regardless of the microscopic details of the medium. While it does not allow for determining the exact critical point, it is able find relations between macroscopic quantities and microscopic ones, like localization length (as well as disorder parameter).

In order to show these connections, it is convenient to begin analysing the problem of the scattering off a single impurity, in one dimension ($d = 1$). Portraying the impurity as a narrow potential barrier located in $x = 0$, a one-particle wave-function can be decomposed into components travelling in the left side (L, $x < 0$) and in the right side (R, $x > 0$), and into the ingoing (in) and outgoing (out) ones:

$$\psi(x) = \begin{cases} \psi_L^{\text{in}} \mathrm{e}^{\mathrm{i}kx} + \psi_L^{\text{out}} \mathrm{e}^{-\mathrm{i}kx}, & x < 0 \\ \psi_R^{\text{in}} \mathrm{e}^{\mathrm{i}kx} + \psi_R^{\text{out}} \mathrm{e}^{-\mathrm{i}kx}, & x > 0 \end{cases},$$

The outgoing components of the wavefunction can be expressed in terms of the complex reflection and transmission coefficients r, t and r', t', respectively from the left and from the right, as follows (see Fig. 1.10):

$$\begin{aligned} \psi_L^{\text{out}} &= r\psi_L^{\text{in}} + t'\psi_R^{\text{in}} \\ \psi_R^{\text{out}} &= t\psi_L^{\text{in}} + r'\psi_R^{\text{in}} \end{aligned}$$

The outgoing component can be thus written as linear combinations of the incoming components, by introducing the scattering matrix S [99, 101–103]:

$$\begin{pmatrix} \psi_L^{\text{out}} \\ \psi_R^{\text{out}} \end{pmatrix} = \mathbf{S} \begin{pmatrix} \psi_L^{\text{in}} \\ \psi_R^{\text{in}} \end{pmatrix} \text{, where } \mathbf{S} = \begin{pmatrix} r & t' \\ t & r' \end{pmatrix} .$$

Since the probability flux must be conserved, the *scattering* matrix $\mathbf{S}$ must be unitary, condition that implies that transmission and reflection probability add up to unity, $|t|^2 + |r|^2 = 1$, and that $r^* t' = -t^* r'$ and the complex-conjugate version of the latter relation. A further constraint comes in the case of a time-reversal invariant scattering potential: by imposing an exchange of the roles of incoming and outgoing waves, that entails $\mathbf{S}^* = \mathbf{S}^{-1}$, one finds $t' = t$ and $r' = -tr^*/t^*$.

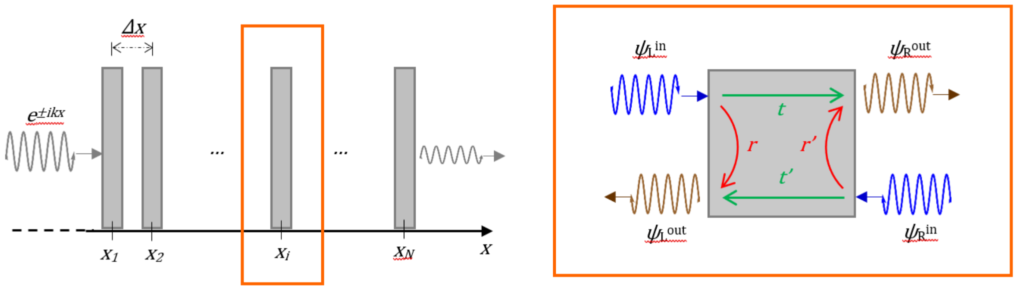

FIGURE 1.10 – Propagation in a one-dimensional waveguide with randomly placed scatterers (left) and detail of a scattering process (right).

In the presence of a large number of scatterers, the use of the scattering matrix is not convenient, since the relation between the total **S** matrix and the individual ones would be very complicated to determine. So, instead of grouping the wave-function components on the basis of time, we assemble them on the basis of the position. This involves the definition of a transfer matrix **M** [103]:

$$\begin{pmatrix} \psi_R^{\text{in}} \\ \psi_R^{\text{out}} \end{pmatrix} = \mathbf{M} \begin{pmatrix} \psi_L^{\text{out}} \\ \psi_L^{\text{in}} \end{pmatrix} \text{, where } \mathbf{M} = \begin{pmatrix} 1/t^* & -r^*/t^* \\ -r/t & 1/t \end{pmatrix} .$$

The transfer matrix thus found has a unit determinant and eigenvalues that are each other's inverses, due to the conditions imposed on **S**. For a sequence of N scatterers characterized by different transmission coefficients and arranged in a row, the total transfer matrix at the two ends can be simply written as the product of the transfer matrices related to each barrier of potential: $\mathbf{M}_{12\ldots N} = \mathbf{M}_N \ldots \mathbf{M}_2 \mathbf{M}_1$. In the case of $N = 2$ obstacles, the complex transmission coefficient reads:

$$t_{12} = \frac{t_1 |t_2|^2}{t_2^* + r_1 r_2^* t_2} \, ,$$

an expression that can be found also by adding up the transmission coefficients associated to each process containing internal reflections, $t_{12} = t_2 t_1 + t_2 r_1' r_2 t_1 + t_2 (r_1' r_2)^2 t_1$, reminding that $r_1' = -t_1 r_1^* / t_1^*$. The transmission probability T_{12} can be written in terms of the phase φ accumulated after one process of internal reflection, in the following form [104]:

$$T_{12}(\varphi) = \frac{T_1 T_2}{|1 - \sqrt{R_1 R_2} \mathrm{e}^{\mathrm{i}\varphi}|^2} \, .$$

If the barriers are distributed randomly in space, with $\Delta x \ll \lambda$, the phase φ can be considered independent of the particular distribution of the obstacles and therefore it can be treated as a random variable, taking values in $[0, 2\pi]$. In the case in which transmission is incoherent, we compute the transmission probability by taking its average value over the phase variable. This is equivalent to averaging over different realizations, characterized by distinct relative positions of the scatterers. The former procedure gives:

$$\overline{T_{12}} = \frac{T_1 T_2}{1 - R_1 R_2} \,. \tag{1.15}$$

The same result as in Eq. (1.15) is reached if a classical propagation is considered, using only the reflection and transmission probabilities R and T respectively. The latter quantity allows us for computing the dimensionless element resistance, that is additive under the inclusion of a further barrier:

$$\frac{1 - \overline{T_{12}}}{\overline{T_{12}}} = \frac{1 - T_1}{T_1} + \frac{1 - T_2}{T_2} \,.$$

The conductance of a sample is related to the transmission probability through Landauer's formula [99]:

$$G = \frac{n_s e^2}{h} \frac{T}{1 - T} \,, \tag{1.16}$$

where n_s denotes the spin degeneracy of the particle. For incoherent transport, the disorder-averaged conductance reduces to:

$$\overline{G} = \frac{n_s e^2}{h} \frac{2\ell}{L} \,, \tag{1.17}$$

where ℓ is the mean free path of the particle. The latter expression can be generalized for higher-dimensional systems, in which a multitude of transmission channels is available, thus getting the usual Ohm's relation:

$$\overline{G} = \sigma_d L^{d-2} \,, \tag{1.18}$$

where σ_d is the conductivity of the hypercubic sample. In the case in which the particles are electrons, the conductivity becomes [100]:

$$\sigma_d = \left(\frac{n_s e^2}{h} \right) \left(\frac{\ell k_F^{d-1}}{d (4\pi)^{d/2-1} \Gamma(d/2)} \right) \,, \tag{1.19}$$

where k_F is the Fermi wave-number of the electrons. In the case of coherent transport the relation for the transmission in Eq. (1.15) can not be easily generalized for a great number of scatterers. If we regard it as a function of the microscopic realizations of disorder, it does not prove to be a self-averaging quantity, since its mean value does not concide with the most likely one. A solution can be traced in the opposite of its logarithm, $\kappa = -\ln T$, namely the extinction coefficient. The average of the latter quantity over the phase shift due to multiple transmission and reflection paths gives

$$\int_0^{2\pi} \frac{\mathrm{d}\varphi}{2\pi} \ln |1 - \sqrt{R_1 R_2} \mathrm{e}^{\mathrm{i}\varphi}| = 0 \,,$$

due to the analiticity of the complex logarithm for all $0 \leq R_1 R_2 < 1$ [103]. The average of the extinction across two consecutive potential barriers is thus additive and does not depend on the order in which the pieces of a sample are added nor on their length [7]:

$$\overline{\ln T_{12}} = \ln T_1 + \ln T_2 \; .$$

For a multitude of scatterers, the average extinction grows linearly with the length of the sample $\overline{\kappa} = -\overline{\ln T} = L/2\ell$. We are thus able to define the typical value of the transmission probability as $T_{typ} := \mathrm{e}^{\overline{\ln T}}$, that, once plugged into disorder-averaged Landauer's formula (Eq. (1.17)), leads to the following expression for the typical conductance $G_{\mathrm{typ}} := \mathrm{e}^{\overline{\ln G}}$:

$$G_{\mathrm{typ}} = \frac{n_s e^2}{h} \frac{\mathrm{e}^{-L/2\ell}}{1 - \mathrm{e}^{-L/2\ell}} \; , \tag{1.20}$$

where in $d = 1$ the conductance drops exponentially fast with L, with a characteristic length $\xi = 2\ell$, known as the localization length. The result can be generalized to higher-dimensional systems with a *quasi-1D* geometry by considering that, for b independent transverse channels along a given direction, the typical transmission behaves as $T_{typ}(bL) = (T_{typ})^b b^{d-1}$.

As a result, the localization length increases with the transverse degrees of freedom as $\xi = 2b\ell$, a relation that has been proved for weakly coupled channels by Dorokhov [105] and independently by Mello, Pereyra and Kumar [106]. In particular, they derived an equation connecting the ditribution function of the eigenvalues of the transmission matrix with the length of the quasi-one-dimensional bar. The relation, known as the DMPK equation [101], has allowed to find analytic estimates for the universal conductance fluctuations in the metallic regime as well as to obtain analytical estimates of the localization length in the limit $b\ell \ll L$ for systems endowed with different global symmetries.

As we have seen, the conductance changes its dependence on the sample length according to kind of transport occurring in the sample (incoherent or coherent). A measure of the total transmission probability is provided by the dimensionless conductance, that is defined as $g = hG_{\mathrm{typ}}/n_s e^2$. Using Eq. (1.20), we can see that, in the limit of small system size, the ohmic law of conductance is recovered (compare Eq. (1.18)):

$$g(L) = \frac{1}{\mathrm{e}^{L/2\ell} - 1} = \begin{cases} 2\ell/L, & L \ll \ell \\ \mathrm{e}^{-L/2\ell}, & L \gg \ell \end{cases} \; . \tag{1.21}$$

The dimensionless conductance can be found also for quasi-1D systems with b transverse channels along each direction, and its dependence on the latter can be cast as $g(bL) = f(b, g(L))$ [29]. According on the size of the sample, one can distinguish three transport regimes: ballistic transport, at $L < \ell$, described by the upper expression in Eq. (1.21), diffusive transport in the interval $\ell < L < \xi$, and strong localization for $L > \xi$, outlined by the lower expression in Eq. (1.21). In three dimensions the localization length can be infinite, so that the localized regime can not be recovered even at large system sizes, as we will see in more detail in the continuation.

A useful quantity for depicting this behaviour is the β-function, introduced by Callan and Symanzik, with the aim of describing the variation of the coupling constant in quantum field theory. For our

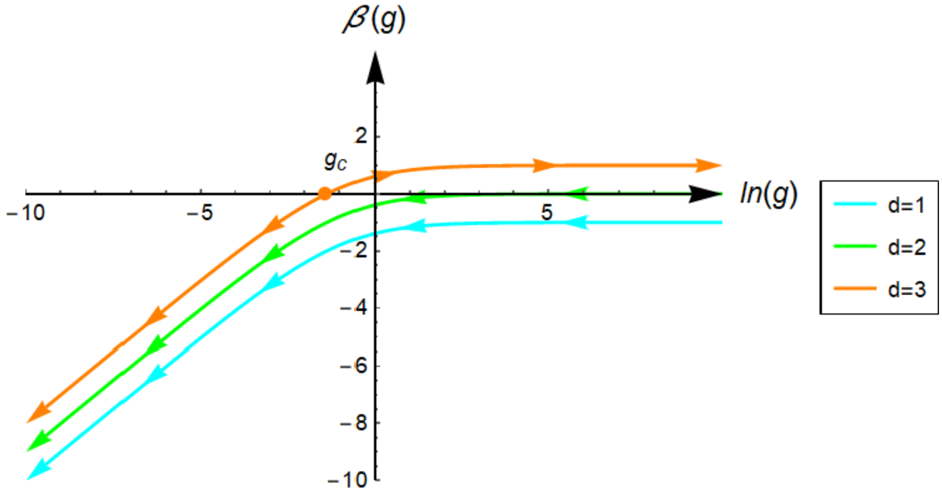

FIGURE 1.11 – Conductance scaling β-function in $d = 1, 2, 3$, determined from Eq. (1.23). The arrows pinpoint its behaviour for increasing system size L: in $d = 1, 2$, g is ohmic in smal samples but exponentially low in greater samples. In $d = 3$, this takes place only if $g < g_c$; in the opposite case the conductance raises with growing L.

purpose, we consider the relation that binds the β-function to the dimensionless conductance g, the so-called renormalization-group equation [7],

$$\beta(g) = \frac{\mathrm{d} \ln g}{\mathrm{d} \ln L} = \frac{L}{g} \frac{\mathrm{d}g}{\mathrm{d}L} , \tag{1.22}$$

where β is a function that depends on the size of the sample only through $g(L)$ and evidences the important role of dimensionality in the behaviour of the latter quantity [29]. For a d-dimensional quasi-1D system (elongated hypercube), $\beta(g)$ can be well approximated by [107]:

$$\beta(g) = d - 1 - (1 + g) \ln \left(1 + g^{-1}\right) . \tag{1.23}$$

In the limit of small system size, $L \ll \ell$, the conductance is large, and the system behaves approximately as in the classical (ohmic) case [107]:

$$\beta(g) \approx d - 2 - \frac{c_d}{g} + O(g^{-2}) ,$$

where c_d is the coefficient associated to the weak-localization correction of the classical result.
In the limit of large sysem size, $L \gg \ell$, the conductance is small and exponential (strong) localization occurs, so the beta function takes the form [107]:

$$\beta(g) \approx \ln \left(g/g_d\right) - g(1 - \ln g) + O(g^2) ,$$

where g_d is a constant of order unity. The behaviour of β as a function of the logarithm of the dimensionless conductance is also depicted in Fig. 1.11 for different system dimensionalities d.

While in 1D systems where $d = 1$, the localization length is $\xi = 2\ell$, as we have seen while expounding coherent transport, in 2D this quantity can be found starting from the integration of the beta function in Eq. (1.22) (with Eq. (1.23)) from $L = L_0 = \ell$ and $g(L_0) =: g_0 = k\ell \gg 1$ in the ohmic regime, thus finding $g(L) = g_0 - c_2 \ln(L/L_0) = k\ell - c_2 \ln(L/\ell)$. This quantity approaches unity at $L = \xi$, the latter being:

$$\xi \approx \ell e^{k\ell/c_2} ,$$

where c_2, as obtained in the framework of self-consistent theory is equal to $2/\pi$ [78]. Therefore, the prediction of the scaling theory in $d = 2$ is that all states are localized, since for large L, the β function is never positive. This means that, as in $d = 1$, the dimensionless conductance always decreases for increasing size, thus signalling an insulating behaviour. To sum up, the dependence of localization length on mean free path according to the system dimension can be written as follows:

$$\xi = \begin{cases} 2\ell & d = 1 \\ \ell \exp\left(\dfrac{\pi k\ell}{2}\right) & d = 2 \end{cases} .$$

In the three-dimensional case, from Eq. (1.23), we notice that at large value of the conductance the beta function is positive, while, at low values is negative: these limiting behaviours in the thermodynamic limit $L \to +\infty$ give rise to two stable fixed points, the metallic or infra-red and the insulating ones, respectively. Between the aforementioned points, an unstable critical point is present, at which the dimensionless conductance is of order unity and $\beta(g_c) = 0$.

Using Eq. (1.18) and Eq. (1.19), we are able to find $g(\ell) = 2(k\ell)^3/3$, from which we can recover the Ioffe-Regel criterion $k\ell \sim 1$, that holds in any disordered system, but whose exact coefficient (of order unity) is not universal: it notably depends on the features of the disordered potential distribution.

In order to characterize the behaviour around the critical point in $d = 3$, it turns out be useful to find the approximate behaviour of the β-function in Eq. (1.23) piecewise in three regimes: the metallic one (when $g > g_+$), the critical one (between $g_- < g < g_+$) and the insulating one ($g < g_-$). We thus have [107]:

$$\beta(g) = \begin{cases} 1 & g > g_+ \\ \dfrac{1}{s} \ln\left(\dfrac{g}{g_c}\right) & g_- < g < g_+ \\ \ln g & g < g_- \end{cases} ,$$

where the values of the extremes of the critical interval are determined by imposing continuity:

$$g_+ = g_c e^s , \qquad g_- = g_c^{-\frac{1}{s-1}} .$$

In the metallic side, we consider a point close to the critical one, $g_{0+} = g_c(1+\epsilon)$, and integrate the beta-function (Eq. (1.22)) over the conductance, from $g = g_{0+}$ to $g \gg 1$, and over the sample length from L_{0+} to $L \gg 1$:

$$\begin{aligned}\ln\left(\frac{L}{L_{0+}}\right) &= \int_{\ln g_{0+}}^{\ln g_+} \frac{s\,\mathrm{d}\ln g'}{\ln\left(g'/g_c\right)} + \int_{\ln g_+}^{\ln g} \mathrm{d}\ln g' = \\ &= s\ln\left(\frac{\ln\left(g_+/g_c\right)}{\ln\left(g_{0+}/g_c\right)}\right) + \ln\left(g/g_+\right)\ ,\end{aligned}$$

By approximating $\ln\left(g_{0+}/g_c\right)$ as $(g_{0+} - g_c)/g_c$, we find for the dimensionless conductance:

$$g = g_c\left(\frac{L}{L_{0+}}\right)\left(\frac{\mathrm{e}}{sg_c}\right)^s (g_{0+} - g_c)^s\ .$$

We can also define in that phase a *correlation length* ξ, starting from $g = g_c L/\xi$, whose denominator diverges at the critical point as:

$$\xi = L_0\left(\frac{sg_c}{\mathrm{e}}\right)^s (g_{0+} - g_c)^{-s}\ .$$

By expressing the conductance difference as a function of the energy $(g_{0+} - g_c) \simeq \frac{\partial g}{\partial E}\big|_{E=E_c}(E - E_c) =: K_E(E - E_c)$, [107], we can write the conductivity σ (in Eq. (1.18)) as:

$$\sigma = \frac{2e^2}{h}\frac{g}{L} = \frac{2e^2}{hL_0}g_c\left(\frac{\mathrm{e}K_E}{sg_c}\right)^s (E - E_c)^s\ , \tag{1.24}$$

a quantity that vanishes at the critical point. Equivalently, expanding g in Taylor series, we an determine an analogous dependence on the disorder strength W: $\sigma \propto (W_c - W)^s$. This behaviour in the vicinity of the critical point is also shared by the diffusion coefficient, which is directly proportional to conductivity [108] and in the case of electrons it is related to the latter quantity as $D = \sigma/\left[n_s e^2 \rho(E_F)\right]$. On the insulating side, instead, if we integrate the beta-function over the conductance from a $g = g_{0-} = g_c(1 - \epsilon)$ until $g \ll 1$, and over the length from L_{0-} to $L \gg 1$, we end up with:

$$\begin{aligned}\ln\left(\frac{L}{L_{0-}}\right) &= \int_{\ln g_{0-}}^{\ln g_-} \frac{s\,\mathrm{d}\ln g'}{\ln\left(g'/g_c\right)} + \int_{\ln g_-}^{\ln g} \mathrm{d}\ln g' = \\ &= s\ln\left[\frac{\ln\left(g_c/g_-\right)}{\ln\left(g_c/g_{0-}\right)}\right] + \ln\left(g/g_-\right)\ .\end{aligned}$$

From the previous relation, we can find a relation for the dimensionless conductance,

$$g = \mathrm{e}^{-2L/\xi}\ , \qquad \text{with} \qquad \xi := \frac{2L_0 \ln g_c^{1/(s-1)}}{g_c^s\left[\ln g_c^{s/(s-1)}\right]^s}(g_c - g_{0-})^{-s}\ ,$$

that decays with a localization length ξ, which diverges at the critical point. Expressing it as a function of the energy [107], using $g_c - g_{0-} = K_E(E_c - E)$, it reads:

$$\xi := \frac{2L_0}{(K_E g_c)^s} \frac{\ln g_c^{1/(s-1)}}{\left[\ln g_c^{s/(s-1)}\right]^s} (E_c - E)^{-s} ,$$

where here, in $d = 3$, the exponent s corresponds to ν. For $d > 2$, the scaling relation between the exponents ν and s (appearing in Eq. (1.24)) is $s = (d-2)\nu$, a result that was retrieved by Wegner [84], starting from the expansion of the beta function in dimension $d = 2 + \epsilon$, slightly above the lower critical dimension for the Anderson localization transition. Similarly to the metallic case, the characteristic length ξ can be expressed in terms of the disorder parameter W in vicinity of the critical point as

$$\xi \propto (W - W_c)^{-\nu} .$$

An equivalent definition of the dimensionless conductance g is provided by the so-called *Thouless number* [109]:

$$g = \frac{\delta E}{\Delta E} = f(L/\xi(E)) . \tag{1.25}$$

In the latter reformulation of the dimensionless conductance, ΔE represents the average energy-level spacing, that can be expressed as the derivative $\mathrm{d}n(E)/\mathrm{d}E$, where $n(E)$ is the cumulative density of states: $n(E) = \int^E \mathrm{d}E' \, L^d \rho(E')$. The quantity at the denominator of Eq. (1.25), δE, denotes instead the energy-level width, given by the geometrical mean of the energy shift which results from switching the boundary conditions from periodic to antiperiodic ones [29]. Approximating excited states as plane waves, a change in boundary conditions results in a variation of the allowed wavevectors $k_i \mapsto k_i + \pi/L$ and thus the energy varies as:

$$\delta E^{ext} = E^{pbc} - E^{apbc} = \frac{\partial E}{\partial k_i} \delta k_i \propto L^{-1} ,$$

whereas for a localized state, the variation is:

$$\delta E^{loc} \propto \mathrm{e}^{-L/\xi(E)} ,$$

thus roughly recovering the scaling behaviour we have previously seen, starting from the transmission probability of a particle.

According to the alternative definition provided in [100], the numerator of Eq. (1.25) can be expressed $2\pi n_s E_T = n_s h/\tau_T$, which is the energy associated to Thouless time τ_T, i.e. the time to diffuse from one boundary of the sample to the other. The latter quantity corresponds to $\tau_T = L^2/D = L^2 d/v\ell$, where D denotes the diffusion coefficient and v the group velocity of the wave-packet. The latter is then localized when it is unable to reach the boundary of a sample, condition that is fulfilled when the Thouless time exceeds the Heisenberg time, that is the longest time in which a wavepacket can

Universality Class	Symmetry of the Hamiltonian		Critical exponent ν		
	Time	Spin	$d = 1$	$d = 2$	$d = 3$
Orthogonal	✓	✓	X	X	1.571 ± 0.02 [76]
Symplectic	✓	X	X	2.73 ± 0.02 [76]	1.375 ± 0.016 [76]
Unitary	✓	✓/X	X	2.71 ± 0.06 [111]	1.438 ± 0.004 [76]

Table 1.1 – Numerical values of the critical exponent ν according to dimension d and global symmetries of the Hamiltonian.

propagate without visiting a region twice.

The critical exponents that characterize the behaviour of conductance (in the metallic case) and localization length (in the insulating one) in dimensions $d > 2$ are regarded as universal, since they are independent of the particular form of the Hamiltonian (for instance, they are not tied up with the disorder potential distribution), but only on its global symmetries. The first universality classes that have been identified are the Wigner-Dyson classes [110], based on the changes in the dynamics under time reversal and spin rotation. Systems described by Anderson Hamiltonian (Eq. (1.9)) are invariant under the aforementioned transformations and belong to the orthogonal universality class. When spin-rotation symmetry is not preserved , unlike the time-reversal one, as, for example, in the presence of spin-orbit coupling (case analysed in Chap. 4), the corresponding class is the symplectic one. In the absence of time-reversal symmetry, instead, like when an external magnetic field is applied, the system belogs to the unitary universality class, regardless of invariance over spin rotations. Labelling the three classes with the indices $\beta = 1, 2, 4$ in the order in which they have been presented, an analytic expression for the localization length in the insulating regime has been derived within the framework of the DMPK approach [101] for quasi-one-dimensional systems with length $L \gg b\ell$:

$$\xi = (\beta b + 2 - \beta)\ell \, .$$

The symmetries listed above, which were identified [112] in relation with three random matrix ensembles (that will be presented in App. A.1), have proven to be far incomplete in the description of disordered systems. Three chiral classes have been in fact identified by Gade [113] in order to elucidate system possessing also chiral symmetry, appearing, for instance, in bipartite lattices, described by tight binding models with randomness concentrated only in the hopping terms. The names of such classes follow those of the three previously enumerated ones. Four further classes have been introduced by Zirnbauer [114] [115], capable to explain the dynamics of random systems lacking chiral symmetry and described by Bogoljubov-de Gennes Hamiltonians, like quasiparticles in disordered superconductors. Unlike chiral classes, the Bogoljubov ones are in greater number since spin-rotation invariance has an impact even in the absence of time-reversal invariance, as it combines with the particle-hole symmetry in a non-trivial way.

1.5 Anderson localization of pairs: previous results

The effects of mutual interactions in the propagation of particles in disordered media represents an important many-body problem that has been investigated since the eighties, focusing in particular on electronic systems. A scaling theory for many-body systems subject to Coulomb interaction was proposed in 1983 by Finkelstein [116] [117], who treated the case in which a magnetic field suppresses the quantum interference contributions responsible for weak localization. It has been shown that electron-electron interactions can reduce the quantum interference effects at the basis of localization. The discovery of anomalously large currents in mesoscopic metallic rings in 2D [118] [119] [120] [121] has fostered the research in the topic [122]. Since the size of the Hilbert space grows exponentially with increasing system size, numerical studies have been restricted to few particles in low dimensions.
In the following paragraphs we will review the most relevant results on the simplest interacting system, the one involving two particles, in lattice with $d = 1, 2$.

1.5.1 1D geometry

The first theoretical investigation of disorder effect on the two-particle problem in a chain was carried out by Dorokhov [123], who pointed out that strong and long-range attractive interactions lead to a remarkable increase of localization length. Soon after, the case of short-range interactions was discussed by Shepelyansky [124], starting from the disordered Hubbard Hamiltonian. The corresponding stationary Schrödinger equation is given by:

$$(v_i + v_j + U\delta_{i,j})\psi_{i,j} - J(\psi_{i+1,j} + \psi_{i-1,j} + \psi_{i,j+1} + \psi_{i,j-1}) = E\psi_{i,j} \ ,$$

where $\psi_{i,j}$ represents the wave-function describing the two-particles at the positions i and j along the chain, whereas U indicates the Hubbard interaction strength. Mapping the original problem into a particular ensemble of band random matrices, he derived an approximate relation between the two-particle and the single-particle localization lengths, denoted as ξ_{tp} and ξ_{sp} respectively, finding that the former length is enhanced for increasing interaction strength U, as

$$\xi_{\mathrm{tp}} \sim \left(\frac{U^2}{32aJ^2}\right)\xi_{\mathrm{sp}}^2 \ . \tag{1.26}$$

Moreover, he underlined that this effect is independent of the sign of interaction when the total energy of the pair, E, is zero. The specific form of the latter relation has been subject of several studies [125–131], examining also the behaviour of the pair localization length in the limits of strong ($U \gg J$) and weak ($U \ll J$) interactions [132]. The physical implications of Shepelyansky's relation were further clarified by Imry's arguments [133], based on the Thouless' block-scaling picture. He began dividing a chain of length La (a being the lattice spacing) into blocks of length ξ_{sp}, thus containing on average ξ_{sp}/a one-particle states, described by wavefunctions $\psi_\alpha(x) \sim \frac{c_\alpha}{\sqrt{\xi_{\mathrm{sp}}}} \mathrm{e}^{-\frac{|x - x_\alpha|}{\xi_{\mathrm{sp}}}}$, where c_α is a complex random phase factor. Analogously as in the single-particle problem (see Eq. (1.25)), Imry defined a dimensionless conductance between neighbouring blocks $g_{\rm tp}$, which has been later proven to be the only scaling variable [134], as:

$$g_{\rm tp} \sim \frac{A_{\rm NB}\langle (I^{\gamma\delta}_{\alpha\beta})^2\rangle}{\Delta E_{\rm tp}}\,,$$

where $\Delta E_{\rm tp} \sim B_{\rm sp} a^2/\xi^2_{\rm sp}$, $B_{\rm sp} \propto J$ being the band width of the one-particle problem, while $\langle\cdot\rangle$ indicates the typical value of the quantity in brackets. The latter, $I^{\gamma\delta}_{\alpha\beta}$, is the interaction matrix element between the single-particle states, labelled by the greek letters and evaluated inside a single block, whereas $A_{\rm NB}$ is a suppression factor which accounts for the superposition between wavefunctions in neighbouring blocks. The interaction matrix element reads:

$$I^{\gamma\delta}_{\alpha\beta} = La \int {\rm d}x \int {\rm d}x' \psi^*_\alpha(x)\psi^*_\alpha(x') U \delta(x-x')\psi_\gamma(x)\psi_\delta(x')\,.$$

Assuming the coefficients c_α are uncorrelated and considering low disorder and interaction ($U, W \lesssim J$), the author reckoned $\langle (I^{\gamma\delta}_{\alpha\beta})^2\rangle$ at $U^2a^3/\xi^3_{\rm sp}$. The two-particle localizaton length was then defined as the length at which $g_{\rm tp} \sim 1$, starting from the ohmic regime, where $g_{\rm tp}/g_{\rm sp} = \xi_{\rm sp}/\xi_{\rm tp}$, in accordance with Eq. (1.18). Then Imry found $\xi_{\rm tp} \sim \xi^2_{\rm sp} U^2/(B^2_{\rm sp}a)$, in rough agreement with Shepelyansky's result.

On the other hand, by mapping the original problem into a single-particle one in $d = 2$ and performing numerical simulations based on transfer-matrix method, a technique that we will illustrate in Chap. 2, Römer et Al. [135] detected the disappearance of the phenomenon for increasing lattice size. However, as pointed out by Frahm et Al. [125], this behaviour is traced back to the inexactitude of the numerical procedure, that led to an estimate of $\xi_{\rm tp}$ deeply influenced by single-particle transport. A different numerical method, based on the evaluation of the two-particle Green's function, a quantity, whose meaning will be elucidated in Chap. 3, was proposed by von Oppen et Al. [136], who suggested a linear correction in $\xi_{\rm sp}$ to Eq. (1.26), and extended the result to particles following the Fermi-Dirac statistics. Moreover, the same group, through a decimation method later proved that interaction delocalizes primarily the center-of-mass motion rather than the relative one [137].

Further research has concerned energy level statistics [127], level curvature [138], time evolution of wave-packets [139][140][141], and the fractal structure of the interaction matrix elements [142][143][144]. An expression for the change in localization length due to short-range interactions in quasi-1D system was obtained using an approach based on nonlinear σ-models [145] and on the truncation of the Hilbert space. Although the effect of interaction-induced enhancement is well established, the specific dependence of ratio $\xi_{\rm tp}/\xi_{\rm sp}$ is still debated at the centre of the band [146][147][148] as well as at finite total energy [146, 149, 150], as portrayed in Fig. 1.12. This figure shows that this effect is strongest at intermediate values of the interaction strength, where $\xi_{\rm tp}/\xi_{\rm sp}$ takes its maximum value: for higher disorder this occurs for increasingly weaker interaction.

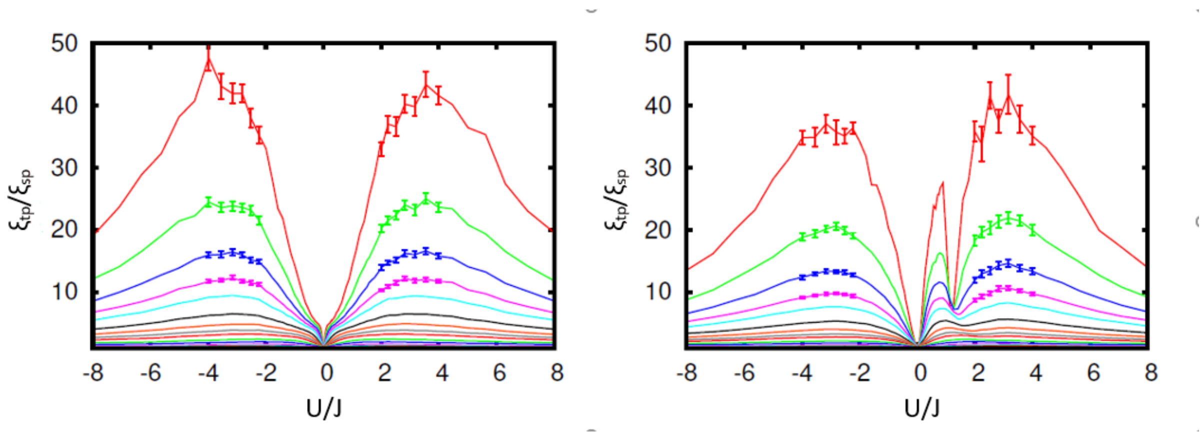

FIGURE 1.12 – Dependence of ratio $\xi_{\mathrm{tp}}/\xi_{\mathrm{sp}}$ on U for $E = 0$ (left panel) and $E = J$ (right panel) and the random-potential values $W = \{0.75, 0.875, 1, 1.25, 1.5, 1.75, 2, 2.5, 3, 4, 5, 6, 7\}J$ corresponding to decreasing curves. Here ξ_{tp} represents the localization length obtained by finite-size scaling at the interaction strength U. The curves are shown on normal scale in the interval $-8J \leq U \leq 8J$ with errorbars for data within the range $2J \leq |U| \leq 4J$ eavluated at the four lowest values of W. The errorbars for the other curves are below line width. From Ref. [146].

1.5.2 2D geometry

For the 2D analogue of the Shepelyansky problem, Thouless block-scaling approach predicts an exponential enhancement of the two-particle localization length, compared to the single-particle counterpart, when interactions are weak. Starting from the approach previously illustrated for the one-dimensional case, Imry [133] partitioned a two-dimensional lattice in blocks of $(\xi_{\mathrm{sp}}/a)^2$ states on average, thus finding for the typical interaction matrix element $\langle (I^{\gamma\delta}_{\alpha\beta})^2 \rangle \sim U^2 a^6/\xi_{\mathrm{sp}}^6$. Under the same conditions on interaction and disorder parameter, he imposed $g_{\mathrm{tp}}(\xi_{\mathrm{tp}}) \sim 1$ and, exploiting the result of perturbation theory $g_2(\xi_{\mathrm{sp}}) \approx g_{20} - \frac{e^2}{\hbar\pi^2} \ln\left(\frac{\xi_{\mathrm{sp}}}{\ell}\right)$ [90], he obtained $\frac{\mathrm{e}^{g_{\mathrm{tp}}(\xi_{\mathrm{tp}})}}{\mathrm{e}^{g_{\mathrm{tp}}(\xi_{\mathrm{sp}})}} \approx \left(\frac{\xi_{\mathrm{sp}}}{\xi_{\mathrm{tp}}}\right)^{e^2/(\hbar\pi^2)}$. The latter equation gives thus [152, 153]:

$$\xi_{\mathrm{tp}} \sim \xi_{\mathrm{sp}} \mathrm{e}^{\frac{\pi^2 \hbar A^2 U^2}{e^2 B_{\mathrm{sp}}^2} \left(\frac{\xi_{\mathrm{sp}}}{a}\right)^2},$$

where the enhancement of ξ_{tp} is particularly large at weak disorder (see Eq. (1.13)), but still finite. The problem was numerically investigated for the first time by Ortuño and Cuevas [151], who extracted the localization length by computing the two-particle Green's function (see also Ref. [154], where the same problem is addressed using energy-level statistics). By performing numerical simulations on relatively short grids of up to 10×62 sites, they observed the signature of an Anderson transition $W = (9.3 \pm 0.2)J$ for $U = J$ and total energy $E = 0$ (centre of the band). They also provided an estimate of the critical exponent $\nu = 2.4 \pm 0.5$. Their results are displayed in Fig. 1.13, where the reduced localization length Λ_M (see Chap. 2 for more in-depth explanations) is represented as a function of the two-particle localization length ξ_{tp} and exhibits the characteristic two-branch structure typical of 3D disordered systems, where both localized (lower branch) and extended (upper branch) states are present.

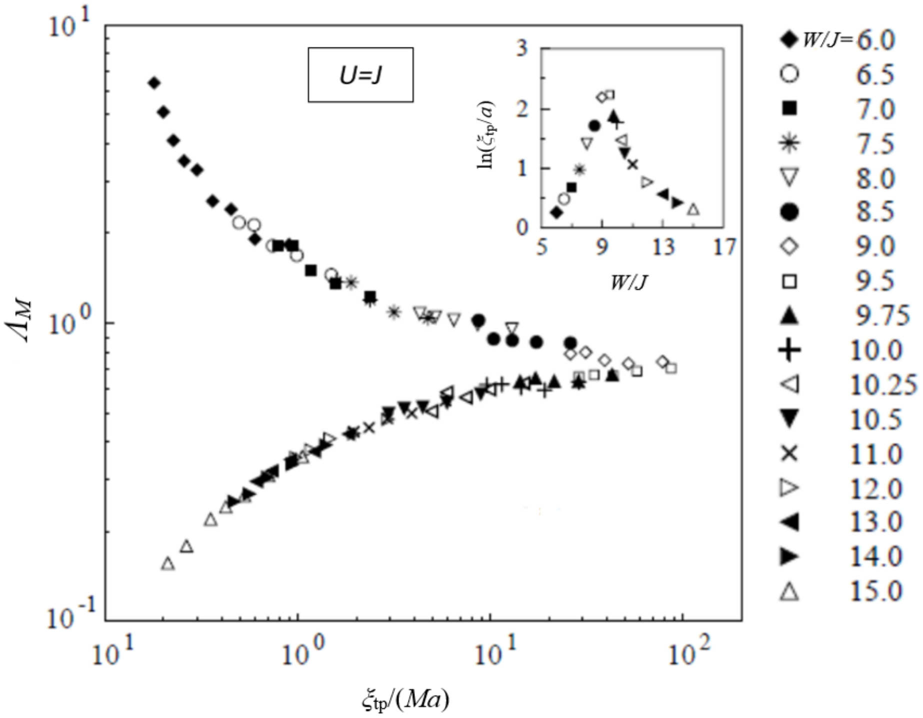

FIGURE 1.13 – Log-log plot of the reduced localization length Λ_M as a function of $\xi_{\rm tp}/(Ma)$ evaluated at 17 different values of the disorder parameter $6J \leq W \leq 15J$. In the inset the dependence of the natural logratihm of $\xi_{\rm tp}$ (in units of the lattice onstant) on the random-potential amplitude in units of tunnelling is shown, at the same energy $E = 0$ and interaction $U = J$. From Ref. [151].

The appearance of this phenomenon was confirmed by Schreiber's group [153] via the decimaton method, obtaining slightly different numbers for the critical disorder stength, $W = (8.1 \pm 0.1)J$. In the same article the authors obtained the phase diagram of localization in the interaction-disorder plane, shown in Fig. 1.14. However Shepelyansky [155] questioned the above results of Ref. [151], suggesting that they were ascribable to finite-size effects due to the smallness of the considered lattices and, based on Imry's arguments, he ruled out the possibility of an Anderson transition in 2D for two short-range interacting particles.

Concerning the case of long-range Coulomb interaction potentials, like those acting in electron gases, the appearance of a metal-insulator transition was also predicted by Shepelyansky [156]. The conjecture was also supported by numerical simulation based on the statistics of energy levels. Defining $s_i := \frac{E_{i+1}-E_i}{\langle \Delta E \rangle}$, where $\langle \Delta E \rangle$ denotes the average energy spacing, and $P(s)$ as the probabiliy distribution of them, the following quantity

$$\eta_D(W) = \frac{\int_0^{s_0} \mathrm{d}s \, [P(s) - P_{WD}(s)]}{\int_0^{s_0} \mathrm{d}s \, [P_P(s) - P_{WD}(s)]} \, . \tag{1.27}$$

was computed for different values of the disorder parameter W. In the definition of η_D in Eq. (1.27), $P_P(s)$ corresponds to Poisson's distribution, signalling localized states, and $P_{WD}(s)$ the Wigner-Dyson distribution, associated to extended states, whose functional form is specified in App. A.1.

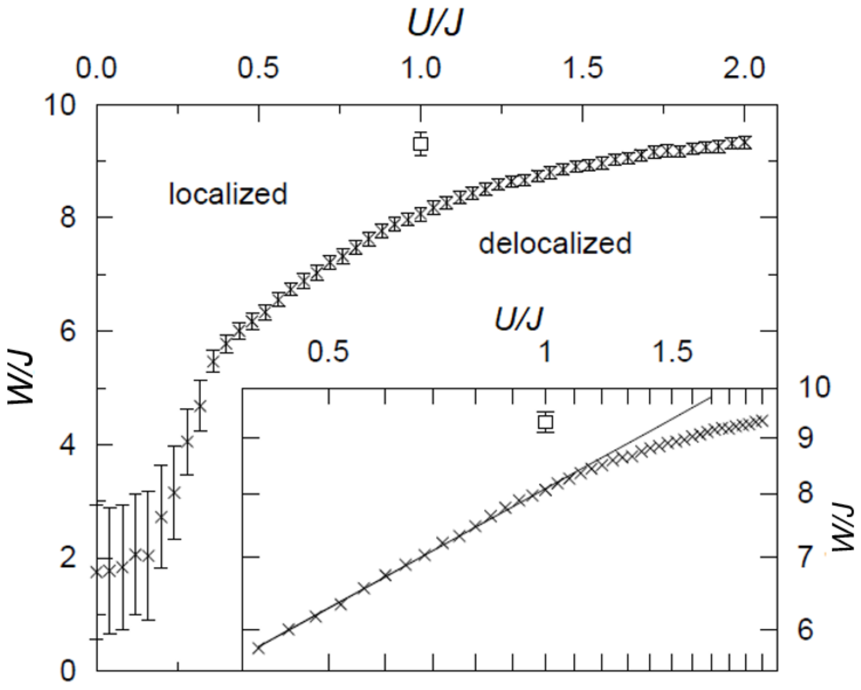

FIGURE 1.14 – Phase diagram of the two-particle Anderson transition in $d = 2$. The data point for $U = J$ indicates the result of Ref. [151]. The error bars represent the error propagation coming from the finite-size scaling procedure (presented in Sec. b)). In the inset the power-law fit to the data for $U \geq 0.4J$ is displayed and the exponent found is 0.36. From Ref. [153].

This method allowed to obtain a critical regime of $P(s)$ in the range $7J \leq W \leq 10J$, where η_D approaches the critical value of the single-particle Anderson model, $\eta_{D,c} = 0.20$.

Recent simulations aiming at inspecting the behaviour of the inverse participation ratio show that, for two hardcore bosons in 2D lattices, the localization length is enhanced by interactions as long as $U \leq 4J$, whereas at higher interaction the two-particle wavefunctions get more extended in the space [157].

In the light of the controversy on the occurrence of a metal-insulator transition in the presence of short-range interactions, the problem in $d = 2$ appears to be still interesting and in Chap. 3 we will present the results of our research on it.

1.6 Conclusions

In this chapter we have shown an overview of Anderson localization as a wavelike phenomenon, providing also a brief survey on the experimental platforms in which it has been sought and observed. We have then illustrated the localization properties of Anderson's model, discussing in details the nature of the eigenstates, the energy spectrum and the phase diagram in three dimensions. One of the main goals of the thesis is to understand how this phase diagram generalizes in the presence of interaction. The link between the spatial behaviour of the wave-functions and the macroscopical properties is highlighted through the description of the scaling theory of localization.

Finally, we discuss the combined effects of interactions and disorder, focusing on the problem of two particles coupled by short-range interactions. Prior to the presentation of our research on the latter topic, we will explain how we tested suitable numerical methods on the single-particle case, already investigated in literature.

CHAPTER 2

NUMERICAL APPROACHES TO ANDERSON TRANSITIONS

In this chapter we present the numerical techniques that we have used in this thesis to estimate the position of the critical point of the Anderson transition. We start by discussing the transfer-matrix technique [15–17,76,158,159], which is the method of choice for disordered lattice system with short-range hopping. In this method the transmission amplitude calculated from quasi-1D bars allows to extract the associated Lyapunov exponent with great accuracy. This technique can also be adapted for continuous systems, as we shall discuss in Chapter 4, where it will be applied to the study of atoms in correlated random potentials.

Next, we present an alternative procedure where the Lyapunov exponent is extrapolated starting from much shorter bars, by appropriately sampling the transmission amplitude along the bar. We illustrate the convergence and the accuracy of this algorithm in the context of the Anderson model in three dimensions. In particular, we show that the results for the position of the mobility edge as well as the value of the critical exponent of the Anderson transition are in very good agreement with the more accurate estimates based on transfer-matrix algorithms.

In the last section we introduce the disorder-averaged density of states, associated to the disordered model. We outline our numerical procedure to compute it from the knowledge of the energy spectrum. We compare our numerical results for the three-dimensional Anderson model with theoretical estimates based on the coherent-potential approximation, noticing a very good agreement. The same approach will be followed in the context of the two-particle problem.

2.1 Computation of the critical point

In this section, two different numerical procedures are presented for the estimation of the localization length of wave-functions in bar-shaped lattices. This quantity, extracted from finite-size systems will be useful in the identification and in the computation of the critical point of Anderson transition of one particle in three dimensions.

2.1.1 Transfer-matrix method

One of the most widely used numerical methods for investigating the problem of one particle in a disordered lattice is the transfer-matrix method, that has proved to be an efficient technique, suitable for a model endowed with short-range hopping, like Anderson's one.
As in the example shown in Sec. 1.4.1 in the presentation of Scaling theory, the transfer-matrix procedure allows one to use a set of quantities evaluated at a given position to express the ones related to an adjacent position. In order to clarify its meaning, we consider wavefunction of a single particle in three dimensions, which satisfies a time-independent Schrödinger equation:

$$\left(-\frac{\hbar^2}{2m}\nabla^2 + U(\boldsymbol{r})\right)\psi(\boldsymbol{r}) = E\psi(\boldsymbol{r}) \ , \tag{2.1}$$

In a bar-shaped lattice with M sites along the transverse directions and $N \gg M$ sites along the longitudinal one, the Laplacian operator can be approximated according to the centered-difference scheme, derived from expansion in Taylor's series up to the second order in the distance,

$$\frac{\partial^2\psi(\boldsymbol{r})}{\partial x^2} \mapsto \frac{\psi_{ijk+1} + \psi_{ijk-1} - 2\psi_{ijk}}{a^2} \ , \tag{2.2}$$

where a is the latting constant and ψ_{ijk} corresponds to $\langle \boldsymbol{r}|\psi\rangle$. Repeating the above approximation to all the coordinates and placing the z axis parallel to the longer side of the lattice, starting from Eq. (2.1) we are left with the relation:

$$\psi_{ijk+1} = \left(\frac{v_{ijk} - E}{J}\right)\psi_{ijk} - \psi_{i-1jk} - \psi_{i+1jk} - \psi_{ij-1k} - \psi_{ij+1k} - \psi_{ijk-1} \ , \tag{2.3}$$

where $i, j = 1, 2, ..., M$ and $k = 1, 2, ..., N$, whereas $J := \frac{\hbar^2}{2ma^2}$ and $v_{ijk} := U_{ijk} - 6J$. This equation, Eq. (2.3), is nothing but a recursive equation having the same form as the one which can be obtained by plugging Anderson Hamiltonian (Eq. (1.9)) into stationary Schrödinger equation $\hat{H}|\psi\rangle = E|\psi\rangle$, where J represents the hopping amplitude and v_{ijk} the random potential at that site. After evaluating the right-hand side of Eq. (2.3) in all sites in the lattice section lying on the $z = ka$ plane, we build a M^2-component vector, $\boldsymbol{\psi}_{k+1} := (\psi_{11k+1}, \psi_{21k+1}, .., \psi_{M1k+1}, \psi_{12k+1}, ..\psi_{MMk+1})^T$, and get the following relation with vectors $\boldsymbol{\psi}_k$ and $\boldsymbol{\psi}_{k-1}$:

$$\begin{pmatrix} \boldsymbol{\psi}_{k+1} \\ \boldsymbol{\psi}_k \end{pmatrix} = \begin{pmatrix} \mathbf{V}_k & -\mathbb{1} \\ \mathbb{1} & \mathbb{0} \end{pmatrix} \begin{pmatrix} \boldsymbol{\psi}_k \\ \boldsymbol{\psi}_{k-1} \end{pmatrix} = \mathbf{T}_k \begin{pmatrix} \boldsymbol{\psi}_k \\ \boldsymbol{\psi}_{k-1} \end{pmatrix} = \prod_{m=k}^{1} \mathbf{T}_m \begin{pmatrix} \boldsymbol{\psi}_1 \\ \boldsymbol{\psi}_0 \end{pmatrix} \ ,$$

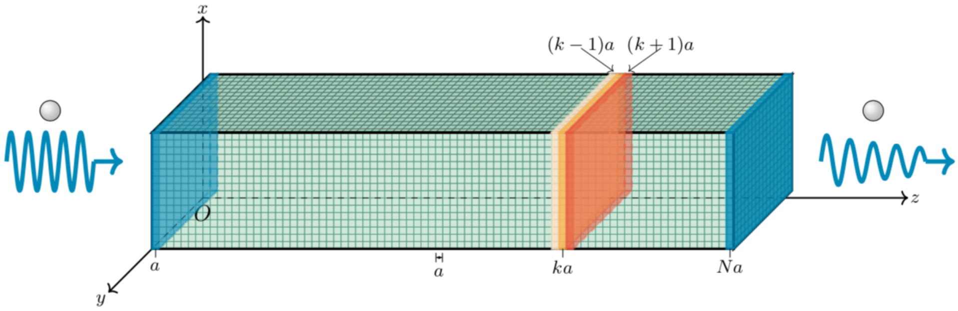

FIGURE 2.1 – Representation of the M^2N elongated random lattice, at whose ends the asymptotic exponential attenuation of a wave-function is estimated through the computation of the localization length.

where $\mathbf{T}_k$ is the transfer matrix and $\mathbb{0}$ is the $M^2 \times M^2$ zero matrix. A peculiar feature of the transfer matrix is that it is symplectic, i.e. it obeys the relation:

$$\mathbf{JTJ} = \mathbf{T}^{-1} \,,$$

where

$$\mathbf{J} = \begin{pmatrix} \mathbb{0} & \mathbb{1} \\ \mathbb{1} & \mathbb{0} \end{pmatrix} .$$

For this reason, the eigenvalues of the transfer matrix occur in pairs (t_i, t_i^{-1}), with eigenvectors $(\boldsymbol{v}_i, \boldsymbol{J}\boldsymbol{v}_i)$, where $i = 1, 2, ..., M^2$.

Furthermore, the matrix $\mathbf{V}_k$ with $k = 1, ..., N$ is a sparse $M^2 \times M^2$ matrix, that, after imposing periodic boundary conditions, takes the following structure:

$$\boldsymbol{V}_k = \begin{pmatrix} \boldsymbol{V}_{1k} & -\mathbb{1} & \mathbb{0} & \cdots & \mathbb{0} & -\mathbb{1} \\ -\mathbb{1} & \boldsymbol{V}_{2k} & -\mathbb{1} & \ddots & \ddots & \mathbb{0} \\ \mathbb{0} & -\mathbb{1} & \boldsymbol{V}_{3k} & \ddots & \ddots & \vdots \\ \vdots & \ddots & \ddots & \ddots & \ddots & \mathbb{0} \\ \mathbb{0} & \ddots & \ddots & \ddots & \ddots & -\mathbb{1} \\ -\mathbb{1} & \mathbb{0} & \cdots & \mathbb{0} & -\mathbb{1} & \boldsymbol{V}_{Mk} \end{pmatrix} ,$$

where each block of the matrix can be written as:

$$\boldsymbol{V}_{jk} = \begin{pmatrix} \frac{v_{1jk}-E}{J} & -1 & 0 & \cdots & 0 & -1 \\ -1 & \frac{v_{2jk}-E}{J} & -1 & \ddots & \ddots & 0 \\ 0 & -1 & \frac{v_{3jk}-E}{J} & \ddots & \ddots & \vdots \\ \vdots & \ddots & \ddots & \ddots & \ddots & 0 \\ 0 & \ddots & \ddots & \ddots & \ddots & -1 \\ -1 & 0 & \cdots & 0 & -1 & \frac{v_{Mjk}-E}{J} \end{pmatrix} .$$

The boundary conditions along the transverse directions allows to reduce effects due to the finiteness of the lattice size.

Labelling with $\mathbf{M}_k := \prod_{m=k}^{1} \mathbf{T}_m$ the transfer-matrix product performed up to the section in the $z = ka$ plane, the product $(\mathbf{M}_N \mathbf{M}_N^\dagger)^{1/N}$ approaches an asymptotic matrix in the limit of $N \to +\infty$, as stated by a theorem due to Oseledec [160]. Denoting the eigenvectors of $\boldsymbol{\Omega}_N := \left(\mathbf{M}_N \mathbf{M}_N^\dagger\right)^{1/2N}$ with $\{\boldsymbol{w}_i^{(N)}\}$, where $i = 1, 2, ..., 2M^2$, the corresponding eigenvalues, $\{\mathrm{e}^{\pm\gamma_i^{(N)}}\}$, appear in couples of opposite sign. In the limit of infinite N, their natural logarithms converge to the Lyapunov exponents γ_j of the system:

$$\lim_{N\to+\infty} \left(\boldsymbol{w}_i^{(N)\,T} \mathbf{M}_N^T \mathbf{M}_N \boldsymbol{w}_i^{(N)}\right)^{1/2N} = \lim_{N\to+\infty} \|\mathbf{M}_N \boldsymbol{w}_i^{(N)}\|^{1/N} = \mathrm{e}^{\gamma_i} .$$

Viewing the z-coordinate as time, the γ_j measure the separation between infinitesimally close trajectories of a dynamical system described by a map given by the transfer matrix $\mathbf{T}$. Any arbitrary vector, representing the wave-function, can be described by a set of vectors whose asymptotic divergence is given by different Lyapunov exponents, and the smallest of them corrsponds to the slowest decay of the wave-function in space, which is equal to the reciprocal of the localization length [105] λ_M of the finite-size system:

$$\lambda_M = \frac{1}{\gamma_{M^2}} ,$$

where the superscript of γ comes from the fact that the exponents are sorted in descending order, $\gamma_1 > \gamma_2 > \cdots > \gamma_{M^2}$. In numerical computations, all Lyapunov exponents γ_i tend to converge towards the highest one, due to round-off errors: to avoid this shortcoming one has to keep all vectors $\boldsymbol{w}_i$, with $i = 1, 2, \ldots, M^2$ orthogonal to each other. Considering an initial vector $\boldsymbol{\phi}^{(1)}$ that contains equally weighted contribution from every eigenvector $\boldsymbol{v}_i$ of $\mathbf{T}_1$, after n iterations of the map, the iterated vector will become approximately equal to

$$\boldsymbol{\phi}^{(n)} \approx \sum_{i=1}^{M^2} \left(\mathrm{e}^{nt_i} \boldsymbol{v}_i + \mathrm{e}^{-nt_i} \mathbf{J} \boldsymbol{v}_i\right) ,$$

in which the fractional weight of the eigenvector corresponding to the smallest positive exponent t_{min} is roughly $w_n = \mathrm{e}^{(t_{min}-t_{max})n}$. When w_n is larger than the accuracy ϵ_{comp} of the machine, the information about t_{min}, necessary to estimate the localization length, is lost and the transfer matrix becomes singular. We are thus required to restore the orthonormality of the columns of $\mathbf{T}$, after an appropriate number of iterations of the transfer-matrix product.

The most direct procedure is provided by the Gram-Schmidt's method, which nevertheless is not very efficient. A faster and more numerically stable algorithm is the one given by the QR factorisation, introduced by Slevin in [159], who proposed to decompose the transfer-matrix product into a $2M^2 \times M^2$ matrix with orthogonal columns $\mathbf{Q}$ and an upper triangular invertible $M^2 \times M^2$ matrix $\mathbf{R}$. Supposing that this decomposition is repeated n_O times, at intervals of n_I transfer-matrix multiplications, the product found at the l-th step of the procedure is:

$$\mathbf{Q}^{(l)}\mathbf{R}^{(l)} = \mathbf{T}_{ln_I}\mathbf{T}_{ln_I-1}...\mathbf{T}_{(l-1)n_I+1}\mathbf{Q}^{(l-1)} \; .$$

where $\mathbf{Q}^{(0)}$ is the orthogonal matrix at the first step. In this way, it is possible to extract the positive Lyapunov exponents $\{\gamma_i\}$ with $i = 1, 2, ..., M^2$ from the diagonal elements of $\mathbf{R}^{(n_O)}$:

$$\gamma_i = \frac{1}{Na} \ln \mathrm{R}_{i,i}^{(n_O)} \; .$$

Since the diagonal elements of the upper triangular matrix appear in decreasing order, the lowest exponent, corresponding to the inverse of the localization length λ_M of the finite-size quasi-1D system, is γ_{M^2}, that we name for the sake of simplicity γ_M.

2.1.2 Green's function technique

An alternative method for analysing the same kind of lattices is the one making use of the Green's function, introduced by MacKinnon and Kramer [18] [161]. Differently from the transfer-matrix one, it is suitable also for dense matrices, as the ones representing the two-body Hamiltonian, as we will see in Chap. 3.

Resuming the one-particle case, applying periodic boundary conditions along transverse directions x and y, but not along z, the Hamiltonian in Eq. (1.9) in the site basis, written as a $M^2N \times M^2N$ matrix, takes a block-tridiagonal form $\mathbf{H} = \mathrm{tridiag}(-\mathbb{1}, \mathbf{H}_i, -\mathbb{1})$, where each block $\mathbf{H}_i$ with $i = 1, 2, \ldots, N$ is a $M^2 \times M^2$ symmetric matrix. At given values of tunneling J, disorder W and energy E, the Green's function can be drawn from the Hamiltonian using

$$\boldsymbol{G}(E) = (E\mathbb{1} - \boldsymbol{H})^{-1} \; . \tag{2.4}$$

Each element of the matrix $\mathbf{G}(E)$ represents the Green's function calculated at the site $(\boldsymbol{r}_m, \boldsymbol{r}_n)$ in the lattice, where $\boldsymbol{r}_m = (x_m, y_m, z_m)^T a$ and $m_m = x_m + (y_m - 1)M + (z_m - 1)M^2$.

Writing it in a $N \times N$ block structure too, its off-diagonal elements belonging to the $M^2 \times M^2$ block $\boldsymbol{G}_{1n}$, where $n \leq N$, are necessary for determining the transmission amplitude between one end of the bar and the slice of the three-dimensional bar lying on the plane $z = na$:

$$t_{1n} = J^2 |\mathrm{Tr}\, \boldsymbol{G}_{1n}|^2 = \sum_{m_1=1}^{M^2} \sum_{m_n=1+(n-1)M^2}^{nM^2} J^2 |G_{m_1 m_n}|^2 \, , \tag{2.5}$$

where the single matrix index is connected to the position of the particle $(x_k, y_k, k)^T a$ in the k-th cross-section of the lattice, shown in Fig. 2.2, through the relation:

$$m_k = x_k + (y_k - 1)M + (k-1)M^2 \, ,$$

in which $k \in \{1, 2, \ldots, n\}$ and $n \leq N$.

a) Recursive method

In the case of matrices with short-range hopping like the one-particle Hamiltonian, a quicker numerical procedure for obtaining $\mathbf{G}$ without diagonalizing $\mathbf{H}$ consists in calculating only the elements in the block $\mathbf{G}_{1N}(E)$ in Eq. (2.5) recursively [161]. Considering lattices with $n \leq N$ sites along z and labelling the $M^2 \times M^2$ blocks into which the Green's function is split as $\mathbf{G}^{(n)}_{i,j}(E)$, with $i, j = 1, 2, .., n$, the following relations can be exploited [79]:

$$\begin{aligned} \mathbf{G}^{(n+1)}_{1,n+1}(E) &= \mathbf{G}^{(n)}_{1,n}(E) \mathbf{G}^{(n+1)}_{n+1,n+1}(E) \\ \mathbf{G}^{(n+1)}_{n+1,n+1}(E) &= \left[E\mathbb{1} - \mathbf{H}^{(n+1)}_{n+1} - J^2 \mathbf{G}^{(n)}_{n,n}(E) \right]^{-1} , \end{aligned} \tag{2.6}$$

where $\mathbf{G}^{(n)}_{1,1}(E) = (E\mathbb{1} - \mathbf{H}^{(1)}_1)^{-1}$ and $\mathbf{H}^{(n+1)}_{n+1}$ is the block of the Hamiltonian related to the lattice with $n+1$ sites along z, evaluated at the right end of the bar.

b) Direct-inversion procedure

To dense matrices, the recursive formula (Eq. (2.6)) in Sec. a) is not applicable, so a more computationally expensive method is needed. In this case, the most direct solution consists in determining $\boldsymbol{G}(E)$ from the inversion of the one-particle Hamiltonian $\boldsymbol{H}$, therefore following Eq. (2.4). Alternatively, the single-particle Hamiltonian $\boldsymbol{H}$ can be diagonalized, thus finding its eigenvalues $\{\varepsilon_s\}$ and eigenvectors $\{\boldsymbol{\phi}_s\}$, where $s = 1, 2, ..., M^2 N$. The Green's function associated to the particle at energy E can be then evaluated as:

$$\mathbf{G}(E) = \sum_{s=1}^{M^2 N} \frac{\boldsymbol{\phi}_s^\dagger \boldsymbol{\phi}_s}{E - \varepsilon_s} \, . \tag{2.7}$$

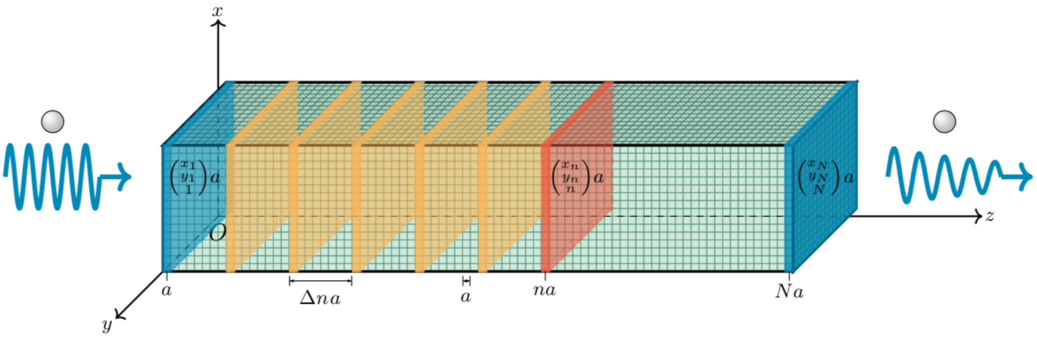

FIGURE 2.2 – Lattice showing the sites (shaded in yellow and red) at which the transmission amplitude t is computed and retained for the subsequent fit, to the end of estimating the Lyapunov exponent characterizing the one-particle wavefunction between the cross-sections lying in $z = a$ and $z = na \leq Na$.

2.1.3 Accuracy test of the direct-inversion method

a) Extraction of the Lyapunov exponent

The Lyapunov exponent associated to the transmission of the particle between the two ends of the bar can be recovered by retaining only the t_{1N} [18]:

$$\gamma_M^{(\mathrm{Tri})}(N) = -\frac{\ln(t_{1N})}{2a(N-1)} , \tag{2.8}$$

where the superscript ‘Tri’ labels the ‘triangular’ method we are using for estimating the quantity. Another method consists in fitting the values of $(n, \ln t_{1n})$ at regular intervals Δn, starting from a n_0 not too small, in order to ensure that the behaviour of the transmission amplitude t_{1n} as a function of the position along the z axis is exponential. Fitting the data $(i\Delta n, \ln t_{1i\Delta n})$ where $i = 1, 2, \ldots, N/\Delta n$ with a straight line $\ln t_{1n} = pn + q$, from the slope p we obtain the Lyapunov exponent between the cross-sections 1 and N as

$$\gamma_M^{(\mathrm{Fit})}(N) = -\frac{p}{2a} . \tag{2.9}$$

The procedure is repeated for many disorder realizations, and the average value $\overline{\gamma}_M(n)$ is found, in order to estimate the reduced localization length $\Lambda_M = (Ma\overline{\gamma}_M)^{-1}$ in Eq. (2.10), which depends on the parameters of the Hamiltonian (E, W, J).

The Lyapunov exponents for different realizations of the random potential allow one to calculate a dimensionless reduced localization length Λ_M, that describes the behaviour of the system under changes of the number of sites along a transverse direction M. Keeping the parameters (E, J) of the

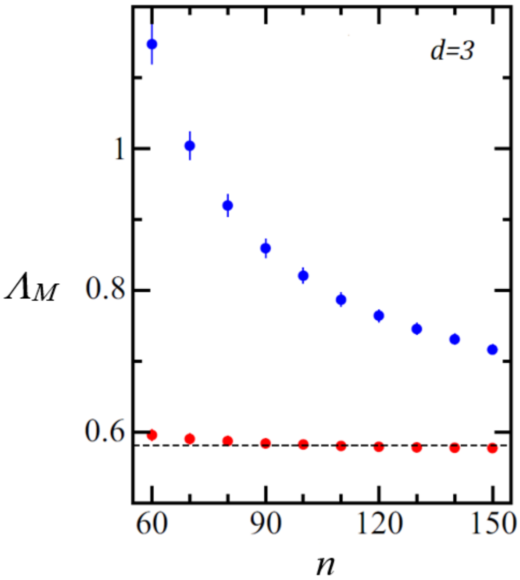

FIGURE 2.3 – Convergence study of the reduced localization length as a function of the position along the z direction in units of lattice constants. The blue points represent the ones found with the usual 'triangular' procedure (Eq. (2.8)) while the ones in red are those found using linear regressions (Eq. (2.9)). The analysis is carried out with by fixing the parameters of the Anderson's Hamiltonian (Eq. (1.9)) as follows: the total energy is $E = 0$ (middle of the band), the typical disorder is $W = 16.5J$. Concerning the lattice, $M = 12$, $N = 150$, whereas $N_{tr} = 701$. The dashed line corresponds to the estimate $\Lambda_M = 0.5814 \pm 0.0004$ obtained from transfer-matrix calculations performed on a bar of length $N = 10^5$ lattice constants after averaging over $N_{tr} = 240$ disorder realizations.

Hamiltonian as fixed, Λ_M can be written as:

$$\Lambda_M(W) = \frac{1}{Ma\overline{\gamma_M(W)}} = f_d\left(\frac{\xi(W)}{M}\right), \tag{2.10}$$

According to the one-parameter scaling ansatz [16], this quantity depends on a characteristic length $\xi(W)$ through a function f_d which is regular in $d \leq 2$, and depends on the universality class. This characteristic length, that corresponds also to the limit $\xi(W) = \lim_{M\to+\infty} \lambda_M(W) = \lim_{M\to+\infty} \overline{\gamma_M}^{-1}$, represents the localization length of the infinite system in $d \leq 2$ as well as in the insulating phase at higher dimensions, or the correlation length in the metallic phase in $d > 2$.

While in $d = 2$ f_d increases monotonically as $f_d(\xi/M) = \xi/M$, in $d = 3$, f_d develops a singular behaviour with an upper branch in which it decreases as $f_d(\xi/M) = M/\xi$ at $W < W_c$ [18], whereas in the lower branch the reduced localization length behaves as in the two-dimensional case [161].

We will illustrate the behaviour of the scaling function around the critical point in next paragraph, while presenting the finite-size scaling technique.

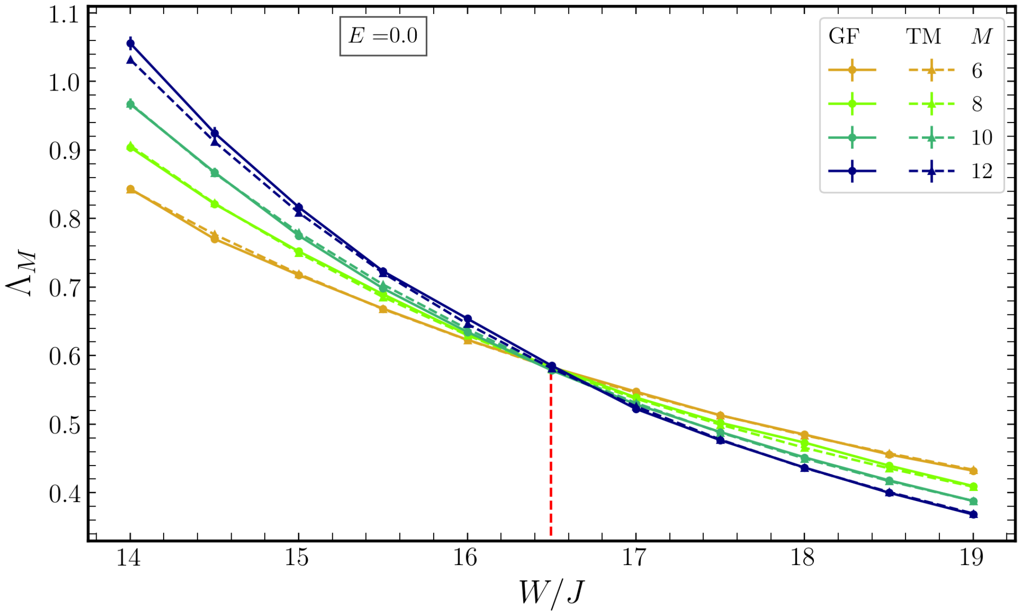

FIGURE 2.4 – The reduced localization length evaluated for different system sizes with transfer-matrix (TM) and Green's function (GF) methods. The common intersection between the curves represents the critical point, at which $\mathrm{d} \ln \Lambda_M / \mathrm{d} \ln M = 0$, highlighted also by the red vertical dashed line.

b) Finite-size scaling analysis

In order to estimate the universal properties such as the critical exponent ν and the reduced localization length Λ_c, and the system-dependent ones, as the critical disorder parameter W_c or the critical energy E_c in $d > 2$, an accurate procedure is provided by the finite-size scaling method [17]. The starting point is the expansion in Taylor series of the reduced localization length around the critical value of the typical random potential amplitude, which separates the localized from the extended states at fixed energy and tunneling. This reduced localization length can thus be written as:

$$\Lambda_M^{(FSS)}(W) = \sum_{i=0}^{m} c_i \big(u_R(W) M^{1/\nu} \big)^i \,, \tag{2.11}$$

where:

$$u_R(W) = \sum_{j=0}^{n} b_j \left(\frac{W - W_c}{W_c} \right)^j \,. \tag{2.12}$$

Since at the critical point $\Lambda_M^{(FSS)}(E, W_c, J)$ is independent of system size M, the coefficient b_0 is set to zero, whereas c_1 is set to unity due to undefined scale or free b_1 as fit parameter.

For a set of values of W and four lattice sizes, to the purpose of finding the best estimate of the parameters $(a_0, a_2, ..., a_m, b_1, .., b_n, W_c, \nu)$, a non-linear fit using Levenberg-Marquardt algorithm is

	ν	Λ_c	W_c/J	N	N_{Tr}
Transfer matrix	1.55 ± 0.02	0.582 ± 0.002	16.49 ± 0.03	50000	240
Green's function	1.58 ± 0.06	0.583 ± 0.006	16.50 ± 0.06	150	1200

TABLE 2.1 – Critical values of the reduced localization length and the random potential amplitude obtained with two different numerical methods starting from N-sites long quasi-1D lattices. The value of the critical exponent ν is in excellent agreement with the one found in [76], exposed in Tab. 1.1.

performed, minimizing the χ^2 with $N_D - 2 - m - n$ degrees of freedom:

$$\chi^2 = \sum_{l=1}^{N_D} \frac{(\Lambda_{M,l}^{(FSS)} - \Lambda_{M,l})^2}{\sigma_l^2} \tag{2.13}$$

where σ_l^2 is the statistic uncertainty on $\Lambda_{M,l}$. To the end of comparing the results obtained with the two numerical methods, we estimated the least Lyapunov exponents fot N_{Tr} realizations of the random potential, then evaluated the reduced localization length and found its critical value as well as the critical exponent and disorder using $\Lambda_M^{(FSS)}$ approximated up to the second order in the expansion. The results are listed in Tab. 2.1, while in Fig. 2.4 the behaviour of Λ_M in the vicinity of the critical point is shown.

Considering $n = m = 3$ in Eq.s (2.14) and (2.12), we have also estimated the behaviour of the reduced localization length as a function of localization length ξ of the infinite-sized lattice, by setting $\xi/a = |u_r(W)|^{-\nu}$ in Eq. (2.14). The separation of Λ_M into two branches near the critical point is shown in Fig. 2.5.

Due to is weaker dependence on number of sites along the z direction (M^6N vs M^8N^4, that can be reduced to M^8N^3 using a particular alogithm for block-tridiagonal matrix inversion, illustrated in Chap. 3), the transfer-matrix method allows for the computation over much longer bars. Since γ_M is a self-averaging quantity, performing simulations on larger lattices allows to lower the number of realizations of the random potential necessary for achieving satisfactory accuracy of the estimates. The finite-size scaling procedure can be also carried out by considering one of the irrelevant scaling variables, as it has been done by Slevin and Ohtsuki [76], who preformed transfer-matrix calculations for the estimates of the Lyapunov exponent. The first irrelevant variable f_I, characterized by the exponent y, contributes to Λ_M with the function $u_I\left(\frac{W-W_c}{W_c}\right)$, so that the reduced localization length is approximated as

$$\Lambda_M^{(\mathrm{FSS})}(W) = \sum_{m=0}^{N_R} \sum_{n=0}^{N_I} c_{mn} \left[f_R(W,M)\right]^m \left[f_I(W,M)\right]^n \ , \tag{2.14}$$

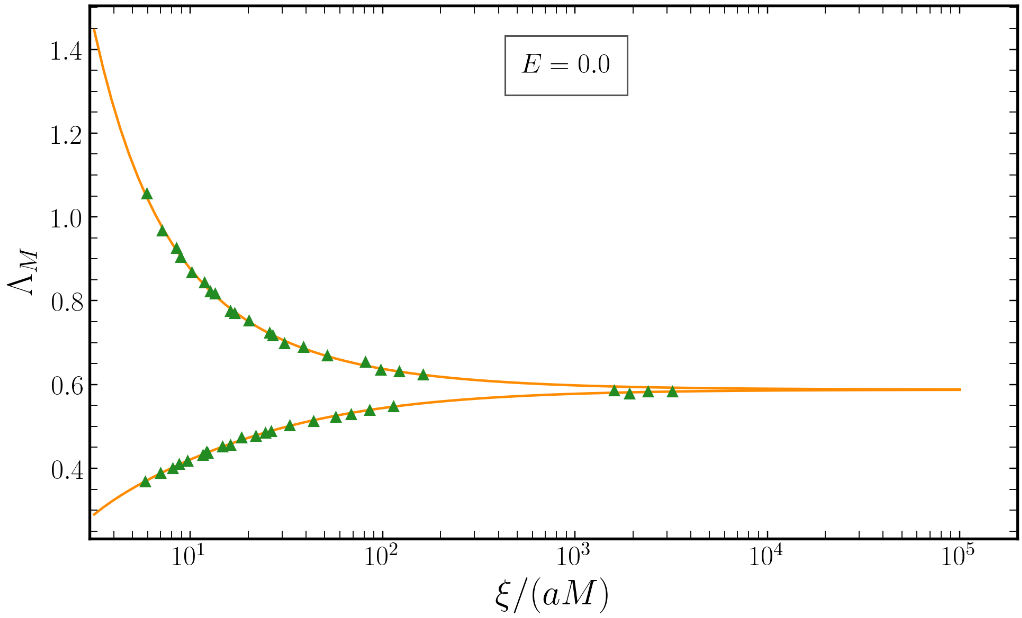

FIGURE 2.5 – The reduced localization length as a function of localization length in units of the transverse side of the lattice. The orange curve has been obtained by fitting the data obtained by means of the Green's function method (GF) in Fig. 2.4 (dark green triangles) with the curve $\Lambda_M^{(\mathrm{FSS})}$ expanded up to the third order in u_R and $(W - W_c)/W_c$, and using the definition $\xi/a = |u_R(W)|^{-\nu}$.

where

$$f_R(W, M) = M^{1/\nu} u_R(W) = M^{1/\nu} \sum_{i=0}^{M_R} a_i \left(\frac{W - W_c}{W_c}\right)^i ,$$

and

$$f_I(W, M) = M^{-y} u_I(W) = M^{-y} \sum_{j=0}^{M_I} b_j \left(\frac{W - W_c}{W_c}\right)^j . \tag{2.15}$$

Setting $c_{01} = c_{10} = 1$ and $a_0 = 0$, the number of parameters of the non-linear fit becomes $N_P = 2 + M_I + M_R + (N_I + 1)(N_R + 1)$ [158], where the critical exponents ν and y as well as the critical disorder W_c are included in the calculation. The reckonings executed by the aforementioned authors led to an estimate of 3.3 ± 0.6 for the exponent y associated to the first irrelevant variable. They also found the critical reduced localization length as $\Lambda_c = 0.577 \pm 0.001$ and the critical disorder parameter as $W_c = (16.536 \pm 0.006)J$, considering a random potential following the uniform distribution. The latter estimate is in full agreement with the one we have obtained, listed in Tab. 2.1.

2.2 Disorder-averaged density of states

Unlike the localization length, the density of states $\bar{\rho}(E)$ averaged over disorder configuration has a smooth behaviour near the critical point and it can be well predicted also analytically. In the follow-

ing, we present a numerical method to determine it and we will compare the results against the ones derived from the Green's function within the coherent potential approximation (CPA).
Considering a cubic lattice with M^3 sites and imposing periodic boundary conditions to the Hamiltonian along the three directions, we begin by diagonalizing the Hamiltonian $\boldsymbol{H}$. Repeating the procedure for N_{tr} disorder realizations, and labelling the eigenvalues as $\{\varepsilon_{\alpha,r}\}$, where $r = 1, 2, \ldots, N_{tr}$ identifies the single configuration of the random potential, the disorder-averaged density of states can be expressed as:

$$\overline{\rho}(E) = \sum_{r=1}^{N_{tr}} \sum_{\alpha=1}^{M^3} \frac{\delta(E - \varepsilon_{\alpha,r})}{N_{tr}(Ma)^3} \,, \tag{2.16}$$

where, thanks to Gershgorin's theorem [162], the eigenvalues of $\mathbf{H}$ are within the interval $\left[-W/2 - 6J, W/2 + 6J\right]$. The expression in the right-hand side of Eq. (2.16) can be reconstructed numerically, starting from the subdivision of the energy interval of interest into a set of $N_b \approx \sqrt{M^3}$ bins of equal width, which at the same time satisfies $\Delta E \ll (W + 12J)$. For each realization of the disordered potential, the number eventualities in each frequency class $\{f(i,r)\}$ with $i = 1, 2, \ldots, N_b$ is counted, then the average value per unit volume is performed, in accordance with Eq. (2.16):

$$\overline{\rho}(i) = \frac{1}{\Delta E a^3} \sum_{r=1}^{N_{tr}} \frac{f(i,r)}{N_{tr} M^3} \,.$$

From this function, an interesting quantity is represented by the band edges, which correspond to the energy values delimiting the region where the disorder-averaged density of states is significantly different from zero. The upper (resp. lower) band-edge position is then evaluated by identifying the upper (resp. lower) energy $E_{\max,l}$ (resp. $E_{\min,l}$) associated to the frequency class f_l such that, considering an ordered set of energies $E_{\max/\min,0} < E_{\max/\min,1} < \cdots < E_{\max/\min,N_b}$ associated to the respective bin, $\overline{f}_{l+1} < 0.5 \leq \overline{f}_l$ (resp. $\overline{f}_{l-1} < 0.5 \leq \overline{f}_l$). Using this criterion, at $W = 5J$ we have been able to find $E_l = \pm(6.53 \pm 0.04)J$ for the upper and the lower band edges respectively.

2.2.1 The coherent potential approximation

As previously disclosed, the density of states can also be well estimated analytically within the CPA, according to which the disordered and uncorrelated potential around a single site can be replaced by an effective medium. This theoretical framework interpolates between the strong- and the low-disorder limits, but is not able to capture the singularities at band edges [81] and it is not suitable for correlated potentials. For a cubic lattice with side $L = Ma$, it can be calculated starting from the ordered system, described by Hamiltonian in Eq. (1.9) with $W = 0$. For a given value of the energy E, the retarded single-site Green's function $G_0(E)$ is translationally invariant, and can be written as:

$$G_0(E) = \lim_{\eta \to 0^+} \iiint_{-\pi/a}^{+\pi/a} \frac{d^3\boldsymbol{k}}{(2\pi)^3} \frac{L^3}{E - \varepsilon(\boldsymbol{k}) + \mathrm{i}\eta} \,, \tag{2.17}$$

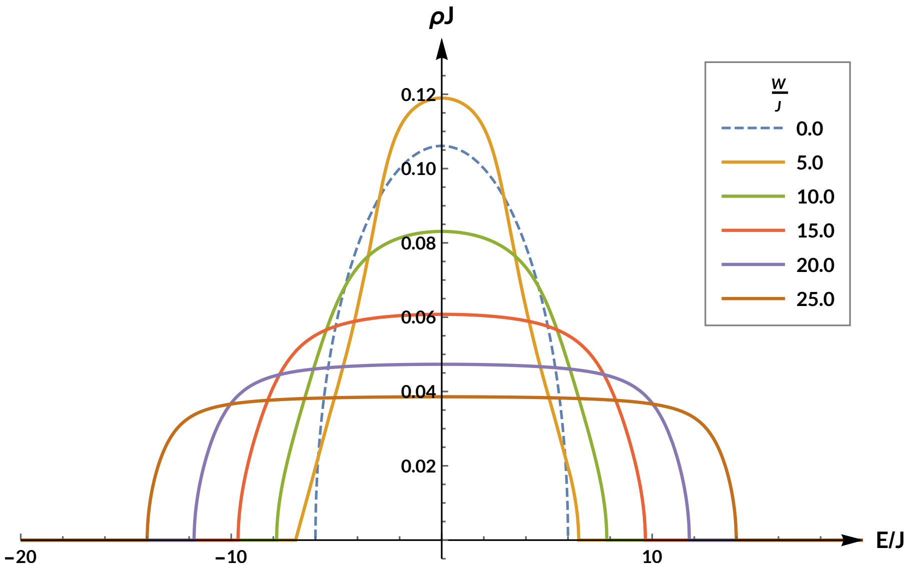

FIGURE 2.6 – The density of states in the CPA approximation, calculated for different disorder typical amplitudes W (solid lines), compared to the density of states of the ordered lattice (dashed line), described by Eq. (2.18), with Eq.s (2.19)-(2.20).

whereas the advanced Green's function is marked by a negative imaginary part at the denominator in Eq. (2.17). Following Joyce [163], the unperturbed Green's function of a cubic lattice can be expressed as

$$G_0(E) = \frac{Q(6/E)}{E} \ , \tag{2.18}$$

where:

$$Q(z) = \frac{1-9\xi(z)^4}{(1-\xi(z)^4)(1+3\xi(z))}\left[\frac{2}{\pi}K(\phi(z))\right]^2 \ . \tag{2.19}$$

Here ξ and k_1 are functions of z defined as:

$$\xi(z) = \left(\frac{1-\sqrt{1-z^2/9}}{1+\sqrt{1-z^2}}\right)^{1/2} \ ,$$

$$\phi(z)^2 = \frac{16\xi(z)^3}{(1-\xi(z))^3(1+3\xi(z))} \ ,$$

where $K(\phi(z))$ is the complete elliptic integral of the first kind:

$$K(\phi(z)) = \int_0^{\pi/2} \frac{\mathrm{d}\theta}{\sqrt{1-\phi(z)^2\sin^2\theta}} \ . \tag{2.20}$$

When disorder is included, the translational invariance of the Green's function is recovered only after averaging over random-potential configurations:

$$\overline{G(E)} := L^3 \iiint\limits_{-\pi/a}^{+\pi/a} \frac{d^3\boldsymbol{k}}{(2\pi)^3}\overline{G_{\boldsymbol{k}}(E)} = L^3 \iiint\limits_{-\pi/L}^{+\pi/L} \frac{d^3\boldsymbol{k}}{(2\pi)^3}\frac{1}{E-\varepsilon(\boldsymbol{k})-\Sigma(E,\boldsymbol{k})} \ .$$

According to the CPA, the effect of the random potential can be reproduced by an effective one, through the presence of a self-energy Σ which is constant in the space of the wave vectors. Calling the Green's function of the disodered system as $\overline{G}$ in the CPA, the latter quantity can be written as:

$$\overline{G(E)} := \left[G_0(E)\right]^{-1} - \Sigma(E) = G_0\left[E-\Sigma(E)\right] \ .$$

Now, the total Green's function operator $\hat{G}(E) := (E-\hat{H}_0-\hat{V})^{-1}$, where $\hat{H}_0$ denotes the Hamiltonian of the ordered system, can be expressed in terms of the so-called t-matrix $\hat{T}$ as $\hat{G} = \hat{\overline{G}} + \hat{\overline{G}}\hat{T}\hat{\overline{G}}$ [164]. Using this definition, the t-matrix, averaged over disorder realizations, must vanish. Considering a single site $\boldsymbol{i}$, $\int \mathrm{d}v_{\boldsymbol{i}}\, p(v_{\boldsymbol{i}})\langle\boldsymbol{i}|\hat{T}|\boldsymbol{i}\rangle = 0$ translates into the self-consistent equation:

$$\int \mathrm{d}v_{\boldsymbol{i}}\, p(v_{\boldsymbol{i}}) \frac{v_{\boldsymbol{i}}-\Sigma}{1-\left[v_{\boldsymbol{i}}-\Sigma\right]G_0\big(E-\Sigma\big)} = 0 \ . \tag{2.21}$$

For a random potential following the uniform distribution (Eq. (1.10)) in the interval $[-W/2, W/2]$, defining for simplicity $g := G_0(E-\Sigma)$, the condition in Eq. (2.21) leads to:

$$W + \frac{1}{g}\ln\left|\frac{2-Wg+2\Sigma g}{2+Wg+2\Sigma g}\right| = 0 \ . \tag{2.22}$$

where the real part of the self-energy represents the shift in energy from $E_{\boldsymbol{k}}$ (Eq. (1.12)) owing to the presence of disorder, coming from the renormalization procedure, whereas the imaginary part can be interpreted as the broadening of the energy distribution or as $2\tau/\hbar$, where τ is the relaxation time appearing in Drude's formula of conductivity. By solving the latter equation, Eq. (2.22), for $\Sigma(E)$ and inserting the self-energy in the disorder-free Green's function (Eq. (2.17)), the density of states, plotted in Fig. 2.6, can be obtained:

$$\rho(E) := -\frac{1}{\pi}\mathrm{Im}\overline{G(E)} = -\frac{1}{\pi}\mathrm{Im}\, G_0\left[E-\Sigma(E)\right] \ . \tag{2.23}$$

By reexpressing the density of states in terms of the advanced Green's function and self-energy, one would obtain an analogous equation as Eq. (2.23), yet differing in the sign on the right-hand side.
The curve resulting from CPA approximation is plotted in Fig. 2.6 for different values of the disorder parameter and in Fig. 2.7 at $W = 5J$, where it is compared against the one computed numerically. The positions of the band edges found numerically prove to be utterly compatible with those predicted by making use of the CPA approximation $E_{be} = \pm 6.5J$ (cf. Fig. 2.6). Although $\overline{\rho}(E)$ is not a scaling quantity (as Λ_M) and its behaviour is smooth around the critical point, larger lattices allow one to

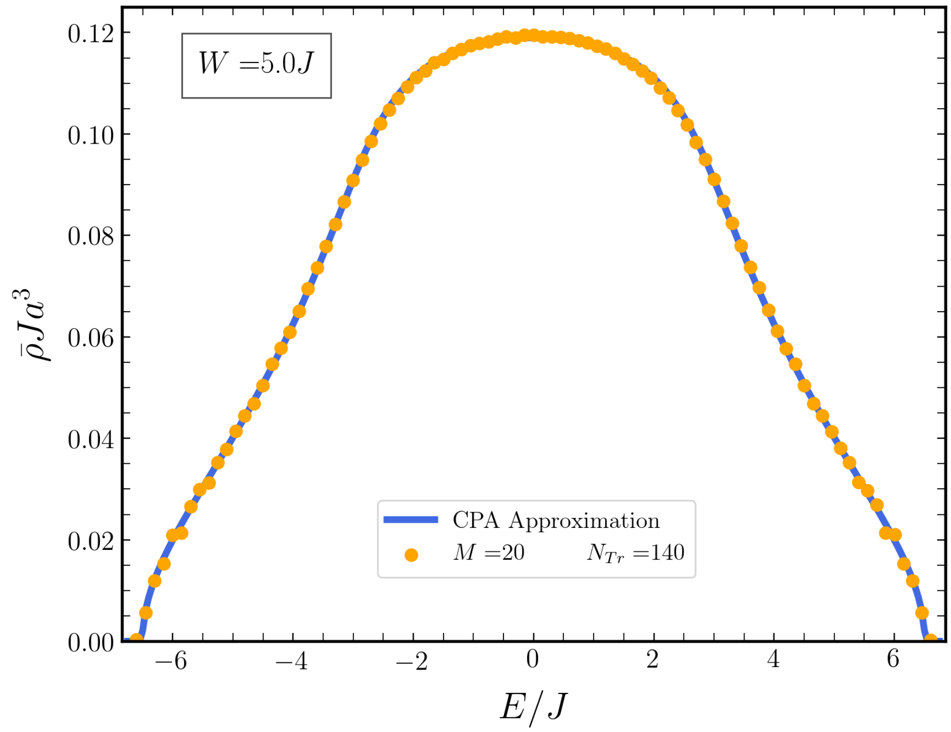

FIGURE 2.7 – The density of states averaged over $N_{tr} = 140$ disorder ralizations calculated numerically at $W = 5J$ (light-orange dots) plotted against the one in the CPA approximation (blue solid line).

estimate the positions of the band edges more precisely, due to the greater number of eigenstates. Therefore, the overlap between the two curves improves as long as N_3 and N_{Tr} are increased.

2.3 Conclusions

In this chapter we have presented two numerical procedures for the extraction of the reduced localization length in bar-shaped grids. The first one is the transfer-matrix, which will be employed in Chapter 4 to investigate Anderson transition of atoms in spatially-correlated potentials upon discretization of the laplacian operator using a high- (fourth-) order finite-difference scheme. The second one is based on a direct calculation of the Green's function via matrix inversion. Differently from the transfer-matrix method, this technique applies to any kind of Hamiltonian, including those with long-range hopping, like the effective model of the pair used in Chapter 3. However, due to the larger computational cost, the length of the bar has to be considerably reduced. We have shown that, in the context of Anderson's model, the Lyapunov exponent can still be extrapolated with sufficient accuracy, by appropriately sampling the logarithm of the transmission amplitude along the short bar. In particular, we have shown that one can extract good estimates for the position of the critical point and the value of the universal exponent of the Anderson transition. This gave us confidence that the same approach can be used for studying the the two-particle problem. For the same model, we have tested our algorithm to compute the disorder-averaged density of states, making use of the energy spectrum of the model previously obtained by exact diagonalization. Again, we have found a very good agreement with well-known analytical results based on the coherent potential approximation.

CHAPTER 3

TWO-PARTICLE TRANSITIONS IN THE ANDERSON-HUBBARD MODEL

Let us consider a disordered quantum many-particle system where all single-particle states are Anderson-localized. A central problem in the field of many-body localization is the stability of the insulating phase with respect to mutual repulsive interactions. Under certain assumptions, it has been shown that the system undergoes a transition to the ergodic (metallic) phase at a finite value of the interaction strength [87].

In this chapter we show that this a similar effect can appear also in a minimal model of two interacting particles (bosons or fermions with opposite spins) moving in a disordered lattice. We start by mapping the original two-body Schrödinger equation into an effective single-particle model, whose properties are investigated numerically. Calculating the matrix associated to such an Hamiltonian turns out to be computationally very challenging, even for systems sizes of say 10 000 sites. To alleviate the numerical effort we have implemented a recursive algorithm for matrix inversion tailored for Hamiltonians with block-tridiagonal structure (only nearest-neighbour hopping). Once the effective Hamiltonian is known, we compute the reduced localization length Λ_M of the system by evaluating the associated resolvent using the direct-matrix-inversion and the finite-size scaling techniques outlined in Chapter 2.

For two-dimensional systems we observe apparent critical points for relatively small lattice sizes, as previously found in Ref. [130, 151]. However, as we increase the system size, the interaction-induced metallic phase shrinks considerably and tends to disappear for the largest lattices that we have explored.

In the remaining, we first perform a detailed analysis of the transition, for zero total energy of the pair and fixed disorder strength, finding results compatible with the orthogonal universality class. Next we build the complete phase diagram in the energy-disorder interaction space. We will interpret our results in light of the disorder-averaged density of states of the effective model.

3.1 Mapping to an effective single-particle model

The starting point of our investigation is an Anderson-Hubbard Hamiltonian, written in the two-particle basis of Wannier functions $\{|\boldsymbol{i},\boldsymbol{j}\rangle\}$. The Hamiltonian is composed of a noninteracting part that can be written as:

$$\hat{H}_0 = \hat{H}_{\text{sp}} \otimes \hat{\mathbb{1}} + \hat{\mathbb{1}} \otimes \hat{H}_{\text{sp}} \ ,$$

where $\hat{H}_{\text{sp}}$ corresponds to Anderson's Hamiltonian (Eq. (1.9)), with an uncorrelated and uniformly-distributed random potential. Considering a short-range interaction, $\hat{U} = U\hat{P}$, where $\hat{P} := \sum_{\boldsymbol{i}} |\boldsymbol{i},\boldsymbol{i}\rangle\langle\boldsymbol{i},\boldsymbol{i}|$, the total two-body Hamiltonian $\hat{H} = \hat{H}_0 + \hat{U}$ reads:

$$\hat{H} = -J \sum_{\{\boldsymbol{i},\boldsymbol{k}\},\boldsymbol{j}} |\boldsymbol{i},\boldsymbol{j}\rangle\langle\boldsymbol{k},\boldsymbol{j}| - J \sum_{\boldsymbol{i},\{\boldsymbol{j},\boldsymbol{k}\}} |\boldsymbol{i},\boldsymbol{j}\rangle\langle\boldsymbol{i},\boldsymbol{k}| + \sum_{\boldsymbol{i},\boldsymbol{j}} |\boldsymbol{i},\boldsymbol{j}\rangle(v_{\boldsymbol{i}} + v_{\boldsymbol{j}})\langle\boldsymbol{i},\boldsymbol{j}| + U\sum_{\boldsymbol{i}} |\boldsymbol{i},\boldsymbol{i}\rangle\langle\boldsymbol{i},\boldsymbol{i}| \ , \tag{3.1}$$

where U represents the on-site interaction strength.
Let $|\psi\rangle$ be a two-particle state, satisfying Schrödinger's equation $(\hat{H}_0+\hat{U})|\psi\rangle = E|\psi\rangle$, we can write:

$$(E\hat{\mathbb{1}} - \hat{H}_0)|\psi\rangle = \hat{G}_0(E)^{-1}|\psi\rangle = \hat{U}|\psi\rangle \ ,$$

where $\hat{G}_0(E)$ represents the Green's function operator of the noninteracting two-particle system. By multiplying the latter equation by $\hat{G}_0(E)$ and projecting on left by the state $\langle\boldsymbol{l},\boldsymbol{m}|$, one gets:

$$\langle\boldsymbol{l},\boldsymbol{m}|\psi\rangle = U\sum_{\boldsymbol{n}} \langle\boldsymbol{l},\boldsymbol{m}|\hat{G}_0(E)|\boldsymbol{n},\boldsymbol{n}\rangle\langle\boldsymbol{n},\boldsymbol{n}|\psi\rangle \ , \tag{3.2}$$

a relation which allows for evaluating $|\psi\rangle$ in the whole two-particle Hilbert space by using only the elements in the subspace of doubly-occupied states, that possesses the same dimension as the one-particle space. A closed equation can thus be derived from Eq. (3.2), involving uniquely the 'diagonal' elements $\Psi(\boldsymbol{n}) := \langle\boldsymbol{n},\boldsymbol{n}|\psi\rangle$ as in [165]:

$$\frac{1}{U}\Psi(\boldsymbol{n}) = \sum_{\boldsymbol{m}} K(\boldsymbol{n},\boldsymbol{m})\Psi(\boldsymbol{m}) \ , \tag{3.3}$$

where $K(\boldsymbol{n},\boldsymbol{m}) = \hat{G}_0(\boldsymbol{n},\boldsymbol{m};E) = \langle\boldsymbol{n},\boldsymbol{n}|\hat{G}_0(E)|\boldsymbol{m},\boldsymbol{m}\rangle$. The equation can thus be interpreted as an eigenvalue equation for an effective single-particle problem, accounting for the center-of-mass motion. The wave-function amplitudes involved in Eq. (3.3), belonging to a subspace of the Hilbert space of the pair, are the most affected by on-site interactions [136], even in the limit of zero particle density. For the other amplitudes, the localization problem does not differ significantly from the one of a single particle [166]. In the absence of disorder the probability amplitude corresponds to delocalized Bloch waves $\Psi(\boldsymbol{n}) \sim \mathrm{e}^{\mathrm{i}\boldsymbol{q}\cdot\boldsymbol{n}}$, where the dimensionless wave-vector $\boldsymbol{q}$ is a conserved quantity. On the other hand, in the strong-disorder limit, $\Psi(\boldsymbol{n})$ represents maximally localized states $\Psi(\boldsymbol{n}) = \delta_{\boldsymbol{n}\boldsymbol{n}_0}$, in which particles must be in the same site to feel the interaction. Importantly, the kernel K in Eq. (3.3) applies for either bosons or fermions with opposite spins in the singlet state and can be expressed in terms of the eigenbasis of the single-particle problem, $H_{\mathrm{sp}}\phi_r(\boldsymbol{n}) = \varepsilon_r\phi_r(\boldsymbol{n})$, as

$$K(\boldsymbol{n},\boldsymbol{m}) = \sum_{r,s=1} \frac{\phi_r(\boldsymbol{n})\phi_s(\boldsymbol{n})\phi_r^*(\boldsymbol{m})\phi_s^*(\boldsymbol{m})}{E-\varepsilon_r-\varepsilon_s}\ , \tag{3.4}$$

where H_{sp} is the one-particle Hamiltonian in Eq. (1.9). Differently from the latter Hamiltonian, the kernel K possesses nonzero terms far from the diagonal, thus representing an effective model with long-range hopping, instead of the nearest neighbour one appearing in the original Anderson's model. Furthermore, it is worth mentioning that the effective Schrödinger's equation (3.3) allows to reconstruct the whole energy spectrum of orbitally symmetric states. This fact is not straightforward, since, representing the effective kernel as a matrix, $\mathbf{K}$, the latter possesses N eigenvales for a lattice with N sites, which is much lower than the dimension of the subspace of orbitally symmetric states, which amounts to $N(N+1)/2$. In order to perform the reconstruction of the spectrum of $\hat{H}$, it is possible indeed to compute the matrix $\mathbf{K}$ and its eigenvalues $\{\lambda_r\}$, with $r=1,2,...,N$ for different values of the eenrgy E, and the energy levels at a given interaction strentgh are subsequently obtained by imposing $\lambda_r(E)=1/U$.

The procedure, which represents a valuable alternative to the exact diagonalization of $\hat{H}$, can be better explained by considering a lattice with $N=2$ and no disorder ($W=0$). In this case, the Hilbert space of symmetric states is spanned by three vectors, $|1,1\rangle$, $|2,2\rangle$ and $(|1,2\rangle+|2,1\rangle)/\sqrt{2}$. The corresponding energy levels of the pair can be found starting from the exact diagonalization of the projected Hamitlonian $\mathbf{H}$, which is the following 3×3 matrix:

$$\mathbf{H} = \begin{pmatrix} U & -\sqrt{2}J & 0 \\ -\sqrt{2}J & 0-\sqrt{2}J & \\ 0 & -\sqrt{2}J & U \end{pmatrix}\ .$$

An explicit calculation of the eigenvalues of $\mathbf{H}$ yields $E=U$ and $E=(U\pm\sqrt{U^2+16J^2})/2$. If we consider the effective kernel instead, we have to begin with the evaluation of the eigenvectors of the one-particle Hamiltonian, represented by the matrix $\mathbf{H}^{(\mathrm{sp})}$,

$$\mathbf{H}^{(\mathrm{sp})} = \begin{pmatrix} 0 & -J \\ -J & 0 \end{pmatrix}\ ,$$

whose eigenvalues are given by $\varepsilon_1=-J$ and $\varepsilon_2=J$. The corresponding eigenvectors are $|\phi_1\rangle = (|1\rangle+|2\rangle)/2$ and $|\phi_2\rangle=(|1\rangle-|2\rangle)/2$. From Eq. (3.3), it follows that

$$\mathbf{K} = \begin{pmatrix} A & B \\ B & A \end{pmatrix}\ ,$$

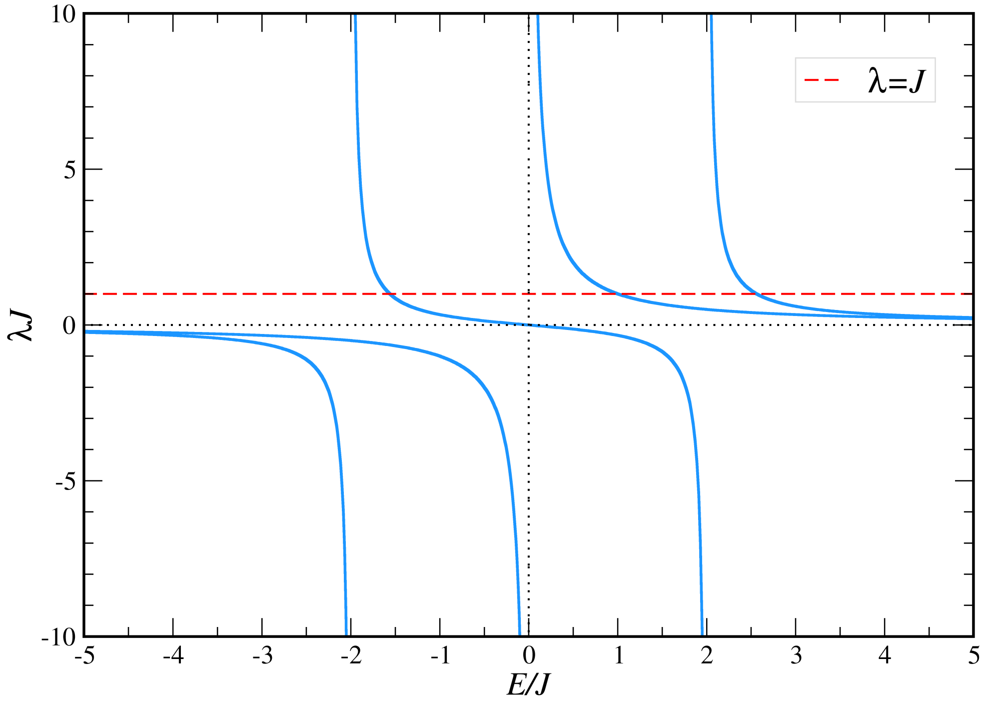

FIGURE 3.1 – Eigenvalues of the matrix K of the effective model of the pair, Eq. (3.3) for a toy model of $N=2$ coupled sites with no disorder, plotted as a function of the energy E of the pair (blues data curves). For a given interaction strength U, the entire spectrum of $N(N+1)/2$ energy levels of orbitally symmetric states of the pair can be obtained by intersecting the data curves with the horizontal line, $\lambda = 1/U$, here shown for $U = J$ (dashed red line). The corresponding three energy levels are $E = -1.56155J$, $E = J$ and $E = 2.56155J$.

where $A = (E/(E^2 - 4J^2) + E^{-1})/2$ and $B = (E/(E^2 - 4J^2) - E^{-1})/2$. The associated eigenvalues of $\mathbf{K}$ are then given by $\lambda_1(E) = A - B = E^{-1}$ and $\lambda_2(E) = A + B = E/(E^2 - 4J^2)$. The condition $\lambda_1 = U^{-1}$ gives $E = U$, whereas $\lambda_2 = U^{-1}$ leads to two solutions, $E = (U \pm \sqrt{U^2 + 16J^2})/2$, allowing to retrieve the energy spectrum found by exact diagonalization.

While in the present example all energy levels can be obtained analytically, in the more general case, it is necessary to compute all the different eigenvalues of $\mathbf{K}$ as a function of the energy, as shown in Fig. 3.1 for $N = 2$. By intersecting the curves $\lambda_r(E)$ with $\lambda = U^1$ one gets the three sought eigenenergies of $\mathbf{H}$ for orbitally simmetric states.

It is important to point out that extracting the *full* energy spectrum of the pair based on the effective model, for a fixed value of the interaction strength U, is computationally demanding as N becomes large. The effective model of the pair is instead very efficient, as compared to exact diagonalization, when the transport properties of the pair are investigated as a function of the interaction strength U, for a fixed value of the total energy E.

3.2 Computation of the effective Hamiltonian matrix

As in the one-particle case, we consider an elongated lattice with $N_d = M^{d-1}N$ sites, with $d = 2, 3$, imposing periodic boundary conditions to the Hamiltonian along the transverse directions. In order to compute the noninteracting two-particle Green's function, we first have to diagonalize the single-particle Hamiltonian, finding its eigenfunctions $\{\boldsymbol{\phi}_s\}$ and eigenvalues $\{\varepsilon_s\}$. The latter quantities are necessary for calculating the matrix elements of the effective kernel $\mathbf{K}$, using Eq. (3.4) [131] [146]:

$$\mathrm{K}_{ij}(E) = \sum_{s=1}^{N_d} \phi^*_{s,i}\phi_{s,j}\mathrm{G}^{(sp)}_{ij}(E-\varepsilon_s) \; , \tag{3.5}$$

where $i, j = 1, 2, \ldots, N_d$ and the one-particle Green's function $\mathrm{G}^{(\mathrm{sp})}_{ij}$ is the one defined in Eq. (2.7). As the double sum over the products of four eigenvector elements in Eq. (3.4) in Eq. (3.5) is computationally slow, the determination of the Green's function at each value of the energy $E-\varepsilon_s$ by inversion of $(E-\varepsilon_s)\mathbb{1} - \boldsymbol{H}^{(\mathrm{sp})}$ is preferable, and for the task we use a specific technique. This method, which we have developed starting from the one proposed by Jain et Al. [167], is intended for block-tridiagonal matrices, like the single-particle Hamiltonian. For the sake of simplicity, to explain its various steps, each $\mathbf{G}^{(\mathrm{sp})\,-1}(E-\varepsilon_s) = (E-\varepsilon_s)\mathbb{1} - \boldsymbol{H}^{(\mathrm{sp})}$, with $s = 1, 2, \ldots, N_d$ is written in the following as $\mathrm{tridiag}\{\mathbb{1}, \boldsymbol{A}_i, \mathbb{1}\}$, where $\boldsymbol{A}_i = (E-\varepsilon_s)\mathbb{1} - \boldsymbol{H}^{(\mathrm{sp})}_i$ are $M^{d-1} \times M^{d-1}$ blocks and $i = 1, 2, \ldots, N$. To the purpose of finding $\mathbf{G}^{(\mathrm{sp})}$, we first have to compute a sequence of $N-1$ $M^{d-1} \times M^{d-1}$ matrices $\{\boldsymbol{S}_1, \boldsymbol{S}_2, \ldots, \boldsymbol{S}_{N-1}\}$ in a recursive fashion, beginning with $\boldsymbol{S}_{N-1} = \boldsymbol{A}_N^{-1}$:

$$\boldsymbol{S}_i = (\boldsymbol{A}_{i+1} - \boldsymbol{S}_{i+1})^{-1} \; , \tag{3.6}$$

where $i = N-2, N-3, \ldots, 1$. Denoting the off-diagonal $M^{d-1} \times M^{d-1}$ blocks of the one-particle Green's function as $\mathbf{G}^{(\mathrm{sp})}_{ij}(E-\varepsilon_s)$ as $\boldsymbol{C}_{ij}$ and the diagonal ones as $\boldsymbol{D}_i$, as the original matrix is symmetric, only $N(N+1)/2$ blocks are needed for achieving a complete knowledge of the inverse matrix. Considering only the elements below the diagonal ($i \leq j$), we determine each block using only the ones on or below the diagonal:

$$\begin{pmatrix} \boldsymbol{C}_{i1} & \boldsymbol{C}_{i2} & \ldots & \boldsymbol{C}_{ii-1} \end{pmatrix} = -\boldsymbol{S}_{i-1} \begin{pmatrix} \boldsymbol{C}_{i-11} & \boldsymbol{C}_{i-12} & \ldots & \boldsymbol{D}_{i-1} \end{pmatrix} \; , \tag{3.7}$$

and

$$\boldsymbol{D}_i = \boldsymbol{S}_{i-1}(\mathbb{1} + \boldsymbol{D}^T_{i-1}\boldsymbol{S}^T_{i-1}) \; . \tag{3.8}$$

This procedure is performed from $i = N-2$ to $i = 1$ and yields to a computational complexity of $NM^{3(d-1)}$ elementary operations instead of $N^3M^{3(d-1)}$ required for the inversion of general $M^{d-1}N \times M^{d-1}N$ matrices.

For example, in the case of a block 4×4 -matrix, the original block tridiagonal matrix and the inverse one can be thus expressed as:

$$\mathbf{G}^{(\mathrm{sp})\,-1} = \begin{pmatrix} \boldsymbol{A}_1 & \mathbb{1} & \mathbb{0} & \mathbb{0} \\ \mathbb{1} & \boldsymbol{A}_2 & \mathbb{1} & \mathbb{0} \\ \mathbb{0} & \mathbb{1} & \boldsymbol{A}_3 & \mathbb{1} \\ \mathbb{0} & \mathbb{0} & \mathbb{1} & \boldsymbol{A}_4 \end{pmatrix}$$

$$\mathbf{G}^{(\mathrm{sp})} = \begin{pmatrix} \boldsymbol{D}_1 & -\boldsymbol{S}_1\boldsymbol{D}_1 & \boldsymbol{S}_2\boldsymbol{S}_1\boldsymbol{D}_1 & -\boldsymbol{S}_3\boldsymbol{S}_2\boldsymbol{S}_1\boldsymbol{D}_1 \\ -\boldsymbol{S}_1\boldsymbol{D}_1 & \boldsymbol{D}_2 & -\boldsymbol{S}_2\boldsymbol{D}_2 & \boldsymbol{S}_3\boldsymbol{S}_2\boldsymbol{D}_2 \\ \boldsymbol{S}_2\boldsymbol{S}_1\boldsymbol{D}_1 & -\boldsymbol{S}_2\boldsymbol{D}_2 & \boldsymbol{D}_3 & -\boldsymbol{S}_3\boldsymbol{D}_3 \\ -\boldsymbol{S}_3\boldsymbol{S}_2\boldsymbol{S}_1\boldsymbol{D}_1 & \boldsymbol{S}_3\boldsymbol{S}_2\boldsymbol{D}_2 & -\boldsymbol{S}_3\boldsymbol{D}_3 & \boldsymbol{D}_4 \end{pmatrix}$$

Since the matrices describing the examined lattices were very large (up to 43 350 sites for the bar with $M = 17$ and $N = 150$), the algebraic operations explained above have been set to a supercomputer, composed of compute nodes with multiple cores. In particular, the evaluation of matrix elements of $\mathbf{K}$ has been carried out in parallel form, by using subroutines from library `MPI` which handle tasks distributed to various nodes. Besides, the diagonalization of the one-particle Hamiltonian has been performed by distributing blocks of matrices among the different processors, using functions from `SCALAPACK` library. The filling of the latter matrix has been accomplished with the aid of `openMP` library for multi-threading computation, able to share out the tasks between the several cores of each node. For the simulation with the largest matrices, mentioned above, the execution of the algorithm has been assigned to 10 nodes composed of 24 cores each, the latters sharing a memory of $120\,Gb$.

3.3 Numerical estimate of the reduced localization length

In order to estimate the Lyapunov exponent of the pair, we first have to compute the off-diagonal elements of the resolvent matrix $\mathbf{G}^{(\lambda)}$ associated to the effective kernel $\mathbf{K}$. Defining $\lambda = U^{-1}$, the latter is given by:

$$\mathbf{G}^{(\lambda)} := (\lambda\mathbb{1} - \mathbf{K})^{-1}.$$

Its off-diagonal elements are necessary for reckoning the transmission amplitude between one end of the bar and the slice of the d-dimensional bar lying on the plane $z = na$:

$$t_{1n} = \sum_{m_1=1}^{M^{d-1}} \sum_{m_n=1+(n-1)M^{d-1}}^{nM^{d-1}} J^2 |G^{(\lambda)}_{m_1 m_n}|^2 \,,$$

where the matrix index m_k is connected to the position $(x_k, y_k, k)^T a$ of the pair on the k-th section of the lattice through the relation:

$$m_k = \begin{cases} x_k + (k-1)M & d=2 \\ x_k + (y_k - 1)M + (k-1)M^2 & d=3 \end{cases},$$

in which $k \in \{1, 2, \ldots, n\}$ and $n \leq N$.For the computation of the Lyapunov exponent associated to the asymptotic behaviour of the two-particle wave-function between the two ends of the bar, we tested, as done in the one-particle case, the consistence between the results found with the usual method (Eq. (2.8)) and those obtained by making linear regressions in Eq. (2.9). From the comparison between the values of Λ_M, we notice that the fitting procedure allows for getting stable and convergent results even when the longitudinal size of the lattice is not very large ($N \sim 10M$) compared to the one of the transverse side. In addition, the choice of the spacing Δn between two neighbouring cross-sections selected for the fit is little influent on the reduced localization length if $N \gtrsim 7M$, as it emerges from Fig. 3.2.

The latter method differs from the one proposed by Ortuño and Cuevas [151], in which the average over the disorder realizations was performed after interpolating the transmission amplitudes. The reduced localization length $\Lambda_M = (Ma\overline{\gamma}_M)^{-1}$ in Eq. (2.10), depending on the parameters of the Hamiltonian (E, W, J, U) has been evaluated at different positions along the z-axis of the bar , both in the $d=2$ and $d=3$ lattices, as shown in Fig. 3.2.

While in Fig. 3.2b we have shown the comparison for a single value of the interaction strength $U = 2J$ close to the critical value $U_c = 2.16J$, whose esitmation will be illustrated in § Par. 3.3.3, in Fig. 3.3 we display Λ_M as a function of U for increasing values of the boundary position n along the bar. From the graph it emerges that effects due to the shortness of the bar are small and appear well inside the metallic region, where they lead to slightly overestimate the correct result.

3.3.1 The effect of boundary conditions

We also analyzed the behaviour of the reduced localization length by varying the boundary conditions imposed to the single-particle Hamiltonian in the transverse directions in both the $d=2$- and the $d=3$-cases, whereas no such constrants are set in the longitudinal direction. In the absence of conditions, the one-particle Hamiltonian loses some tunneling terms, thus enhancing the confinement of the wavefunction. This results in increased Lyapunov exponents, and therefore, in a decreased reduced localization length. The effect is more pronounced at high interactions U.

As pointed out by Ohtsuki and Slevin [168] [158] concerning the one-particle case in $d=3$, the common crossing point between the curves $\Lambda_M(W)$ plotted for different values of M can even disappear where no conditions are imposed along transverse directions. By considering the first

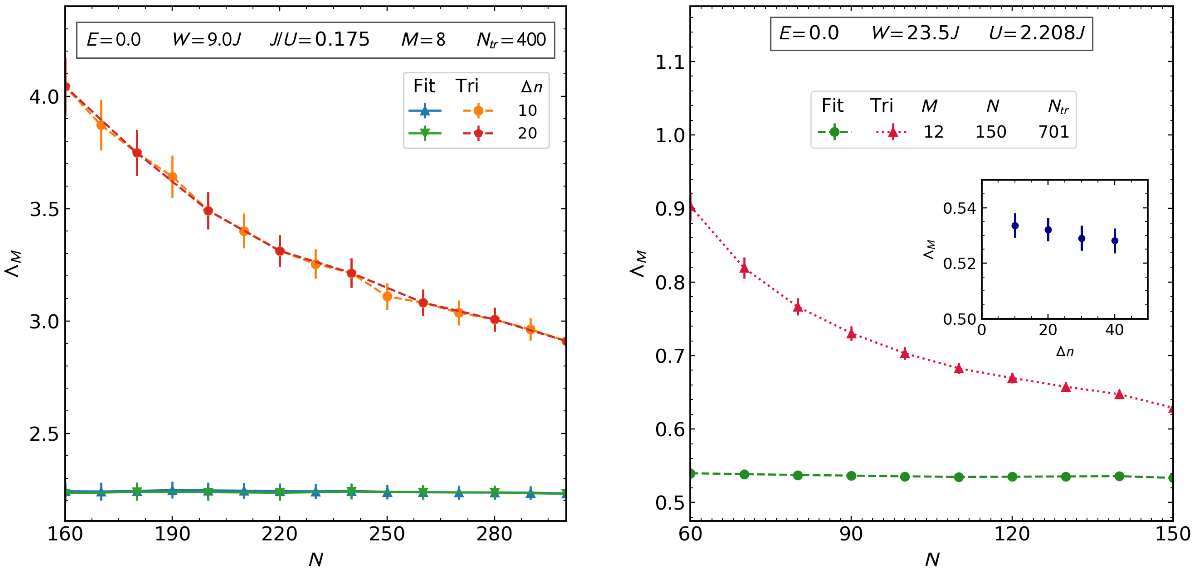

(A) $d = 2$

(B) $d = 3$

Figure 3.2 – The reduced localization length Λ_M obtained using linear regression (Eq. (2.9)) of the transmission amplitudes is here plotted versus the one got by retaining only t_{1N}, within the usual 'triangular' method (Eq. (2.8)), in two- and three-dimensional random lattices. Besides, data recovered with different fitting step Δn are compared: in the 2-dimensional case $\Delta n = \{10, 20\}$ (A), whereas in the 3-dimensional one (B) only the results with $\Delta n = 10$ are plotted in the main graphic area, whereas the inset shows only the reduced localization length at $N = 150$, that is estimated at four different values of Δn. The parameters of the systems, as well as the number of realizations N_{tr}, are specified in the upper squares.

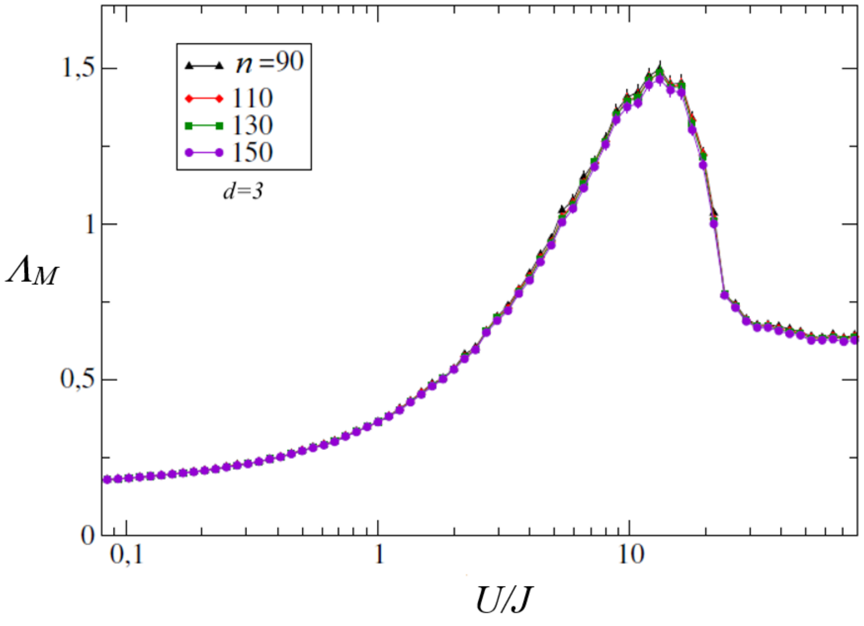

Figure 3.3 – Reduced localization length of the pair, calculated via the fitting method, as a function of the interaction strength U for increasing values $n = 90, 110, 130, 150$ of the right-boundary position along the bar. The other parameters are the same as in Fig. 3.2b.

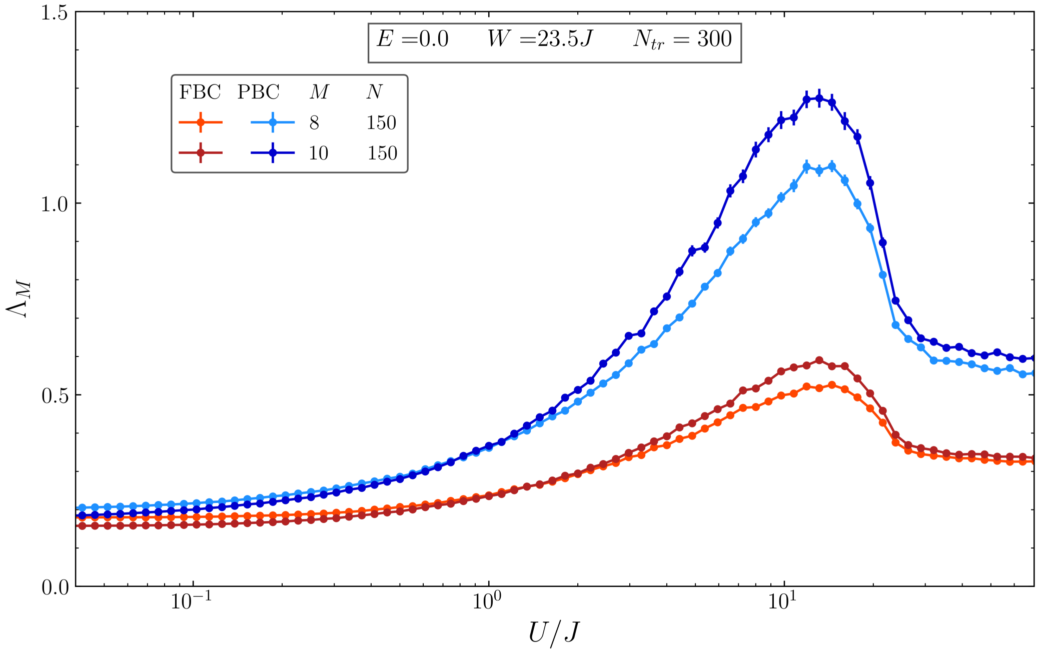

FIGURE 3.4 – Reduced localization length in $d = 3$, plotted as a function of the interaction strength U in tunneling units, using two different sizes $M = \{8, 10\}$. The red curves portray the Λ_M found with free boundary conditions, while the ones in blue represent the case in which periodic conditions are present along transverse directions.

irrelevant variable f_I characterized by the exponent y in the finite-size expansion of Λ_M (cf. Eq.s (2.14) and (2.15)) around the critical point, they corrected the Λ_M found numerically by subtracting the irrelevant variable with the parameters obtained by nonlinear fits, retaining terms up to the first order in f_I in the series in Eq. (2.14),

$$\Lambda_M \to \Lambda_M - f_I \sum_{m=0}^{N_R} c_{m1} f_R^m \ .$$

This operation eventually leads to the recovery of a critical value of disorder W_c compatible with the one found imposing periodic boundary conditions $W_{c,\text{orth}}^{(\text{pbc})} = 16.536J$, as well as critical exponents ν and y in accordance with the ones of the orthogonal universality class. Nevertheless, the critical value of the reduced localization length Λ_c remained lower than $\Lambda_{c,\text{orth}} \approx 0.577$, reflecting the fact that the transmission coefficient depends on boundary conditions [169]. A similar conclusion has been reached through the study of the statistics of level spacings [170], by searching for the value of the disorder at which the probability density function turns from the Poissonian, revealing localized states (described by Eq. (A.19)), to the Wigner-Dyson one, signalling the presence of extended states in Eq. (A.18), as seen in App. A.1. We predict that these considerations on the single-particle states apply also to the case of two particles subject to short-range interactions.

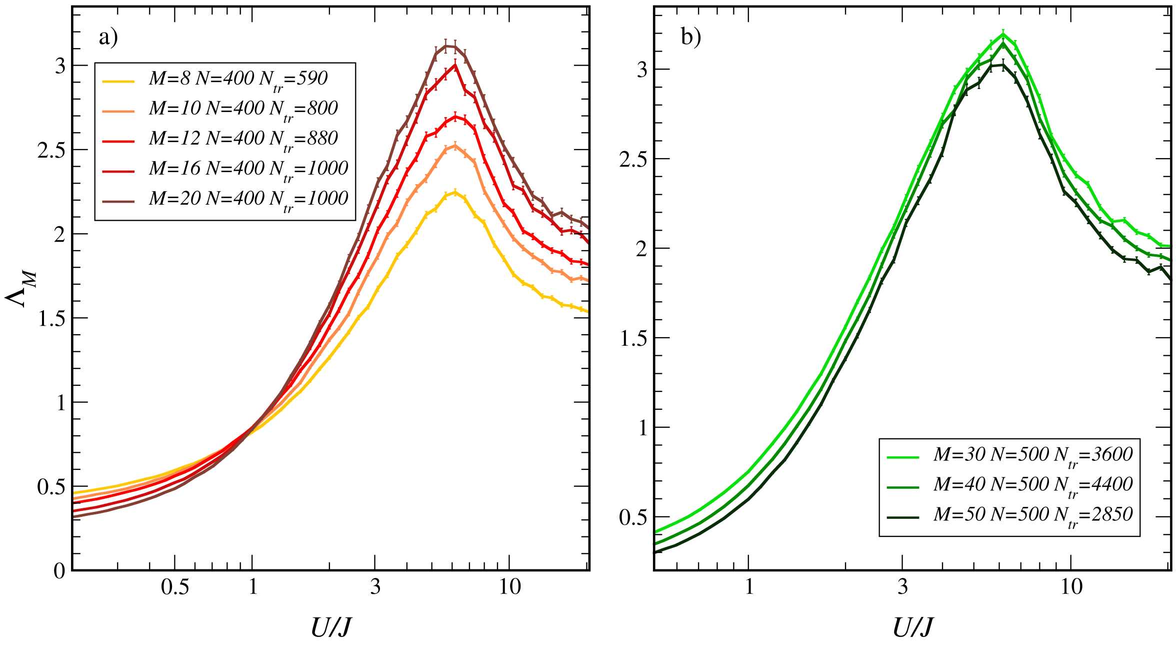

FIGURE 3.5 – Reduced localization length plotted as a function of the interaction strength in tunneling units. For the larger lattices, shorter bars with $N \sim 10M$ and a lower number of realizations N_{tr} have been considered, thus getting rougher curves. While for small M (see Panel a) a drifting intersection between the curves $\Lambda_M(U)$ is detected, at higher sizes M (shown in Panel b) the crossing disappears, suggesting an insulating behaviour in the whole interval of U.

3.3.2 Absence of Anderson transitions in 2D systems

Following in the wake of previous investigations [151] [153] on the two-particle problem, we have studied the reduced localization length Λ_M at zero total energy of the pair, varying the interaction strength U instead of the random potential W. Since the aforementioned publications revealed a transition at $U = J$ and $W_c = (9.3 \pm 0.5)J$ and $W_c = (8.1 \pm 0.1)J$ respectively, we have focused our attention in that region of the space of the parameters.

Observing the behaviour of the localization length at $W = 9J$ as a function of interaction strength, we first noticed that the curves portrayed for different $M < 25$ in Panel a in Fig. 3.5, cross each other in the region $0.73J \lesssim U \lesssim 1.05J$, where $0.69 \leq \Lambda_M \leq 0.88$, thus suggesting a confirmation of the aforementioned claims. However, a closer look to the crossing region signals that the intersections between the curves slightly swerve at increasing lattice size; in particular the deviations are more marked for $M = 20$.

With the aim of understanding the behaviour of the position of the crossing point, we examined larger lattices, with $M = \{30, 40, 50\}$, considering also longer bars with $N = 500$, in order to guarantee an aspect ratio large enough. As shown in Panel b of Fig. 3.5, the peak height reaches its maximum for $M = 30$, then the curves $\Lambda_M(U)$ for $M = 40$ and $M = 50$ do not intersect neither with the former, nor between each other. In the whole interaction range examined, the reduced localization length Λ_M decreases for increasing M, thus indicating the absence of Anderson transitions.

This leads to conclude that the results of the previous works, based on lattices with $M = 10$ and

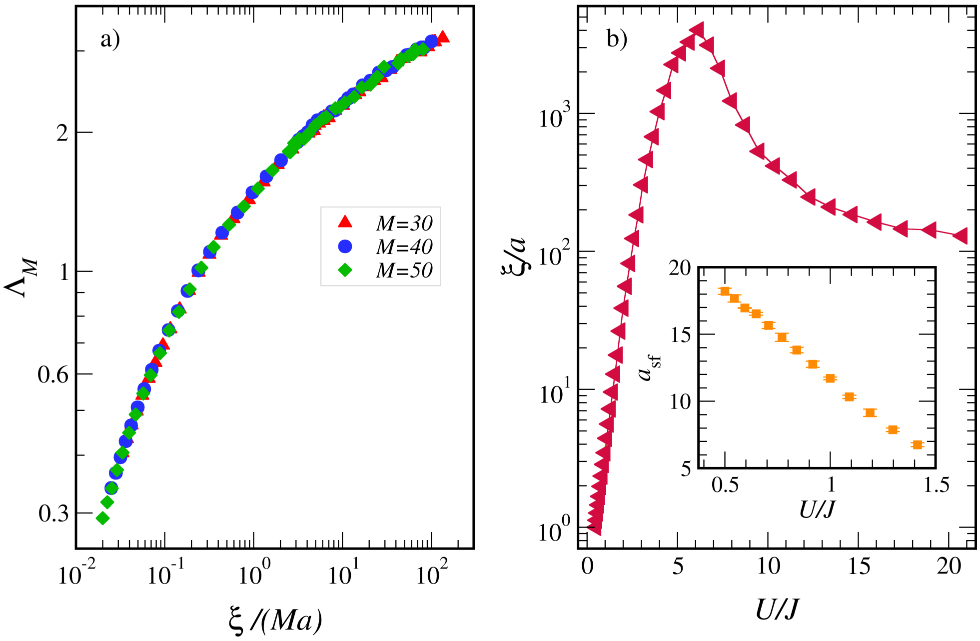

Figure 3.6 – Behaviour of the reduced localization length as a function of the localization length of the infinite lattice ξ in units of the length of the transverse side (Panel a) plotted in logarithmic scale along the two axes. The points have been extracted from the data related to the lattices with $M = \{30, 40, 50\}$ and $N = 500$ in the whole range of values of the interaction strength represented in Fig. 3.5. The dependence of ξ on interaction strength is shown in Panel b (solid red curve) adopting logarithmic scale for the y axis, whereas the exponential curve describing the behaviour at low interactions is represented by the dashed light-green curve. The inset of Panel b displays the value of the scale factor a_{sf}, obtained by fitting the data for each value of U with the law on the right-hand side of Eq. (3.10). The estimated value of a_{sf} does not converge for weak interactions, signalling that the strongly localized regime is never fully reached in our simulations.

$N = 62$ at most, were plagued by considerable finite-size effects. As a consequence, we are driven to affirm that the presence of short-range interactions do not lead to a metal-insulator transition in two-dimensional systems, as in the single-particle Anderson model.

A further proof of this statement can be traced by inspecting the behaviour of the reduced localization length as a function of the characteristic length ξ, which depends on the parameters of the Hamiltonian but not on the lattice size, as shown by Eq. (2.10). We thus tested the one-parameter scaling ansatz, $\Lambda_M = f(\xi/M)$, by following a similar procedure to the one presented in [161], for fixed values of the total energy and the disorder parameter. Denoting as N_U the number of values of the interaction strength U available, we consider the N_U curves obtained by connecting with straight lines the values of $\ln \Lambda$ found at N_M different values of $\ln M$. Let Λ_i be one of the $N_M N_U$ numerical values available of the reduced localization length, the horizontal line $\ln \Lambda = \ln \Lambda_i$ generally intersects N_i curves obtained for different U. In order to keep track of these events, we define the matrix η in such a way that $\eta_{ij} = 1$ if the curve for $U = U_j$ is crossed, otherwise $\eta_{ij} = 0$. Defining $\ln M_{ij}$ as the value of $\ln M$ at which the curve for $U = U_j$ intersects the line $\ln \Lambda = \ln \Lambda_i$, we sought ξ as the length (depending on interaction) which minimizes the variance $\mathrm{Var}\,[\xi]$ of the values of $(\ln M - \ln \xi(U))$ corresponding to each value of $\ln \Lambda$:

$$\mathrm{Var}\,[\xi] = \sum_{i=1}^{N_M N_U} \left\{ \frac{1}{N_i} \sum_{j=1}^{N_U} \eta_{ij} \Big[\ln M_{ij} - \ln \xi(U_j) \Big]^2 - \left[\frac{1}{N_i} \sum_{j=1}^{N_U} \eta_{ij} \big(\ln M_{ij} - \ln \xi(U_j) \big) \right]^2 \right\}, \tag{3.9}$$

where $N_i = \sum_{j=1}^{N_U} \eta_{ij}$ represents the total number of crossing points obtained for each Λ_i value. The minimization condition for $\mathrm{Var}\,[\xi]$ thus reads:

$$\sum_j \left\{ \sum_i \eta_{ij} \left(\frac{1}{N_i^2} - \frac{\delta_{jk}}{N_i} \right) \right\} \ln \xi(U_j) = \sum_j \left\{ \sum_i \eta_{ij} \left(\frac{1}{N_i^2} - \frac{\delta_{jk}}{N_i} \right) \ln M_{ij} \right\} .$$

This yields to a system of linear equations where the matrix of coefficients is singular: this means that there is a shift of the absolute origin of $\ln M - \ln \xi$, or of the mean corresponding to the variance in Eq. (3.9). Nevertheless, the system can be solved by means of a least-squares algorithm which allows for finding the minimum-norm solution, that represents the physical values of ξ up to an overall scale factor. The latter quantity, denoted as a_{sf}, can be in principle obtained starting from a nonlinear regression,

$$\Lambda_M = \left(\frac{a_{\text{sf}} \xi}{M} \right) + b \left(\frac{a_{\text{sf}} \xi}{M} \right)^2 , \tag{3.10}$$

as it was proposed by Kramer at Al. [161], when Λ_M is sufficiently small (e.g. $\Lambda_M \lesssim 10^{-1}$), a condition that can be fulfilled at weak interactions and strong disorder. However, in our case these conditions are not satisfied by the data and, when $0.5J \leq U \leq J$, a_{sc} varies from 19.2 to 12.5, so that an absolute scale of ξ cannot be precisely estimated, as shown by the curve in the inset of Panel b of Fig. 3.6, where a_{sf} is extracted for different (small) U and exhibits still a marked dependence on the interaction: it grows linearly as U decreases. The values of ξ plotted in both panels of Fig. 3.6 are therefore deprived of such factor, that at $U = 0.5J$ amounts to 18.2 ± 0.3, a value which provides a lower bound for a_{sf}.

Despite this, we found a doubly-branched behaviour of Λ_M as a function of $\xi/(Ma)$, qualitatively similar to the one shown in Fig. 2.5 in Chap. 2, using small-sized lattices (characterized by $M = \{8, 10, 12\}$ and $N = 400$), thus retrieving the signature of a metal-insulator transition as in Ref. [151] (see Fig. 3).

The scenario changes, as only the data for the largest lattices are considered ($M = \{30, 40, 50\}$), as displayed in Panel a of Fig. 3.6, where Λ_M as the universal scaling function of $\xi/(Ma)$ possesses a single branch: this reflects the insulating behaviour already noticed in Panel b of Fig. 3.5, and a slight deviation of the data from the common curve is due to the data found near the maximum of Λ_M (located precisely at $U = 4.362J$), where the curves $\Lambda_M(U)$ for $M = 40$ and $M = 50$ appear very close, as it emerges from Panel b of the latter figure. In the Panel b of Fig. 3.6 the behaviour of the localization length ξ is shown as a function of interaction, which displays a nonmonotonic trend, with a large enhancement (of up to four orders of magnitude) in the range $0.5J \leq U \lesssim 6.182J$. Differently from the prediction of Shepelyansky [152] and Imry [133], the localization length does not obey the relation $\xi \propto \xi_{\rm sp} \mathrm{e}^{B(U\xi_{\rm sp}/J)^2}$, but follows more probably an exponential law, the curve $\xi = A\mathrm{e}^{BU/J}$, represented by the short-dashed line in Panel b of Fig. 3.6, where $A \approx 0.295$ and $B \approx 2.469$ in the interaction interval $0.5J \leq U \leq 1.295J$. This discrepancy can be probably traced back to the fact that the aforementioned predictions are valid for lower interactions ($U \lesssim 0.1J$), which have not been explored in our numerical simulations.

3.3.3 Characterization of Anderson transitions in 3D systems

The critical point of the metal-insulator transition can be identified by studying the behaviour of Λ_M as a function of the interaction strength U and for increasing values of the transverse size M. In the metallic phase, Λ_M increases with M, while in the insulating regime Λ_M decreases for M large enough. Exactly at the critical point Λ_M becomes scale-invariant, that is $\lim_{M\to+\infty} \Lambda_M = \Lambda_c$, where Λ_c is a constant of order unity, which only depends on the universality class of the model and on the specific choice of boundary conditions. For example, the Anderson model belongs to the orthogonal universality class, where $\Lambda_{c,\rm orth} = 0.576$ (see Tab. 1.1) assuming periodic boundary conditions in the transverse directions. In Fig. 3.7 we plot our numerical results for the reduced localization length as a function of the interaction strength for increasing values of M assuming $W = 23.5J$, so that all single-particle states are localized. Since $E = 0$, the value of Λ_M is independent of the sign of U, so hereafter we assume $U > 0$. We see that interactions favour the delocalization of the pair and lead to an Anderson transition around $U = 2J$.

Identifying the precise position of the critical point is not straightforward, because the crossing point drifts towards stronger interactions and upwards as M increases, due to finite-size effects. Simulating systems with even larger values of M is computationally prohibitive: the data for $M = 17$, obtained by averaging $N_{\rm tr} = 700$ disorder realizations, required already 750.000 hours of computational time on a state-ofthe-art supercomputer, and the curve is not particularly smooth. As shown in the inset of Fig. 3.8, the height of the crossing point for the largest system sizes (couples $M = \{12, 17\}$ and $M = \{15, 17\}$) becomes closer and closer to $\Lambda_{c,\rm orth}$, suggesting that also the effective model for the pair belongs to the orthogonal universality class. In this case, no significant further drift is expected. To verify this hypothesis, we need to compute the critical exponent ν related to the divergence of the localization length at the critical point, $\xi_2 \propto |U - U_c|^{-\nu}$, and compare it with the numerical value $\nu_{\rm orth} = 1.573 \pm 0.009$ known [76] for the orthogonal class.

For the analysis of the transport properties of the pair we base ourselves on the one-parameter scaling ansatz, whose validity for the problem of two particles subject to Hubbard interactions was demonstrated by Frahm et Al. [134], starting from a σ-model and a DMPK approach for bound pairs. In light of this ansatz, for large enough M, as seen in § b), the reduced localization length can be written in terms of a reduced localization length f as

$$\Lambda_M^{(FSS)} = f\left[u(\omega)M^{1/\nu}\right] \ , \tag{3.11}$$

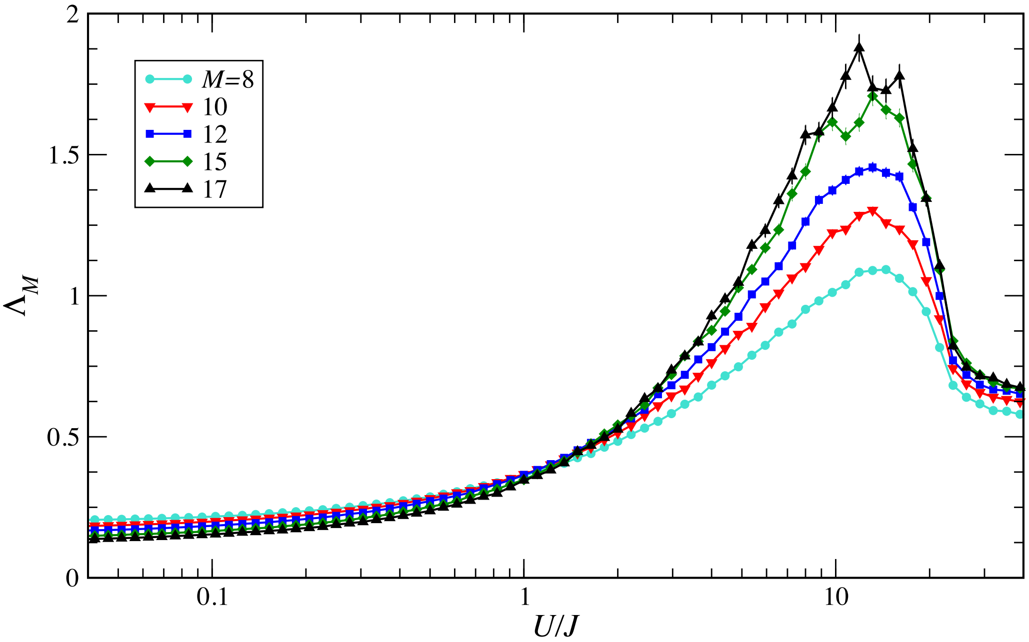

Figure 3.7 – The reduced localization length as a function of interaction strength in units of tunneling amplitude, for increasing values of the number of sites of the bar along each transverse direction $M = \{8, 10, 12, 15, 17\}$. The energy of the pair is $E = 0$ and the disorder strength is $W = 23,5J$, implying that all single-particle states are localized. The transition takes place at the point where all data curves with sufficiently large M cross.
.

where u is a function of the variable $\omega = (U - U_c)/U_c$, measuring the distance from the critical point. Close to it, we can expand the reduced localization lengths u and f in Eq. (3.11) in Taylor series up to orders m and n, respectively, as

$$u(\omega) = \sum_{j=0}^{m} b_j \omega^j \ ,$$

and

$$f(x) = \sum_{j=0}^{n} a_j x^j \ ,$$

Following Slevin [76] [17], we set $b_0 = 0$, $a_1 = 1$, and $a_0 = \Lambda_c$. The coefficients a_j and b_j, as well as U_c and ν, are then obtained via a multilinear fit. We extract the critical exponent by fitting the (smoothest) data for $M = 12$ and $M = 15$ in Fig. 3.7 (a) with the ansatz in Eq. (3.11). The latter should in principle include also irrelevant variables, describing the drift of the crossing point. However, unlike U_c and Λ_c, the value of the critical exponent is much less sensitive to these variables. For $n = m = 2$ we obtain $\nu = 1.64 \pm 0.13$, in full agreement with the universal value. All other crossings yield consistent results for ν.

Having found that on-site interactions do not change the universality class of the transition, we can use this information to estimate U_c. Expanding the Λ_M in terms of the leading irrelevant scaling field, similarly to what was done in Chap. 2 (cf. Eq.s (2.14) and (2.15)), as a function of the interaction,

$$\Lambda_M(\omega) = \sum_m \sum_n^{N_I} a_{mn} \left(M^{1/\nu} \sum_i b_i \omega^i \right)^m \left(M^{-y} \sum_j c_j \omega^j \right)^n ,$$

setting $a_{01} = a_{10} = 1$ and $b_0 = 0$ as in [76], at first order in ω one finds that:

$$\Lambda_M(\omega) = a_{00} + c_0 M^{-y} + b_1 M^{1/\nu}\omega + c_1 M^{-y}\omega , \tag{3.12}$$

where y is the critical exponent of the first irrelevant field. Since we have shown that the system behaves as one belonging to the orthogonal universality class, $\nu = \nu_{\text{orth}}$ and $y_{\text{orth}} = 3.3 \pm 0.6$ [76]. Besides, when $M \to +\infty$ and $\omega = 0$ (i.e. $U = U_c$) we expect that $\lim_{M\to+\infty} \Lambda_M(0) = \Lambda_{c,\text{orth}}$, which implies that $a_{00} = \Lambda_{c,\text{orth}}$. However, at finite number of sites M along each transverse direction, $\Lambda_M(U \equiv U_M) = \Lambda_{c,\text{orth}}$ at $U_M \neq U_c$, so ω_M is nonzero. Using Eq. (3.12), one can discover that it amounts to:

$$\omega_M = -\frac{c_0 M^{-y}}{b_1 M^{1/\nu} + c_1 M^{-y}} .$$

Reminding that $\omega_M = (U_M - U_c)/U_c$, the relation between U_M and U_c becomes, approximating ω_M at the leading term in M,

$$U_M = U_c + aM^{-b} , \tag{3.13}$$

where $a = -c_0 U_c / b_1$ is a dimensional constant and $b = 1/\nu_{\text{orth}} + y_{\text{orth}}$. The expression in Eq. (3.13) concides with the one obtained by Campostrini et Al. [171] for the estimate of the position of critical points, starting from crossing points between curves at finite M [172].
In 3.8 we show that the values of U_M extracted from our data curves for $M = \{10, 12, 15\}$ do vary linearly as a function of M^{-b}. A linear fit to the data then yields $U_c = (2.16 \pm 0.04)J$ [173].

3.4 Disorder-averaged density of states

As seen in Sec. 3.1, a closed equation can be derived for the two-particle wavefunction in the basis of doubly-occupied states. This eigenvalue equation (Eq. (3.3)) can be regarded as a time-independent Schrödinger equation of an effective single-particle problem, whose eigenvalues are represented by the values of $1/U$, whereas the total energy E becomes a parameter of the 'Hamiltonian':

$$\sum_{\boldsymbol{m}} K(\boldsymbol{n}, \boldsymbol{m}) \Psi_v(\boldsymbol{m}) = \lambda_v \Psi_v(\boldsymbol{n}) := \frac{1}{U_v} \Psi_v(\boldsymbol{n}) , \tag{3.14}$$

where $K(\boldsymbol{n}, \boldsymbol{m}) = G_0(\boldsymbol{n}, \boldsymbol{m}; E)$ is the effective kernel and $\Psi_v(\boldsymbol{n}) := \langle \boldsymbol{n}, \boldsymbol{n} | \Psi_v \rangle$. From the eigenvalues of $\mathbf{K}$, which accounts for the motion of the center of mass of the pair, we can write the

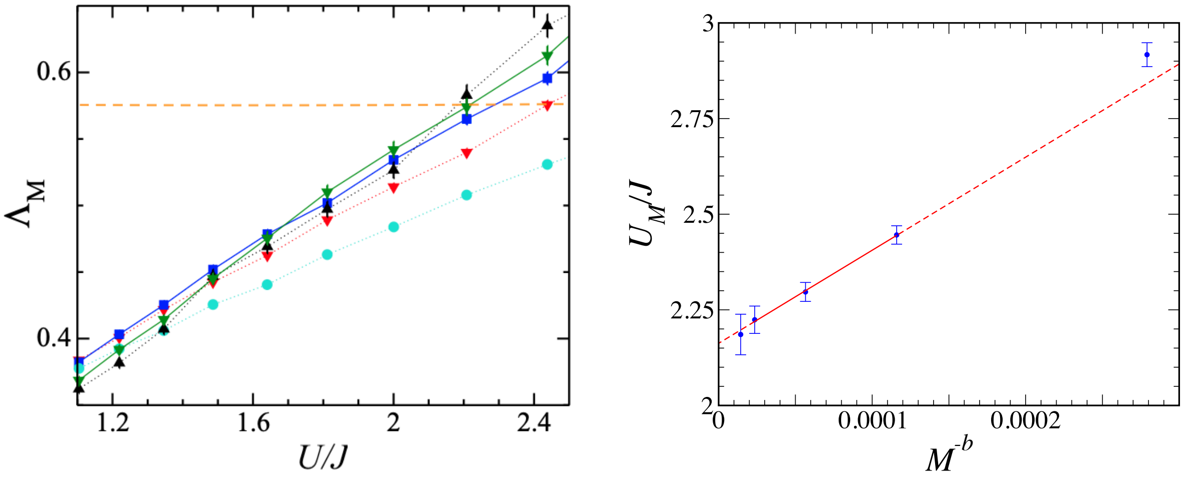

(A)

(B)

FIGURE 3.8 – The reduced localization length as a function of interaction strength in units of tunneling amplitude (A). The ones found at $\Lambda_M = \Lambda_{c,\text{orth}}$ (dashed orange line), denoted as U_M/J, at five different values of M^{-b} (cf. Eq. (3.13)), with $M = \{8, 10, 12, 15, 17\}$ (B). The line that fits the U_M with $M = \{10, 12, 15\}$ [173], averaged over an higher number of disorder realizations, is plotted in red. The intercept of the line obtained by regression corresponds to the critical value U_c/J.
.

disorder-averaged density of states per unit volume as:

$$\overline{\rho_{\mathrm{K}}}(\lambda) = \frac{1}{V_d} \sum_{v} \overline{\delta(\lambda - \lambda_v)} \,, \tag{3.15}$$

where V_d denotes the volume of the lattice. In the atomic limit, in which tunneling is weak compared to the random potential, we can outline the behaviour of the disorder-averaged density of states $\overline{\rho_{\mathrm{K}}}$, by beginning from the expectation values of the effective kernel in the two-particle basis $\{|\boldsymbol{m}, \boldsymbol{n}\rangle\}$. Writing the noninteracting two-particle Green's function operator as $\hat{G}_0(E) = (\hat{A} + \hat{T})^{-1}$, where $\hat{A} = \sum_{\boldsymbol{m},\boldsymbol{n}} (E - v_{\boldsymbol{m}} - v_{\boldsymbol{n}}) |\boldsymbol{m}, \boldsymbol{n}\rangle\langle \boldsymbol{m}, \boldsymbol{n}|$ is the contribution of the on-site energies, whereas $\hat{T} = -J \sum_{\boldsymbol{k},\{\boldsymbol{m},\boldsymbol{n}\}} \big(|\boldsymbol{k}, \boldsymbol{m}\rangle\langle \boldsymbol{k}, \boldsymbol{n}| + |\boldsymbol{m}, \boldsymbol{k}\rangle\langle \boldsymbol{n}, \boldsymbol{k}| \big)$ denotes the one of the hopping, the operator can be approximated to the second order in the tunnelling term as:

$$\hat{G}_0(E) = (\hat{A} + \hat{T})^{-1} \approx \big(\hat{\mathbb{1}} - \hat{A}^{-1} \hat{T} + \hat{A}^{-1} \hat{T} \hat{A}^{-1} \hat{T} \big) \hat{A}^{-1} \,, \tag{3.16}$$

Noticing that the second term in the right-hand side of Eq. (3.16) gives no contribution to the matrix elements evaluated between states with double occupancy $\langle \boldsymbol{n}, \boldsymbol{n} | \hat{G}_0(E) | \boldsymbol{m}, \boldsymbol{m}\rangle$, the latters become:

$$\begin{aligned} \langle \boldsymbol{n}, \boldsymbol{n} | \hat{G}_0(E) | \boldsymbol{m}, \boldsymbol{m}\rangle = & \left[\frac{1}{E - 2v_{\boldsymbol{m}}} + J^2 \sum_{\{\boldsymbol{k},\boldsymbol{l}\}} \frac{\delta_{\boldsymbol{k}\boldsymbol{n}} \delta_{\boldsymbol{l}\boldsymbol{m}}}{(E - 2v_{\boldsymbol{k}})^2 (E - v_{\boldsymbol{k}} - v_{\boldsymbol{l}})} \right] \delta_{\boldsymbol{m},\boldsymbol{n}} + \\ & + J^2 \sum_{\{\boldsymbol{k},\boldsymbol{l}\}} \frac{\delta_{\boldsymbol{k}\boldsymbol{n}} \delta_{\boldsymbol{l}\boldsymbol{m}}}{(E - 2v_{\boldsymbol{k}})(E - v_{\boldsymbol{l}} - v_{\boldsymbol{k}})(E - 2v_{\boldsymbol{l}})} \,. \end{aligned} \tag{3.17}$$

The second term at the right-hand side of Eq. (3.17) accounts for the processes in which one particle hops from a site to a neighbouring one, while the second particle is at rest. The third term in that equation represents instead the processes in which both electrons tunnel from one site to the same neighbouring site, thus leading an effective hopping for the pair. Retaining terms up to the first order in the approximation of the matrix element in Eq. (3.17), we can rewrite the density of states $\bar{\rho}_G(\lambda)$ using the probability distribution of the uniform on-site disorder $P(v) = W^{-1}\Theta\big(\frac{W}{2} - |v|\big)$ as:

$$\overline{\rho_{\mathrm{K}}}(\lambda) \approx \frac{1}{V_d}\int \mathrm{d}v\, P(v)\delta\left(\lambda - \frac{1}{E-2v}\right) = \frac{1}{2W\lambda^2 V_d}\Theta\left(W - \left|E - \frac{1}{\lambda}\right|\right) . \tag{3.18}$$

The latter relation means that, in the strong disorder regime $W \gg J$, the density $\overline{\rho_{\mathrm{K}}}(\lambda)$ develops tails descending as λ^{-2} when $W \geq E$ in the region where $\lambda \geq 1/(E+W)$ and $\lambda \leq 1/(E-W)$. The same scenario takes place as long as $W \leq E$, in the intervals $\lambda \geq 1/(E-W)$ and $\lambda \leq 1/(E+W)$.

3.4.1 Numerical computation

In order to analyse the density of states, that is a quantity that behaves regularly in vicinity of the critical point, we consider cubic lattices (with $N \equiv M$) in which periodic boundary conditions are imposed to the single-particle Hamiltonian in all d directions. As a result, $\boldsymbol{H}^{(\mathrm{sp})}$ does not possess a block-tridiagonal structure any more, since it contains two nonzero blocks $\boldsymbol{H}^{(\mathrm{sp})}_{1M} = \boldsymbol{H}^{(\mathrm{sp})}_{M1} = -\mathbb{1}$. The computation of the effective kernel in Eq. (3.5) therefore can not be performed using the algorithm presented in Sec. 3.2.

A sharp-witted strategy to perform $N_d = M^d$ inversions of matrices required in Eq. (3.5) can now be applied by decomposing the $\boldsymbol{G}^{(\mathrm{sp})\,-1}(E-\varepsilon_s)$ into the sum of a block-tridiagonal matrix $\boldsymbol{B}$ and the product between a $M^d \times M^{d-1}$ matrix $\boldsymbol{U}$ and a $M^{d-1} \times M^d$ one, denoted as $\boldsymbol{V}$. Matrix $\boldsymbol{B}$ corresponds to the $\mathbf{G}^{(\mathrm{sp})\,-1}$ obtained leaving the free boundary conditions along z appearing in Sec. 3.2, with modified blocks $\boldsymbol{A}'_1 = \boldsymbol{A}_1 + \boldsymbol{A}_N^{-1}$ and $\boldsymbol{A}'_N = 2\boldsymbol{A}_N$ and can thus be inverted using the recursive relations in Eq.s (3.6), (3.7) and (3.8). The rectangular matrices $\boldsymbol{U}$ and $\boldsymbol{V}$ must be composed of the following $M^{d-1} \times M^{d-1}$ blocks respectively:

$$\boldsymbol{U} = \begin{pmatrix} \boldsymbol{A}_N^{-1} & \mathbb{0} & \cdots & \mathbb{0} & \mathbb{1} \end{pmatrix} ,$$

and

$$\boldsymbol{V} = \begin{pmatrix} \mathbb{1} & \mathbb{0} & \cdots & \mathbb{0} & -\boldsymbol{A}_N \end{pmatrix} .$$

Using Woodbury's identity[1], the single-particle Green's function can be evaluated as follows:

$$\mathbf{G}^{(\mathrm{sp})} = (\boldsymbol{B} + \boldsymbol{U}^T\boldsymbol{V})^{-1} = \boldsymbol{B}^{-1} - \boldsymbol{B}^{-1}\boldsymbol{U}^T(\mathbb{1} + \boldsymbol{V}\boldsymbol{B}^{-1}\boldsymbol{U}^T)\boldsymbol{V}\boldsymbol{B}^{-1} .$$

---

[1] Let $\boldsymbol{A}$ be a $N \times N$ matrix, $\boldsymbol{U}$ a $N \times M$ one with $M \leq N$, $\boldsymbol{V}$ a $M \times N$ and $\boldsymbol{C}$ a $M \times M$ matrix. Then $(\boldsymbol{A} + \boldsymbol{U}\boldsymbol{C}\boldsymbol{V})^{-1} = \boldsymbol{A}^{-1} - \boldsymbol{A}^{-1}\boldsymbol{U}(\boldsymbol{C}^{-1} + \boldsymbol{V}\boldsymbol{A}^{-1}\boldsymbol{U})\boldsymbol{V}\boldsymbol{A}^{-1}$.

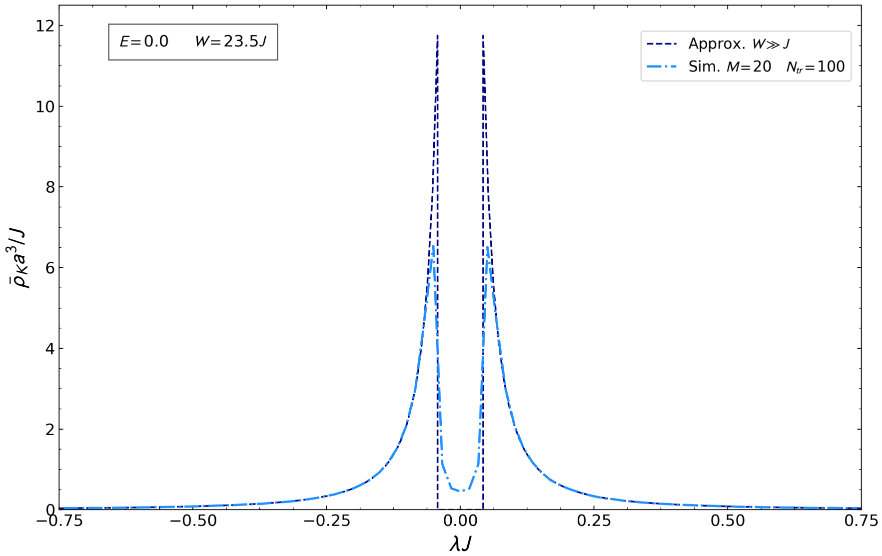

FIGURE 3.9 – The disorder-averaged density of states $\overline{\rho_{\mathrm{K}}}$ (in units of lattice constant and inverse of tunnelling), evaluated at $E = 0$ and $W = 23.5J$, plotted as a function of the λ in units of the hopping amplitude (red solid line). The dashed curve represents the density in the atomic limit, where tunneling is neglibile compared to the typical value of the random potential. Edited, from Ref. [173].

Compared to the algorithm illustrated in Sec. 3.2, the one presented above leads to an increase of a factor (about) two in the number of elementary operations necessary for the computation, but remains still advantageous with respect to standard algorithms for the inversion of symmetric matrices.

Once obtained the effective kernel $\mathbf{K}$, it is diagonalized, finding its eigenvalues λ_i and eigenvectors $\mathbf{\Psi}_i$, with $i = 1, 2, \ldots, M^d$. From the spectrum determined for different realizations of the random potential, $\overline{\rho_{\mathrm{K}}}$ is thus derived as explained in Sec. b), by partitioning the region of interest into N_b bins of equal width $\Delta\lambda$ and counting the number of eventualities in each frequency class $\{f(i, r)\}$, where $i = 1, 2, \ldots, N_b$ and $r = 1, 2, \ldots, N_{tr}$. Hence the disorder-averaged density of states in the i-th bin reads:

$$\overline{\rho}(i) = \frac{1}{\Delta\lambda a^3} \sum_{r=1}^{N_{tr}} \frac{f(i,r)}{N_{tr} M^d} \, . \tag{3.19}$$

3.4.2 Zero total energy

At the same values of total energy E and disorder W at which the critical beahviour has been studied (see Fig. 3.7), we have estimated the density of states, which exhibits a nonmonotonic behaviour as a function of $\lambda = U^{-1}$. In particular, as highlighted in Fig. 3.9, $\overline{\rho_{\mathrm{K}}}$ displays two peaks at $\lambda = \pm W^{-1}$, where the reduced localization length Λ_M nearly reaches its maxima, whereas its power-law tails behave in considerable accordance with the approximation $K(\boldsymbol{n}, \boldsymbol{m} \approx \delta_{\boldsymbol{nm}}/(E - 2v_{\boldsymbol{n}})$ of Eq. (3.18) describing the atomic limit. Indeed, in order to interact, the two particles must lie on the same site $\boldsymbol{n}$, so the total energy is given by $E = U + 2V_{\boldsymbol{n}} = 0$, implying $|U| = 2|V_{\boldsymbol{n}}| \leq W$. Nevertheless, at high interactions ($|U| \gg J$) $\overline{\rho_{\mathrm{K}}}$ does not vanish and remains finite, contrarily to Eq. (3.18), thus signalling

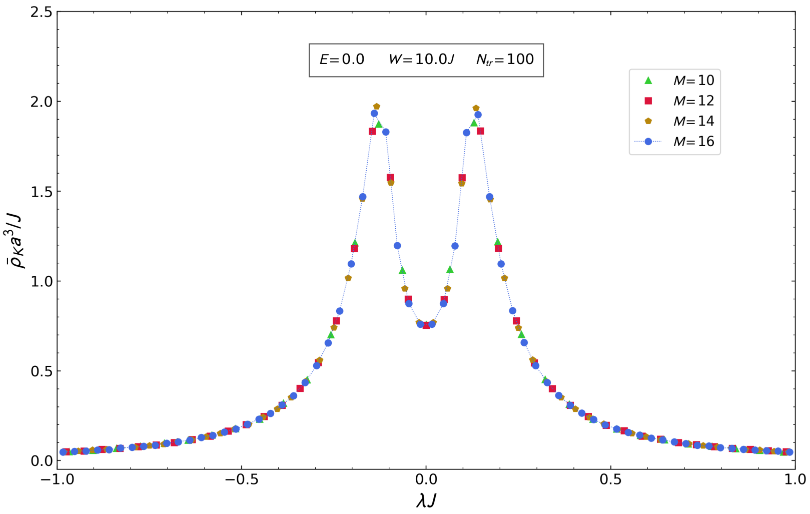

FIGURE 3.10 – The disorder-averaged density of states $\overline{\rho_K}$, evaluated at $E = 0$ and $W = 23.5J$, plotted as a function of the λ using three different lattice sides ($M = \{10, 12, 14, 16\}$).

that tunnelling effects are still relevant. The latter become more pronounced if disorder strength W is reduced. Besides, the doubly-peaked structure of the density reflects the fact that the two-particle energy levels are closer and likely to mix together, giving rise to level hybridization and, ultimately, to a metallic behaviour. On the contrary, where that quantity is lower, the two-particle wave-functions are more spaced out in energy and levels tend to repel even at finite but small U.

As expected, since density is smooth around the critical point, its behaviour is independent of lattice size, as shown in Fig. 3.10, although some minor finite-size effects are present at high interactions ($\lambda \approx 0$). At decreasing disorder parameter W, the height of the peaks lowers and the tails broaden, as displayed in Fig. 3.11 in the right panel. At $W \lesssim 4J$, a region where all one-particle states are extended (cf. Fig. 1.8), the density exhibits an only maximum at high interactions, while preserving its parity symmetry (Fig. 3.11 in the left panel).

3.4.3 Finite total energy

When the total energy is fixed at a finite value, the density of states loses its parity symmetry in the interaction domain, and the effect is much pronounced at low disorder, where the quantity is finite only at negative values of the interaction. In particular, at very low disorder, $\overline{\rho_K}$ is peaked around $\lambda \approx E^{-1}$ as shown in the left panel of Fig. 3.12 and its tails descend almost symmetrically from this value, thus reminding the behaviour of the single-particle ρ as a function of energy, plotted in Fig. 2.6. As we will see in next paragraph, where this similarity will be explained quantitatively, the analogy persists even in the phase diagram in the (U, W) plane.
At higher disorder this symmetry is progressively lost and a slower decay of $\overline{\rho_K}$ is detected at low interactions, whereas the peak broadens, assuming a form which approaches the one of a plateau (see the right panel in Fig. 3.12). For $W \gtrsim 9J$, the left tail, endowed with decreasing steepness, eventually mingles with the descending upper part, while the right tail gets (increasingly) slanting.

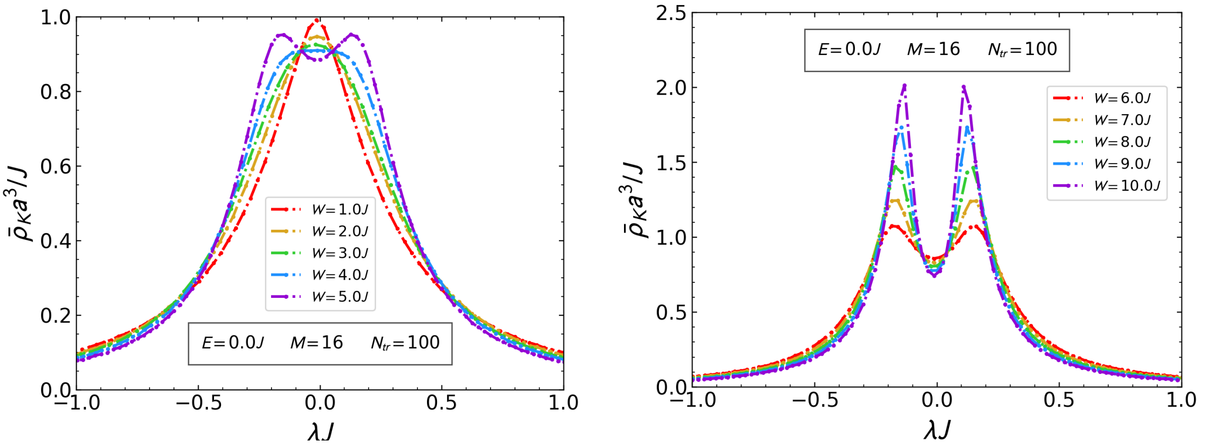

FIGURE 3.11 – The density of states $\overline{\rho_{\mathrm{K}}}$, averaged over $N_{tr} = 100$ disorder realizations, plotted as a function of λ. The former quantity, evaluated at $E = 0$, is shown at low values of the random potential ($J \leq W \leq 5J$) on the left panel and at higher values ($6J \leq W \leq 10J$) on the right one. The lattice side is now kept fixed at $16a$.

When $W \gtrsim 20J$ at positive interactions a second peak appears, whose height increases at growing typical values of the random potential (Fig. 3.13).

3.5 Phase diagrams

3.5.1 Zero total energy

Based on the fact that the transition in $d = 3$ belongs to the orthogonal universality class, as asserted in Sec. 3.3.3, we determined the position of the phase boundary between localized and extended

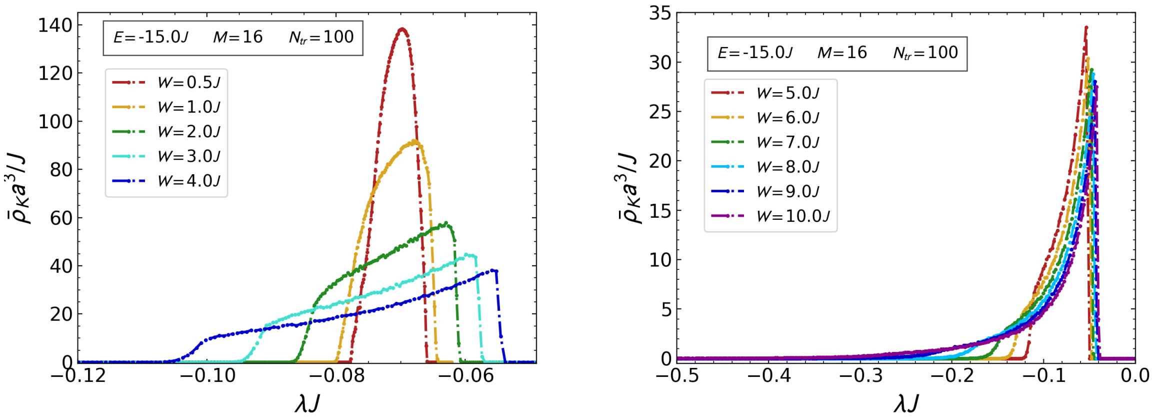

FIGURE 3.12 – The density of states at $E = -15J$, averaged over $N_{tr} = 100$ disorder realizations and plotted as a function of λ. The curve in the left panel is evaluated at low values of the random-potential amplitude ($0.5J \lesssim W 4J$), while $\overline{\rho_{\mathrm{K}}}(\lambda)$ on the right one at higher ones ($6J \lesssim W 10J$). The lattice side is kept fixed again at $16a$.

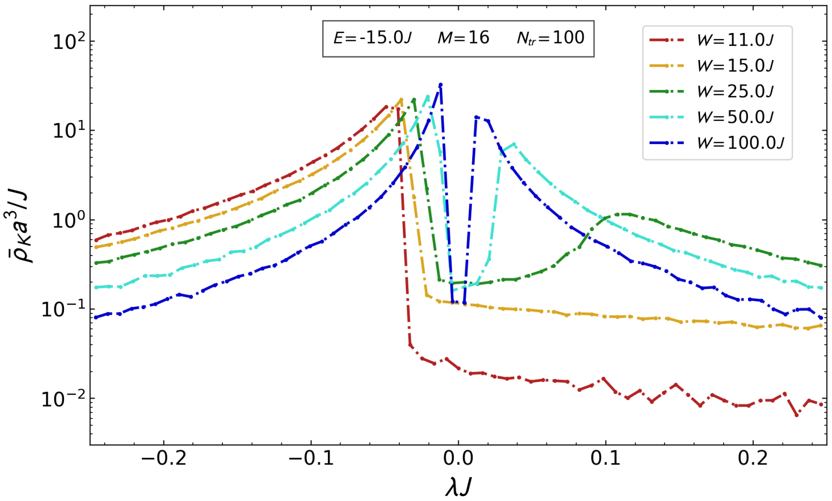

FIGURE 3.13 – The density of states at $E = -15J$, averaged over $N_{tr} = 100$ disorder realizations and plotted (in logscale) as a function of λ. The curve $\overline{\rho_{\rm K}}(\lambda)$ is evaluated in a wide range of random-potential amplitudes, from $W = \{11J, 15J, 25J, 50J, 100J\}$, while the lattice side is kept fixed again at $16a$.

states of the pair in the (U, W) plane. For each value of the disorder strength, we calculate the reduced localization length as a function of U for $M = \{10, 12, 15\}$ and extrapolate the critical point from the scaling behaviour of the U_M values. To save computer resources, we have limited the number of disorder realizations resulting in larger error bars for U_c. Moreover, for $W \leq 21J$, we have calculated the intercept by discarding also the data for $M = 10$, as the relative deviation $(U_M - U_c)/U_c$ increases as W decreases. The obtained results, which are independent of the sign of the interaction parameter, are displayed in Fig. 3.15 . We see that the Anderson transition for a pair with zero total energy occurs in a region where all single-particle states are localized (see Fig. 1.8). For $23.7J \leq W \leq 25.9J$ the system is endowed with two distinct critical points resulting in a nonmonotonic behavior of the phase boundary.

This feature can be understood in light of discussion of the density of states in Sec. 3.4.2, from which one expects that weakly interacting states are the first to be localized by disorder, whereas states with $|U| \sim W$ are the most robust against localization. Indeed, for disorder strengths such that $23, 7J \leq W \leq 25, 9J$, the system possesses two distinct critical points. As an example, in Fig. 3.14 (right panel) we display Λ_M versus U/J calculated at $W = 24, 5J$ for three different values $M = 10, 12, 15$ of the transverse size of the bar. We can indeed distinguish two critical points, $U_c = 4.04J$ and $U_c = 23.7J$, values of the interaction strength between the states are delocalized at zero total energy. As W increases, the two critical points get progressively closer, until they merge around $U = 14J$ for $W = 25.9J$. For $W < 16.54J$, all pair states with zero total energy are extended, as illustrated in Fig. 3.14 (left panel) for $W = 14J$. In fact, at this disorder strength, Λ_M grows with system size for any value of the interaction strength, implying diffusive behaviour. Besides, it is worth mentioning that a nonmonotonic behavior of the critical disorder strength versus

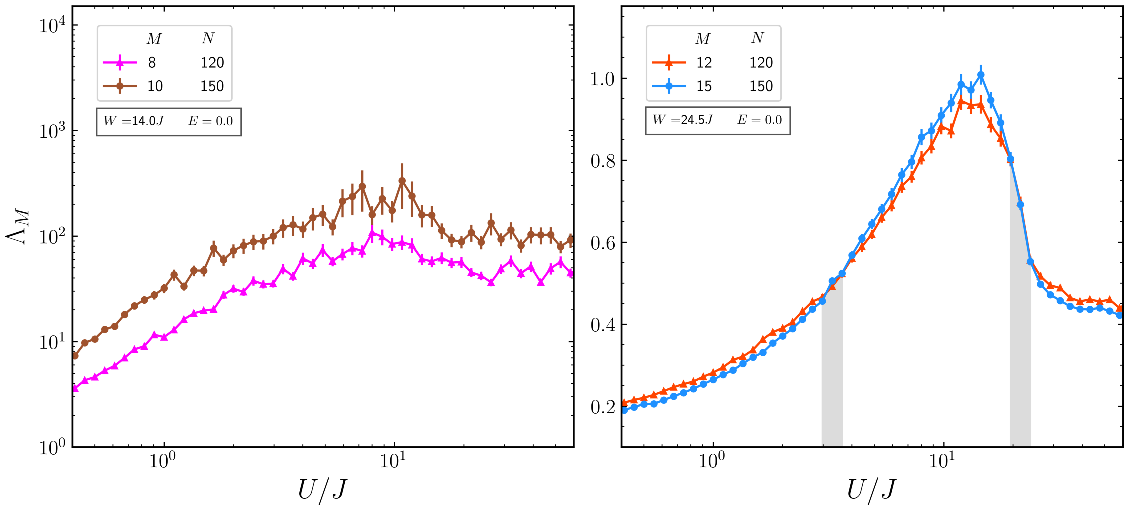

FIGURE 3.14 – Right panel: Reduced localization length of the pair as a function of the interaction strength U calculated at $W = 24.5J$ and total energy $E = 0$ for three different values of the transverse size of the bar, $M = \{10, 12, 15\}$. The shaded areas highlight the regions in which two critical points, $U_c = 4.04J$ and $U_c = 23.7J$, are detected. The length of the bar is $150a$ and the number of disorder realizations is $N_{tr} = 200$. Left panel: The same quantity as in the previous one, evaluated at $W = 14J$ and total energy $E = 0$ for two different values of the transverse size of the bar, $M = 10$ and $M = 12$. The bar is again $150a$ long, whereas the values of Λ_M are obtained by averaging over $N_{tr} = 100$ different realizations of the random potential.

U was also obtained for the ground state of the Anderson-Hubbard model at finite fillings in earlier theoretical studies based, respectively, on the dynamical mean-field theory [174] and on the self-consistent theory of localization [175].

3.5.2 Finite total energy

Straying from the band centre, the scenario becomes richer and, as we will see in the phase phase diagrams that follow, Anderson transitions can now occur at more than one value of the disorder parameter, fixing energy and interaction strength. We continue our investigation on the phase diagram of the two-particle system by first analysing the transport properties at the Hubbard subband $E = U$. Resuming our effective model, described by the kernel K in Eq. (3.3), assuming $E \sim U \gg W, J$, the former quantity can be expanded in terms of the one-particle eigenenergies ε_r of the Hamiltonian in Eq. (1.9), as follows:

$$K(\boldsymbol{n}, \boldsymbol{m}) = \sum_{r,s} \frac{\phi_r^*(\boldsymbol{m})\phi_s^*(\boldsymbol{m})\phi_r(\boldsymbol{n})\phi_s(\boldsymbol{n})}{E} \sum_{l=0} \left(\frac{\varepsilon_r + \varepsilon_s}{E}\right)^l . \tag{3.20}$$

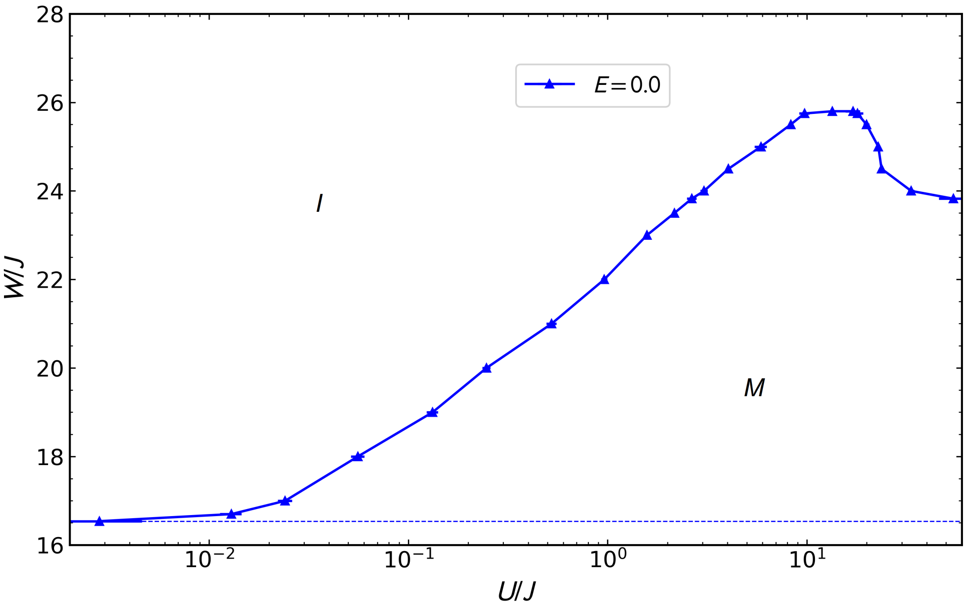

Figure 3.15 – Main panel: phase boundary between localized and extended states in the (U, W) plane, computed for a pair with zero total energy, $E = 0$. The dashed horizontal line corresponds to the noninteracting limit, $W = W_{c,\mathrm{sp}} = 16.54J$. The diagram holds for both attractive and repulsive interactions.

Using the orthonormality relations,

$$\begin{aligned} \sum_s \phi_s^*(\boldsymbol{m})\phi_s(\boldsymbol{n}) &= \delta_{\boldsymbol{m},\boldsymbol{n}} \ , \\ \sum_{\boldsymbol{n}} \phi_s^*(\boldsymbol{n})\phi_r(\boldsymbol{n}) &= \delta_{rs} \ , \end{aligned}$$

and retaining the terms up to the second order in E^{-1} in the series in the right-hand side of Eq. (3.20), one gets an extension to three-dimensional lattices of the result found in [165]:

$$K(\boldsymbol{n},\boldsymbol{m}) \simeq \frac{\delta_{\boldsymbol{m},\boldsymbol{n}}}{E}\left(1 + \frac{2}{E}v_{\boldsymbol{n}} + \frac{4(v_{\boldsymbol{n}}^2 + 3J^2)}{E^2}\right) + \frac{2J^2}{E^3}\delta_{\{\boldsymbol{m},\boldsymbol{n}\}} \ , \tag{3.24}$$

where $\delta_{\{\boldsymbol{m},\boldsymbol{n}\}}$ is the Kronecker delta which does not vanish only when $\boldsymbol{m}$ and $\boldsymbol{n}$ refer to nearest-neighbour sites. The latter equation, plugged into Eq. (3.14), leads to an effective model with nearest-neighbour tunneling and modified random pontential and energy:

$$\hat{H}_{\mathrm{eff}}\Psi(\boldsymbol{n}) = \frac{2J^2}{E}\sum_{i=1}^{3}\Psi(\boldsymbol{n}+\mathbf{e}_i) + \frac{2J^2}{E}\sum_{i=1}^{3}\Psi(\boldsymbol{n}-\mathbf{e}_i) + \frac{2v_{\boldsymbol{n}}(E+2v_{\boldsymbol{n}})}{E}\Psi(\boldsymbol{n}) = E_{\mathrm{eff}}\Psi(\boldsymbol{n}) \ , \tag{3.25}$$

where $\mathbf{e}_i$ are the unit vectors along the three orthogonal axes and E_{eff} is the effective total energy,

$$E_{\text{eff}} = \frac{E(E-U)}{U} - \frac{12J^2}{E} \, . \tag{3.26}$$

At the leading order in E^{-1}, the disorder parameter and the hopping amplitude in the new Hamiltonian, denoted with the subscript eff, can be expressed as:

$$J_{\text{eff}} = -\frac{2J^2}{E} \, , \tag{3.27a}$$

$$W_{\text{eff}} = 2W \, . \tag{3.27b}$$

When $E = U$, the energy of the new effective model with short-range hopping reads $E_{\text{eff}} = -12J^2/U = 6J_{\text{eff}}$. Differently from the atomic limit $W \gg J$ (see Eq. (3.17)), the tunneling terms of the new effective model in Eq. (3.25) do not depend on the specific values of the disordered potential at the two edges of a bond. Remarkably, the effective Hamiltonian $\hat{H}_{\text{eff}}$ obtained under the aforementioned conditions and approximations shares the same form of Anderson's model in Eq. (1.9), so in that regime of parameters the localization properties can be inferred from known results of that model. In particular, at large interactions and low W, $K(\boldsymbol{n}, \boldsymbol{m})$ in Eq. (3.14) takes the form of a single-particle Anderson Hamiltonian (Eq. (1.9)), with modified disorder, tunnelling and energy and unveils the localization properties of molecular states, in which the two particles are bound with each other.

Now, since at $E_{\text{sp}} = 6J_{\text{sp}}$, the critical disorder parameter in the original Anderson's model in $d = 3$ (Eq. (1.9)) satisfies $W_{c,\text{sp}} \simeq 16J_{\text{sp}}$, the same relation must hold for the effective Hamiltonian in Eq. (3.25), so, using Eq.s (3.27a) and (3.27b), we find that $W_{c,\text{eff}} \simeq 16J_{\text{eff}}$ implies:

$$W_c = -\frac{W_{c,\text{sp}}(6J)J}{E} \, , \tag{3.28}$$

which means that, at $E \sim U$, $W_c \approx \frac{-16J^2}{U}$.

In the following, we will first examine the phase diagram obtained numerically in the subband $E = U$, then we will proceed with the analysis of the diagrams traced at fixed energy, where the interval in which a reentrant behaviour of the phase boundary shows up.

This feature, as shown in Panel a of Fig.3.16 can be explained by the change in the nature of the pair states for increasing disorder. Neglecting Lifshitz-tail regions, where the single-particle density of states is exponentially suppressed, the energy band of a single particle broadens with disorder according to $-\varepsilon_{\text{BE}}(W) \leq \varepsilon \leq \varepsilon_{\text{BE}}(W)$, where the numerical band edges $\pm\varepsilon_{\text{BE}}(W)$ are computed for a given disorder strength within the coherent potential approximation, illustrated in Sec. 2.2.1. As a consequence, the energy spectrum of *two* noninteracting particles is bound to the interval $-2\varepsilon_{\text{BE}}(W) \leq \varepsilon_1 + \varepsilon_2 \leq 2\varepsilon_{\text{BE}}(W)$. For given values of E and W, we say that a state is *scattering*-like if the total energy of the pair lies inside the two-particle noninteracting spectrum, that is $-2\varepsilon_{\text{BE}}(W) \leq E \leq 2\varepsilon_{\text{BE}}(W)$. These states correspond to the yellow region in the energy-disorder

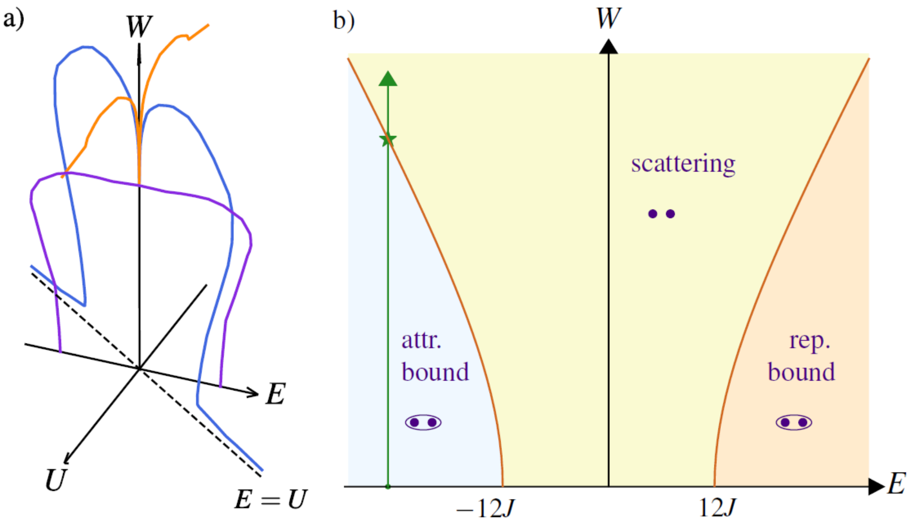

FIGURE 3.16 – In Panel a the critical disorder strength W_c for pair localization is plotted as a function of the Hubbard interaction U and the total energy E. The orange and the blue data curves represent cuts along the planes $E = 0$ and $E = U$. For vanishing interactions, the phase boundary (violet data curve) coincides with the single-particle mobility edge calculated in Ref. [79], under the change of variable $E = -2\varepsilon$, where ε is the energy of a single particle. Panel b highlights the nature of the pair state as a function of energy and disorder. The two (brown) solid lines define the numerical band edges $E = \pm 2\varepsilon_{\mathrm{BE}}(W)$ of the non-interacting two-particle energy spectrum for a given disorder strength W and divide the plane in three regions, marked out by states of different nature: scattering states, attractively and repulsively bound states. For $|E| > 12J$, the state changes from molecular to scattering-like as the disorder strength increases (solid vertical arrow), generating multiple Anderson transitions. From Ref. [176].

plane shown in Fig.3.16b. States which are not scattering-like are called *molecular*. In the same figure we distinguish between attractively bound states, occurring for $E < -2\varepsilon_{\mathrm{BE}}(W)$ (cyan region), and repulsively bound states, which are defined for $E > 2\varepsilon_{\mathrm{BE}}(W)$ (orange region).

As in the zero-energy case, owing to the not neglible finite-size effects, we extracted the critical values of interaction strength using the critical exponents ν_{orth} and y_{orth} estimated in [76], assuming again that the transitions belong to the orthogonal universality class. In the case where $E = U$, at $M = 8, 10, 12$ we initially identified W_M as the value at which $\Lambda_M = \Lambda_{c,\mathrm{orth}}$, starting from reduced localization lengths extracted by averages over $N_{tr} = 100 \div 200$ realizations of the random potential. We then executed linear regressions over the disorder variable, at fixed values of the coupling between the two particles,

$$W_M = W_c + aM^{-b} \, , \tag{3.29}$$

where $a = -c_0 W_c / b_1$ is a dimensional constant and $b = 1/\nu_{\mathrm{orth}} + y_{\mathrm{orth}}$. The latter relation (in Eq. (3.29)) can be determined by rewriting the right-hand side of Eq.s (2.14) and (2.12) in first-order approximation in $(W - W_c)/W_c$. We also noticed pronounced finite-size effects around the point of the phase boundary where the tangent is parallel to the y-axis, as displayed in Fig. 3.17. The phase boundary thus obtained is compared to the one found at $E = 0$ in Fig. 3.15, where also the approximate curve given by Eq. (3.28), derived from the effective model at $U \gg W$ is portrayed.

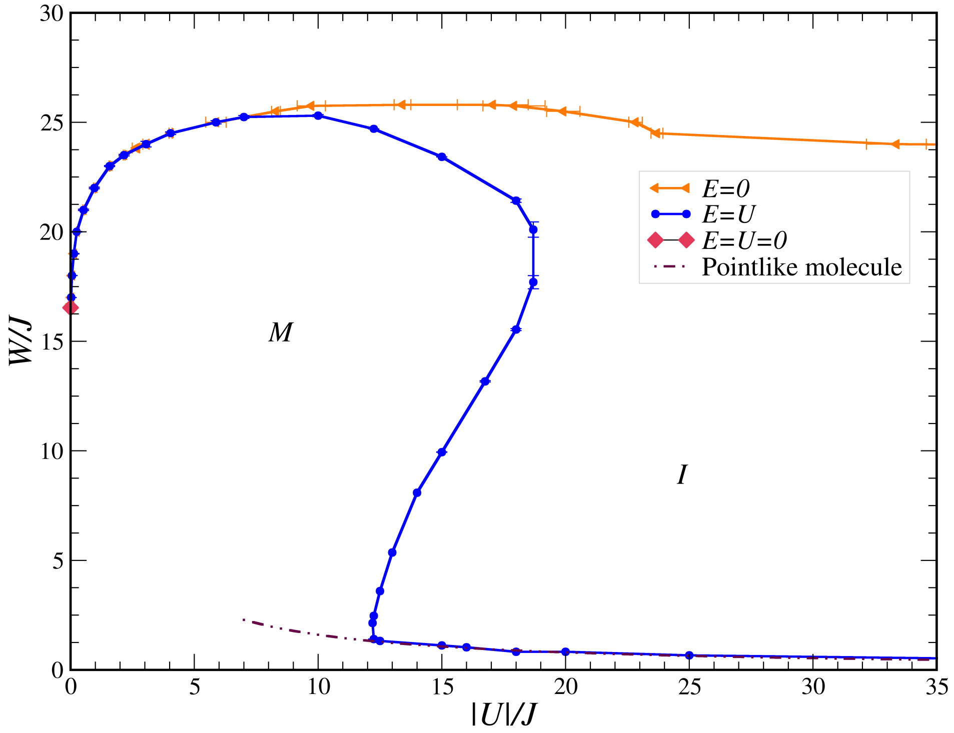

Figure 3.17 – Phase boundaries between localized and extended states in the (U, W) plane, where the quantities are expressed in terms of the tunnelling amplitude. The curve obtained at finite energy $E = U < 0$ is plotted in cyan, while the one determined at $E = 0$, corresponding to the one in Fig. 3.15, is grey coloured. The doubly dotted and dashed curve represented in dark purple indicates in turn the boundary estimated in the framework of the effective one-particle Anderson model, in Eq. (3.28), thus describing a pointlike molecule. The magenta dot indicates the critical point found in [76], in the absence of interactions. Edited, from Ref. [176].

Contrarily to the zero-energy case, where interactions favour delocalization, at $E = U \gg W$, they give rise to confinement of molecular states at weak disorder ($W \lesssim 2.5J$). The critical value of the random-potential parameter W decreases as $|U|$ increases since, according to Eq. (3.27a) with the $E = U$ constraint, the hopping amplitude is lowered under this variation of the interaction strength. A unique critical W at fixed interaction is possible until the energy E is low enough to prevent the occupation of scattering states, in which particles are kept apart by long distances. As shown in Fig. 3.17, the phase boundary in that region follows very well the one predicted by Eq. (3.28), based on the effective model with short-range hopping. As $|U| \lesssim 18.7J$, the band of delocalized scattering states becomes available and the phase boundary displays a s-like behaviour in the interval $12.2J \lesssim |U| \lesssim 18.4J$: here the two-particle system undergoes three metal-insulator transitions as W is raised. In that case, therefore, interactions favour the delocalization of those states. Furthermore, at strong disorder ($16.5J \lesssim W \lesssim 25J$) and $|E| \lesssim 7J$, the phase boundary follows the one found at zero total energy, displaying a nonmonotonic behaviour.

In order to explore the dynamics of the system at finite energy more in-depth, we have traced the phase diagram at $E = -15J$, an energy value located within the region ($12.2J \lesssim |E| \lesssim 18.4J$) where multiple critical values of W are present at fixed energy and interaction. As in the case in

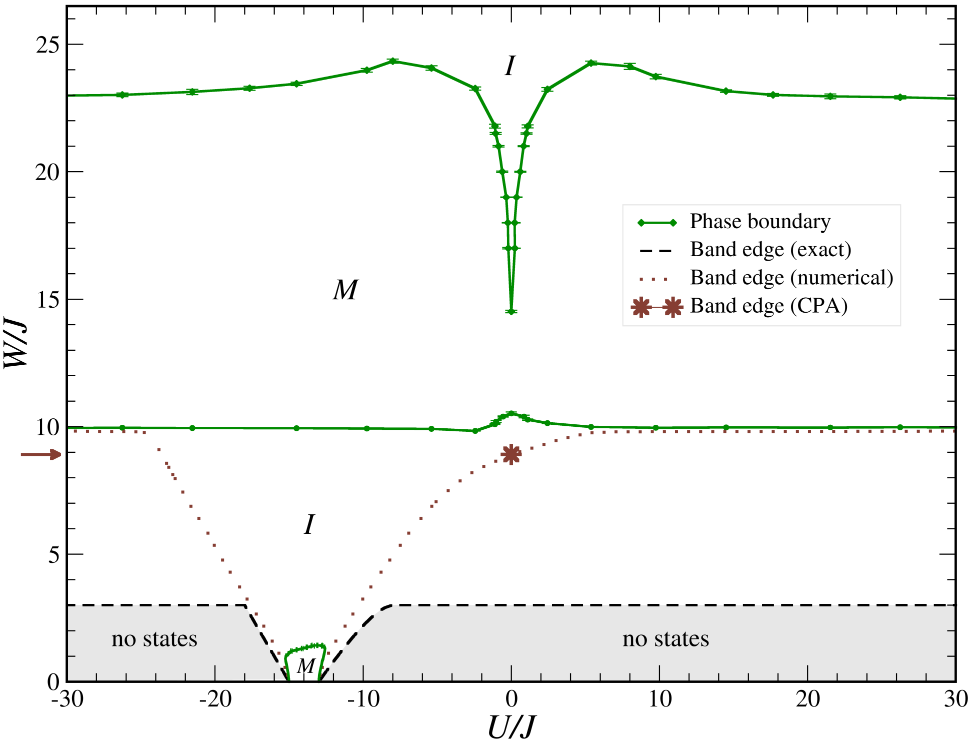

FIGURE 3.18 – Phase boundary between localized and extended states in the (U, W) plane, where the quantities are expressed in terms of the tunnelling amplitude and evaluated at $E = -15J$ (green solid curve). At low disorder parameter the numerically obtained band edge is also represented (dotted curve), together with the one extracted by resorting to the analysis of the translationally-invariant lattice (Eq. (3.32)), portrayed by the long-dashed curve. The star denotes the band edge found in the one-particle case at $\varepsilon = -E/2$, using the coherent-potential approximation, illustrated in Sec. 2.2.1. The brown arrow on the left indicates the disorder value at the latter band edge, separating the region of molecular states (below that threshold) from the one of scattering states (above). From Ref. [176].

which $E = U$ (Fig. 3.17), we have performed simulations in lattices with $M = \{8, 10, 12\}$ along each transverse direction and averaged the Lyapunov exponents over $N_{tr} = 100 \div 300$ realizations of the random potential. As done for the zero-energy case in Sec. 3.5.1, keeping the disorder constant, we made linear regressions over (M^{-b}, U_M), to the end of extrapolating the critical values of interaction strength in Eq. (3.13) in the regions where the phase boundary in the (U, W) plane is not approximately parallel to the x-axis. When the latter condition is not fulfilled, the fitting procedure using Eq. (3.29) has been carried out, in particular in the regions where $9.7J \lesssim W \lesssim 10.5J$ and $23J \lesssim W \lesssim 25J$, resorting also, in the former interval, to simulations in lattices with $M = 15$, since finite-size effects are more relevant there. The latter occur also in the one-particle case, leading to lower values of the reduced localization length at the crossing point between the curves $\Lambda_M(W)$ evaluated varying M.

The phase diagram thus obtained exhibits a region at $W \lesssim 1.5J$ where the boundary calls back the one of the single-particle problem in the (E, W) plane. From the effective model for molecular states, we would expect that all these states are localized for $W > -(16/15)J \approx 1.1027J$ according to Eq. (3.28), a value that is slightly smaller than the value inferred from Fig.s 3.18 and 3.21. Morevoer,

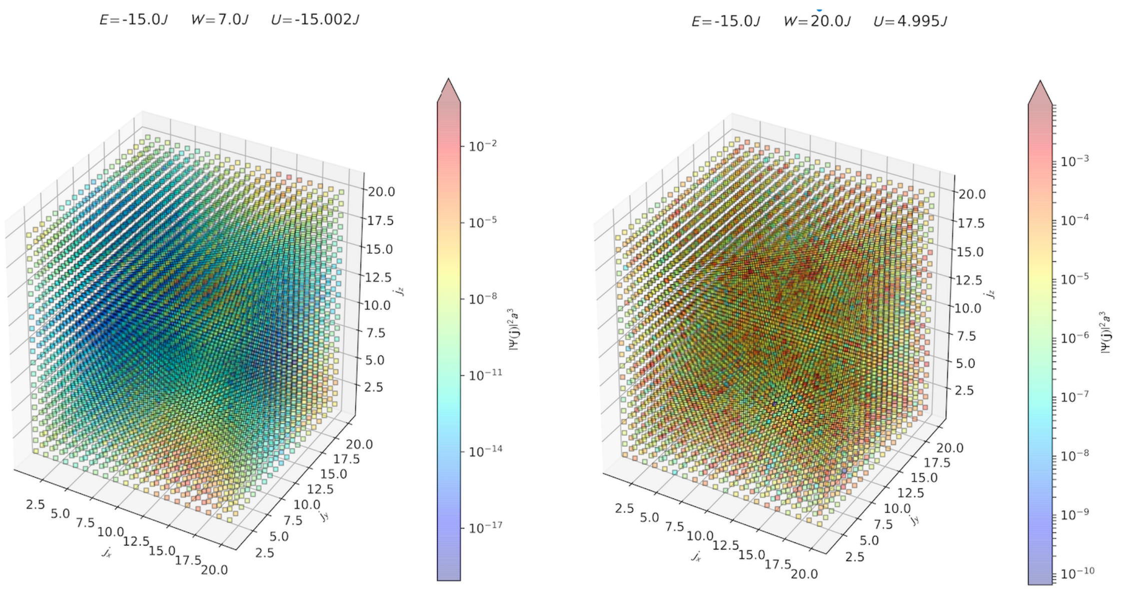

(A) Localized state

(B) Extended state

FIGURE 3.19 – The probability density $|\Psi|^2$ associated to the effective one-particle eigenvalue problem in Eq. (3.14) as a function of the coordinates (in unit of the lattice constant a) $\boldsymbol{j}$ of the center-of-mass of the pair at $E = -15J$ in lattices with $M = 20$. In Fig. 3.19a a localized state at $U \approx -15J$ is displayed, where the effects due to imposition of periodic boundary conditions along all three directions are visible. In Fig. 3.19b a delocalized eigenfunction is plotted instead, where the probability density does not exhibit an exponential decrease in space. In both the graphs, $|\Psi|^2$ is shown in decimal-logarithmic scale.

according to that model (see Eqs. (3.27a) and (3.26)), the phase boundary $W(U)$ is symmetric under reflections around the axis $U = E^3/(E^2 + 12J^2)$, a feature which is not fully present when $E = -15J$, as shown in Fig. 3.21, but that would appear more clearly at lower total energies. A closer look to the latter phase diagram reveals other discrepancies with the effective tight-binding model, whose phase boundary is represented by the doubly dotted-dashed curve, extracted using the numerical data of Ref. [79] and exploiting the relations in Eq.s (3.26)-(3.27b). In the absence of disorder, the latter model predicts a band-width equal to $12J_{\text{eff}} = 1.6J$, which is smaller than the correct value by a comparable factor. Besides, the unperturbed band edges are given by the solution of $E_{\text{eff}} = \pm 6J_{\text{eff}}$, yielding $U = E$ ans $U = E^3/(24J^2 + E^2) \approx -13.55J$. The difference can be reduced by considering fifth-order terms in E^{-1} in Eq. (3.20), since fourth-order ones give zero contribution, and one thus obtains $E_{\text{eff}} = E^2(U^{-1} - 12J^2E^{-3} - 240J^4E^{-5})$ and a larger tunnelling rate, $J_{\text{eff}} = -2J^2E^{-1} - 120J^4E^{-3} = 0.169J$. Using that value, one recovers a band-width of $2.028J$, in good agreement with the numerical phase diagram. Further deviations from the numerical value may be traced back to the different probability distribution of the random potential in the effective Anderson model (in Eq. (3.25)) if fifth-order terms in E^{-1} are included. As pointed out in [14] in the noninteracting case, the distribution of the on-site energies can indeed modify the position of the phase boundary. Nevertheless, the latter quantity is close to the one predicted by the tight-binding scheme when $E \approx U$.

The behaviour of the system can be better disclosed by observing the reduced localization length as a function of interaction, shown in Fig. 3.20. From the latter it emerges that at $W = J$, Λ_M possesses two critical points at $U_c = (-15.211 \pm 0.013)J$ and $U_c = (-12.671 \pm 0.002)J$, in panel (a), among which the states are extended and correspond to the ones inside the lobe on the bottom of Fig. 3.18. Outside that interaction range, the two-particle wave-functions are exponentially localized, property that persists at increasing disorder (until $9.8J$) and concerns eventually the whole range of couplings U (cf. panels (b) to (d) in Fig. 3.20). At the same time Λ_M develops two minima at negative interactions (already visible at $W = 3J$) which shift towards lower $|U|$ at greater typical values of the random potential. As an example showing the insulating behaviour in this disorder range, the eigenfunction of K in Eq. (3.14) related to the eigenvalue $\lambda = -0.0667J^{-1}$ at $W = 7J$ is portrayed in Fig. 3.19a.

A major change occurs when the disorder exceeds the value calculated at the right band edge of Anderson's single-particle model (in Eq. (1.9)) at $\varepsilon = -E/2 = 7.5J$. Using the coherent-potential approximation and solving Eq. (2.22) at that energy, the quantity corresponds to $W(7.5J) = 8.91J$. Above this value of the disorder parameter, pinpointed in Fig. 3.18 by the brown arrow on the left side, scattering states start playing a role, and the average distance between the two particle is enhanced, whereas the molecular band merges with the continuum of U values. This results in an increase in the reduced localization length and in the displacement of its minimum value, from negative interaction towards $U = 0$, as shows in panel (d) of Fig. 3.20, portraying $\Lambda_M(U)$ at $W = 9.4J$. In the disorder interval $9.8J \leq W \leq 24.3J$ a second region where the behaviour of the system is metallic appears. The states involved here are the scattering ones, little modified by the presence of interaction. In particular, at $U = 0$ the lower critical point is positioned at $W_c = (10.52 \pm 0.06)J$, in good agreement with the one-particle phase boundary found within the coherent potential approximation [81] at energy $\varepsilon_c = -E/2$ (Fig. 1.8), while the upper critical point lies at $W_c = (14.52 \pm 0.05)J$, a result consistent with the numerical one of Bulka et Al. [79] at the same value ε_c. The lower boundary delimiting the metallic phase is almost independent of the coupling except in the weakly-interacting region. This descends from the fact that the states involved at this level of disorder describe particles located in sites far apart, which do not feel the presence of interaction, because the overlap between orbitals is very small.

At $W = 10J$, the curves Λ_M with $M = \{8, 10, 12, 15\}$, plotted in panel 3.20 (f), exhibit a minimum in $U = 0$, a maximum at $U \simeq -2.5J$ and saturate at high repulsive and attractive interactions. They signal a metallic behaviour for all U except at $|U| \lesssim J$. A similar behaviour of Λ_M is detected at $W = 11J$, in Fig. 3.20 (g), where the reduced localization length obtained with different lattice sizes approach at the origin, although without intersecting among themselves, thus signalling a metallic regime in the whole U range we have examined. An example of extended wavefunctions is plotted in Fig. 3.19b, where the eigenstate of K related to the eigenvalue $U = 0.2J$ at $W = 20J$ shows sizeable fluctuations (amounting even to several orders of magnitude) in the scale of a lattice constant a.

As in the case of zero energy (Fig. 3.15), the upper phase boundary possesses a nonmonotonic be-

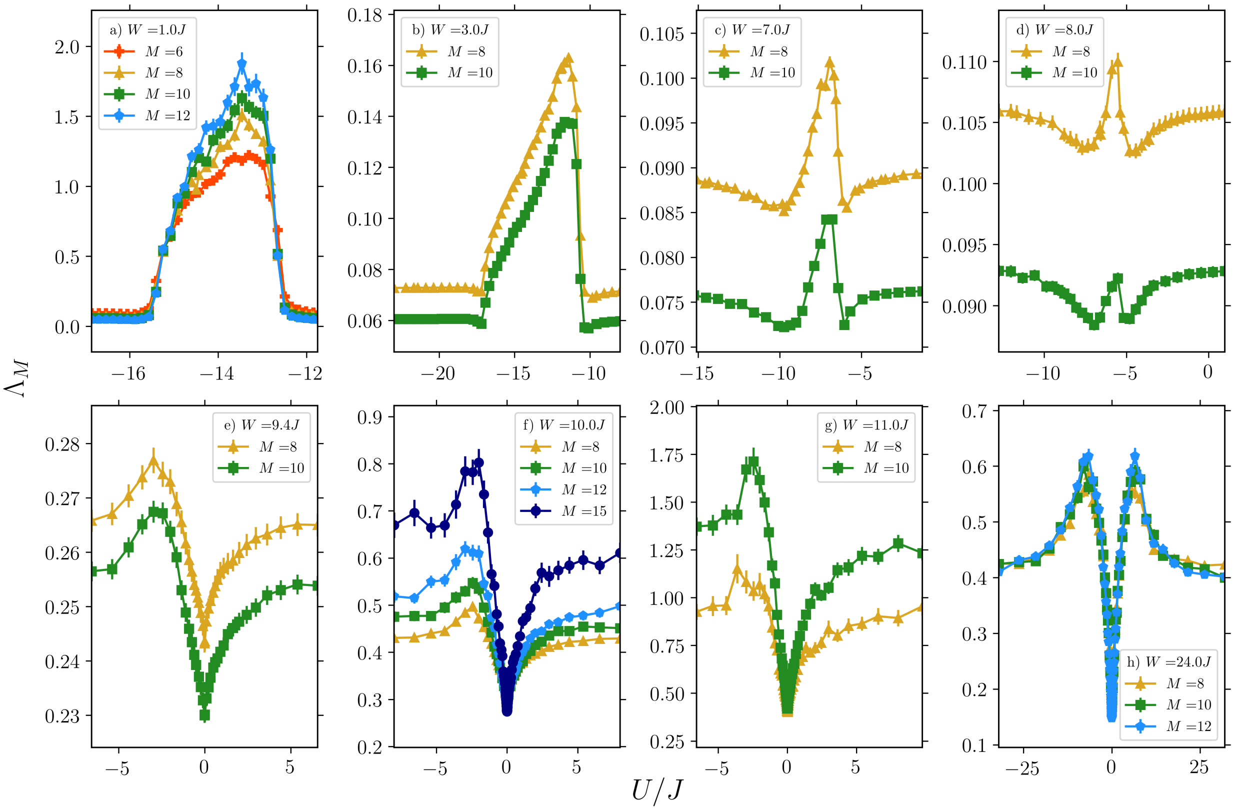

FIGURE 3.20 – The reduced localization length as a function of interaction strength in tunneling units at finite total energy $E = -15J$. Λ_M is computed at different values of the disorder strength $W = \{1, 3, 7, 8, 9, 10, 11, 24\}J$, starting from the top-left panel to the bottom-right one. Edited, from Ref. [176].

haviour, with a slight asymmetry according to the sign of interactions: $W_c^{\max,<} = (24.33 \pm 0.08)J$ when the two-particle potential is attractive and $W_c^{\max,>} = (24.26 \pm 0.07)J$ when it is repulsive. This trend can also be noticed in the $\Lambda_M(U)$ curves at $W = 24J$, where four Anderson transitions are expected to occur, analogously to the situation in which the two particles lie at the center of the band.

In the phase diagram in Fig. 3.18 and its zoomed lobe, in Fig. 3.21, explained through the effective model in Eq. (3.24), the position of the numerical band edge is also represented.

The latter quantity is estimated from the disorder-averaged density of states $\overline{\rho_{\mathrm{K}}}$ in Eq. (3.18), evaluated using Eq. (3.19). Following the method detailed in Sec. 2.2, we first subdivided the range in $\lambda = U^{-1}$ into N_b bins, ordered in ascending way in λ. We then identified the upper (resp. lower) edge in interaction $U_{\max}$ (resp. $U_{\min}$) as the minimum (resp. maximum) value of zeta in the bin l whose frequency, averaged over $N_{tr} = 100$ disorder realizations, satisfies $\bar{f}_{l-1} < 0.5 \leq \bar{f}_l$ (resp. $\bar{f}_{l+1} < 0.5 \leq \bar{f}_l$). Each of the interaction edges, represented by a dotted curve in the (U, W) plane, has a monotonic behaviour and approaches the phase boundaries at both vanishing disorder and $W = (9.84 \pm 0.01)J$. However, especially when the density of states possesses slowly decaying tails, the band-edge position seems to be slightly sensitive to the system size as well as to the choice

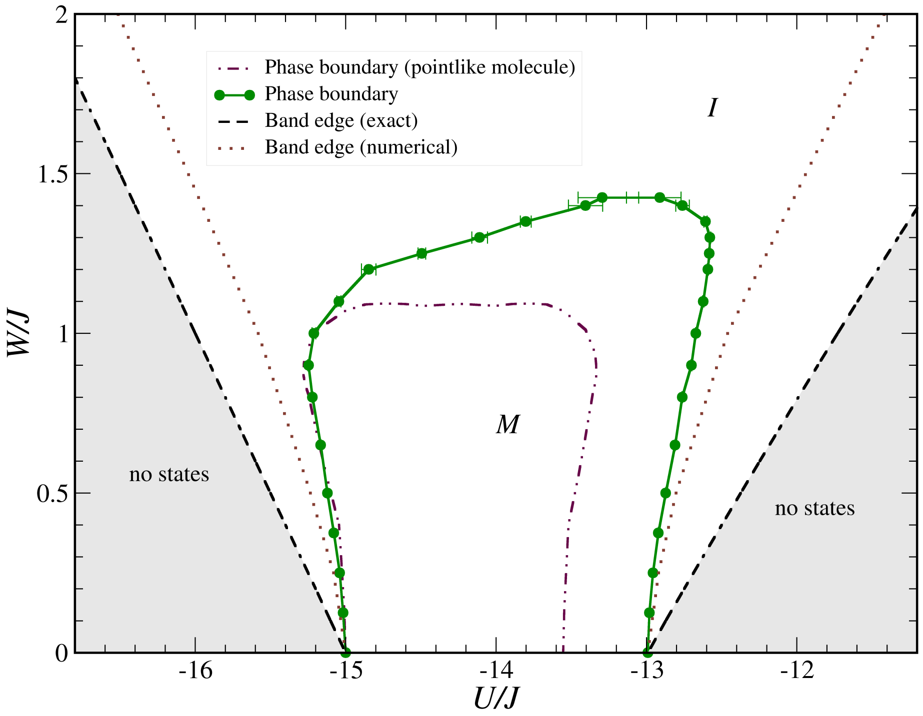

FIGURE 3.21 – Phase boundary between localized and extended states in the (U, W) plane, evaluated at $E = -15J$ (green solid curve) in the low-disorder region, where $E \sim U$ and the molecular states are involved. The numerically obtained band edge is also represented (dotted curve), together with the one extracted by resorting to the analysis of the translationally-invariant lattice (in Eq. (3.31) on the right side and $W = E - U$ with $W \leq 3J$ on the left side), portrayed by the long-dashed curves. Edited, from Ref. [176].

of the extremes of the interval of λ. Nevertheless, at vanishing interaction, the numerical band edge shown in Fig.3.18 lies in very appreciable agreement with the one found for the one-particle problem with energy $\varepsilon = -E/2$ applying the coherent-potential approximation, detailed in Sec. 2.2.1. Denoting the latter value of the band edge as $W_{\rm sp}^{\rm be} \approx 8.91J$, for higher disorder values we also find that the denisty of states expressed in terms of the disorder strength as $\tilde{\rho}_K(U) = \overline{\rho_{\rm K}}(\lambda)\lambda^2$ becomes nonzero in the noninteracting limit, $\tilde{\rho}_K(0) \neq 0$: it is therefore a specific feature of the scattering nature of the states of the pair.

To the end of determining the position of the exact band edge, depicted by the dashed curves in Fig.s 3.18 and 3.21, we resorted to the ordered lattice model (Eq. (3.1) with $W = 0$), writing a two-particle eigenfunction of the complete system as $\Psi(\boldsymbol{n}, \boldsymbol{n}) = {\rm e}^{{\rm i}\boldsymbol{q}\cdot\boldsymbol{n}a}\psi_{\boldsymbol{q}}(\boldsymbol{0})$, thus separating the center-of-mass coordinate from the relative coordinates [177]. Plugging this ansatz in the eigenvalue equation for K (Eq. (3.3)) whose matrix elements are given by Eq. (3.4) and using the one-particle eigenbasis $\{\phi_{\boldsymbol{k}}\}$, in Eq. (1.11), with the eigenvalues in Eq. (1.12), we found the relation:

$$\frac{1}{U} = \frac{1}{N_s}\sum_{\boldsymbol{k}} \frac{1}{E - \varepsilon_{\boldsymbol{k}} - \varepsilon_{\boldsymbol{q}-\boldsymbol{k}}}\,, \tag{3.30}$$

where N_s is the number of lattice sites. For a fixed energy $E = -15J$, and considering now a lattice potential with constant value $W/2$, the lowest value of U is determined by solving Eq. (3.30) with $\boldsymbol{q} = (\pi, \pi, \pi)^T a^{-1}$ and replacing E zith $E - W$ at the denominator in its right-hand side. This gives the relation $W = E - U$, which is plotted as the long-dashed line on the bottom-left part of Fig.s 3.18 and 3.21 in the disorder range $0 \leq W \leq 3J$. In the ordered system, $W = 3J$ represents indeed the lower limit at which the interval of available values of U is unlimited, as it can be deduced by Eq. (3.30), reminding that $\varepsilon_k = -2J \sum\limits_{s=1}^{3} \cos k_s a$. When the lattice potential amounts to $W/2$ on each site (the highest possible value according the distribution in Eq. (1.10)), at $E = -15J$, the highest value of U below which states do not exist is obtained by setting $\boldsymbol{q} = \mathbf{0}$ in Eq. (3.30). Under the latter condition, in the limit of infinite-sized lattices, Eq. (3.30) can be rewritten as:

$$\frac{1}{U} = \iiint\limits_{-\pi/a}^{\pi/a} \frac{\mathrm{d}^3 \boldsymbol{k}}{(2\pi)^3} \frac{1}{E + 4J\sum_{s=1}^{3} \cos k_s a} \, . \tag{3.31}$$

Recalling the parity of the cosine, the latter equation can be reexpressed by making use of Bessel's integrals of the first kind:

$$\frac{1}{U} = \iiint\limits_{-\pi/a}^{\pi/a} \frac{\mathrm{d}^3 \boldsymbol{k}}{(2\pi)^3} \int_0^{+\infty} \mathrm{d}t \, \mathrm{e}^{E + 4J\sum_{s=1}^{3} \cos k_s a} = \int_0^{+\infty} \mathrm{d}t \, \mathrm{e}^{Et} I_0(4Jt) := h(E) \quad . \tag{3.32}$$

Replacing again E with $E + W$ in Eq. (3.32) in order to account for the potential and performing the integration for different values of $W \geq 0$, one obtains $h(E + W)$, whose reciprocal is plotted in the phase diagrams above mentioned as the long-dashed curve appearing in their bottom-right part.

Moreover, from the exact band edge it is possible to estimate the effective tunneling rate, through $12J_{\text{eff}} = 1/h(E) - E$, and then the bandwidth, getting $2.01J$, a result in optimal agreement with the one obtained by including fifth-order terms in the approximation of the effective kernel K. The exact and the numerical band edges converge in the absence of disorder, whereas when $W \neq 0$ they stray abruptly and the numerical one follows closely the phase boundary as in Fig. 1.8 in $0 \leq W \leq 0.5J$. Interestingly, the states close to the right band edge have smaller binding energy as compared to the rest of the band of molecular states.

For higher two-particle energy E, the scenario changes significantly and, in particular, the metallic regions in the parameters space can merge. This is the situation we gather at $E = -12.25J$, whose phase diagram is portrayed in Panel a of Fig. 3.22. Here, the upper phase boundary preserves its symmetry under parity of U, and slightly shifts towards higher disorder, reaching $W_{c,\max} = (24.97 \pm 0.05)J$. The minimum, touched at zero interaction, is located at $W_c = (15.91 \pm 0.03)J$, a value consistent with the estimate of Bulka et Al. [79], visible again in Fig. 1.8. At the same time, the lower phase boundary, separating extended scattering states from localized, ones moves towards lower disorder values, eventually merging with the one of molecular states. The unbinding of molecular states and

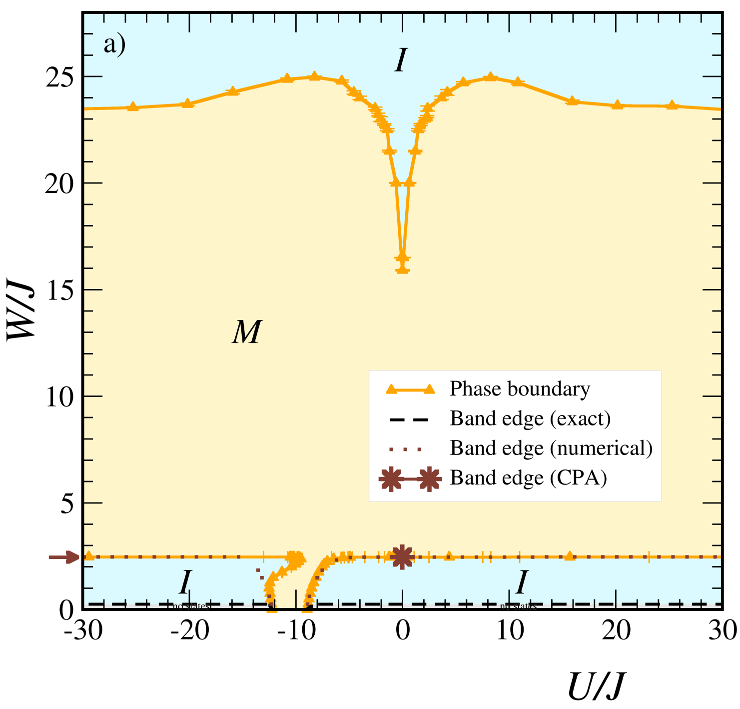

FIGURE 3.22 – In Panel a the phase boundary between localized and extended states is plotted in the (U, W) plane, evaluated at $E = -12.25J$ and expressed in units of the tunneling amplitude. The change in the topology of the metallic region with respect to the case shown in Fig. 3.18 is highlighted by the slight shades in the regions of extended and localized states. Panel b displays a zoom of the phase diagram in the low-disorder regime, where the region of extended scattering states merges with the one of delocalized molecular states. Edited, from Ref. [176].

the subsequent delocalization of scattering states occur almost simultaneously at $W = 2.465J$. The area in which molecular states are extended gets wider, since, at decreasing $|E|$, hopping between nearest-neighbour sites becomes more effective and higher-order corrections of the effective disorder parameter $W_{\text{eff}} = 2W$ in Eq. (3.27b) begin to be increasingly relevant.

Besides the full kernel is needed to explain the breaking of the pair into scattering states and their subsequent delocalization. The scenario changes in the opposite direction, when the phase diagram at $E = -18J$ is analysed, thus considering an higher $|E|$ compared to the case in which $E = -15J$. In this situation, represented in Panel a of Fig. 3.23, the asymmetry under the inversion of $\text{sgn}\,(U/J)$ gets more marked, and indeed $W^R_{c,\text{max}} = (22.1 \pm 0.1)J$ and $W^L_{c,\text{max}} = (22.7 \pm 0.2)J$, where R (resp. L) label the quantity at positive (resp. negative) interaction strength. This mirrors the fact that the disorder-averaged density of states possesses a less prominent peak at positive λ, as it can be noticed from Panel b of Fig. 3.24. Besides, at low interactions there are no extended states, so the two metallic region at postive and negative interactions are separated, coherently with the one-particle phase diagram, in which a $\varepsilon_c = E/2 = 9J$ the behaviour is insulating for any W. In the area in which molecular states are involved, the extended part appears to shrink although more symmetric with respect to $U = E^3/(E^2 + 12J^2)$, therefore pointing out that the pointlike model (in Eq. (3.25)) becomes more representative of the dynamics of the system, as pointed by Panel b of Fig. 3.23.

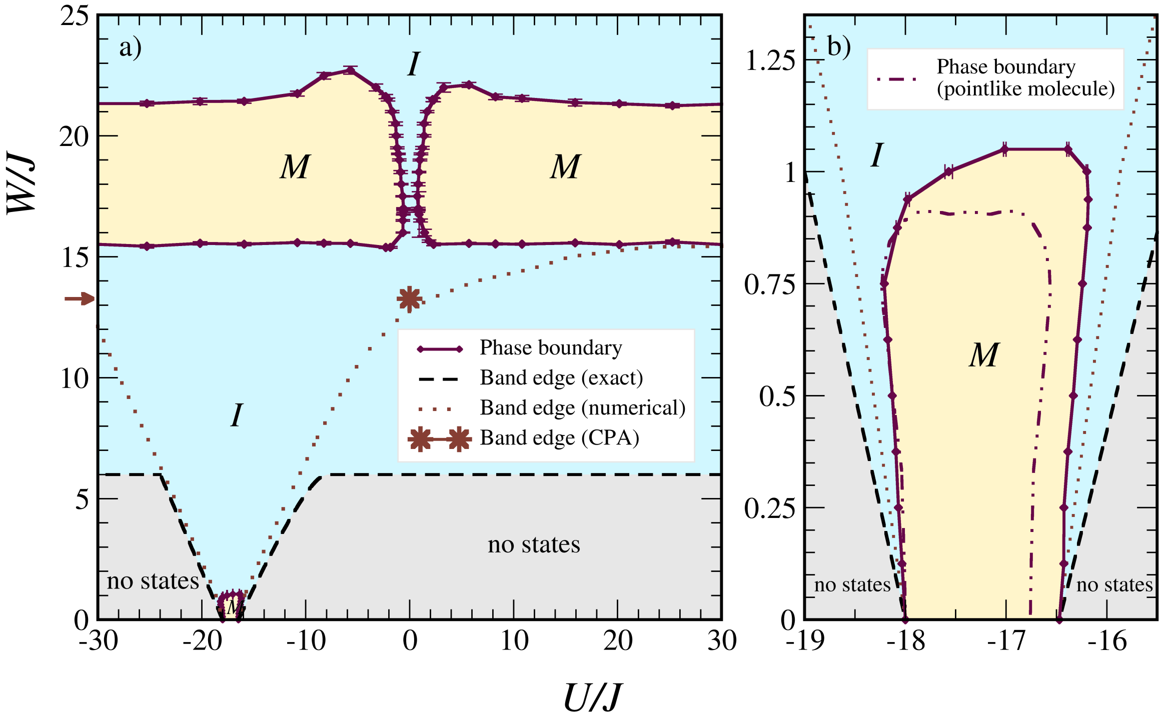

FIGURE 3.23 – In Panel a the phase boundary between localized and extended states is plotted in the (U, W) plane, evaluated at $E = -18J$ and expressed in units of the tunneling amplitude. The phase boundary obtained within the pointlike approximation, represented by the doubly dot-dashed curve, is also portrayed, highlighting a better agrrement with respect to the case of $E = -15J$, in Fig. 3.21. Edited, from Ref. [176].

This behaviour can be also observed in the density of states $\overline{\rho_{\mathrm{K}}}$, which is significant in a more restricted interval of λ and thus, to a lesser extent, of interaction strength. Thanks to the mitigation of hopping (in Eq. (3.27a)), a lowering of the maximum critical value of W is detected at $W \approx J$, in accordance with Eq. (3.28). While comparing the Panels a of Fig.s 3.22 and 3.23, we notice that the closeness of the numerical band edge and the CPA at $U = 0$ is lower when $E = -18J$, due to more marked finite-size effects: in the latter case $W^{\mathrm{be}}(U \equiv 0) \approx 12.79J$, whereas $W^{\mathrm{be}}_{\mathrm{sp}}(\varepsilon = -E/2) \approx 13.26J$.

We finally assessed the agreement between the numerical phase boundaries in the limit of vanishing interactions and the one-particle phase diagram reported in Ref. [79]. In order to do this, we plotted the phase boundary of the latter diagram in the energy-disorder plane, showing also the errorbars. Moreover, for a more direct comparison, we evaluated the critical disorder and the exact and numerical phase boundaries at the total energy $E = 2\varepsilon$ of the pair. For this reason, the exact band edges appearing in [79] at $W_j = - \mp 2\varepsilon - 12J$, where $j = L, R$ indicates the left and the right edges respectively, become $W_j = - \mp E - 12J$ in Fig. 3.25. Accordingly, the numerical band edge at $W = W*$, corresponding to the crossing from molecular to scattering states, is fixed by the condition $E = \pm 2\varepsilon_{\mathrm{be}}(W^*)$, yielding $\varepsilon = \varepsilon_{\mathrm{be}}(W^*)$, as expected. As guides to the eyes we plotted also the dot-dashed lines corresponding to the total energy at which we built the previously shown

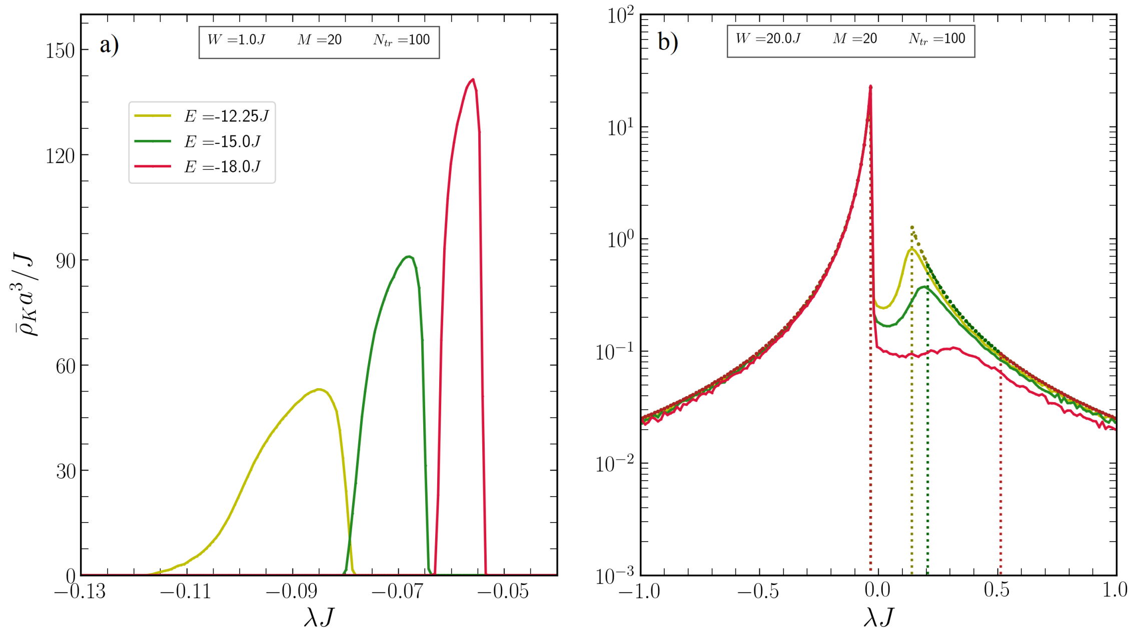

FIGURE 3.24 – The averaged density of states $\overline{\rho_{\mathrm{K}}}$ (Eq. (3.15)) at $E = \{-12.25, -15, -18\}$, evaluated at $W = 1J$ (Panel *a*) and at $W = 20J$ (Panel *b*), and plotted as a function of $\lambda := J/U$. The solid curves are obtained after averaging over $N_{tr} = 100$ realizations of the random potentials. In the figure on the right, the dotted lines represent the density of states in the limit $W \gg J$ (Eq. (3.18)), where the quantity in ordinate vanishes when $(E - W)^{-1} \leq \lambda \leq (E + W)^{-1}$. Edited, from Ref. [176].

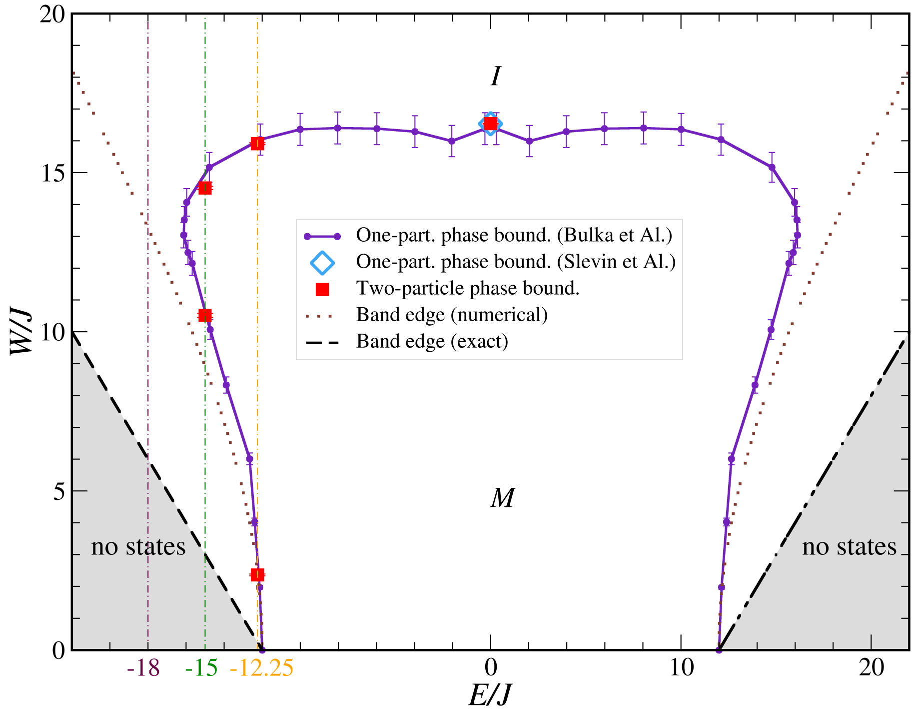

FIGURE 3.25 – Comparison between the single-particle and the two-body mobility edges for vanishing interactions.The red squares denote the two-body data calculated for zero total energy, $E = -12.25J$ (light-orange dashed line) and $E = -15J$ (green dashed line). For $E = -18J$ no critical point is found. The result obtained for $E = 0$ by Slevin and Ohtsuki in [76] is also shown by the light blue diamond. The violet line corresponds instead to the numerical data from Ref. [79], upon the change of variable $E = 2\varepsilon$. As in the previous phase diagrams, the dotted and the long-dashed lines represent the numerical and the exact band edges respectively. Edited, from Ref. [176].

two-particle phase diagrams. While noticing that at $E = -18J$ no transitions are detected at $U \to 0$, we observe that our numerical results for the two-particle mobility edge are fully consistent (within the numerical accuracy) with the single-particle counterpart.

3.6 Conclusions and perspectives

In this chapter we have presented our main results on the combined effects of disorder and interaction based on a thorough analysis of the two-particle problem.

For two-dimensional systems, we showed that previous reports [151] [153] of interaction-induced Anderson transitions in two dimensions were actually plagued by finite-size effects. This is in agreement with the general rule that 2D Anderson transitions are forbidden in the orthogonal universality class.

In three-dimensional systems we showed that, for zero total energy of the pair, the metal-insulator transitions takes place in a region of disorder strength, where all single-particle states are localized. We noticed that finite-size effects are much stronger than what observed in the single-particle case, although both transitions belong to the same universality class. In particular, the inclusion of the first irrelevant variable in the finite-size scaling ansatz has been crucial to pinpoint the correct position of the mobility edge. We found that, while interactions favour the delocalization of scattering states, the effect is the opposite for tightly-bound states. This feature gives rise to a very rich phase diagram, like in the $E = U$ Hubbard subband, where the phase boundary exhibits a doubly reentrant (S-like) behaviour. To better understand our results, we performed a thorough analysis of the effective density of states.

Our results provide a firm ground for further studies of the interplay of disorder and interactions in quantum many-body systems. Our approach can be applied to a variety of two-particle systems, including Cooper pairs in strongly-disordered superconductors [178] and electron-hole bound states (excitons) in semiconductors.

CHAPTER 4

2D ANDERSON TRANSITION IN SPIN-ORBIT COUPLED GASES

So far we have considered models where the spin degree of freedom plays no role. In this chapter we will focus instead on a system where spin-rotational symmetry is broken by spin-orbit interactions, coupling the spin with the momentum of the particle. In particular the former quantity rotates during the motion, resulting in destructive interference between the direct and the time-reversed paths, thus weakening localization.

This phenomenon, known as weak anti-localization, is well predicted by the Scaling Theory: the beta function can become positive as in 3D systems. For sufficiently strong spin-orbit coupling, an Anderson transition appears even in two dimensions. This picture has been fully confirmed by ensuing numerical works, where mobility edges in $d = 2$ have indeed been reported together with estimates [179–184]. Weak anti-localization has been experimentally detected in 2D electrong gases in semiconductor quantum wells [185] and at a surface of topological insulators [186].

More recently, artificial spin-orbit coupling for cold atoms has been reported in experiments [187][188]. The simplest source of disorder in cold-atom systems is provided by laser speckles, which can be obtained by shining a laser through a diffusive plate [189], resulting in a spatially correlated random potential.

In this chapter we address the localization properties of a single atom subject to the combined action of the spin-orbit interaction and the disordered potential. After introducing the speckle potential, we show how to generate it numerically. We further show how to numerically implement a disordered potential with given on-site distribution and correlation function, with emphasis on Gaussian-like functions. Next we briefly outline the origin of optically-induced spin-orbit interactions in ultracold atoms, comprising linear Rashba [190] and Dresselhaus terms. We then illustrate a modified transfer-matrix algorithm resulting from a fourth-order discretization of the continuum Hamiltonian.

We show that the linear regime is not a specific property of the speckle potential, but appears also for other kinds of disorder sources. In the wake of a previous work [191] pointing out the existence of a new regime, where the mobility edge E_c varies linearly with the disorder strength, we also show

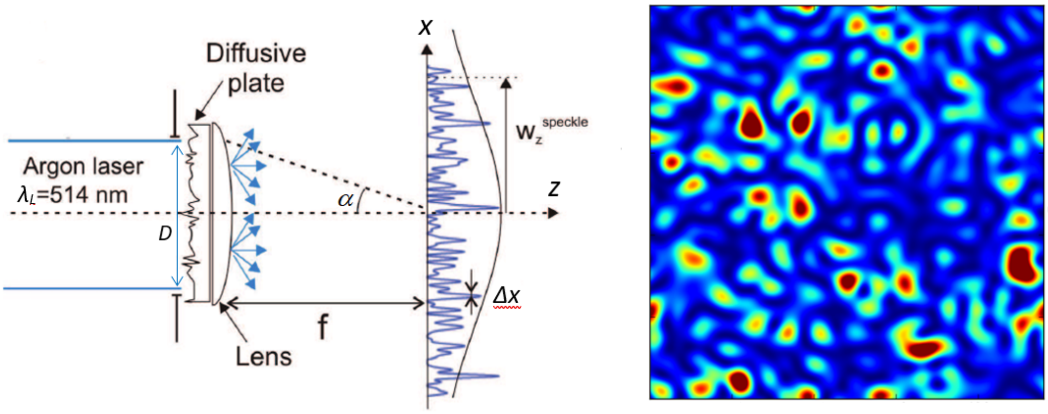

FIGURE 4.1 – An example of speckle potential in $d = 2$, shown on the right. On the left an experimental setup fo its generation is sketched: the speckle pattern is produced by shining a laser beam with wavelength λ_L and width D on a ground glass plate forming an angle α seen from the focal plane at distance f from a lens, placed in front of the diffusive medium. Edited, from Ref. [194].

how the slope and the intercept of E_c behave near the persistent spin-helix symmetry point [192], where the Rashba and Dresselhaus constants have equal magnitude and the $SU(2)$ symmetry of the Hamiltonian is restored.

4.1 Spatially correlated random potentials

In the previous chapters we have dealt with uncorrelated disorder, as proposed in the original Anderson's model. The presence of finite-range correlations can give rise to variations in the position of the critical energy in $d = 3$ [193], as mentioned in Sec. 1.3, but, as proved by recent numerical studies, do not affect the universality class of the transitions in $d = 3$ [193] and $d = 2$ [191].

In the presence of an electric field oscillating with a frequency ω far detuned from the atomic transition frequencies, the dipole moment of the particle can be written as the product of the polarizability constant and the eternal field. Depicting the atom as a two-level system, having an excited state with low decay frequency Γ, the interaction energy can be written as:

$$V(\boldsymbol{r}) = \frac{3\pi\varepsilon_0 c^3\Gamma}{\omega_A^3(\omega - \omega_A)}|\mathcal{E}(\boldsymbol{r})|^2 := K|\mathcal{E}(\boldsymbol{r})|^2 \tag{4.1}$$

where ω_A denotes the atomic transition frequency and $\mathcal{E}(\boldsymbol{r})$ the complex amplitude of the electric field. When the latter comes from monochromatic light scattered at a rough surface (in the scale of the optical wavelength), it can be expressed, according to Huygens' principle, as a linear superposition of amplitudes coming from uncorrelated scatterers. Owing to the irregularity of the medium, the phases arising from different regions can be treated as random variables, which contribute to an electrical field amplitude that, in the presence of a large number of scatterers, has normally distributed real and imaginary parts,

$$P(\mathrm{Re}\{\mathcal{E}\},\mathrm{Im}\{\mathcal{E}\}) = \frac{1}{2\pi\sigma_\epsilon}\mathrm{e}^{-|\mathcal{E}|^2/2\sigma_\epsilon^2}\ , \tag{4.2}$$

Making use of the relation in Eq. (4.1), in which the sign of the potential is essentially given by the one of the frequency detuning, the probability density function in Eq. (4.2) can be rewritten as a function of the potential V and the phase $\phi := \arctan\left[\mathrm{Im}\{\mathcal{E}\}/\mathrm{Re}\{\mathcal{E}\}\right]$. Performing the substitution and integrating over the latter variable, one gets the Rayleigh law:

$$\tilde{P}(V) = \frac{\Theta(VV_0)}{V_0}\exp\left(-\frac{V}{V_0}\right)$$

where $V_0 = 2\sigma_\epsilon^2 K$ is a constant that coincides with the mean value of V. A positive value of V_0 indicates blue-detuned laser speckles, whereas a negative one signals red-detuned speckles. In the following we shall focus on blue-detuned speckles, as employed in recent experiments [56] [57] [58], shifting also the potential by its mean value $V \mapsto V - V_0$, so that its distribution $\tilde{P}$ becomes the following:

$$P_{\mathrm{Speckle}}(V) = \frac{\Theta(V+V_0)}{V_0}\exp\left(-\frac{V+V_0}{V_0}\right)\ , \tag{4.3}$$

whose variance satisfies $\overline{V^2} = V_0^2$. The electric field amplitude on a plane far apart from the diffusive plate can be expressed in terms of the one measured just after the aperture, denoted as $\epsilon(\boldsymbol{r})$ as follows:

$$\mathcal{E}(\boldsymbol{r}) = \int \mathrm{d}\boldsymbol{r}'\varepsilon(\boldsymbol{r}')h(\boldsymbol{r}-\boldsymbol{r}')\ , \tag{4.4}$$

where $h(\boldsymbol{r})$ represents the point spread function, dependent on the geometry of the diffusor. From the latter relation, the spatial correlation $C(\boldsymbol{r})$ can be written as:

$$C(\boldsymbol{r}) := \overline{V(\mathbf{0})V(\boldsymbol{r})} = V_0^2\left|\frac{\overline{\mathcal{E}(\boldsymbol{r})\mathcal{E}^*(\mathbf{0})}}{\overline{|\mathcal{E}(\boldsymbol{r})|^2}}\right|^2 = V_0^2\left|\frac{h(\boldsymbol{r})}{h(\mathbf{0})}\right|^2\ .$$

For a circular aperture, the Fourier transform of the point spread function corresponds to an Airy disk, $\widetilde{h}(\boldsymbol{k}) = \Theta(k_0 - |\boldsymbol{k}|)$ [195], where $k_0 = \alpha k_L$, α being the aperture angle and k_L the wave vector of the laser beam, as shown in Fig. 4.1. Switching to the space of coordinates, by using $\int_0^{2\pi}\mathrm{d}\theta e^{-ikr\cos\theta} = 2\pi J_0(kr)$ and $\int_0^{k_0}\mathrm{d}kJ_0(kr)k = J_1(k_0r)k_0/r$, $J_n(x)$ being the Bessel function of order n, we get

$$C(\boldsymbol{r}) = V_0^2\frac{4J_1^2(r/\sigma)}{(r/\sigma)^2}\ , \tag{4.5}$$

where $\sigma = 1/k_0 = 1/(\alpha k_L)$ is the speckle correlation length [196], which depends on the distance f between the diffuser and the plane placed far apart through $\alpha = D/2f$, where D corresponds to the diameter of the plate, as displayed in Fig. 4.1.

In the subsequent computations we will express all energies in units of the correlation energy $E_\sigma =$

$\hbar^2/(2m\sigma^2)$, and we will consider random potential amplitudes V_0 of nearly the same order of that energy, so that the De Broglie wavelength λ_{dB} of the particle is roughly comparable to the correlation length [193]. In the limit in which the latter quantity is much smaller than λ_{dB}, the speckle potential is seen instead as essentially uncorrelated.

4.1.1 Numerical generation of the random potentials

To the purpose of understanding how a change in the features of a random potential affects the occurrence of Anderson transitions, we consider two different potentials: the one generating the speckle pattern, with distribution in Eq. (4.3) with correlation given by Eq. (4.5), and a normally-distributed one, with Gaussian correlation. Their on-site probability distributions and correlations are plotted in Fig. 4.2.

a) Speckle potential

Unlike in the previously analyzed systems, in this case the random potentials are correlated and their numerical generation is not straightforward. In order to reproduce the speckle potential, of the form illustrated in Sec. 4.1 with a correlation given by Eq. (4.5), we first generated the normalized electric field amplitudes $\epsilon(\boldsymbol{i})$ where $\boldsymbol{i} := (i_x, i_y)$ denotes the position within the lattice, in units of the lattice spacing Δ. The real and the imaginary part of $\epsilon(\boldsymbol{i})$ are normally distributed random variables, with zero mean and unit variance. To lend a Besselian correlation, as in Eq. (4.5), to the random variables, the convolution between the latter amplitude and the point spread function is performed in momentum space. Defining $g(\boldsymbol{i}) := \sum_{\boldsymbol{j}} h(\boldsymbol{i}-\boldsymbol{j})\epsilon(\boldsymbol{j})$, that quantity in Fourier space becomes:

$$\tilde{g}(\boldsymbol{k}) = \tilde{\epsilon}(\boldsymbol{k})\tilde{h}(\boldsymbol{k}) = \tilde{\epsilon}(\boldsymbol{k})\Theta(\sigma^{-1} - |\boldsymbol{k}|) ,$$

since the Fourier transform of the point spread function is an Airy disk. From $g(\boldsymbol{i})$, its square modulus $f(\boldsymbol{i}) := |g(\boldsymbol{i})|^2$ has been computed, together with its spatial average f_{avg}, thus finding a potential which takes values from the probability distribution in Eq. (4.3):

$$V_{\mathrm{Speckle}}(\boldsymbol{i}) = V_0 \left[\frac{f(\boldsymbol{i})}{f_{\mathrm{avg}}} - 1 \right] .$$

b) Gaussian potential

The Gaussian potential follows an on-site probability distribution function given by:

$$P(V) = \frac{1}{\sqrt{2\pi}V_0} \mathrm{e}^{-\frac{V^2}{2V_0^2}} , \tag{4.6}$$

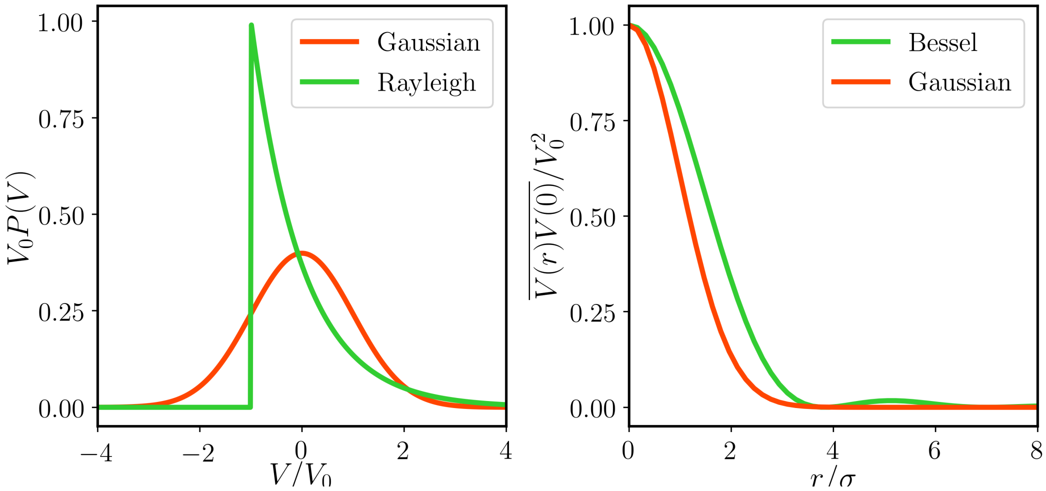

FIGURE 4.2 – In the left panel the probability distribution functions of the two disordered potentials studied are represented in units of V_0^{-1}. In the right panel the autocorrelation function is portrayed in units of V_0^2 as a function of the distance r/σ in units of the correlation length.

where V_0 represents its standard deviation. The autocorrelation function has also a Gaussian profile, with a correlation length σ corresponding to one standard deviation:

$$C(\boldsymbol{r}) = V_0^2 \mathrm{e}^{-\frac{r^2}{2\sigma^2}} \, . \tag{4.7}$$

The spatial behaviour of this potential is compared to the one of the speckle potential (Eq. (4.3)) in Fig. 4.3, where also the respective correlation functions are plotted. Besides, the constant V_0 has the same meaning in the two spatial distributions and corresponds to the square root of their respective variances. For achieving the Gaussian potential, like the ones used in [197] and [193], we began by generating a real random variable following the normal distribution, $s(\boldsymbol{k})$, and then, in momentum space, we impressed a Gaussian correlation on it by carrying out the following convolution:

$$\tilde{u}(\boldsymbol{k}) := \tilde{s}(\boldsymbol{k}) \sqrt{\frac{2}{\pi}} \mathrm{e}^{-\frac{\boldsymbol{k}^2\sigma^2}{2}} \, ,$$

as the Fourier transform of the normal distribution is also a Gaussian. Afterwards, in coordinate space, the random potential is evaluated as:

$$V_{Gauss}(\boldsymbol{i}) = V_0 \frac{\mathrm{Re}\left[u(\boldsymbol{i})\right]}{MN} \, .$$

Considering a square grid of $M = 5\,000 \equiv N$ sites per side, we have tested the behaviour of the potential and the correlation function in the two cases above presented, and the latter quantity has been plotted against the exact function in Fig. 4.3. The result obtained by averaging over $N_{tr} = 112$

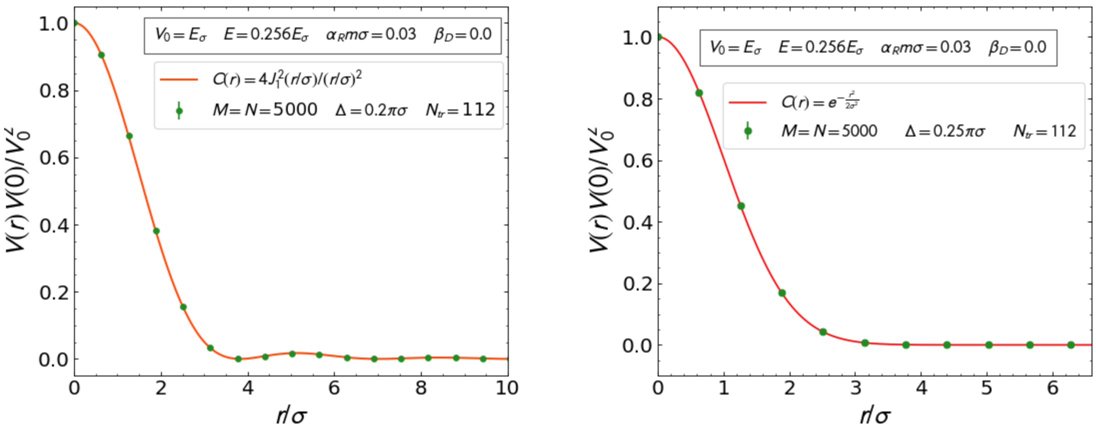

(A) Bessel correlation

(B) Gaussian correlation

FIGURE 4.3 – Spatial correlations of the random potentials, following the Rayleigh (A) and the Gaussian (B) probability distributions, plotted as a function of the distance plotted as a function of the distance in units of the correlation length σ. The data have been obtained from square lattices with $M \equiv N = 5000$ sites per side and $\Delta = 0.2\pi\sigma$ (A) and $\Delta = 0.25\pi\sigma$ (B), setting the same parameters of the Hamiltonian. The results are in excellent agreement with the analytical formulae in Eqs. (4.5) (A) and (4.7) (B), represented by the orange/red solid curves.

realizations of the random potential agrees very well with the exact curve. In particular, in the left panel of that figure, there are 6 sampling points between the origin, $r = 0$, and the first zero of the correlation function, which occurs at $r/\sigma = 3.83171$.

4.2 Synthetic Spin-orbit couplings

As announced in the introduction, spin-orbit coupling in cold-atom systems mimics the one present in certain materials. For example, in a lattice lacking mirror symmetry along the z axis, there can be a static electric field $\boldsymbol{E} = E_0 \hat{e}_z$, an electron moving with momentum $\hbar\boldsymbol{k}$ feels a magnetic field due to relativistic corrections of $\boldsymbol{B}_{\mathrm{SO}} = \frac{\hbar E_0}{m_e c^2}(k_x \hat{e}_y - k_y \hat{e}_x)$. The magnetic field then acts on the magnetic dipole moment of the particle $\boldsymbol{\mu} = -\frac{ge\hbar}{4m_e}\boldsymbol{\sigma}$ as $-\boldsymbol{\mu} \cdot \boldsymbol{B}_{\mathrm{SO}}$, thus originating the following interaction term in the total Hamiltonian:

$$H_R = \frac{ge\hbar^2 E_0}{4m_e^2 c^2}(k_x \sigma_y - k_y \sigma_x) := \alpha_R (k_x \sigma_y - k_y \sigma_x) \, , \tag{4.8}$$

where g is the dimensionless magnetic moment, α_R denotes Rashba constant and σ_i with $i = x, y$ refer to two Pauli matrices. This linear spin-orbit coupling term (Eq. (4.8)) is known as the Rashba contribution [190], and arises in semiconductor heterostructures [192] which exhibit symmetry under operations from the C_{4v} point group, representing the one of the symmetries of a square. The Dresselhaus term comes instead from a lack of inversion symmetry of the material, and its particular form depend on the symmetry of the material and contains odd powers of the particle momentum [198].

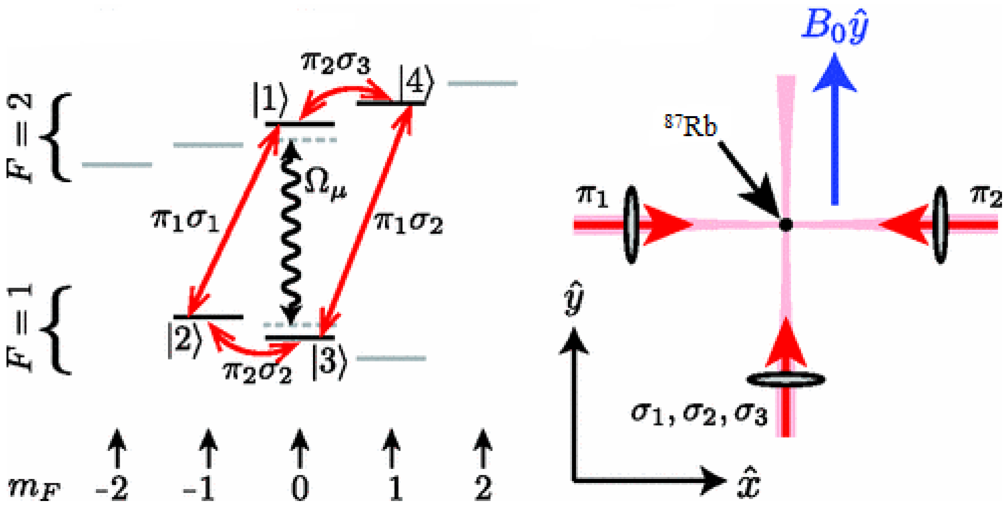

FIGURE 4.4 – An example of the generation of an artificial spin-orbit coupling with cold neutral atoms: a four-level ring coupling scheme with ^{87}Rb atoms, involving hyperfine states $|F, m_F\rangle$ Raman-coupled by five lasers, marked as σ_i with $i = 1, 2, 3$ and π_j with $j = 1, 2$, the formers three being circularly polarized and the latters being linearly polarized. In the panel on the left, each red curve represents a two-photon Raman transition, with polarizations denoted by the field symbols. The ring states are mapped into physical states according to $|1\rangle \equiv |2, 0\rangle$, $|2\rangle \equiv |1, -1\rangle$, $|3\rangle \equiv |1, 0\rangle$ and $|4\rangle \equiv |2, 1\rangle$. A microwave field with coupling frquency Ω_μ shifts the internal states $|1, 0\rangle$ and $|2, 0\rangle$. In the panel on the right, a constant magnetic field is displayed, as well as the arrangement of the lasers and the atomic sample. From Ref. [199].

We adopt the term which proceeds from invariance under operation from the dihedral group D_{2d}:

$$H_D = \beta_D(k_x\sigma_y + k_y\sigma_x) \; , \tag{4.9}$$

where β_D is the Dresselhaus constant, whose form is determined using perturbation theory and the Kane model for semiconductors.

The interaction terms just presented in Eq.s (4.8) and (4.9) can be engineered in gases of cold atoms, as previously disclosed. This can be realized by coupling selected internal atomic states with counterpropagating laser fields, which link atomic motion in the plane (x, y) to the particle's spin, creating the characteristic spin-orbit coupled energy-momentum dispersion relations [192] [199]. The system which allows to obtain this effect is shown in Fig. 4.4, displaying the configuration proposed by Campbell et Al. [199]. In particular the Rashba and Dresselhaus constants depend on the lasers' wave-number k_L and the light-matter coupling strength Ω [199] as:

$$\alpha_R = \frac{\hbar^2 k_L}{2m_A} \qquad\qquad \beta_D = \frac{\hbar^2 \delta k_L}{2\sqrt{2}m_A\Omega} \; ,$$

where $\delta := \omega_A - \omega_L$ denotes the detuning between the atomic and the light frequency. Object of our investigation is a single atom of mass m and spin $s = 1/2$ subject to a linear spin-orbit coupling, whose Hamiltonian can be written in the following form:

$$H = \left[\frac{\hbar^2(k_x^2 + k_y^2)}{2m} + V(\boldsymbol{r})\right]\mathbb{1}_2 + \alpha_R(k_y\sigma_x - k_x\sigma_y) + \beta_D(k_y\sigma_x + k_x\sigma_y)\ . \tag{4.10}$$

The continuous random potential is represented by $V(\boldsymbol{r})$, which is now endowed with spatial correlation $C(\boldsymbol{r})$, as illustrated in Sec. 4.1. The absence of that potential yields split energy bands, whose dispersion is given by:

$$E_{\boldsymbol{k}} = \frac{\hbar^2 k^2}{2m} \pm \sqrt{(\alpha_R + \beta_D)^2 k^2 - 4\alpha_R\beta_D k_x^2}\,, \tag{4.11}$$

where $k := |\boldsymbol{k}|$. The previous relation, Eq. (4.11), in the case of pure Rashba or Dresselhaus coupling, simplifies to $E_k = \frac{\hbar^2 k^2}{2m} \pm \eta k$, where $\eta = \alpha_R, \beta_D$. Under this condition, the ground-state occurs at $k = m\eta$, where the energy reads:

$$E_{m\eta} = -\frac{m\eta^2}{2}\ . \tag{4.12}$$

4.3 Identification of the critical point

In order to sudy the behaviour of wavefunctions inside the disordered lattice, we made use of the transfer-matrix method illustrated in Sec. 2.1.1, based on strip-sized lattices with width $M\Delta$ and length $L\Delta$, where $L \gg M$.

The stationary Schrödinger equation $H\Psi = E\Psi$ has thus been discretized on the lattice, by replacing first- and second- order partial derivatives by expressions containing finite differences. Unlike in the original Anderson problem (Eq. (1.9)), owing to the fact that spin-orbit interaction acts differently according to spin orientation, we write a single-atom wavefunction as a two-component spinor $\Psi = \left(\psi_\uparrow \psi_\downarrow\right)^T$ which, in a discretized lattice, is represented by a vector with components labelling the position in the grid $\psi_\beta(\boldsymbol{r} = \Delta i\boldsymbol{e}_x + \Delta j\boldsymbol{e}_y) \mapsto \psi_{i,j,\beta}$, where $\beta =\uparrow,\downarrow$ denotes the spin index.

Differently from the previously mentioned case, the approximation to the second order in Δ, in Eq. (2.2), is no longer sufficient for obtaining converged results for the Lyapunov exponent, so we have to resort to a finer discretization scheme, the fourth-order one, which however requires an higher computational cost.

As pointed out in [191], the former approximation leads to reliable results only when $\Delta \lesssim 0.2\pi\sigma$ at low spin-orbit coupling constant ($m\alpha_R\sigma \sim 10^{-2}$), while the latter scheme yields stable results at $\Delta \lesssim 0.3\pi\sigma$, at fixed $M\Delta$. The advantage of the second method becomes evident at higher couplings: when $m\alpha_R\sigma \sim 1$, the first procedure is not reliable even at $\Delta \approx 0.1\pi\sigma$, while the second one is trustworthy at $\Delta \lesssim 0.15\pi\sigma$. Therefore, we express the first derivative in the latter scheme, which is used thereafter, reads

$$\partial_x\psi_\beta \mapsto \frac{\left(-\psi_{i+2,j,\beta} + \psi_{i-2,j,\beta} + 8\psi_{i+1,j,\beta} - 8\psi_{i-1,j,\beta}\right)}{12\Delta}\,, \tag{4.13}$$

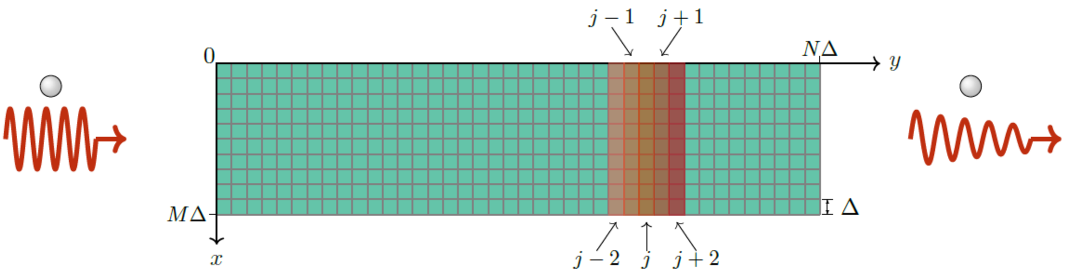

FIGURE 4.5 – A sketch of the lattice with MN sites, at whose ends the transmission amplitude has been calculated through the transfer-matrix method. At each step, the wavefunction has been evaluated using the values obtained in the first four rows behind, highlighted by paler shades of red.

and the second-order spatial derivative becomes in turn:

$$\partial_{xx}\psi_\beta \mapsto \frac{\left(-\psi_{i+2,j,\beta} + \psi_{i-2,j,\beta} + 16\psi_{i+1,j,\beta} + 16\psi_{i-1,j,\beta} - 30\psi_{i,j,\beta}\right)}{12\Delta^2} \; . \tag{4.14}$$

In general, discretization effects become more important as α_R or β_D increase, and the lattice constant must satisfy $\Delta < \min(\sigma, \ell_{\mathrm{SO}})$, where the latter quantity, denoting the spin-precession length, in the case of pure Rashba and Dresselhaus couplings, corresponds to $\pi/(m\eta)$, in which $\eta = \alpha_R, \beta_D$. With the aim of reducing finite-size effects, we imposed periodic boundary conditions for Ψ along the transverse side of the lattice, as previously done in Chaps. 2 and 3. By placing the y axis parallel to the longer side of the bar and discretizing the derivatives as in Eq.s (4.13) and (4.14), we can express the wavefunction at $(i, j+2)\Delta$ in terms of the ones along the lines $y = \{j-2; j-1; j; j+1\}\Delta$ as shown in Fig. 4.5, thus finding one recursive relation for each spin orientation. These equalities correspond to:

$$\begin{aligned}
\psi_{ij+2,\uparrow} = {} & a_2\psi_{i+2j,\uparrow} + a_1\psi_{i+1j,\uparrow} + a_{ij}\psi_{ij,\uparrow} + a_1^*\psi_{i-1j,\uparrow} + a_2^*\psi_{i-2j,\uparrow} + \\
& + b_1\psi_{ij+1,\uparrow} + b_{-1}\psi_{ij-1,\uparrow} + b_{-2}\psi_{ij-2,\uparrow} + \\
& + c_2\psi_{i+2j,\downarrow} + c_1\psi_{i+1j,\downarrow} + c_{ij}\psi_{ij,\downarrow} - c_1^* a_1\psi_{i-1j,\downarrow} - c_2^*\psi_{i-2j,\downarrow} + \\
& + d_1\psi_{ij+1,\downarrow} + d_{-1}\psi_{ij-1,\downarrow} + d_{-2}\psi_{ij-2,\downarrow} \; ,
\end{aligned} \tag{4.15}$$

and

$$\begin{aligned}
\psi_{ij+2,\uparrow} = {} & -c_2^*\psi_{i+2j,\uparrow} - c_1^*\psi_{i+1j,\uparrow} - c_{ij}^*\psi_{ij,\uparrow} - c_1 a_1\psi_{i-1j,\uparrow} - c_2\psi_{i-2j,\uparrow} + \\
& - d_1^*\psi_{ij+1,\uparrow} - d_{-1}^*\psi_{ij-1,\uparrow} - d_{-2}^*\psi_{ij-2,\uparrow} + \\
& + a_2^*\psi_{i+2j,\downarrow} + a_1^*\psi_{i+1j,\downarrow} + a_{ij}\psi_{ij,\downarrow} + a_1\psi_{i-1j,\downarrow} + a_2\psi_{i-2j,\downarrow} + \\
& + b_1\psi_{ij+1,\downarrow} + b_{-1}\psi_{ij-1,\downarrow} + b_{-2}\psi_{ij-2,\downarrow} \; ,
\end{aligned} \tag{4.16}$$

where the coefficients denoted by latin letters depend on the parameters J, K and Γ as well as on the random potential through the relations:

$$\begin{aligned}
a_2 &= \frac{\mathrm{i}\Gamma K - 1}{1+K^2} & a_1 &= \frac{8(2-\mathrm{i}\Gamma K)}{1+K^2} & a_{ij} &= \frac{E - V_{ij} - 60J}{J(1+K^2)} \\
b_1 &= \frac{8(2+K^2)}{1+K^2} & b_{-1} &= \frac{8(2-K^2)}{1+K^2} & b_{-2} &= \frac{K^2-1}{1+K^2} \\
c_2 &= \frac{iK+\Gamma}{1+K^2} & c_1 &= -\frac{8(\Gamma+2\mathrm{i}K)}{1+K^2} & c_{ij} &= -\mathrm{i}K\frac{(E - V_{ij} - 60J)}{J(1+K^2)} \\
d_1 &= -\frac{8\mathrm{i}K}{1+K^2} & d_{-1} &= -\frac{24\mathrm{i}K}{1+K^2} & d_{-2} &= \frac{2\mathrm{i}K}{1+K^2} \, ,
\end{aligned}$$

in which J, K and Γ are defined as the following functions of the parameters of Hamiltonian (Eq. (4.10)):

$$J := \frac{\hbar^2}{24m\Delta^2} \qquad K := \frac{\alpha_R + \beta_D}{12\Delta J} \qquad \Gamma := \frac{\alpha_R - \beta_D}{12\Delta J} \, .$$

Starting from the relations just found, Eq.s (4.15) and (4.16), we thus derive an iterative formula which connects the values of the wave-function in the rows $\{j+2, j+1, j, j-1\}$ to the ones in the rows $\{j+1, j, j-1, j-2\}$. Denoting as $\Psi_j := (\Psi_{1j,\uparrow}, \Psi_{2j,\uparrow}, \ldots, \Psi_{Mj,\uparrow}, \Psi_{1j,\downarrow}, \Psi_{2j,\downarrow}, \ldots, \Psi_{Mj,\downarrow})^T$, the j-th transfer-matrix multiplication step reads:

$$\begin{pmatrix} \boldsymbol{\psi}_{j+2} \\ \boldsymbol{\psi}_{j+1} \\ \boldsymbol{\psi}_{j} \\ \boldsymbol{\psi}_{j-1} \end{pmatrix} = \mathbf{T}_j \begin{pmatrix} \boldsymbol{\psi}_{j+1} \\ \boldsymbol{\psi}_{j} \\ \boldsymbol{\psi}_{j-1} \\ \boldsymbol{\psi}_{j-2} \end{pmatrix} = \mathbf{M}_j \begin{pmatrix} \boldsymbol{\psi}_{2} \\ \boldsymbol{\psi}_{1} \\ \mathbf{0} \\ \mathbf{0} \end{pmatrix} ,$$

where $\mathbf{T}_j$ represents the $8M \times 8M$ transfer-matrix associated to the j-th row, whereas $\mathbf{M}_j = \prod_{k=j}^{1} \mathbf{T}_k$ is its product. From the latter we extract the least Lyapunov exponent by following the procedure illustrated in Sec. 2.1.1, taking care of the loss of orthogonality of its eigenvectors by performing QR reorthogonalizations each $n_I = 10$ iterations of the transfer-matrix product, using now unitary $8M \times 4M$ $\boldsymbol{Q}$ matrices. The least Lyapunov exponent describing the slowest decay rate of an eigenfunction is then averaged over $N_{tr} = 336$ configurations of the random potential, to the end of evaluating the reduced localization length (Eq. (2.10)), expressed as

$$\Lambda_M := \frac{1}{M\Delta\overline{\gamma}} \, ,$$

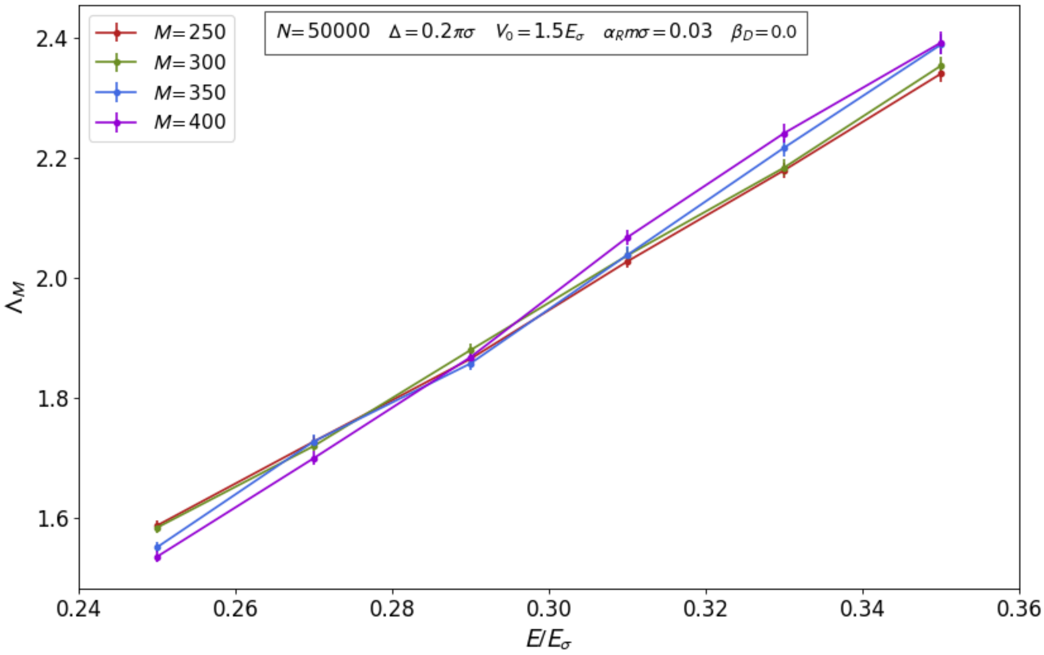

FIGURE 4.6 – The reduced localization as a function of energy in units of the correlation energy $E_\sigma = (m\sigma^2)^{-1}$ in vicinity of the mobility edge. The quantities refer to a speckle potential with Bessel correlation and $V_0 = 1.5E_\sigma$. The lattices are all $N = 50\,000$ sites long and the Lyapunov exponents have been averaged over $N_{tr} = 336$ disorder realizations. Λ_M increases when the system is in the metallic regime, while it decreases in the insulating one, approaching to $\xi M \Delta$ at high system sizes.

and studying its behaviour near the critical point. In the critical region, we expand Λ_M in Taylor series as a function of energy, retaining only the relevant scaling variable, due to the small finite size effects. Within this finite-size scaling framework, the reduced localization length can be expressed as:

$$\Lambda_M^{(\mathrm{FSS})} = f\left[u(\omega)M^{1/\nu}\right] = \sum_{k=0}^{n} a_k \left[u(\omega)M^{1/\nu}\right]^k , \tag{4.17}$$

where $\omega := (E - E_c)/E_c$ and $u(\omega) = \sum_{j=0}^{m} w_j \omega^j$. Similarly to what was done in Sec. b), we set $a_1 = 1$ and $w_0 = 0$. Assuming that the transition belongs to the symplectic universality class, characterized by $\Lambda_{c,\mathrm{symp}} = 1.844 \pm 0.002$ [183] [184] and $\nu_{\mathrm{symp}} = 2.73 \pm 0.02$ (cf. Tab. 1.1), we performed nonlinear least-squares regressions using $m + n$ parameters, where $m = n = 3$, starting from the data $\{(E, \Lambda_M)\}$ found at different M near the critical point. The behaviour of Λ_M in this region is shown in Fig. 4.6, where the random potential in the lattice is the Rayleigh one with Bessel correlation function.

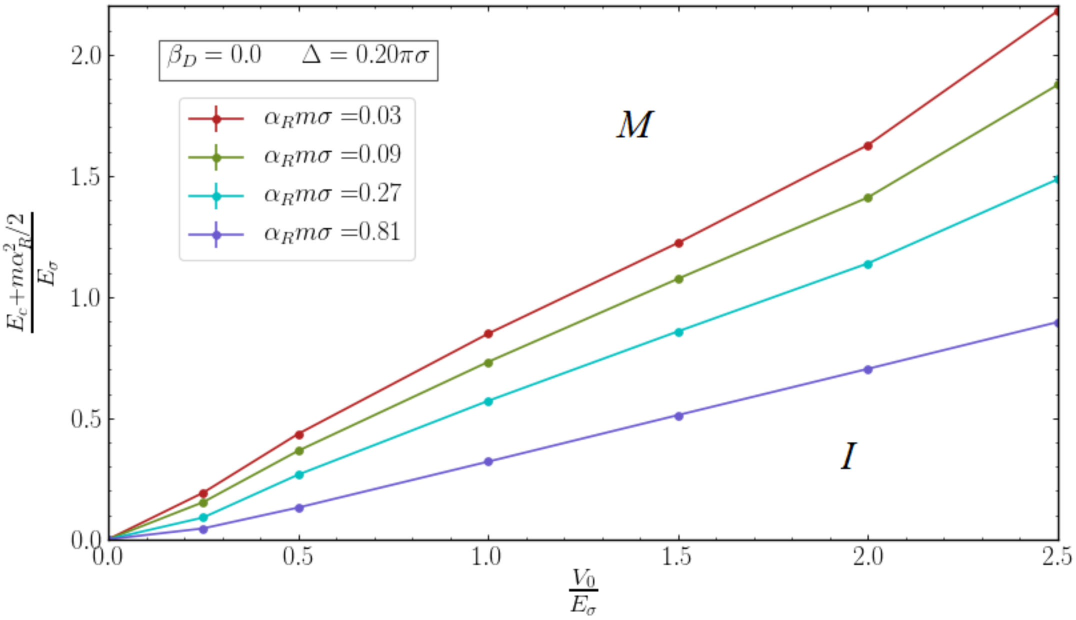

FIGURE 4.7 – Mobility edge E_c of the 2D Anderson transition separating low-energy localized states ($E < E_c$) from high-energy diffusive states ($E > E_c$), plotted as a function of the standard deviation V_0 of the disordered potential following a Gaussian distribution. The phase boundaries are estimated for different values of the Rashba constant, satisfying $0.03 \leq \alpha_R/(m\sigma) \leq 0.81$, keeping $\beta_D = 0$. In the computations, the Lyapunov exponents have been averaged over $56 \leq N_{tr} \leq 336$ disorder configurations, whereas the length of the lattice has been mantained fixed at $50\,000\Delta$, where $\Delta = 0.2\pi\sigma$.

4.4 Phase diagram

After having tested the compatibility of the mobility edges obtained through the method described in the previous paragraph and the values already known in literature [191] for the speckle potential, we will focus our attention on the case in which the potential on the lattice follows the normal distribution (Eq. (4.6)) with Gaussian correlations (Eq. (4.7)). Considering a pure Rashba coupling and adopting a discretization fine enough to ensure convergence of Λ_M, we have estimated the mobility edge starting from lattices with size $M = \{200, 250, 300, 350, 400\}$ at a disorder parameter in the range $[0.25, 2.5]\,E_\sigma$. The procedure, based again on the finite-size scaling in Eq. (4.17), has been carried out for four different values of the Rashba constant, satisfying $0.03 \leq \alpha_R m\sigma \leq 0.25$. At the end of these computations, we have noticed the appearance of a linear behaviour of the position of the mobility edge as a function of V_0 in the interval $0.5E_\sigma \leq V_0 \leq 2.0E_\sigma$, for all the values of the α_R. Nevertheless small deviations from linearity show up for low Rashba coupling strengths. The former feature of the phase boundary, in the case of the speckle potential, has been identified only at low disorder ($V_0 \lesssim 0.5E_\sigma$) at $\alpha_R m\sigma = 0.03$, detecting also negative slopes as soon as $\alpha_R \gtrsim 0.3/(m\sigma)$. Contrarily to that case, here we do not observe any 'kink' of the curve and the slope seems to be not very sensitive to the interaction constant: by decreasing the latter of a factor 27, the former raises of a factor 2.44, as displayed in Fig. 4.7, where we show in ordinate the mobility edge from which the ground-state energy E_0, in Eq. (4.12), has been subtracted. Even if these results have been obtained with a pure Rashba coupling, they remain valid also in the case of a pure Dresselhaus coupling, because switching to the latter interaction equals to performing a transformation $k_x \mapsto -k_x$.

4.5 Crossover towards the orthogonal universality class

Now we consider the full Hamiltonian of Eq. (4.10), including both the Rashba and the Dresselhaus, in order to study the behaviour of the critical energy as a function of the two constants, which contribute to weak antilocalization in a non-additive way [200]. To this end, we can write the coupling constants functions of a common constant λ_{SO} and a mixing angle θ, defined as follows:

$$\alpha_R = \lambda_{\mathrm{SO}} \cos\theta \qquad\qquad \beta_D = \lambda_{\mathrm{SO}} \sin\theta \ ,$$

Since the critical energy is invariant under a transformation $\theta \mapsto \pi/2 - \theta$, the relevant range of theta reduces to $0 < \theta < \pi/4$. In particular, at $\theta = \pi/4$, it has been found that the system possesses an $\mathrm{SU}(2)$ spin-rotation symmetry and is robust against spin-independent disorder [201] [202]. Indeed, under the latter condition, the Hamiltonian of Eq. (4.10) becomes:

$$H = \left(\frac{\hbar^2 \boldsymbol{k}^2}{2m} + V(\boldsymbol{r}) \right) \mathbb{1}_2 + 2\beta_D k_y \sigma_x \ ,$$

which now commutes with σ_x, and therefore a common basis of eigenstates for the two operators can be found. Denoting the eigenstates of σ_x as $s_{x,\pm} = \pm 1$, the Hamiltonian decouples into two scalar operators,

$$H_\pm = \frac{\hbar^2 \boldsymbol{k}^2}{2m} + V(\boldsymbol{r}) \pm 2\beta_D k_y \ ,$$

in which the disorder acts on the two spin components separately, as in systems belonging to the orthogonal universality class. Since both spin-rotation and time-inversion symmetries are preserved, we predict that the mobility edge E_c diverges in $d = 2$. Fixing the value of $\lambda_{\mathrm{SO}} = 0.03/(m\sigma)$, representing the magnitude of the 'vector' of coupling constants, we estimated the slope p of the phase boundary within the region $0.5 \leq V_0/E_\sigma \leq 2.0$ of a speckle potential and the intercept q at different mixing angles θ. The two quantities, plotted in Fig. 4.8, exhibit an abrupt increase, while $\theta \to \pi/4 \approx 0.785$ is approached, highlighting a strong dependence of the mobility edge on θ near the crossover with the orthogonal universality class. This result is consistent with the behaviour of the critical energy in [191]. Concerning the nature of the divergence at $\theta \to \pi/4$, according to Wegner's renomalization-group approach [203], the presence of a spin-orbit coupling in $d = 2 + \epsilon$ would translate in a correction to E_c characterized by a power-law with an exponent $1/(2\nu_{\mathrm{orth}})$ [204]. Since in $d = 2$, ν_{orth} diverges, the behaviour of the mobility edge is not described by a power-law of $|\alpha_R - \beta_D|$, but by a logarithmic relation. To prove this deduction, we performed regressions for slope

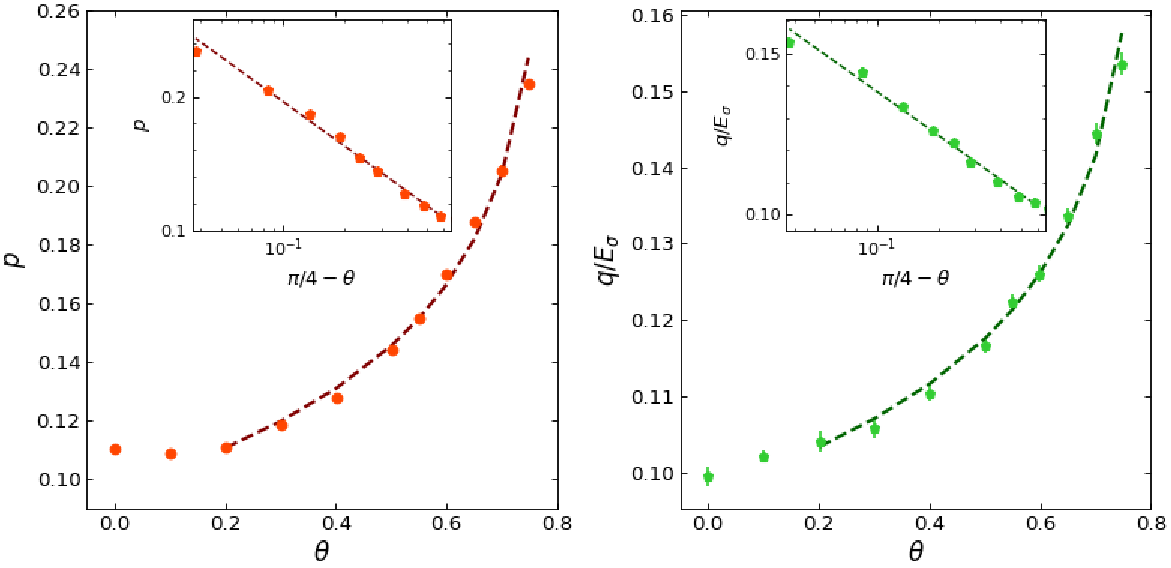

Figure 4.8 – Behaviour of the slope p and intercept q of the phase boundary (coloured dots) as functions of the mixing angle θ between Rashba and Dresselhaus couplings, plotted in linear scale (main panels) and using logarithmic scale on the x-axis (insets). In the computations λ_{SO} has been fixed at $\lambda_{\mathrm{SO}} = 0.03/(m\sigma)$ while the speckle potential has been chosen as the random potential. The critical energies have been extracted using the values of the critical exponent and reduced localization length estimated in [184], with the finite-size scaling technique illustrated in Sec. 4.3. The scaling function has been computed based on a number of disorder configurations N_{tr} ranging from 112 to 196, in lattices with $M = \{150, 200, 250\}$ sites along the transverse side and $N = 50\,000$ sites along the longitudinal one and a lattice constant $\Delta = 0.25\pi\sigma$. The dashed curves, portrayed in both the insets and the main panels, represent the fitting functions $\zeta = -a_\zeta \ln(\pi/4 - \theta) + b_\zeta$, where $\zeta = p, q$ within the interval $0.2 \leq \theta \leq 0.75$, showing the logarithmic divergences near the persistent spin-helix symmetry point.

p and intercept q within the range $0.2 \leq \theta \leq 0.75$: denoting the two aforementioned quantities as ζ we fitted the data (θ, ζ) with the curves $\zeta = -a_\zeta \ln(\pi/4 - \theta) + b_\zeta$. Noticing a satisfactory agreement between the data and the interpolating curves, we found $a_p = 0.049 \pm 0.002$ and $b_p = 0.085 \pm 0.003$ as the parameters of the fitting curve for the slope, and $a_q = (0.0198 \pm 0.0009)E_\sigma$ and $b_q = (0.093 \pm 0.002)E_\sigma$ in the case of the intercept.

4.6 Conclusions and perspectives

In this chapter we have presented our results for 2D Anderson transitions for atoms in spatially correlated disorder in the presence of artificial spin-orbit coupling.

We found that the linear regime observed for the mobility edge, reported in Ref. [191] also occurs for other kinds of randomness, in particular Gaussian disorder, provided the spin-orbit coupling strength is not too weak.

We also showed that the slope p and the intercept q of the straight line $E_c = pV_0 + q$ diverge logarithmically where the Rashba coupling becomes equal to the Dresselhaus one. This divergence signals the restoration of the $SU(2)$ spin-rotation invariance, signalling the crossover of the model from the symplectic to the orthogonal universality class.

In the future it would be interesting to develop a theoretical approach which is able to explain the observed logarithmic divergence. The regime of strong spin-orbit interaction is also worth exploring. This requires to use more sophisticated higher-order discretization schemes.

CONCLUSIONS

In this thesis we have reported our original results concerning interaction-induced Anderson transitions. All the presented data have been obtained using state-of-the-art supercomputers with a total computational cost around 2.5 millions hours of CPU time, most of which have been dedicated to the analysis of the two-particle system. The intrinsic complexity of the subject and the numerical approach has forced us to pay particular attention to the efficiency and the stability of the codes against memory leaks. The final code that we used for production exhibits an hybrid `MPI-openMP` structure, allowing for both multi-threading and parallel computation. We stress that the implementation of the recursive technique for matrix inversion exploiting the block-tridiagonal structure of the single-particle (Anderson) model, discussed in Sec. 3.2, has been instrumental to obtain all numerical results that we presented in Chapter 3.

As we have seen in Chapter 1, Anderson localization is a very general wavelike phenomenon. Quantum systems offer the possibility to investigate new regimes where the wave describes a many-body system of interacting particles. In Chapter 2 we present the numerical procedure used for extracting the position of the critical point. In particular, we distinguish between the well-known transfer-matrix method, which is very efficient but it applies only to models with short-range hopping and an alternative method based on a direct computation in short bars. This method, which applies for any kind of Hamiltonian, has been benchmarked against the transfer-matrix in 3D in the context of Anderson model, and systematically used in Chapter 3 to study localization properties of the pair.

Starting from well-known results for the localization properties of a single particle, we have investigated the interaction-induced metal-insulator transition in a two-body system. We have found that such transitions are absent in two-dimensional systems, in contrast with previous claims. For three-dimensional disordered systems, where the existence of a mobility edge is well established, we have shown that the transition can take place in a regime where all single-particle states are localized. This opens an interesting connection with many-body localization, where a similar situation can occur [30] [87], which is worth exploring in the future.

We also revealed that the phase diagram in the energy-disorder-interaction space exhibits a rich and counter-intuitive structure due to the opposite effects of interactions on the localization of scattering and of bound states. A peculiar feature of the effective model of the pair, not shared with the original Anderson's model, described by the matrix $\mathbf{K}$, is that its whole spectrum can contain only extended states for finite interval of disorder strength, whose size depends on the specific value of the total energy of the pair. A microscopic explanation of this interesting effect is still an open problem. Our numerical procedure adopted for the computation of the elements of $\mathbf{K}$ provides also an effective tool to investigate the localization properties of two-particle states ranging from Cooper pairs [178] to excitons in semiconductors [166]. Concerning the former system, the Gor'kov equation for the pairing field [205] shares an analogous form as the eigenvalue equation (3.3) with K given by Eq. (3.4), and can be exploited for estimating the critical temperature T_c of superconductivity as a function of the disorder parameter W.

When a term able to break spin-rotation invariance is added to the single-particle Anderson's Hamiltonian, a phase transition in two dimensions becomes possible. Considering a spatially correlated speckle potential, we have inspected the behaviour of the phase boundary near the persistent spin-helix symmetry point, where the Rashba and the Dresselhaus spin-orbit coupling strengths become equal. In the vicinity of this point, the two-dimensional system features a logarithmic divergence reflecting the crossover to the orthogonal universality class. Furthermore, after switching from speckle to Gaussian potential, we noticed a linear behviour in the phase boundary for different Rashba coupling strengths, when the spin-orbit interaction is sufficiently strong: we verified that this effect is independent of the specific properties of the disordered potential, calling for further theoretical developments. The results of Chapter 4 can also provide a basis to develop an higher-order discretization scheme, leading to a tight-binding model with longer-range hopping. This opens the interesting perspective of using such schemes to reduce the computation burden also in other models with a spatially-correlated disorder.

Appendices

APPENDIX A

A.1 Random matrix theory

The features of the Anderson Hamiltonian can be also explained by making use of some results of random matrix theory. This theory is able to explain the properties of matrices arising from different dynamical systems and finds applications in several branches of physics, including nuclear, condensed-matter and statistical physics, and even in other disciplines, aside from mathematics [112]. Interpreting the single-particle Hamiltonian $\boldsymbol{H}$ as a random matrix with an diagonal part $\boldsymbol{V}$, representing the on-site energies, and a deterministic off-diagonal part $\boldsymbol{T}$, containing the tunneling amplitudes, it has been proved that, in the metallic regime, $\boldsymbol{H}$ possesses spectral properties consistent with the ones of a Gaussian random ensemble [206], especially at high dimensions d [207]. These ensembles, composed of matrices with indipendent and identically distributed elements following Gaussian's distribution, describe quantum non-integrable ergodic systems, according to a conjecture due to Bohigas, Giannoni and Schmit [208].

In particular, systems endowed with both time-reversal and spin-inversion symmetries, like the ones characterized by the Hamiltonian in Eq. (1.9), are described by the Gaussian orthogonal ensemble (GOE), made up of real symmetric matrices that are invariant under the following transformations,

$$\boldsymbol{H} \to \boldsymbol{W}^T \boldsymbol{H} \boldsymbol{W} \ ,$$

where

$$\boldsymbol{W}^T \boldsymbol{W} = \mathbb{1} \ .$$

Systems in which time-inversion symmetry is broken are represented by matrices from Gaussian Unitary Ensemble instead, as in the case of a particle subject to a magnetic field. On the other hand, for systems in which rotational invariance is broken, like those where the hopping is spin-dependent, the corresponding ensemble is the gaussian symplectic one (GSE). The local and the global properties of the spectrum of gaussian ensembles hold for a larger class of random marices [209], the Wigner matrices, that are hermitian matrices with independent and identically distributed entries with zero mean and finite variance.

Labelling each Gaussian ensemble cited above with an index $\beta = 1, 2, 4$, in the respective order, known as Dyson's index [101], the joint probability density of the eigenvalues $\{E_1, ..., E_N\}$ of $N \times N$ gaussian matrices is given by [112]:

$$P(E_1, ..., E_N) = C_{N,\beta} \exp\left\{-\frac{\beta}{2}\sum_{k=1}^{N} E_k^2\right\} \prod_{i<j} |E_i - E_j|^{\beta}$$

where

$$\begin{aligned} C_{N,\beta} &= \left(\int_{-\infty}^{+\infty} \cdots \int_{-\infty}^{+\infty} \prod_{i<j} |E_i - E_j|^{\beta} \prod_{k=1}^{N} \exp\left\{-\frac{\beta}{2}E_k^2\right\}\right)^{-1} = \\ &= \frac{\beta^{N/2} \beta^{\beta N(N-1)/4} \left[\Gamma(1+\beta/2)\right]^N}{(2\pi)^{N/2} \prod_{i=1}^{N} \Gamma\left(1 + \frac{j\beta}{2}\right)} . \end{aligned}$$

For all three gaussian ensembles, in the limit of $N \to +\infty$, the density of states converges to the Wigner semicircle law:

$$\rho_N(E) = \begin{cases} \frac{\sqrt{2N}}{\pi}\sqrt{1 - \frac{E^2}{2N}}, & -\sqrt{2N} \le E \le +\sqrt{2N} \\ 0, & E > \sqrt{2N} \text{ and } E < -\sqrt{2N} \end{cases} .$$

Another important feature of Gaussian random matrices is the level spacing statistics, which varies according to the ensemble that is considered. Denoting the normalized spacings as

$$s_i := \frac{E_{i+1} - E_i}{\langle E_{i+1} - E_i \rangle} = N\rho(E_i)(E_{i+1} - E_i) ,$$

where $i = 0, 1, \ldots, N-1$, in which a higher subscript refers to greater energy eigenvalue, the probability density $P_N(s)$ associated to a $N \times N$ matrix approaches, even in the thermodynamic limit of $N \to +\infty$, the one found in the $N = 2$ case. The latter corresponds to the so-called Wigner surmise:

$$P_{WD}(s) = c_\beta s^\beta e^{-a_\beta s^2} , \tag{A.18}$$

where the constants c_β and a_β depend on the statistical enseble as illustrated in Table 1 .9. The fact that the probability of finding two energy levels arbitrarily close to each other is zero, as $P(s)$ vanishes at the origin, reflects the 'repulsion' between the energy levels, that is a typical feature of extended states, resulting from the hybridization of adjacent orbitals.

In the insulating regime, localized states have uncorrelated eigenvalues, and the distribution of the energy level spacings follows Poisson's law

$$P_P(s) = e^{-s} , \tag{A.19}$$

Ensemble	β	c_β	a_β
GOE	1	$\frac{\pi}{2}$	$\frac{\pi}{4}$
GUE	2	$\frac{32}{\pi^2}$	$\frac{4}{\pi}$
GSE	4	$\frac{2^{18}}{3^6\pi^3}$	$\frac{64}{9\pi}$

FIGURE .9 – Values of the coefficients appearing in Eq. (A.18) for the different Gaussian ensembles, associated to the three Wigner-Dyson universality classes introduced in § 1.4.1.

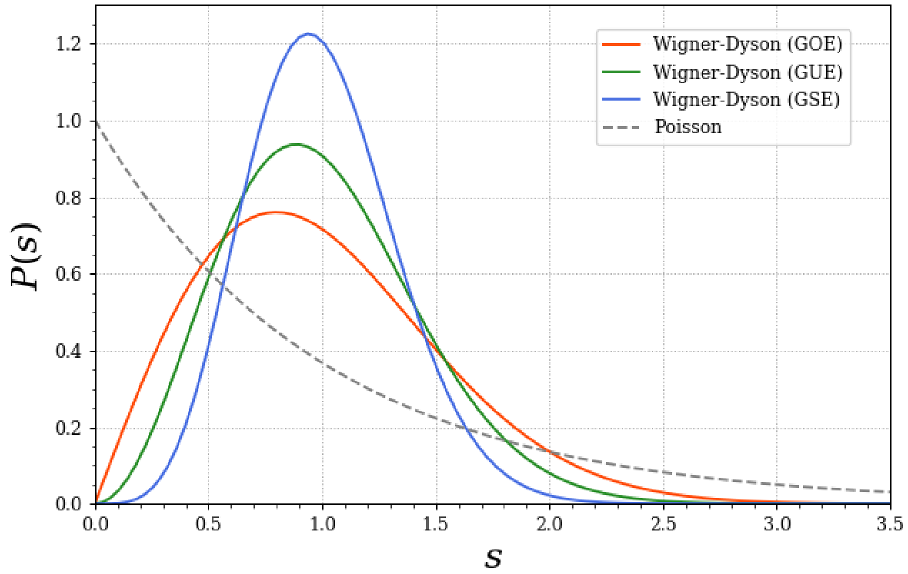

FIGURE .10 – Behaviour of the probability density function of the normalized energy-level spacings according to the three different gaussian ensembles, describing the metallic states. Comparison of the latter with the Poisson distribution, accounting for the localized regime.

that is the one that characterizes quantum integrable systems, according to a conjecture of Barry and Tabor [210]. Taking up Anderson's model, when these states are close in energy, they are centered in far-away lattice sites, and do not overlap: the spectrum thus exhibits level clustering. The statistics of level spacings thus allows for distinguishing the localized from the extended states and it has been used extensively for this purpose [207] [211] [154].

In more recent works, the change in the probability distribution is studied through the variable

$$r_i := \frac{\min\{s_i, s_{i-1}\}}{\max\{s_i, s_{i-1}\}}$$

known as the reduced gap ratio [21] [212] [213], which characterizes the correlation between adjacent energy gaps. Notice that this quantity is independent of the average spacing between the energy levels. In the insulating phase, this random variable takes values from the following distribution:

$$P_P(r) = \frac{2}{(1+r)^2} \, . \tag{A.20}$$

When the model belongs to the orthogonal universality class, in the metallic phase the proabability distribution of the reduced gap ratio is given by:

$$P_{\mathrm{WD}}(r) = \frac{27}{4}\frac{r+r^2}{(1+r+r^2)^{5/2}} \, . \tag{A.21}$$

From Eq. (A.20) and (A.21), one finds that the mean values of the reduced gap ratio for the two distributions are given by $\langle r \rangle_P = 0.38629$ and $\langle r \rangle_{\mathrm{WD}} = 0.5307$ respectively. Therefore, the reduced gap ratio has become a useful tool to pinpoint the position of the critical point of Anderson transitions [21, 214]. In particular, for lattice models, it has been found that at the critical point the gap ratio takes the universal value $\langle r \rangle_c = 0.513 \pm 0.05$.

Beyond the three well-known universality classes, other classes have been discovered in more recent years. For instance, the three gaussian chiral ensembles representing the chiral universality classes possess a further symmetry and is composed of complex matrices that can be written in the following block off-diagonal form:

$$\boldsymbol{H} = \begin{pmatrix} \mathbb{0} & \boldsymbol{h} \\ \boldsymbol{h}^\dagger & \mathbb{0} \end{pmatrix} ,$$

which satisfy the relation $\boldsymbol{H} = -\tau_z \boldsymbol{H} \tau_z$, where $\tau_z = \sigma_z \otimes \mathbb{1}$ and σ_z is a Pauli matrix. These matrices describe systems like bipartite lattices, modelled by tight-binding Hamiltonians whose tunneling terms are random and account for hopping between the two sublattices, whereas on-site energies are absent or constant: this particular structure favours the occurrence of delocalized eigenstates.

RESUMÉ SUBSTANTIEL

Cette thèse porte sur l'étude de la localization d'Anderson de particules quantiques dans des potentiels désordonnés, un phénomène qui se manifeste par la suppression de la propagation d'un paquet d'onde à cause de l'interference destructive entre les ondes engendrées par la diffusion contre les impuretées.

Au niveau microscopique, ce phénomène est lié à un changement profond du comportement des fonctions d'onde, qui deviennent spatialement localisées. Le passage d'un état localisé à un état délocalisé correspond à une transition de phase métal-isolant, la transition d'Anderson. L'apparition de cette transition depend de la classe d'universalité du modèle microscopique, ainsi que à la dimension du réseau: en l'absence de champs magnétiques et d'interactions spin-orbite, le phénomène peut se vérifier seulement dans des réseaux tridimensionnels.

La transition d'Anderson est diffiicile à étudier analytiquement, car elle survient dans un régime non perturbatif. Par conséquent, le calcul numérique est un outil fondamental pour toute analyse quantitative, de l'identification du point critique au calcul des exposants universels associés. Parmi les modèles qui ont plus contribués à notre compréhension du sujet, il y a celui d'Anderson, qui décrit une particule qui se deplace par effet tunnel d'un site à un autre d'un réseau discret en présence d'un potentiel extérieur aléatoire. L'Hamiltonien correspondant, est défini par:

$$\hat{H}_{\mathrm{sp}} = -J \sum_{\{\boldsymbol{i},\boldsymbol{j}\}} |\boldsymbol{i}\rangle\langle\boldsymbol{j}| + \sum_{\boldsymbol{i}} v_{\boldsymbol{i}} |\boldsymbol{i}\rangle\langle\boldsymbol{i}| \,, \tag{.22}$$

où $\boldsymbol{i} \in \mathbb{Z}^d$ indique le site dans le réseau d-dimensionnel, J est le terme de saut. Le désordre apparait par le biais de l'énergie locale $v_{\boldsymbol{i}}$, qui correspond à une variable aléatoire independant uniformement distribuée dans l'intervalle $[-W/2, +W/2]$, où W est un nombre réel. En $d \leq 2$, toutes les états propres de l'Hamiltonien (.22) sont exponentielment localisés,

$$|\psi_\beta(\boldsymbol{i})| \sim \mathrm{e}^{-|\boldsymbol{i}-\boldsymbol{i}_{0,\beta}|/\xi_\beta} \,, \tag{.23}$$

où ξ_β represente la longueur de localisation de l'état propre ψ_β, centré sur le site $\boldsymbol{i}_{0,\beta}$. En trois dimensions, par contre, ils existent deux valeurs critiques $E_{c,1}$, $E_{c,2}$ de l'énergie de la particule, appelés seuils de mobilité, separent les états localisés, décrits par l'Eq. (.23), des états délocalisés. Cela donne lieu à un diagramme de phase dans le plan énergie-désordre en Fig. 1.8. La relation entre le comportement spatial des fonctions d'onde et les propriétés macroscopiques du milieu est mise en évicence par la théorie du scaling, qui est également éclairée. Dans le même chapitre, nous abordons ensuite le problème de la localisation à deux corps, en rappelant les résultats connus en literature et les questions ouvertes, qui font l'objet de cette thèse.

L'identification du point critique de la transition d'Anderson passe par le calcul numérique du logarithme de l'amplitude de transmission entre les deux extremités d'une barre quasi-unidimensionnelle, caractérisée par une section carrée de coté Ma, où a represente le pas, et par une longueur Na, telle que $N \gg M$. Ce calcul permet d'extraire la longueur de localisation reduite Λ_M du modèle à partir duquel la position du point critique s'obtient par la technique du *finite-size scaling*. Dans le chapitre 2, qui est préparatoire aux chapitres 3 et 4, nous présentons deux différentes méthodes pour l'évaluation précise de Λ_M. La première, celle de la matrice de transfert, est la méthode de référence car elle permet de simuler des systèmes de grande taille. Cependant, elle s'applique seulement à des Hamiltoniens avec tunneling à courte portée. La deuxième méthode, qui s'appuie sur l'évaluation directe de la fonction de Green à un corps, a un champ d'application plus général, mais sa complexité numérique ne permet d'aborder que des barres relativement courtes. Ici nous montrons qu'il est néanmoins possible d'évaluer Λ_M avec une précision satisfaisante. Pour cela, nous vérifions que, dans le cas de l'Hamiltonien d'Anderson (.22), on obtient des résultats cohérent avec la méthode de la matrice de transfert, pourvu que une régression linéaire des données soit effectuée.
Dans le même chapitre, nous discutons en détail la méthode numérique suivie pour l'évaluation de la densité d'états moyennée sur les N_{tr} différentes réalisations du désordre

$$\overline{\rho}(E) = \sum_{r=1}^{N_{tr}} \sum_{\alpha=1}^{M^3} \frac{\delta(E - \varepsilon_{\alpha,r})}{N_{tr}(Ma)^3} ,$$

où $\varepsilon_{\alpha,r}$ representent les valeurs propres de l'Hamiltonien d'Anderson (.22) relatifs à la configuration r du potentiel aléatoire. Nous constatons un très bon accord avec la prédiction issue de l'approximation de potentiel cohérent (CPA), en Fig. 2.7.

Ce système est décrit par l'Hamiltonien d'Anderson-Hubbard:

$$\hat{H} = -J \sum_{\{\boldsymbol{i},\boldsymbol{k}\},\boldsymbol{j}} |\boldsymbol{i},\boldsymbol{j}\rangle\langle\boldsymbol{k},\boldsymbol{j}| - J \sum_{\boldsymbol{i},\{\boldsymbol{j},\boldsymbol{k}\}} |\boldsymbol{i},\boldsymbol{j}\rangle\langle\boldsymbol{i},\boldsymbol{k}| + \sum_{\boldsymbol{i},\boldsymbol{j}} |\boldsymbol{i},\boldsymbol{j}\rangle(v_{\boldsymbol{i}} + v_{\boldsymbol{j}})\langle\boldsymbol{i},\boldsymbol{j}| + U \sum_{\boldsymbol{i}} |\boldsymbol{i},\boldsymbol{i}\rangle\langle\boldsymbol{i},\boldsymbol{i}| ,$$

où U indique la force d'interaction. Pour ce modèle, on peut demontrer que les élements diagonaux de l'amplitude $\Psi(\boldsymbol{n}) := \psi(\boldsymbol{n},\boldsymbol{n})$ de la fonction d'onde à deux corps satisfont l'équation aux valeurs propres suivante,

$$\frac{1}{U}\Psi(\boldsymbol{n}) = \sum_{\boldsymbol{m}} K(\boldsymbol{n},\boldsymbol{m})\Psi(\boldsymbol{m}) , \tag{.24}$$

où les élements de la matrice K sont liés à la fonction de Green à deux corps en l'absence d'interaction par la relation $K(\boldsymbol{n},\boldsymbol{m}) := \langle \boldsymbol{n},\boldsymbol{m}|(E\hat{\mathbb{1}} - \hat{H}_0)^{-1}|\boldsymbol{n},\boldsymbol{m}\rangle$. Ici $\hat{H}_0 := \hat{H}(U=0)$, tandis que E represente l'énergie totale de la paire. Nous considérons dorenavant (.24) comme un'équation de Schrödinger à un corps éfficace, où K joue le rôle de l'Hamiltonien et la valeur propre $\lambda := U^{-1}$ correspond à la pseudo-énergie. Ce chapitre est consacré à l'étude des propriétés de localisation de ce modèle efficace. Nous expliquons d'abord l'algorithme utilisé pour le calcul des élements de matrice de K, à l'aide de techniques recursives. Ensuite nous démontrons que les transitions d'Anderson à deux corps prédites en dimension deux par des précedents travaux sont probablement des effets de taille finie. Dans le reste du chapitre, nous examinons le cas tridimensionnel, ce qui represente également un grand défi au niveau numérique. Nous commençons par démontrer que les transitions d'Anderson du modèle efficace donnent des exposants critiques en accord avec ceux de la classe orthogonale (Fig. 3.8), ce qui nous permet d'estimer la position du point critique par la méthode du finite-size scaling. Puis, nous avons établi le diagramme de phase dans le plan interaction-désordre (en Fig. 3.15), pour une paire d'énergie nulle ($E=0$), en observant que la transition a lieu dans un régime où tous les états à une particule sont localisés. Ce résultat est en accord avec les prédictions de la localisation à plusieurs corps, appelée many-body localization. Nous expliquons le comportement non monotone du seuil critique W_c du désordre en fonction de U en analysant le comportement de la dénsité d'états du modèle efficace (Fig. 3.9).

Pour des valeurs d'énergie non nulles, $|E| > 12J$, nous montrons que la topologie du diagramme de phase est modifiée par la présence d'états moleculaires, qui sont très sensibles aux effets du désordre. En effet, ces états correspondent à des situations où $E \sim U$ et la paire se comporte comme une particule ponctuelle, qui obéit à un modèle d'Anderson avec des paramètres rénormalisés par l'interaction,

$$\frac{2J^2}{E}\sum_{i=1}^{3}\Psi(\boldsymbol{n}+\mathbf{e}_i) + \frac{2J^2}{E}\sum_{i=1}^{3}\Psi(\boldsymbol{n}-\mathbf{e}_i) + \frac{2v_{\boldsymbol{n}}(E+2v_{\boldsymbol{n}})}{E}\Psi(\boldsymbol{n}) = E_{\text{eff}}\Psi(\boldsymbol{n}) \,,$$

où $E_{\text{eff}} = E(E-U)/U - 12J^2/E$ et $\mathbf{e}_i$, avec $i=1,2,3$, sont les trois vecteurs unitaires le long des trois axes orthogonaux. En partant de cet effet nous avons construit le diagramme de phase le long la direction $E=U$, où le mélange d'états diffusifs et liés donne lieu à un diagramme de phase avec une double renfoncement (Fig. 3.17).

Si dans les chapitres précédents nous avions negligé le dégré de liberté de spin dans nos calculs, dans le chapitre 4 nous considérons un système qui brise la symétrie $SU(2)$ et dont le modèle appartient à une classe d'universalité différente, la classe sympléctique. Cette situation se vérifie lorsque une particule est soumise à une interaction spin-orbite, qui modifie les effets d'intérférence et favorise la delocalisation de la particule. Ainsi des transitions d'Anderson en dimension deux deviennent possibles dans cette classe.

Nous étudions ce transition dans le contexte d'atomes froids soumis à l'effet conjoint d'un potentiel désordonné, $V(\boldsymbol{r})$, et d'un couplage spin-orbite artificiel, de type Rashba-Dresselhaus. L'Hamiltonien correspondant est:

$$H = \left[\frac{\hbar^2(k_x^2+k_y^2)}{2m} + V(\boldsymbol{r})\right]\mathbb{1}_2 + \alpha_R(k_y\sigma_x - k_x\sigma_y) + \beta_D(k_y\sigma_x + k_x\sigma_y)\ . \tag{.25}$$

où α_R et β_D symbolisent respectivement les constants de couplage de Rahsba et Dresselhaus. Nous étudions le seuil de mobilité E_c de la transition en variant les deux propriétés caractèristiques du désordre, à savoir la distribution de probabilité $P(V)$ et la fonction de correlation $C(\boldsymbol{r}) := \overline{V(\boldsymbol{0})V(\boldsymbol{r})}$. Pour $\beta_D = 0$, nous avons vérifié l'existance d'un régime où le seuil de mobilité varie linéairement avec l'intensité V_0 du désordre, définie par $V_0^2 := \overline{V(\boldsymbol{0})^2}$ (Fig. 4.7). Lorsque les couplages Rashba et Dresselhaus prendent la même valeur, $\alpha_R = \beta_D$, l'invariance $SU(2)$ est rétablie et le modèle (.25) tombe dans la classe orthogonale, où toute transition d'Anderson en dimension deux est interdite. Dans le régime linéaire mentionné ci-dessus, nous étudions le comportement du seuil de mobilité en variant le couplage de Dresselhaus de $\beta_D = 0$ à $\beta_D = \alpha_R$, où E_c diverge. Ainsi, nous avons decélé une divergence logarithmique de la pente e de l'intercepte du seuil de mobilité (Fig. 4.8).

LIST OF PUBLICATIONS

Peer-reviewed articles

1. **Mobility edge of two interacting particles in three-dimensional random potentials**
   F. Stellin, G. Orso
   Physical Review B, 99, 224209 (2019)
2. **Two-body mobility edge in the Anderson-Hubbard model in three dimensions: molecular versus scattering states**
   F. Stellin, G. Orso
   arXiv:2004.03506, (2020).

Poster presentations

1. **Wave scattering, Paris (France)**
   Workshop of the "Complèxe" research grouping of CNRS
   Anderson localization of two interacting particles in 2D and 3D random potentials
   April 2019
2. **Complex 2018, Cargèse (France)**
   Thematic school of the "Complèxe" research grouping of CNRS
   Anderson localization of cold atoms in random potentials
   May 2018
3. **Cold atoms and quantum transport, Les Houches (France)**
   Predoctoral school of the "Atomes froids" research grouping of CNRS
   Anderson localization of cold atoms in random potentials
   October 2017

BIBLIOGRAPHY

[1] P. W. Anderson; "Absence of Diffusion in Certain Random Lattices"; Phys. Rev. **109**, pp. 1492–1505 (1958).

[2] G. Feher; "Electron Spin Resonance Experiments on Donors in Silicon. I. Electronic Structure of Donors by the Electron Nuclear Double Resonance Technique"; Phys. Rev. **114**, pp. 1219–1244 (1959).

[3] I. Lifshitz; "Structure of the energy spectrum of impurity bands in disordered solid solutions"; Sov. Phys. JETP **17**, pp. 1159–1170 (1963).

[4] I. Lifshitz; "Energy spectrum structure and quantum states of disordered condensed systems"; Sov. Phys. Usp. **7**, pp. 549–573 (1965).

[5] N. Mott; "Conduction in glasses containing transition metal ions"; Journal of Non-Crystalline Solids **1**, pp. 1 – 17 (1968)ISSN 0022-3093.

[6] D. J. Thouless; "Electrons in disordered systems and the theory of localization"; Phys. Rep. **13**, pp. 93–142 (1974).

[7] E. Abrahams, P. W. Anderson, D. C. Licciardello & T. V. Ramakrishnan; "Scaling Theory of Localization: Absence of Quantum Diffusion in Two Dimensions"; Phys. Rev. Lett. **42**, pp. 673–676 (1979).

[8] F. Wegner; "Electrons in Disordered Systems. Scaling near the Mobility Edge"; Z. Phys. **B25**, p. 327 (1976).

[9] F. Wegner; "The mobility edge problem: Continuous symmetry and a conjecture"; Z. Phys. B Cond. Matt. **35**, pp. 207–210 (1979). ISSN 1431-584X.

[10] K. B. Efetov, A. I. Larkin & Khemlnitskii; "Interaction of diffusion modes in the theory of localization"; Zh. Eksp. Teor. Fiz. **79**, p. 1120 (1980).

[11] D. Vollhardt & P. Wölfle; "Anderson Localization in $d \leq 2$ Dimensions: A Self-Consistent Diagrammatic Theory"; Phys. Rev. Lett. **45**, pp. 842–846 (1980).

[12] D. Vollhardt & P. Wölfle; "Diagrammatic, self-consistent treatment of the Anderson localization problem in $d \leq 2$ dimensions"; Phys. Rev. B **22**, pp. 4666–4679 (1980).

[13] R. Abou-Chacra, D. J. Thouless & P. W. AndersonJournal of Physics C: Solid State Physics **6**, pp. 1734–1752 (1973).

[14] B. Kramer & A. MacKinnon; "Localization: theory and experiment"; Rep. Prog. Phys. **56**, pp. 1469–1564 (1993).

[15] K. Slevin & T. Ohtsuki; "Numerical verification of universality for the Anderson transition"; Phys. Rev. B **63**, p. 045108 (2001).

[16] J.-L. Pichard & G. Sarma; "Finite size scaling approach to Anderson localisation"; Journal of Physics C: Solid State Physics **14**, pp. L127–L132 (1981).

[17] B. Kramer, A. MacKinnon, T. Ohtsuki & K. Slevin; "Finite-Size Scaling Analysis of the Anderson Transition"; Int. J. Mod. Phys. B **24**, pp. 1841–1854 (2010).

[18] A. MacKinnon & B. Kramer; "One-Parameter Scaling of Localization Length and Conductance in Disordered Systems"; Phys. Rev. Lett. **47**, pp. 1546–1549 (1981).

[19] B. I. Shklovskii, B. Shapiro, B. R. Sears, P. Lambrianides & H. B. Shore; "Statistics of spectra of disordered systems near the metal-insulator transition"; Phys. Rev. B **47**, pp. 11487–11490 (1993).

[20] I. Varga, E. Hofstetter, M. Schreiber & J. Pipek; "Shape analysis of the level-spacing distribution around the metal-insulator transition in the three-dimensional Anderson model"; Phys. Rev. B **52**, pp. 7783–7786 (1995).

[21] V. Oganesyan & D. A. Huse; "Localization of interacting fermions at high temperature"; Phys. Rev. B **75**, p. 155111 (2007).

[22] A. B. Chhabra, C. Meneveau, R. V. Jensen & K. R. Sreenivasan; "Direct determination of the f(α) singularity spectrum and its application to fully developed turbulence"; Phys. Rev. A **40**, pp. 5284–5294 (1989).

[23] A. Rodriguez, L. J. Vasquez, K. Slevin & R. A. Römer; "Critical Parameters from a Generalized Multifractal Analysis at the Anderson Transition"; Phys. Rev. Lett. **105**, p. 046403 (2010).

[24] M. A. Paalanen, T. F. Rosenbaum, G. A. Thomas & R. N. Bhatt; "Critical Scaling of the Conductance in a Disordered Insulator"; Phys. Rev. Lett. **51**, pp. 1896–1899 (1983).

[25] T. Schwartz, G. Bartal, S. Fishman & M. Segev; "Transport and Anderson localization in disordered two-dimensional photonic lattices"; Nature **446**, pp. 52–55 (2007).

[26] S. E. Skipetrov & Y. M. Beltukov; "Anderson transition for elastic waves in three dimensions"; Phys. Rev. B **98**, p. 064206 (2018).

[27] R. Weaver; "Anderson localization of ultrasound"; Wave Motion **12**, pp. 129 – 142 (1990). ISSN 0165-2125.

[28] E. Larose, L. Margerin, B. A. van Tiggelen & M. Campillo; "Weak Localization of Seismic Waves"; Phys. Rev. Lett. **93**, p. 048501 (2004).

[29] M. Lewenstein, A. Sanpera & V. Ahufinger; *Ultracold atoms in optical lattices* (Oxford University Press, Oxford) (2012).

[30] D. M. Basko, I. L. Aleiner & B. L. Altshuler; "Metal-insulator transition in a weakly interacting many-electrom system with localized single-particle states"; Ann. Phys. **321**, pp. 1126–1205 (2006).

[31] A. Aspect & M. Inguscio; "Anderson localization of ultracold atoms"; Physics Today **62**, p. 30 (2009).

[32] A. Ioffe & A. Regel; "Non-crystalline, amorphous and liquid electronic semiconductors"; Prog. Semicon. p. 237 (1960).

[33] S. Katsumoto; "The metal-insulator transition in a persistent photoconductor"; in "Localization, Proceedings of the International Conference on Localization," , edited by K. A. Benedict & J. T. Chalker; Conference Series; p. 17 (Institute of Physics, Bristol, UK) (1991).

[34] D. Belitz & T. R. Kirkpatrick; "The Anderson-Mott transition"; Rev. Mod. Phys. **66**, pp. 261–380 (1994).

[35] S. Bogdanovich, M. P. Sarachik & R. N. Bhatt; "Scaling of the Conductivity with Temperature and Uniaxial Stress in Si:B at the Metal-Insulator Transition"; Phys. Rev. Lett. **82**, pp. 137–140 (1999).

[36] A. Lagendijk, B. A. van Tiggelen & D. S. Wiersma; "Fifty years of Anderson Localization"; Physics Today **62**, p. 24 (2009).

[37] S. E. Skipetrov & J. H. Page; "Red light for Anderson localization"; New Journal of Physics **18**, p. 021001 (2016).

[38] H. De Raedt, A. Lagendijk & P. de Vries; "Transverse Localization of Light"; Phys. Rev. Lett. **62**, pp. 47–50 (1989).

[39] A. Simbula, M. Schatzl, L. Zagaglia, F. Alpeggiani, L. C. Andreani, F. Schäffler, T. Fromherz, M. Galli & D. Gerace; "Realization of high-Q/V photonic crystal cavities defined by an effective Aubry-André-Harper bichromatic potential"; APL Photonics **2**, p. 056102 (2017).

[40] S. Aubry & G. André; "Analyticity breaking and Anderson localization in incommensurate lattices"; Ann. Israel Phys. Soc. **3**, p. 18 (1980).

[41] D. Wiersma, P. Bartolini, A. Lagendijk & R. Righini; "Localization of light in a disordered medium"; Nature **390**, pp. 671–673 (1997).

[42] M. Störzer, P. Gross, C. M. Aegerter & G. Maret; "Observation of the Critical Regime Near Anderson Localization of Light"; Phys. Rev. Lett. **96**, p. 063904 (2006).

[43] T. Sperling, L. Schertel, M. Ackermann, G. J. Aubry, C. M. Aegerter & G. Maret; "Can 3D light localization be reached in 'white paint'?" New Journal of Physics **18**, p. 013039 (2016).

[44] N. Garcia & A. Z. Genack; "Anomalous photon diffusion at the threshold of the Anderson localization transition"; Phys. Rev. Lett. **66**, pp. 1850–1853 (1991).

[45] A. A. Chabanov, M. Stoytchev & A. Z. Genack; "Statistical signatures of photon localization"; Nature (London) **404**, pp. 850–853 (2000).

[46] S. E. Skipetrov; "Localization Transition for Light Scattering by Cold Atoms in an External Magnetic Field"; Phys. Rev. Lett. **121**, p. 093601 (2018).

[47] L. A. Cobus, S. E. Skipetrov, A. Aubry, B. A. van Tiggelen, A. Derode & J. H. Page; "Anderson Mobility Gap Probed by Dynamic Coherent Backscattering"; Phys. Rev. Lett. **116**, p. 193901 (2016).

[48] H. Hu, A. Strybulevych, J. H. Page, S. E. Skipetrov & B. A. van Tiggelen; "Localization of ultrasound in a three-dimensional elastic network"; Nat. Phys. **4**, pp. 945–948 (2008).

[49] S. Fishman, D. R. Grempel & R. E. Prange; "Chaos, Quantum Recurrences, and Anderson Localization"; Phys. Rev. Lett. **49**, pp. 509–512 (1982).

[50] F. L. Moore, J. C. Robinson, C. Bharucha, P. E. Williams & M. G. Raizen; "Observation of Dynamical Localization in Atomic Momentum Transfer: A New Testing Ground for Quantum Chaos"; Phys. Rev. Lett. **73**, pp. 2974–2977 (1994).

[51] G. Casati, I. Guarneri & D. L. Shepelyansky; "Anderson transition in a one-dimensional system with three incommensurable frequencies"; Phys. Rev. Lett. **62**, pp. 345–348 (1989).

[52] J. Chabé, G. Lemarié, B. Grémaud, D. Delande, P. Szriftgiser & J. C. Garreau; "Experimental Observation of the Anderson Metal-Insulator Transition with Atomic Matter Waves"; Phys. Rev. Lett. **101**, p. 255702 (2008).

[53] G. Lemarié, B. Grémaud & D. Delande; "Universality of the Anderson transition with the quasiperiodic kicked rotor"; EPL (Europhysics Letters) **87**, p. 37007 (2009).

[54] J. Billy, V. Josse, Z. Zuo, A. Bernard, B. Hambrecht, P. Lugan, D. Clément, L. Sanchez-Palencia, P. Bouyer & A. Aspect; "Direct observation of Anderson localization of matter-waves in a controlled disorder"; Nature **453**, pp. 891–894 (2008).

[55] G. Roati, C. d'Errico, L. Fallani, M. Fattori, C. Fort, M. Zaccanti, G. Modugno, M. Modugno & M. Inguscio; "Anderson localization of a non-interacting Bose-Einstein condensate"; Nature (London) **453**, pp. 895–898 (2008).

[56] S. S. Kondov, W. R. McGehee, J. J. Zirbel & B. DeMarco; "Three-Dimensional Anderson Localization of Ultracold Matter"; Science **334**, pp. 66–68 (2011). ISSN 0036-8075.

[57] F. Jendrzejewski, A. Bernard, K. Muller, P. Cheinet, V. Josse, M. Piraud, L. Pezzé, L. Sanchez-Palencia, A. Aspect & P. Bouyer; "Three-dimensional localization of ultracold atoms in an optical disordered potential"; Nat. Phys. **8**, pp. 398–403 (2012).

[58] G. Semeghini, M. Landini, P. Castilho, S. Roy, G. Spagnolli, A. Trenkwalder, M. Fattori, M. Inguscio & G. Modugno; "Measurement of the mobility edge for 3D Anderson localization"; Nature Physics **11**, pp. 554–559 (2015).

[59] M. Pasek, G. Orso & D. Delande; "Anderson Localization of Ultracold Atoms: Where is the Mobility Edge?" Phys. Rev. Lett. **118**, p. 170403 (2017).

[60] S. F. Edwards; "A new method for the evaluation of electric conductivity in metals"; Philos. Mag. **3**, p. 1020 (1958).

[61] P. Wölfle & R. N. Bhatt; "Electron localization in anisotropic systems"; Phys. Rev. B **30**, pp. 3542–3544 (1984).

[62] F. M. Izrailev & A. A. Krokhin; "Localization and the Mobility Edge in One-Dimensional Potentials with Correlated Disorder"; Phys. Rev. Lett. **82**, pp. 4062–4065 (1999).

[63] L. Sanchez-Palencia, D. Clément, P. Lugan, P. Bouyer & A. Aspect; "Disorder-induced trapping versus Anderson localization in Bose–Einstein condensates expanding in disordered potentials"; New Journal of Physics **10**, p. 045019 (2008).

[64] N. W. Ashcroft & N. D. Mermin; *Solid State Physics* (Saunders College, New York) (1976).

[65] P. Biswas, P. Cain, R. Römer & M. Schreiber; "Off-Diagonal Disorder in the Anderson Model of Localization"; physica status solidi (b) **218**, pp. 205–209 (2000).

[66] H. Hermann & J. Schreiber; "Localization of electron wave functions in a one-dimensional model including off-diagonal disorder"; physica status solidi (b) **67**, pp. K93–K96 (1975).

[67] A. Eilmes, R. A. Römer & M. Schreiber; "The two-dimensional Anderson model of localization with random hopping"; Eur. Phys. J. B **1**, pp. 29–38 (1998).

[68] T. Kawarabayashi & T. Ohtsuki; "Diffusion of electrons in random magnetic fields"; Phys. Rev. B **51**, pp. 10897–10904 (1995).

[69] E. N. Economou & P. D. Antoniou; "Localization and off-diagonal disorder"; Solid State Communications **21**, pp. 285–288 (1977).

[70] D. Weaire & V. Srivastava; "Numerical results for Anderson localisation in the presence of off-diagonal disorder"; Solid State Communications **23**, pp. 863 – 866 (1977). ISSN 0038-1098.

[71] J. Stein & U. Krey; "Numerical studies on the Anderson localization problem"; Physica A: Statistical Mechanics and its Applications **106**, pp. 326 – 343 (1981)ISSN 0378-4371.

[72] D. Delande, J. C. Garreau & B. A. Sanchez-Palencia, L. and van Tiggelen; "La localisation forte d'Anderson"; Images de la Physique pp. 70–74 (2009).

[73] D. Bruns, R. Haenel & G. Tom; "Anderson Localization"; (2017); unpublished.

[74] G. Czycholl, B. Kramer & A. MacKinnon; "Conductivity and localization of electron states in one dimensional disordered systems: Further numerical results"; Zeitschrift für Physik B Condensed Matter **43**, pp. 5–11 (1981).

[75] M. Kappus & F. Wegner; "Anomaly in the band centre of the one-dimensional Anderson model"; Zeitschrift für Physik B Condensed Matter **45**, pp. 15–21 (1981).

[76] K. Slevin & T. Ohtsuki; "Critical exponent for the Anderson transition in the three-dimensional orthogonal universality class"; New Journal of Physics **16**, p. 015012 (2014).

[77] P. Markoš; "Numerical analysis of the Anderson localization"; Acta Physica Slovaca **5**, pp. 561–685 (2006). ISSN 0323-0465.

[78] E. Abrahams; *50 Years of Anderson Localization* (World Scientific) (2010).

[79] B. Bulka, M. Schreiber & B. Kramer; "Localization, quantum interference, and the metal-insulator transition"; Z. Phys. B: Condensed Matter **66**, pp. 21–30 (1987). ISSN 1431-584X.

[80] J. Kroha, T. Kopp & P. Wölfle; "Self-consistent theory of Anderson localization for the tight-binding model with site-diagonal disorder"; Phys. Rev. B **41**, pp. 888–891 (1990).

[81] J. Kroha; "Diagrammatic self-consistent theory of Anderson localization for the tight-binding model"; Physica A: Statistical Mechanics and its Applications **167**, pp. 231 – 252 (1990). ISSN 0378-4371.

[82] R. J. Bell & P. Dean; "Atomic vibrations in vitreous silica"; Disc. Faraday Soc. **50**, pp. 55–61 (1970).

[83] A. Brezini & N. Zekri; "Overview on some aspects of the theory of localization"; Phys. Stat. Sol. (b) **169**, pp. 253–301 (1992).

[84] F. Wegner; "Inverse participation ratio in 2+ϵ dimensions"; Zeitschrift für Physik B Condensed Matter **36**, pp. 209–214 (1980). ISSN 1431-584X.

[85] T. Ando & H. Fukuyama (Editors); *Anderson Localization, Proceedings of the International Symposium, Tokyo, Japan, August 16–18, 1987*; 28 (Springer-Verlag Berlin Heidelberg) (1988).

[86] F. Evers & A. D. Mirlin; "Anderson transitions"; Rev. Mod. Phys. **80**, pp. 1355–1417 (2008).

[87] A. Scardicchio & T. Thiery; "Perturbation theory approaches to Anderson and Many-Body Localization: some lecture notes"; Technical Report arXiv:1708.01234 [cs.IT]; ArXiV (2017).

[88] W. Kirsch & B. Simon; "Comparison theorems for the gap of Schrödinger operators"; J. Funct. Anal. **75**, pp. 396–410 (1987).

[89] D. J. Thouless; "A relation between the density of states and a range of localization for one-dimensional random systems"; J. Phys. C: Sol. St. Phys. **5**, p. 77 (1972).

[90] P. A. Lee & T. V. Ramakrishnan; "Disordered electronic systems"; Rev. Mod. Phys. **57**, pp. 287–337 (1985).

[91] T. V. Ramakrishnan; "Metal insulator transitions"; in "Proc. Indian Nat. Sci. Acad.", , volume 52, edited by C. Glattli, M. Sanquer & J. Trân Thanh Vân; pp. 217–231 (1986).

[92] F. Wegner & R. Oppermann; "Disordered System with n Orbitals per Site: $1/n$ Expansion"; Z. Phys. B Cond. Matt. **34**, pp. 327–348 (1979). ISSN 1431-584X.

[93] K. Efetov; *Supersymmetry in Disorder and Chaos* (Cambridge University Press, Cambridge, UK) (1997).

[94] E. P. Wigner; "On a Class of Analytic Functions from the Quantum Theory of Collisions"; Ann. Math. **53**, pp. 36–67 (1951)ISSN 0003486X.

[95] L. P. Gorkov & G. M. Eliashberg; "Minute Metallic Particles in an Electromagnetic Field"; Sov. Phys. JETP **21**, pp. 940–947 (1965).

[96] A. D. Mirlin & Y. V. Fyodorov; "Distribution of local densities of states, order parameter function, and critical behavior near the Anderson transition"; Phys. Rev. Lett. **72**, pp. 526–529 (1994).

[97] V. Dobrosavljević, A. A. Pastor & B. K. Nikolić; "Typical medium theory of Anderson localization: A local order parameter approach to strong-disorder effects"; Europhys. Lett. **62**, pp. 76–82 (2003).

[98] D. Vollhardt & P. Wölfle; "Self-Consistent Theory of Anderson Localization"; in "Electronic Phase Transitions," , edited by Hanke, W. and Kopaev Yu. V.; pp. 1–78 (Elsevier) (1992).

[99] R. Landauer; "Electrical resistance of disordered one-dimensional lattices"; Philos. Mag. **21**, pp. 863–867 (1970).

[100] E. Akkermans & G. Montambaux; *Mesoscopic physics of electrons and photons* (Cambridge University Press, Cambridge) (2007).

[101] C. W. J. Beenakker; "Random-matrix theory of quantum transport"; Rev. Mod. Phys. **69**, pp. 731–808 (1997).

[102] J.-L. Pichard; "Random Matrix Theory of Scattering in Chaotic and Disordered Media"; in "Waves and Imagin through Complex Media," , edited by P. Sebbah; pp. 125–140 (Kluwer Academic Publishers, London) (2001).

[103] C. A. Müller & D. Delande; "Les Houches 2009 - Session XCI: Ultracold Gases and Quantum Information"; in "Disorder and interference: localization phenomena," , edited by C. Miniatura, L.-C. Kwek, B. Ducloy, M.and Grémaud, B.-G. Englert, L. F. Cugliandolo & A. Ekert (Oxford University Press, Oxford, UK) (2011).

[104] P. W. Anderson, D. J. Thouless, E. Abrahams & D. S. Fisher; "New method for a scaling theory of localization"; Phys. Rev. B **22**, pp. 3519–3526 (1980).

[105] O. N. Dorokhov; "Transmission coefficient and the localization length of an electron in N bound disordered chains"; JETP Lett. **36**, pp. 318–321 (1982).

[106] P. A. Mello, P. Pereyra & N. Kumar; "Macroscopic approach to multichannel disordered conductors"; Annals of Physics **181**, pp. 290–317 (1988).

[107] D. Arovas; "Lecture notes on Condensed Matter Physics"; (2010).

[108] S. Chakravarty & A. Schmid; "Weak localization: The quasiclassical theory of electrons in a random potential"; Physics Reports **140**, pp. 193 – 236 (1986). ISSN 0370-1573.

[109] P. Singha Deo; "Thouless conductance formula in one dimension and its relevance to persistent-current experiments"; Phys. Rev. B **55**, pp. 13795–13798 (1997).

[110] E. P. Wigner; "Characteristic Vectors of Bordered Matrices With Infinite Dimensions"; Ann. Math. **62**, pp. 548–564 (1955)ISSN 0003486X.

[111] H. Obuse, A. Furusaki, S. Ryu & C. Mudry; "Two-dimensional spin-filtered chiral network model for the $\mathbb{Z}_2$ quantum spin-Hall effect"; Phys. Rev. B **76**, p. 075301 (2007).

[112] M. L. Mehta; *Random Matrices*; 3rd edition (Elsevier Academic Press, San Diego) (2004).

[113] R. Gade & F. Wegner; "The n = 0 replica limit of U(n) and U(n)SO(n) models"; Nuclear Physics B **360**, pp. 213 – 218 (1991). ISSN 0550-3213.

[114] M. R. Zirnbauer; "Supersymmetry for systems with unitary disorder: circular ensembles"; Journal of Physics A: Mathematical and General **29**, pp. 7113–7136 (1996).

[115] A. Altland & M. R. Zirnbauer; "Nonstandard symmetry classes in mesoscopic normal-superconducting hybrid structures"; Phys. Rev. B **55**, pp. 1142–1161 (1997).

[116] A. M. Finkelstein; "Influence of Coulomb interaction on the properties of disordered metals"; Zh. Eksp. Teor. Fiz. **84**, p. 168 (1983).

[117] C. Castellani, C. Di Castro, P. A. Lee, M. Ma, S. Sorella & E. Tabet; "Spin fluctuations in disordered interacting electrons"; Phys. Rev. B **30**, pp. 1596–1598 (1984).

[118] L. P. Lévy, G. Dolan, J. Dunsmuir & H. Bouchiat; "Magnetization of mesoscopic copper rings: Evidence for persistent currents"; Phys. Rev. Lett. **64**, pp. 2074–2077 (1990).

[119] S. V. Kravchenko, G. V. Kravchenko, J. E. Furneaux, V. M. Pudalov & M. D'Iorio; "Possible metal-insulator transition at $B = 0$ in two dimensions"; Phys. Rev. B **50**, pp. 8039–8042 (1994).

[120] D. Popović, A. B. Fowler & S. Washburn; "Metal-Insulator Transition in Two Dimensions: Effects of Disorder and Magnetic Field"; Phys. Rev. Lett. **79**, pp. 1543–1546 (1997).

[121] M. P Sarachik & S. V Kravchenko; "Novel phenomena in dilute electron systems in two dimensions"; Proceedings of the National Academy of Sciences of the United States of America **96**, pp. 5900–2 (1999).

[122] T. Giamarchi & B. S. Shastry; "Persistent currents in a one-dimensional ring for a disordered Hubbard model"; Phys. Rev. B **51**, pp. 10915–10922 (1995).

[123] O. N. Dorokhov; "Localization of two bound particles in a one-dimensional random potential"; Zh. Eksp. Teor. Fiz. **71**, p. 360 (1990).

[124] D. L. Shepelyansky; "Coherent Propagation of Two Interacting Particles in a Random Potential"; Phys. Rev. Lett. **73**, pp. 2607–2610 (1994).

[125] K. Frahm, A. Müller-Groeling, J.-L. Pichard & D. Weinmann; "Scaling in Interaction-Assisted Coherent Transport"; EPL (Europhysics Letters) **31**, p. 169 (1995).

[126] P. Jacquod & D. L. Shepelyansky; "Hidden Breit-Wigner Distribution and Other Properties of Random Matrices with Preferential Basis"; Phys. Rev. Lett. **75**, pp. 3501–3504 (1995).

[127] D. Weinmann & J.-L. Pichard; "Level Statistics and Localization for Two Interacting Particles in a Random Potential"; Phys. Rev. Lett. **77**, pp. 1556–1559 (1996).

[128] P. Jacquod, D. L. Shepelyansky & O. P. Sushkov; "Breit-Wigner Width for Two Interacting Particles in a One-Dimensional Random Potential"; Phys. Rev. Lett. **78**, pp. 923–926 (1997).

[129] P. H. Song & D. Kim; "Localization of two interacting particles in a one-dimensional random potential"; Phys. Rev. B **56**, pp. 12217–12220 (1997).

[130] M. Leadbeater, R. Römer & M. Schreiber; "Interaction-dependent enhancement of the localisation length for two interacting particles in a one-dimensional random potential"; The European Physical Journal B - Condensed Matter and Complex Systems **8**, pp. 643–652 (1999). ISSN 1434-6036.

[131] K. Frahm; "Interaction induced delocalization of two particles: large system size calculations and dependence on interaction strength"; The European Physical Journal B - Condensed Matter and Complex Systems **10**, pp. 371–378 (1999). ISSN 1434-6036.

[132] I. V. Ponomarev & P. G. Silvestrov; "Coherent propagation of interacting particles in a random potential: The mechanism of enhancement"; Phys. Rev. B **56**, pp. 3742–3759 (1997).

[133] Y. Imry; "Coherent Propagation of Two Interacting Particles in a Random Potential"; EPL (Europhysics Letters) **30**, p. 405 (1995).

[134] K. Frahm, A. Müller-Groeling & J.-L. Pichard; "Two interacting particles in a random potential: mapping onto one parameter localization theories without interaction"; Zeitschrift für Physik B Condensed Matter **102**, pp. 261–275 (1997).

[135] R. A. Römer & M. Schreiber; "No Enhancement of the Localization Length for Two Interacting Particles in a Random Potential"; Phys. Rev. Lett. **78**, pp. 515–518 (1997).

[136] F. von Oppen, T. Wettig & J. Müller; "Interaction-Induced Delocalization of Two Particles in a Random Potential: Scaling Properties"; Phys. Rev. Lett. **76**, pp. 491–494 (1996).

[137] P. H. Song & F. von Oppen; "General localization lengths for two interacting particles in a disordered chain"; Phys. Rev. B **59**, pp. 46–49 (1999).

[138] Akkermans, E. & Pichard, J.-L.; "Level curvatures, spectral statistics and scaling for interacting particles"; Eur. Phys. J. B **1**, pp. 223–227 (1998).

[139] F. Borgonovi & D. L. Shepelyansky; "Enhancement of localization length for two interacting kicked rotators"; Nonlinearity **8**, p. 877 (1995).

[140] F. Borgonovi & D. L. Shepelyansky; "Particle propagation in a random and quasi-periodic potential"; Physica D: Nonlinear Phenomena **109**, pp. 24–31 (1997).

[141] O. Halfpap, T. Kawarabayashi & B. Kramer; "Quantum diffusion of interacting particles in a random potential"; Ann. Phys. Leipzig **7**, p. 483 (1998).

[142] Waintal, X. & Pichard, J.-L.; "Two interacting particles in a disordered chain I: Multifractality of the interaction matrix elements"; Eur. Phys. J. B **6**, pp. 117–121 (1998). ISSN 1434-6028.

[143] Waintal, X., Weinmann, D. & Pichard, J.-L.; "Two interacting particles in a disordered chain II: Critical statistics and maximum mixing of the one body states"; Eur. Phys. J. B **7**, pp. 451–456 (1999).

[144] S. De Toro Arias, X. Waintal & J.-L. Pichard; "Two interacting particles in a disordered chain III: Dynamical aspects of the interplay disorder-interaction"; The European Physical Journal B - Condensed Matter and Complex Systems **10**, pp. 149–158 (1999). ISSN 1434-6036.

[145] J. Richert & H. A. Weidenmüller; "Localization properties of two interacting electrons in a disordered quasi one-dimensional potential"; Journal of Physics A: Mathematical and General **36**, pp. 3281–3288 (2003).

[146] Frahm, Klaus M.; "Eigenfunction structure and scaling of two interacting particles in the one-dimensional Anderson model"; Eur. Phys. J. B **89**, p. 115 (2016).

[147] D. O. Krimer, R. Khomeriki & S. Flach; "Two interacting particles in a random potential"; Pis. v Zh. Eksp. Teor. Fiz. **94**, pp. 438–444 (2011).

[148] D. O. Krimer & S. Flach; "Interaction-induced connectivity of disordered two-particle states"; Phys. Rev. B **91**, p. 100201 (2015).

[149] D. Thongjaomayum, A. Andreanov, T. Engl & S. Flach; "Taming two interacting particles with disorder"; Phys. Rev. B **100**, p. 224203 (2019).

[150] D. Thongjaomayum, S. Flach & A. Andreanov; "Multifractality of correlated two-particle bound states in quasiperiodic chains"; arXiv:2003.00698 (2020)`arXiv:2003.00698[cond-mat.dis-nn]`.

[151] M. Ortuño & E. Cuevas; "Localized to extended states transition for two interacting particles in a two-dimensional random potential"; Europhysics Letters **46**, p. 7 (1999).

[152] D. L. Shepelyansky; "Proceedings of the XXXI Rencontres de Moriond"; in "Correlated fermions and transport in mesoscopic systems," , edited by T. Martin, G. Montambaux & J. Trân Thanh Vân; pp. 201–210 (Editions Frontières, Gif-sur-Yvette, France) (1996).

[153] R. Römer, M. Leadbeater & M. Schreiber; "Numerical results for two interacting particles in a random environment"; Annalen der Physik **8**, pp. 675–684 (1999).

[154] E. Cuevas; "Critical Spectral Statistics in Two-Dimensional Interacting Disordered Systems"; Physical Review Letters **83**, p. 140 (1999).

[155] D. L. Shepelyansky; "Proceedings of the XXXIV Rencontres de Moriond"; in "Quantum Physics at Mesoscopic Scale," , edited by C. Glattli, M. Sanquer & J. Trân Thanh Vân; pp. 99–103 (EDP, ZAP Courtaboeuf, Les Ulis, France) (2000).

[156] D. L. Shepelyansky; "Three-dimensional Anderson transition for two electrons in two dimensions"; Phys. Rev. B **61**, pp. 4588–4591 (2000).

[157] T. Chattaraj; "Localization Parameters for Two Interacting Particles in Disordered Two-Dimensional Finite Lattices"; Condensed Matter **3** (2018). ISSN 2410-3896.

[158] K. Slevin & T. Ohtsuki; "Corrections to Scaling at the Anderson Transition"; Phys. Rev. Lett. **82**, pp. 382–385 (1999).

[159] K. Slevin, Y. Asada & L. I. Deych; "Fluctuations of the Lyapunov exponent in two-dimensional disordered systems"; Phys. Rev. B **70**, p. 054201 (2004).

[160] V. I. Oseledets; "A multiplicative ergodic theorem. Characteristic Ljapunov, exponents of dynamical systems"; Transactions of the Moscow Mathematical Society **19**, pp. 197–231 (1968).

[161] A. MacKinnon & B. Kramer; "The scaling theory of electrons in disordered solids: Additional numerical results"; Zeitschrift für Physik B Condensed Matter **53**, pp. 1–13 (1983). ISSN 1431-584X.

[162] G. H. Golub & C. F. van Loan (Editors); *Matrix Computations*; 3rd edition (Johns Hopkins University Press, Baltimore) (1996).

[163] G. S. Joyce; "On the cubic modular transformation and the cubic lattice Green functions"; Journal of Physics A: Mathematical and General **31**, pp. 5105–5115 (1998).

[164] G. Rickayzen; *Green's Functions and Condensed Matter*; 1st edition (Academic Press, London) (1980).

[165] G. Dufour & G. Orso; "Anderson Localization of Pairs in Bichromatic Optical Lattices"; Phys. Rev. Lett. **109**, p. 155306 (2012).

[166] H.-Y. Xie; *Anderson localization in disordered systems with competing channels*; Ph.D. thesis; Scuola Internazionale Superiore di Studi Avanzati, Trieste (2012).

[167] J. Jain, H. Li, S. Cauley, C.-K. Koh & V. Balakrishnan; “Numerically Stable Algorithms for Inversion of Block Tridiagonal and Banded Matrices”; Purdue Electrical and Computer Engineering Technical Reports p. 13 (2007).

[168] T. Brandes & S. Kettemann (Editors); *Anderson Localization and Its Ramifications*; Lecture Notes in Physics (Springer-Verlag Berlin Heidelberg) (2003).

[169] C. M. Soukoulis, X. Wang, Q. Li & M. M. Sigalas; “What is the Right Form of the Probability Distribution of the Conductance at the Mobility Edge?” Phys. Rev. Lett. **82**, pp. 668–668 (1999).

[170] D. Braun, G. Montambaux & M. Pascaud; “Boundary Conditions at the Mobility Edge”; Phys. Rev. Lett. **81**, pp. 1062–1065 (1998).

[171] M. Campostrini, M. Hasenbusch, A. Pelissetto, P. Rossi & E. Vicari; “Critical behavior of the three-dimensional XY universality class”; Phys. Rev. B **63**, p. 214503 (2001).

[172] V. Privman, P. C. Hohenberg & A. Aharony; “Universal Critical-Point Amplitude Relations”; in “Phase Transitions and Critical Phenomena,” , volume 14, edited by C. Domb & J. L. Lebowitz; chapter 1 (Academic Press, New York) (1991).

[173] F. Stellin & G. Orso; “Mobility edge of two interacting particles in three-dimensional random potentials”; Phys. Rev. B **99**, p. 224209 (2019).

[174] K. Byczuk, W. Hofstetter & D. Vollhardt; “Anderson Localization vs. Mott-Hubbard metal-insulator transition in disordered, interacting lattice fermion systems”; International Journal of Modern Physics B **24**, pp. 1727–1755 (2010). `https://doi.org/10.1142/S0217979210064575`.

[175] P. Henseler, J. Kroha & B. Shapiro; “Self-consistent study of Anderson localization in the Anderson-Hubbard model in two and three dimensions”; Phys. Rev. B **78**, p. 235116 (2008).

[176] F. Stellin & G. Orso; “Two-body mobility edge in the Anderson-Hubbard model: molecular versus scattering states”; (2020); `arXiv:2004.03506`.

[177] M. Valiente Cifuentes; *Few quantum particles on one dimensional lattices*; Ph.D. thesis; Humboldt-Universität zu Berlin, Mathematisch-Naturwissenschaftliche Fakultät I (2010).

[178] M. A. Sulangi & J. Zaanen; “Quasiparticle density of states, localization, and distributed disorder in the cuprate superconductors”; Phys. Rev. B **97**, p. 144512 (2018). `https://link.aps.org/doi/10.1103/PhysRevB.97.144512`.

[179] T. Ando; “Numerical study of symmetry effects on localization in two dimensions”; Phys. Rev. B **40**, pp. 5325–5339 (1989).

[180] U. Fastenrath, G. Adams, R. Bundschuh, T. Hermes, B. Raab, I. Schlosser, T. Wehner & T. Wichmann; "Universality in the 2D localization problem"; Physica A: Statistical Mechanics and its Applications **172**, pp. 302 – 308 (1991). ISSN 0378-4371.

[181] T. Kawarabayashi, T. Ohtsuki, K. Slevin & Y. Ono; "Anderson Transition in Three-Dimensional Disordered Systems with Symplectic Symmetry"; Phys. Rev. Lett. **77**, pp. 3593–3596 (1996).

[182] L. Schweitzer & I. K. Zharekeshev; "Scaling of level statistics and critical exponent of disordered two-dimensional symplectic systems"; Journal of Physics: Condensed Matter **9**, pp. L441–L445 (1997).

[183] Y. Asada, K. Slevin & T. Ohtsuki; "The Anderson Transition in Two-Dimensional Systems with Spin-Orbit Coupling"; Phys. Rev. Lett. **89**, p. 256601 (2002).

[184] Y. Asada, K. Slevin & T. Ohtsuki; "Numerical estimation of the β-function in 2D systems with spin-orbit coupling"; Phys. Rev. B **70**, p. 035115 (2004).

[185] S. Datta & B. Das; "Electronic analog of the electro-optic modulator"; Applied Physics Letters **56**, pp. 665–667 (1990). `https://doi.org/10.1063/1.102730`.

[186] B. A. Bernevig, T. L. Hughes & S.-C. Zhang; "Quantum Spin Hall Effect and Topological Phase Transition in HgTe Quantum Wells"; Science **314**, pp. 1757–1761 (2006). ISSN 0036-8075.

[187] H. Zhai; "Degenerate Quantum Gases with Spin-Orbit Coupling"; Rep. Prog. Phys. **78**, p. 026001 (2015).

[188] L. Huang, Z. Meng, P. Wang, P. Peng, S.-L. Zhang, L. Chen, D. Li, Q. Zhou & J. Zhang; "Experimental realization of two-dimensional synthetic spin–orbit coupling in ultracold Fermi gases"; Nat. Phys. **12**, p. 540 (2016).

[189] D. Clément, A. F. Varón, J. A. Retter, L. Sanchez-Palencia, A. Aspect & P. Bouyer; "Experimental study of the transport of coherent interacting matter-waves in a 1D random potential induced by laser speckle"; New Journal of Physics **8**, pp. 165–165 (2006).

[190] Y. A. Bychkov & E. I. Rashba; "Oscillatory effects and the magnetic susceptibility of carriers in inversion layers"; Journal of Physics C: Solid State Physics **17**, pp. 6039–6045 (1984). `https://doi.org/10.10888/0022-3719/17/33/015`.

[191] G. Orso; "Anderson Transition of Cold Atoms with Synthetic Spin-Orbit Coupling in Two-Dimensional Speckle Potentials"; Phys. Rev. Lett. **118**, p. 105301 (2017).

[192] V. Galitski & I. B. Spielman; "Spin–orbit coupling in quantum gases"; Nature **494**, pp. 49–54 (2013).

[193] D. Delande & G. Orso; “Mobility Edge for Cold Atoms in Laser Speckle Potentials”; Phys. Rev. Lett. **113**, p. 060601 (2014).

[194] P. Bouyer; “Quantum gases and optical speckle: a new tool to simulate disordered quantum systems”; Reports on Progress in Physics **73**, p. 062401 (2010).

[195] M. Piraud & L. Sanchez-Palencia; “Tailoring Anderson localization by disorder correlations in 1D speckle potentials”; Eur. Phys. J. Spec. Top. **217**, pp. 91–102 (2013).

[196] R. C. Kuhn, C. Miniatura, D. Delande, O. Sigwarth & C. A. Müller; “Localization of Matter Waves in Two-Dimensional Disordered Optical Potentials”; Phys. Rev. Lett. **95**, p. 250403 (2005).

[197] R. Zimmermann & C. Schindler; “Coherent potential approximation for spatially correlated disorder”; Phys. Rev. B **80**, p. 144202 (2009).

[198] G. Dresselhaus; “Spin-Orbit Coupling Effects in Zinc Blende Structures”; Phys. Rev. **100**, pp. 580–586 (1955).

[199] D. L. Campbell, G. Juzeliūnas & I. B. Spielman; “Realistic Rashba and Dresselhaus spin-orbit coupling for neutral atoms”; Phys. Rev. A **84**, p. 025602 (2011).

[200] F. G. Pikus & G. E. Pikus; “Conduction-band spin splitting and negative magnetoresistance in A_3B_5 heterostructures”; Phys. Rev. B **51**, pp. 16928–16935 (1995).

[201] B. A. Bernevig, J. Orenstein & S.-C. Zhang; “Exact SU(2) Symmetry and Persistent Spin Helix in a Spin-Orbit Coupled System”; Phys. Rev. Lett. **97**, p. 236601 (2006).

[202] J. D. Koralek, C. P. Weber, J. Orenstein, B. A. Bernevig, S.-C. Zhang, S. Mack & D. D. Awschalom; “Emergence of the persistent spin helix in semiconductor quantum wells”; Nature **458**, pp. 610–613 (2009).

[203] F. J. Wegner; “Crossover of the mobility edge behaviour”; Nuclear Physics B **270**, pp. 1 – 9 (1986). ISSN 0550-3213.

[204] D. Jung, S. Kettemann & K. Slevin; “Anderson metal-insulator transitions with classical magnetic impurities”; Phys. Rev. B **93**, p. 134203 (2016).

[205] M. V. Feigel’man & L. B. Ioffe; “Superfluid density of a pseudogapped superconductor near the superconductor-insulator transition”; Phys. Rev. B **92**, p. 100509 (2015).

[206] C. E. Porter; *Statistical Theories of Spectra: Fluctuations* (Academic Press, New York) (1965).

[207] S. Evangelou; *Random Matrix Theory and Anderson Localisation*; pp. 375–381 (Springer US, Boston, MA) (1991); ISBN 978-1-4684-5940-1.

[208] O. Bohigas, M. J. Giannoni & C. Schmit; "Characterization of Chaotic Quantum Spectra and Universality of Level Fluctuation Laws"; Phys. Rev. Lett. **52**, pp. 1–4 (1984).

[209] E. Tarquini; *Anderson Localization in high dimensional lattices*; Ph.D. thesis; Université Paris-Sud (2016).

[210] V. M. Barry & M. Tabor; "Level clustering in the regular spectrum"; Proc. R. Soc. Lond. A **356** (1977).

[211] Y. V. Fyodorov & A. D. Mirlin; "Statistical properties of random banded matrices with strongly fluctuating diagonal elements"; Phys. Rev. B **52**, pp. R11580–R11583 (1995).

[212] S. D. Geraedts, R. Nandkishore & N. Regnault; "Many-body localization and thermalization: Insights from the entanglement spectrum"; Phys. Rev. B **93**, p. 174202 (2016).

[213] P. Roushan, C. Neill, J. Tangpanitanon, V. M. Bastidas, A. Megrant, R. Barends, Y. Chen, Z. Chen, B. Chiaro, A. Dunsworth, A. Fowler, B. Foxen, M. Giustina, E. Jeffrey, J. Kelly, E. Lucero, J. Mutus, M. Neeley, C. Quintana, D. Sank, A. Vainsencher, J. Wenner, T. White, H. Neven, D. G. Angelakis & J. Martinis; "Spectroscopic signatures of localization with interacting photons in superconducting qubits"; Science **358**, pp. 1175–1179 (2017). ISSN 0036-8075.

[214] E. Fratini & S. Pilati; "Anderson localization of matter waves in quantum-chaos theory"; Phys. Rev. A **91**, p. 061601 (2015).